Some Electrochemical Aspects of the Becher Process

Yadran Marinovich B. Sc. (Hons.)

This thesis is presented for the degree of Doctor of Philosophy of

Murdoch University

1997

I declare that this thesis is my own account of my research and contains as its main content work which has not been previously submitted for a degree at any tertiary institution.

Yadran Marinovich

Abstract

The Becher process is used to upgrade ilmenite (~60% TiO_2) to synthetic rutile (92-95% TiO_2). Reduced ilmenite ($FeTiO_2$) is an intermediate mineral product and the industrial process whereby metallic iron is corroded from the TiO_2 matrix (leaving synthetic rutile) using air and ammonium chloride solutions is termed aeration. This thesis is concerned with the electrochemistry of the corrosion reaction that is the heart of this aeration step.

Synthetic rutile is almost exclusively used as a feedstock for the chloride process which produces pigment grade TiO_2. The Becher process is but one a number of processes that produce feedstocks for the chloride process. Together with the Becher process, these alternative processes are briefly reviewed in Chapter 1 followed by a detailed review of the Becher aeration step. Also included in Chapter 1 is a brief review of the thermodynamics for the iron-water system and, following a literature review on ferrous-ammine chemistry, a new Eh-pH diagram for the iron-water-ammonia system is presented using recently published data.

The investigation of the electrochemistry of anodic iron dissolution in Chapter 3 reveals some interesting results about the influence of aqueous NH_4Cl. An air-formed film only a few monolayers thick (9-18 Å) passivates iron after surface preparation. Ammonium ion is responsible for the rapid removal of this film after immersion which then allows fast active dissolution to occur upon anodic polarisation. Without ammonium ion the air-formed film passivates the iron during polarisation. Ammonium ion also increases the active dissolution current density while chloride inhibits active dissolution. However, chloride is responsible for breaking down the air- and anodically-formed films at relatively high anodic potentials. The activation energy for anodic iron dissolution in 0.2 M NH_4Cl up to 150°C is reported.

In Chapter 4 it is shown that oxygen is reduced on iron via a 4-electron mechanism in air-saturated 0.2 M NH_4Cl and that reduction is diffusion controlled. On gold, every oxygen molecule requires between 0 and 4 electrons depending on the potential. The oxygen reduction current density is proportional to the oxygen partial pressure up to 300 kPa. At 300 kPa oxygen partial pressure, the current density nearly doubled between 80 and 130°C due to the combination of three different effects.

In Chapter 5 it is shown that in air-saturated 0.2 M NH_4Cl the air-formed film inhibits iron corrosion for the first 20 to 30 minutes but then is removed allowing iron to

corrode quickly and uniformly. γ-FeOOH forms continuously as a porous film adhering to the surface and begins to inhibit corrosion only after 3 hours immersion. Ammonium ion is necessary for the removal of the air-formed film while chloride alone results in the localised breakdown of the film leading to pitting corrosion. However, above pH 7.5, the air-formed film is stable even in the presence of ammonium ion and, in the presence of chloride, pitting corrosion also results. Even though iron corrosion is essentially oxygen diffusion controlled at ambient pressures, the corrosion rate is not proportional to the oxygen partial pressure due to the formation of a thick γ-FeOOH film. Increasing the temperature to above 80°C increases the corrosion rate at high pressure largely due to solubilisation of the thick film.

A novel application of the carbon paste electrode technique to the investigation of the electrochemistry of anodic iron dissolution from whole reduced ilmenite grains is described in Chapter 6. Anodic dissolution is potential dependent but strongly limited by an air-formed passive film. Ammonium ions do not assist in the removal of this film; rather, chloride ions were found to increase the anodic current density by assisting in the breakdown of the air-formed passive film. Also presented in this Chapter is some preliminary evidence linking the variability of the aeration time with the stability of the air-formed film: the less stable the air-formed film, the shorter the aeration time.

Contents

Abstract *i*

Contents *iii*

List of Figures *vii*

List of Tables *xiii*

List of Symbols *xiv*

Publications *xvi*

Acknowledgments *xvii*

1. Introduction *1*

1.1 UPGRADING TITANIFEROUS MINERALS 1

1.1.1 Commercial production of feedstock for TiO_2 pigment production 2

1.1.1.1 Slagging 2

1.1.1.2 The Becher process 2

1.1.1.3 The Benelite process 3

1.1.1.4 The Ishihara process 4

1.1.2 Other methods of producing synthetic rutile 4

1.1.2.1 Ball milling 4

1.1.2.2 High pressure selective acid leaching 4

1.1.2.3 Selective chlorination 5

1.1.2.4 The Murso process 5

1.1.2.5 The Summit process 5

1.1.3 TiO_2 Pigment Production 6

1.1.3.1 The sulphate process 6

1.1.3.2 The chloride process 6

1.2 THE AERATION STEP OF THE BECHER PROCESS 6

1.3 THERMODYNAMICS FOR THE IRON-WATER AND IRON-WATER-AMMONIA SYSTEM 12

1.3.1 The iron-water system 12

1.3.2 The iron-water-ammonia system at 25°C 14

1.3.2.1 New activity-pH and Eh-pH diagrams for the iron-water-ammonia system at 25℃ 17

1.4 AIMS OF THIS WORK 22

2. Experimental *23*

2.1 AMBIENT PRESSURE ELECTROCHEMISTRY 23

2.1.1 Electrodes 23

2.1.2 Equipment 23

2.1.3 Solutions 23

2.2 HIGH PRESSURE ELECTROCHEMISTRY 24

2.2.1 Electrodes 24

2.2.2 Equipment 24

2.2.3 Solutions 26

3. The Anodic Dissolution of Pure Iron *27*

3.1 INTRODUCTION 27

3.1.1 Electrochemistry of iron in slightly acid solutions 27

3.1.2 Influence of ammonia and chloride on iron electrochemistry 30

3.1.2.1 Ammonia 30

3.1.2.2 Chloride ion 31

3.2 EXPERIMENTAL 32

3.3 RESULTS AND DISCUSSION 32

3.3.1 Influence of electrolyte composition on iron electrochemistry at 30°C 32

3.3.1.1 $NaClO_4$ 33

3.3.1.2 NaCl 36

3.3.1.3 NH_4ClO_4 39

3.3.1.4 NH_4NO_3 42

3.3.1.5 NH_4Cl 44

3.3.1.6 Effect of Ammonium and Chloride Ions 48

3.3.2 The pH dependence of anodic iron dissolution in 0.2 M NH_4Cl at 30°C 50

3.3.3 Temperature dependence of anodic iron dissolution in 0.2 NH_4Cl 55

3.4 CONCLUSIONS 57

4. The Electrochemical Reduction of Oxygen *58*

4.1 INTRODUCTION 58

4.1.1 Oxygen reduction on iron and steel 60

4.1.2 Oxygen reduction on gold 61

4.1.3 Oxygen solubility as a function of temperature and partial pressure 62

4.2 EXPERIMENTAL 64

4.3 RESULTS AND DISCUSSION 65

4.3.1 Oxygen reduction on pure iron 65

4.3.1.1 Air-saturated 0.2 M NH_4Cl at 30°C 65

4.3.1.2 The effect of pH 68

4.3.2 Oxygen reduction on pure gold 70

4.3.2.1 Air-saturated 0.2 M NH_4Cl at 30°C 70

4.3.2.2 Oxygen reduction at high temperature and pressure 74

4.4 CONCLUSIONS 78

5. Aqueous Corrosion of Pure Iron by Dissolved Oxygen79

5.1 INTRODUCTION 79

5.1.1 Corrosion mechanisms 80

5.1.2 Corrosion rates 80

5.1.2.1 The meaning of the polarisation resistance (R_p) and the calculation of a corrosion rate 80

5.1.2.2 Linear Polarisation (LP) 82

5.1.2.3 Potentiodynamic polarisation or the Tafel technique 83

5.1.2.4 Electrochemical Impedance Spectroscopy (EIS) 84

5.1.3 Corrosion of iron by dissolved oxygen in mildly acidic and neutral aqueous solutions – a literature review. 89

5.2 EXPERIMENTAL 95

5.2.1 Ambient pressure electrochemistry 95

5.2.1.1 Solutions 95

5.2.1.2 Equipment 95

5.2.2 High pressure electrochemistry 95

5.2.2.1 Solutions 95

5.3 RESULTS AND DISCUSSION 96

5.3.1 Corrosion of pure iron in air-saturated 0.2 M NH_4Cl 96

5.3.1.1 The effect of immersion time 96

5.3.1.2 The effect of pH 99

5.3.1.3 The effect of temperature 100

5.3.1.4 The effect of electrode rotation speed 103

5.3.1.5 The effect of electrolyte composition 107

5.3.1.6 The effect of anodic and cathodic polarisation 109

5.3.2 Corrosion of pure iron at elevated oxygen partial pressures in 0.2 M NH_4Cl. 111

5.3.2.1 The effect of oxygen partial pressure 111

5.3.2.2 The effect of temperature at 300 kPa oxygen partial pressure 113

5.4 CONCLUSIONS 114

6. The Electrochemistry of Reduced Ilmenite 116

6.1 INTRODUCTION 116

6.1.1 Composition and morphology of reduced ilmenite 116

6.2 EXPERIMENTAL 118

6.2.1 Electrodes 118

6.2.1.1 Preparation of carbon pastes 118

6.2.2 Equipment 119

6.2.3 Solutions 119

6.3 RESULTS AND DISCUSSION 119

6.3.1 The Fe^{3+}/Fe^{2+} couple 119

6.3.2 The iron oxide carbon paste electrode 121

6.3.3 Voltammetric study of anodic iron dissolution in model reduced ilmenite systems 123

6.3.3.1 Iron powder carbon paste electrode 124

6.3.3.2 Iron powder-additive carbon paste electrode 126

6.3.4 Voltammetric study of reduced ilmenite 132

6.3.4.1 Reduced ilmenite carbon paste electrode 132
6.3.4.2 Individual reduced ilmenite grains embedded in the surface of a carbon paste electrode 134
6.3.4.3 Comparison of different reduced ilmenites 135
6.3.4.4 The effect of electrolyte composition 137
6.3.4.5 The effect of temperature 139
6.4 CONCLUSIONS 140

7. Conclusions 142
7.1 CONCLUDING REMARKS 142
7.1.1 The variability of the aeration time 142
7.1.2 The intrinsic slowness of aeration 143
7.1.3 The poor understanding of the role of ammonium chloride 143
7.2 SUGGESTIONS FOR FUTURE WORK 144
7.2.1 Reduced ilmenite and the variability of aeration 144
7.2.2 Oxygen corrosion of iron 144
7.2.3 Anodic iron dissolution 145
7.2.4 Iron thermodynamics 145

Appendices 146

Bibliography 148

List of Figures

Figure 1.1 A schematic diagram of the processes and products in the titanium industry. The Becher process is used to upgrade chlorinatable ilmenite to synthetic rutile. 2

Figure 1.2 Eh-pH diagram for the iron-water system at 25°C considering Fe, $Fe(OH)_2$ and γ-FeOOH, from Misawa [36]. 13

Figure 1.3 Eh-pH diagram for the iron-water system at 80°C with iron activity of 0.5 M, from Ward [37]. 14

Figure 1.4 Eh-pH diagram for the iron-water system at 150°C, from Biernat and Robins [38]. 14

Figure 1.5 a) Eh-pH diagram for the iron-water-ammonia system where $[Fe^{2+}] = 10^{-4}$ M and $[NH_4^+] + [NH_3] = 1.0$ M and, b) Activity-pH diagram where $[NH_4^+] + [NH_3] = 1.0$ M and E = -0.3 V (*she*) at 25°C, from reference [46]. 16

Figure 1.6 Ammonia activity-pH diagram for iron-water-ammonia system where $[Fe] = 10^{-4}$ M and Eh = -0.3 V at 25°C, from reference [46]. 16

Figure 1.7 Activity-pH diagram for the Fe^{II} speciation and solubility for a saturated $Fe(OH)_2$ solution at 25°C. Ferrous-ammine thermodynamic data from reference [45]. $[NH_4^+] + [NH_3] = 0.2$ M. 18

Figure 1.8 Activity-pH diagram showing Fe^{II} speciation and solubility for a saturated $Fe(OH)_2$ solution at 25°C. Ferrous-ammine thermodynamic data from reference [41]. $[NH_4^+] + [NH_3] = 0.2$ M. 19

Figure 1.9 Measured and calculated total Fe^{II} solubilities at 25°C. Calculated from the thermodynamic data in Table 1.2. 20

Figure 1.11 Calculated Eh-pH diagram for the iron-water-ammonia system. [Fe] $= 1\times10^{-3}$ M. $[NH_4^+] + [NH_3] = 1$ M and $[NH_4^+] + [NH_3] = 5$ M. The area of difference for $[NH_4^+] + [NH_3] = 1$ M is shown as a dotted line. The dashed lines represent the limits of stability for water. 21

Figure 2.1 Schematic diagram of the high pressure high temperature rotating disc electrode assembly. 25

Figure 3.1 Cyclic voltammograms for an iron rotating disc electrode (1000 rpm) in 0.2 M $NaClO_4$ at 50 mV s^{-1}. Anodic scan started from the open circuit potential (OCP). Cycle number indicated. T = 30.0°C. pH = 6.5. 33

Figure 3.2 Cyclic voltammograms for a stationary iron disc electrode in 0.2 M $NaClO_4$ at 50 mV s^{-1}. Anodic scan started from the open circuit potential (OCP). Cycle number indicated. T = 30.0°C. pH = 6.5. 35

Figure 3.3 Cyclic voltammograms for an iron rotating disc electrode (1000 rpm) in 0.2 M NaCl at 50 mV s^{-1}. Anodic scan started from the open circuit potential. T = 30.0°C. pH = 6.6. 37

Figure 3.4 Cyclic voltammograms for a stationary iron disc in 0.2 M NaCl at 50 mV s^{-1}. Cathodic scan started from the open circuit potential. Cycle number indicated; (·····) = second cathodic going scan after sweep reversal at E_{Ra} = 0.1 V. T = 30.0°C. pH = 6.6. Inset: 1st anodic scan with expanded current scale. 38

Figure 3.5 Cyclic voltammogram for a stationary iron disc in 0.2 M NaCl at 50 mV s^{-1}. Anodic scan started from the open circuit potential. T = 30.0°C. pH = 6.6. 39

Figure 3.6 Cyclic voltammogram for an iron rotating disc electrode (1000 rpm) in 0.2 M NH_4ClO_4 at 50 mV s^{-1}. Anodic scan started from the open circuit potential (OCP). T = 30.0°C. pH = 5.3. 40

Figure 3.7 Cyclic voltammograms for a stationary iron disc electrode in 0.2 M NH_4ClO_4 at 50 mV s^{-1} showing the effect of cathodic reversal potential (E_{Rc}). Cycle number indicated. T = 30.0°C. pH = 5.3. 41

Figure 3.8 Cyclic voltammogram for an iron rotating disc electrode (1000 rpm) in 0.2 M NH_4NO_3 at 50 mV s^{-1}. Cathodic scan started from the open circuit potential (OCP). T = 30.0°C. pH = 5.6. 42

Figure 3.9 Cyclic voltammograms for a stationary rotating disc electrode in 0.2 M NH_4NO_3 at 50 mV s^{-1}. Cathodic scan started from the open circuit potential. T = 30.0°C. pH = 5.6. Inset: Expanded current scale. 43

Figure 3.10 Cyclic voltammogram for an iron rotating disc electrode (1000 rpm) in 0.2 M NH_4Cl at 50 mV s^{-1}. Anodic scan started from the open circuit potential (OCP). T = 30.0°C. pH = 4.8. 45

Figure 3.11 Cyclic voltammograms for a stationary iron disc electrode in 0.2 M NH_4Cl at 50 mV s^{-1}. Anodic scan started from the open circuit potential (OCP). Cycle number indicated. T = 30.0°C. pH = 4.8. 45

Figure 3.12 Cyclic voltammograms for a stationary iron disc electrode in 0.2 M NH_4Cl at 50 mV s^{-1}. Anodic scan started from the open circuit potential (OCP). (a) 0 s wait time at OCP and (b) 22 s wait time at OCP after the first potential cycle. Cycle number indicated. T = 30.0 °C. pH = 4.8. 46

Figure 3.13 Cyclic voltammogram for a stationary iron disc electrode in 0.2 M NH_4Cl containing 4.5 mM Fe^{2+} at 50 mV s^{-1}. Cathodic scan initiated from the open circuit potential. Cycle number indicated. T = 30.0°C. 47

Figure 3.14 Cyclic voltammograms for an iron rotating disc electrode in various 0.2 M electrolyte solutions at 50 mV s^{-1}. T = 30.0°C. 49

Figure 3.15 The open circuit potential (OCP) for an iron rotating disc electrode (1000 rpm) in 0.2 M NH_4Cl as a function of pH. T = 30.0°C. Immersion time = 5 minutes. 50

Figure 3.16 Anodic polarisation curves for an iron rotating disc electrode (1000 rpm) in 0.2 M NH_4Cl as a function of pH at 1 mV s^{-1}. T = 30.0°C. 51

Figure 3.17 a) Peak potential (E_{pII}) and b) the logarithm of the peak current (I_{pII}) as a function of pH, from Figure 3.16. 54

Figure 3.18 Anodic polarisation curves for an iron rotating disc electrode (1000 rpm) in 0.2 M NH_4Cl at various temperatures at 1 mV s^{-1}. pN_2 = 300 kPa. 55

Figure 3.19 Arrhenius plot for anodic iron dissolution at -0.60 V, from Figure 3.18. 56

Figure 4.1 Solubility of oxygen in pure water as a function of temperature, and at various oxygen partial pressures, calculated using equation (4.14) (⋯○⋯) and equation (4.15) (—■—). 63

Figure 4.2 Potentiodynamic (————, 10 mV s^{-1}) and potentiostatic (- - - -◇- - - -) polarisation curves for oxygen reduction on iron in air-saturated 0.2 M NH_4Cl at various electrode rotation speeds. T = 30.0°C. 65

Figure 4.3 Levich plot for oxygen reduction on iron in air-saturated 0.2 M NH_4Cl at -0.8 V from Figure 4.2. 66

Figure 4.4 Dependence of i^{-1} against $\omega^{-1/2}$ for potentiostatic oxygen reduction on iron in air-saturated 0.2 M NH_4Cl at different potentials. T = 30.0°C. 67

Figure 4.5 Dependence of i^{-1} against $\omega^{-1/2}$ for potentiodynamic oxygen reduction on iron in air-saturated 0.2 M NH_4Cl at different potentials. T = 30.0°C. 68

Figure 4.6 Potentiodynamic polarisation curves for oxygen reduction on an iron rotating disc electrode (1000 rpm) in air-saturated 0.2 M NH_4Cl at various pH values. T = 30.0°C. 69

Figure 4.7 Potentiodynamic (————, 10 mV s^{-1}) and potentiostatic (- - - -◇- - - -) polarisation curves for oxygen reduction on gold in air-saturated 0.2 M NH_4Cl at various rotation speeds. T = 30.0°C. 70

Figure 4.8 Levich plots for potentiostatic oxygen reduction on gold in air-saturated 0.2 M NH_4Cl at different potentials. T = 30.0°C. 71

Figure 4.9 Levich plot for potentiodynamic oxygen reduction on gold in air-saturated 0.2 M NH_4Cl at different potentials. T = 30.0°C. 72

Figure 4.10 Koutecky-Levich plot for potentiostatic oxygen reduction on gold in air-saturated 0.2 M NH_4Cl at various potentials. T = 30.0°C. 73

Figure 4.11 Koutecky-Levich plot for potentiodynamic oxygen reduction on gold in air-saturated 0.2 M NH_4Cl at different potentials. T = 30.0°C. 74

Figure 4.12 Potentiodynamic (10 mV s^{-1}) polarisation curves for oxygen reduction (pO_2 = 300 kPa) on a gold rotating disc electrode (1000 rpm) in 0.2 M NH_4Cl at various temperatures. 75

Figure 4.13 Potentiodynamic polarisation curves (10 mV s^{-1}) for a gold rotating disc electrode (1000 rpm) in 0.2 M NH_4Cl at different oxygen partial pressures. T = 80°C. 76

Figure 4.14 Diffusion limited current density (i_l) at -0.73 V on a gold rotating disc electrode (1000 rpm) in 0.2 M NH_4Cl as a function of the oxygen partial pressure. T = 80°C. 76

Figure 4.15 Potentiodynamic polarisation curves (10 mV s^{-1}) for oxygen reduction on gold in 0.2 M NH_4Cl at various electrode rotation speeds. pO_2 = 285 kPa. T = 150°C. 77

Figure 4.16 Levich plot for oxygen reduction on gold in oxygen saturated 0.2 M NH_4Cl at -0.63 V. pO_2 = 285 kPa. T = 150°C. 77

Figure 5.1 A simple equivalent circuit. 84

Figure 5.2 Commonly used graphical representations of corrosion impedance data. Schematic plots for the impedance response of the equivalent circuit in Figure 5.1 a) Nyquist plot, b) Bode phase angle plot and c) Bode |Z| plot. 86

Figure 5.3 A schematic diagram of a Nyquist plot exhibiting a capacitive and an inductive loop. Modified from Epelboin *et al.* [87]. 87

Figure 5.4 An equivalent circuit including a Warburg semi-infinite diffusion impedance component (*W*). 89

Figure 5.5 Schematic Nyquist plot showing the impedance response of the Warburg equivalent circuit in Figure 5.4. 89

Figure 5.6 Typical trends in R_p (from LP) and E_{corr} as a function of immersion time for an iron rotating disc electrode (1000 rpm) in air-saturated 0.2 M NH_4Cl. T = 30.0°C. 96

Figure 5.7 FTIR spectrum of the corrosion product from an iron rotating disc electrode in air-saturated 0.2 M NH_4Cl. Italicised bold numbers are infrared bands for γ-FeOOH [156]. Note: ***b*** = broad. 97

Figure 5.8 Nyquist EIS plots for an iron rotating disc electrode (1000 rpm) in air-saturated 0.2 M NH_4Cl at various immersion times. T = 30.0°C. 98

Figure 5.9 R_p (from LP, 20 minutes after immersion) for an iron rotating disc electrode (1000 rpm) as a function of pH in air-saturated 0.2 M NH_4Cl. At pH 8.14, R_p was measured using EIS. T = 30.0°C. 99

Figure 5.10 Polarisation resistance (R_p) (from LP and EIS, 50 minutes after immersion) for an iron rotating disc electrode (1000 rpm) in air-saturated 0.2 M NH_4Cl as a function of temperature. The error bars indicate twice the standard error in the mean. 101

Figure 5.11 Corrosion potential (E_{corr}) for an iron rotating disc electrode (1000 rpm) in air-saturated 0.2 M NH_4Cl as a function of temperature. The error bars indicate twice the standard error in the mean. 102

Figure 5.12 Polarisation curves for an iron rotating disc electrode (1000 rpm) in air-saturated 0.2 M NH_4Cl at various temperatures at 10 mV s^{-1}. 75 minutes after immersion. 103

Figure 5.13 Polarisation resistance (R_p) for an iron disc electrode in air-saturated 0.2 M NH_4Cl (from LP and EIS) as a function of electrode rotation speed. T = 30.0°C. 104

Figure 5.14 Experimental (hollow markers) and calculated (———) Nyquist plots for iron in air-saturated 0.2 M NH_4Cl at various electrode rotation speeds. T = 30.0°C. 105

Figure 5.15 Experimental (hollow markers) and calculated (———) Bode Z′ plots for iron in air-saturated 0.2 M NH_4Cl at various electrode rotation speeds. T = 30.0°C. 105

Figure 5.16 Potentiodynamic polarisation curves for iron in air-saturated 0.2 M NH_4Cl at different electrode rotation speeds. Scan rate = 1 mV s^{-1}. T = 28°C. 107

Figure 5.17 Potentiodynamic polarisation curves for an iron rotating disc electrode (1000 rpm) in air-saturated 0.2 M solutions of various electrolytes. T = 30.0°C. Scan rate = 1 mV s^{-1}. 108

Figure 5.18 Experimental (hollow markers) and calculated (———) Nyquist EIS plots for an iron rotating disc electrode (1000 rpm) in air-saturated 0.2 M NH_4Cl at various overpotentials with respect to the corrosion potential (E_{corr}). T = 30.0°C. 30 minutes after immersion. 110

Figure 5.19 Polarisation resistance (R_p) for an iron rotating disc electrode (1000 rpm) in 0.2 M NH_4Cl as a function oxygen partial pressure. 60 minutes immersion. T = 30°C 112

Figure 5.20 Polarisation resistance (R_p) for an iron rotating disc electrode (1000 rpm) in 0.2 M NH_4Cl as a function of immersion time at 300 kPa oxygen partial pressure. T = 30°C. 113

Figure 5.21 Polarisation resistance (R_p) for an rotating iron disc electrode (1000 rpm) in 0.2 M NH_4Cl as a function of temperature at 300 kPa oxygen partial pressure. T = 30°C. 114

Figure 6.1 Cyclic voltammograms for (a) 1mM Fe^{2+} and (b) FeOOH sol (1 mM Fe^{3+}) in 0.2 M NH_4Cl solution with a stationary (———) and rotating (1000 rpm, ---------) carbon paste disc electrode at 50mV s^{-1}. Cycle number indicated. T = 30°C. 120

Figure 6.2 Cyclic voltammograms for a stationary lepidocrocite carbon paste disc electrode (1:19 γ-FeOOH:carbon paste by weight) in 0.2 M NH_4Cl at 50 mV s^{-1}. Cycle number indicated. T = 30.0°C. 122

Figure 6.3 Cyclic voltammograms for Koch Light iron powder in 0.2 M NH_4Cl at 50 mV s^{-1}. The effect of different iron powder:carbon paste weight ratios. Inset: Cyclic voltammograms with expanded current density scale (First cycle only). T = 30.0°C. 124

Figure 6.4 Cyclic voltammogram for Johnson Matthey (———) and Koch Light (---------) iron powders in 0.2 M NH_4Cl with a carbon paste (1:15, iron:carbon paste) electrode at 50 mV s^{-1}. Rotation speed = 1000 rpm. First cycle only. T = 30.0°C. 126

Figure 6.5 Cyclic voltammograms for Koch Light iron powder in 0.2 M NH_4Cl at 50 mV s^{-1}. The effect of different additives: No additive (iron powder only), synthetic rutile (SR 1 and SR 2), natural rutile (Rutile), TiO_2 pigment and alumina. Second cycle only. Rotation speed = 1000 rpm. T = 30.0°C. 127

Figure 6.6 Cyclic voltammograms for Johnson Matthey iron powder in 0.2 M NH_4Cl at 50 mV s^{-1}. The effect of different additives: No additive

(iron powder only), synthetic rutile (SR 1 and SR 2), natural rutile (Rutile), TiO_2 pigment and alumina. Second cycle only. Rotation speed = 1000 rpm. T = 30.0°C. 128

Figure 6.7 Cyclic voltammogram for reduced ilmenite in 0.2 M NH_4Cl at 50 mV s^{-1}. Cycle number indicated. T = 30.0°C. 132

Figure 6.8 Cyclic voltammograms for various iron electrodes in 0.2 M NH_4Cl at 50 mV s^{-1}. Koch Light iron powder with synthetic rutile (KLFe+SR), Johnson Matthey iron powder (JMFe), Koch Light iron powder (KLFe), pure iron disc (Bulk Fe) and reduced ilmenite (RI) with a carbon paste electrode. Stationary electrode except for JMFe (1000 rpm). 133

Figure 6.9 Cyclic voltammograms for a single reduced ilmenite grain embedded on the surface of a carbon paste electrode in 0.2 M NH_4Cl at 50 mV s^{-1}. Stationary electrode. Cycle number indicated. T = 30.0°C. 134

Figure 6.10 Cyclic voltammograms for reduced ilmenite X, Y and Z in 0.2 M NH_4Cl at 50 mV s^{-1}. a) first cycle b) fourth cycle. Rotating electrode (1000 rpm). T = 30.0°C. 136

Figure 6.11 Cyclic voltammograms for reduced ilmenite in different 0.2 M electrolyte solutions at 50 mV s^{-1}. a) NaCl and NH_4Cl and b) NH_4ClO_4 and $NaClO_4$ solutions. Rotating (1000 rpm) carbon paste disc electrode. T= 30.0°C. 137

Figure 6.12 The fourth potential cycle cyclic voltammograms for a rotating (1000 rpm) reduced ilmenite carbon paste electrode in 0.2 M NH_4Cl, $NaClO_4$, NaCl and NH_4ClO_4 at 50 mV s^{-1}. T= 30.0°C. 138

Figure 6.13 Cyclic voltammograms for reduced ilmenite in 0.2 M NH_4Cl at different temperatures. a) first cycle b) fourth cycle. Rotating carbon paste electrode (1000 rpm). Scan rate = 50 mV s^{-1}. 139

List of Tables

Table 1.1 Cumulative formation constants for ferrous-ammine complexes at 25°C. 15

Table 1.2 Gibbs free energy of formation ($G°_{f\ 25°C}$) for the iron-water-ammonia system at 25°C. 17

Table 3.1 Tafel slope for iron in the prepassive range at different pH values, from Figure 3.16. The error bars indicate twice the standard error in the mean. 52

Table 3.2 Tafel slope for iron in the prepassive range at various temperatures, from Figure 3.18. 56

Table 4.1 Number of electrons (n) for oxygen reduction on gold at various potentials, from Figure 4.8 and Figure 4.9. 72

Table 5.1 Corrosion data from Juttner *et al.* [147] for an iron disc electrode in air-saturated 0.5 M Na_2SO_4. pH = 6. T = 25°C. b_a = 0.040 V dec^{-1}. The type of reference electrode was not stated in the original paper. 90

Table 5.2 Corrosion data from Silverman and Carrico [151] for mild steel in air-saturated water at different electrode rotation speeds. T = 32°C. 93

Table 5.3 Corrosion current density (i_{corr}) for iron in air-saturated low conductivity water (solution E, pH = 7.2~7.5) calculated using polarisation resistance (R_p), cathodic (c) and anodic (a) Tafel extrapolation techniques. From Yang *et al.* [152]. T = 29.4°C. *sce* reference. 93

Table 5.4 Corrosion current densities (i_{corr}) calculated from weight loss for iron in 3.5% NaCl at various oxygen partial pressures. From reference No. 67 in [119]. 95

Table 5.5 Fitted equivalent circuit parameters for the EIS data in Figure 5.14. 106

Table 5.6 Polarisation resistance (R_p) and corrosion potential (E_{corr}) for an iron rotating disc electrode (1000 rpm) in various 0.2 M electrolytes 50 minutes after immersion. T = 30.0°C except for NaCl, T = 28.7°C. 108

Table 5.7 Equivalent circuit parameters for iron at various overpotentials with respect to E_{corr}, from Figure 5.18. 30 minutes after immersion. 111

Table 6.1 Anodic current densities for Koch Light and Johnson Matthey iron powder from, Figure 6.5 and Figure 6.6. 129

Table 6.2 Sessile drop contact angles for 0.2 M NH_4Cl on Koch Light and Johnson Matthey iron powder carbon paste containing different additives. T = 22°C. 130

List of Symbols

Symbol	Meaning
ω	Angular frequency, rad s^{-1}. Where $\omega = 2\pi f$
τ	time constant, s
σ	Warburg diffusion coefficient, $\Omega\ s^{-0.5}$
β	Cumulative formation constant
υ	Potential sweep rate, mV s^{-1}
B	Composite Tafel parameter, V
b_a	Anodic Tafel parameter, V
b_c	Cathodic Tafel parameter, V
C_b	Bulk dissolved oxygen concentration, mol cm^{-3}
C_{dl}	Double layer capacitance, F cm^{-2}
C_i	Molarity of species *i*, M
ΔE	Alternating current excitation voltage, V
D	Diffusion coefficient, $cm^2\ s^{-1}$
E	Overpotential, V
E_a	Activation energy, kJ mol^{-1}
E_{corr}	Corrosion potential, V
E_p	Peak potential, V
E_{Ra}	Anodic reversal potential, V
E_{Rc}	Cathodic reversal potential, V
f	Frequency, Hz
F	Faraday constant, 96485 C
Fe_M	Metallic iron content
Fe_T	Total iron content
H	Henry's law constant, kPa
i	Total current density, A cm^{-2}
i_{corr}	Corrosion current density, A cm^{-2}
i_k	Activation controlled current density, A cm^{-2}
i_l	Diffusion limited current density, A cm^{-2}

List of Symbols (continued)

Symbol	Meaning
I_p	Peak current density, A cm^{-2}, mA cm^{-2}
j	$\sqrt{-1}$
k	Rate constant, m s^{-1}
K_i	Solubility constant for species *i*
mpy	mils per year (corrosion rate)
|Z|	Modulus of impedance Z_f, Ω cm^2
α	Constant phase element
n	Number of electrons
ν	Kinematic viscosity, cm^2 s^{-1}
p_g	Gas partial pressure, kPa
Q_a	Anodic charge, C
Q_c	Cathodic charge, C
RC	Resistor-capacitor parallel couple
R_{Me}	Polarisation resistance for metal dissolution, Ω cm^2
R_p	Polarisation resistance, Ω cm^2
R_s	Uncompensated solution resistance, Ω cm^2
R_t	Charge transfer resistance, Ω cm^2
S	Solubility of oxygen in the electrolyte solution, M
S_0	Solubility of oxygen in pure water, M
sce	Saturated calomel electrode
she	Standard hydrogen electrode
t_{corr}	Corrosion time, hours
W	Warburg diffusion impedance, Ω cm^2
x_g	Mole fraction of dissolved gas
Z'	In-phase component of impedance, Ω cm^2
Z''	Out-of-phase component of impedance, Ω cm^2
Z_f	Impedance, Ω cm^2
Z_W	Warburg diffusion impedance, Ω cm^2

Publications

(i) Refereed papers as joint author

"An electrochemical study of reduced ilmenite carbon paste electrodes", Y. Marinovich, S. Bailey, J. Avraamides, and S. Jayasekera, J. App. Electrochem. 25:823 (1995).

"Pressure leaching of reduced ilmenite: electrochemical aspects", S. Jayasekera, Y. Marinovich, J. Avraamides, and S. Bailey, Hydrometallurgy 39:183 (1995).

(ii) Conference Papers (Oral Presentations)

"The corrosion of pure iron by dissolved oxygen in aqueous ammonium chloride", J. Avraamides, S. Bailey, Y. Marinovich, and J. Pang, 10th Australasian Electrochemistry Conference, Goldcoast, 1997.

"An electrochemical investigation of the removal of iron from reduced ilmenite", Y. Marinovich, S. Bailey, J. Avraamides, and S. Jayasekera, AIMM Proc. Conf., 1996; p 237 .

"The electrochemistry of iron corrosion by oxygen from 30 to 150°C in ammonium chloride solutions", Y. Marinovich, Corrosion and Prevention 95, Perth, 1995.

"A high pressure high temperature rotating disk electrode study of iron corrosion by oxygen", Y. Marinovich, S. Jayasekera, S. Bailey, and J. Avraamides, 46th International Society of Electrochemistry Conference, Xiamen, 1995.

Acknowledgments

I wish to express my sincere thanks and appreciation to my supervisors, each of whom have contributed uniquely to this work. Dr Stuart Bailey for his advice, encouragement and for his valued friendship. Dr Jim Avraamides for his efficient professionalism and guidance. Dr James Pang for his ever pragmatic and direct advice. And Professor Ritchie for his depth of understanding.

Financial support from Murdoch University, the A. J. Parker Cooperative Research Centre for Hydrometallurgy and the Minerals and Energy Research Institute of Western Australia is gratefully acknowledged.

To all of the staff of the school of Applied Chemistry, past and present, I thank you for making my stay in the department professionally rewarding and personally enriching. Some people deserve a special mention: Professor Jeff Dunn and Mr Barry Thornton for their experienced advice and understanding; Dr Bill van Bronswijk for efficiently modifying his DAPA boards so they could be used on the M173 potentiostat; Dr Peter Sheppard, who gets things done with little fuss and with a smile too; Mr David Walton for his invaluable work in constructing electrodes and other special equipment.

The design and construction of the high pressure high temperature rotating disc electrode system by Dr S Jayasekera and the staff at the Mineral Processing Laboratory is gratefully acknowledged. I am also grateful to Mr Kleber Klaux at Murdoch University for sharing his rotating disc electrode construction expertise and to Mr Jialong Zheng for the use of his data acquisition software.

Special thanks to Mr Brian Kinsella for his exceptional kindness for which I am most grateful. Ms Jean Edwards for her countless kindnesses. Thanks to Dr Yong-jun Tan for being a constant source of inspiration throughout this work. I owe many thanks to Raymond Homsany, Nick Welham and David Atkins for their friendship and support. I wish to thank the Himeji Institute of Technology for their inaugural summer seminar program which I found so rewarding. I especially wish to thank Dr Ouchi and Professor Sugie.

Finally, to my Mother and Father, Dennis, Katica and Graeme to whom I owe the most. I love you all very much.

1 Introduction

The Becher process is used in Western Australia to convert some of the state's abundant ilmenite reserves to synthetic rutile which is worth around 6 times as much as ilmenite. In 1993-94, the total value of heavy mineral sand exports from Western Australia was $318 million. Synthetic rutile sales amounted to $154 million and accounted for the largest share of this industry's value [1]. For 1996 it was forecast that Australia will export 353 000 tons of synthetic rutile worth $201 million [2]. This amount represents around 60% of the world's total output of synthetic rutile.

This Chapter is divided into three sections. The first section describes current industrial processes used for upgrading titanium minerals for the production of titanium dioxide pigment and for the production of feedstock for these pigment processes, of which the Becher process is but one. The second section is a detailed review of the literature on the aeration step of the Becher process. The third section is a summary of the thermodynamics of the iron-water and iron-water-ammonia systems which are relevant to the aeration step. Finally, the objectives of this research are detailed.

1.1 UPGRADING TITANIFEROUS MINERALS

Figure 1.1 provides a schematic summary of the processes and products in the titanium industry, some of which will be described in more detail in the next section. Pigment is produced by two different paths: the chloride process and the sulphate process. Most of the future growth in pigment production is expected to be via the chloride process rather than the sulphate process; this trend is already evident [3]. Due to reserves of natural rutile – the traditional feedstock for the chloride process – not being able to meet demand, alternative feedstocks have been sought. Ilmenite, is an abundant titaniferous mineral however its TiO_2 content is, in most cases, too low to be a suitable feedstock for the chloride process. The Becher process is one of four commercial processes used to produce a feedstock for the chloride process from ilmenite.

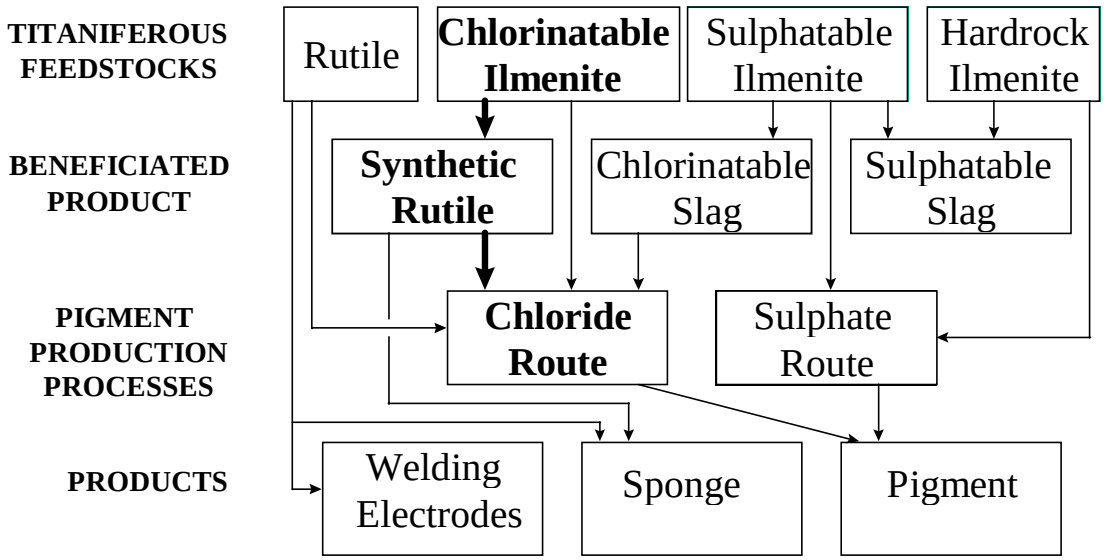

Figure 1.1 A schematic diagram of the processes and products in the titanium industry. The Becher process is used to upgrade chlorinatable ilmenite to synthetic rutile.

1.1.1 Commercial production of feedstock for TiO_2 pigment production

The feedstock production processes are listed below in order of decreasing global production.

1.1.1.1 Slagging

Slagging is a purely pyrometallurgical process that involves smelting ilmenite at high temperatures. Current operations using this process produce pig iron and a slag containing from 71-90% TiO_2 depending on the plant [3]. The smelting process removes only iron oxide while other non reducible oxides, such as MgO and CaO, remain in the slag. The major advantage of this technique is that pig iron is a saleable by-product which assists in the economics. Major producers include Quebec Iron and Titanium (QIT) in Sorel Canada and Richards Bay Minerals Tisand, Richards Bay South Africa. Other producers include K/S Ilmenitt Smelteverket in Norway and smaller plants are located at Sichuan and Guangxi in China.

1.1.1.2 The Becher process

The Becher Process [4, 5] upgrades ilmenite ($FeOTiO_2$, ~60% TiO_2) to synthetic rutile (92-95% TiO_2). There are several plants in Western Australia using this process. It involves two main steps termed “reduction” and “aeration”. In the reduction step ilmenite is heated with coal at about 1100°C for between 13 and 16 hours producing reduced ilmenite: a mineral intermediate consisting of a titanium oxide (Ti^{IV}, Ti^{III} and

Ti^{II}) matrix honeycombed with metallic iron. Often, sulphur or copperas ($FeSO_4.7H_2O$) is added to the ilmenite-coal feed into the kiln resulting in the formation of acid soluble transition metal sulphides (*eg.* MnS) which can then be more effectively removed during subsequent steps.

In the aeration step, metallic iron in reduced ilmenite is removed by corrosion with oxygen in a dilute ammonium chloride solution (0.5-1.6% w/v). Since the corrosion reaction is exothermic, the slurry temperature usually rises to about 80°C. Aeration can be quite variable, taking between 12 and 20 hours to reach completion. This gives the synthetic rutile product and a finely dispersed iron oxide by-product. After separation of the oxide from the mixture, the synthetic rutile is subjected to a mild sulphuric acid leach which removes any last traces of metallic iron and reduces the Mn impurity levels as well.

Disadvantages of the Becher process include the intrinsically slow rate of iron removal which results in long aeration times. The synthetic rutile product can contain relatively high levels of impurities depending on the characteristics of the feed material. Also, the variability in the aeration time and the variability of oxide type produced are both operational problems that can also affect the level of impurities. Disposal of the oxides itself is a direct economic loss. However this process is economically viable due to the low capital costs (since relatively simple technology is involved) and low operating costs. In addition, the cheap availability of local Collie coal – which is particularly suitable for this type of reduction – and low NH_4Cl consumption, also helps the economics.

1.1.1.3 The Benelite process

The Benelite Process was developed in order to overcome operational drawbacks associated with the direct acid leaching of ilmenite. In India there are plants located in Kerala, Sahuparum and Orissa. The Malaysian Titanium Corporation operates a plant in Ipoh, Malaysia and Kerr McGee operates a plant in Alabama, United States of America.

This process involves the partial reduction of ilmenite by heating with coal in a rotary kiln. The resultant ferrous oxide is more soluble and consequently the partially reduced ilmenite can be leached using a ferrous chloride solution of much lower acid concentration (20% HCl) [6]. The spent ferric chloride leach liquor is then processed to regenerate ferrous chloride and HCl which is recycled [7].

1.1.1.4 The Ishihara process

At present there is only one plant in Japan using this process to produce about 40 to 50 kt/year of synthetic rutile. This process [8] consists of five steps [7]:

a) Partial reduction of ilmenite ($Fe^{3+} \rightarrow Fe^{2+}$) with coke in a rotary kiln
b) Magnetic separation of coke from partially reduced ilmenite
c) Leaching of partially reduced ilmenite at 130°C for 8 hours using sulphuric acid
d) Filtration and washing
e) Calcination at 800°C

The product is more than 95% TiO_2. The waste acid from the leaching step is either sent to an ammonium sulphate plant as a raw material or it is re-used by adding make-up acid.

1.1.2 Other methods of producing synthetic rutile

Many other methods for producing synthetic rutile have been investigated in the literature. The following is only a cursory and selective summary of this body of work and is presented in reverse chronological order.

1.1.2.1 Ball milling

Recent work has shown that after milling ilmenite with coal the temperature for reduction to metallic iron decreased with increasing milling time [9, 10]. However mixing separately milled ilmenite and carbon powders resulted in only a slight decrease in the temperature for reduction to occur. Thermally treated milled powders also resulted in better iron and titanium separation after leaching compared with the Becher process. The improved separation was found mainly to be due to less reduction of rutile to TiO_{2-x} phases occurring. The leaching step also occurred much faster than during the conventional Becher process mainly due to a decrease in the particle size (~50 μm). This technique is not practical since very long milling times are required in order to produce the desired beneficial effects.

1.1.2.2 High pressure selective acid leaching

Heng *et al.* [11] described a method that, like the Becher process, involves the metallisation of iron in ilmenite by heating with coal. However unlike the Becher process, metallic iron is then removed using sulphuric acid (8-12 g L^{-1}, 170-190°C) and oxygen (303-606 kPa above the water vapour pressure). Iron removal is very fast, taking only 10-30 minutes. The short aeration time also reduces the attritioning of particles.

Another advantage is that manganese impurities from the original ilmenite are removed avoiding the need of a separate acid leach step as performed in Becher process.

1.1.2.3 Selective chlorination

This process involves the partial or total chlorination of ilmenite resulting in a product containing about 97% TiO_2 [3, 7]. In the partial chlorination of ilmenite, only the iron is chlorinated while for total chlorination both the iron and titanium are chlorinated [12]. Selective chlorination is achieved by keeping the temperature of the fluidised bed relatively low. The unaffected TiO_2 residue is then washed to remove soluble chlorides and dried. Iron is removed as ferric chloride which is burned with oxygen to regenerate chlorine and form the iron oxide by-product. Technical difficulties associated with economically recycling the chlorine gas and selling the iron oxide by-product have prevented commercialisation.

1.1.2.4 The Murso process

The Murso Process [13] involves oxidising all of the iron in ilmenite to Fe^{3+} at 900-950°C and then reducing Fe^{3+} back to Fe^{2+} by heating to 800-850°C with coal. The "synthetic ilmenite" is then leached with 20% HCl at 105-110°C giving a product containing more that 95% TiO_2. Unlike the Becher process, impurities like Mn, Mg, Al and V are removed. This process is considered to be so facile due to the production of an altered ilmenite that differs in its micro-structure from the original ilmenite by containing a large number of lattice defects. This apparently greatly increases the chemical reactivity compared to natural ilmenite. Pilot scale plants proved the feasibility of the process however construction of the first commercial plant during the 1970's was deferred due to the poor global economic outlook at the time [7].

1.1.2.5 The Summit process

The Summit process [14] is one of a number of processes in the literature that involve the use of $FeCl_3$ to remove the iron from reduced ilmenite [15-17]. The ilmenite is subjected to a pre-oxidation in order to maximise the degree of metallisation during the subsequent reduction step. The metallic iron is then leached from the reduced ilmenite using ferric chloride solution. The heart of the process is the regeneration of $FeCl_3$ by oxidising the resultant $FeCl_2$ solution with oxygen from air, which gets around the problem of safely disposing of acidic iron wastes. A disadvantage of the technique is that impurities like Mn, Mg and Al are not removed. However, due to its high capital and operating costs, the process has not been commercialised.

1.1.3 TiO_2 Pigment Production

1.1.3.1 The sulphate process

Ground ilmenite or titanium rich slag is digested in sulphuric acid producing a titanium sulphate solution. Only these titanium sources can be used since both natural and synthetic rutiles are not attacked by sulphuric acid. Fe^{3+} is reduced to Fe^{2+} with scrap metal, crystallised as copperas by cooling the solution, and separated. Hydrolysis is then effected by boiling the solution, precipitating TiO_2, which is then washed and calcined.

Disadvantages of this process include high capital and operating costs since large quantities of water, sulphuric acid and steam are required. Another very significant drawback is the economic and environmental cost of disposing of the ferrous sulphate waste by-product.

1.1.3.2 The chloride process

Natural rutile, synthetic rutile and high titanium slag are the usual feedstocks for the chloride process. DuPont in the United States actually uses high grade ilmenite (61% TiO_2) for direct chlorination which was not previously considered economic due to high chlorine consumption [3]. Dooley [18] compared the chemical and economic aspects of using ilmenite and rutile as feedstocks for the chloride process. The high capital and operating cost of dechlorinating iron chloride produced from the direct chlorination of ilmenite erodes the economic advantage of the lower raw material cost of ilmenite.

The first stage of the chloride process is the reduction of the TiO_2 feedstock with coke in the presence of chlorine gas to form $TiCl_4$ gas. The gas is purified by reaction with various materials, [7] followed by distillation. Purification by distillation is a significant advantage of the chloride process over the sulphate process. In the second major step $TiCl_4$ gas is oxidised at high temperature to form pure TiO_2. Chlorine is recovered from this process and recycled. The product still requires further milling and/or chemical processing to give specific pigment properties.

1.2 THE AERATION STEP OF THE BECHER PROCESS

Put most simply, the aeration step is a corrosion reaction where iron is oxidised by dissolved oxygen to ferrous ions:

$$Fe \rightarrow Fe^{2+} + 2e^{-} \quad (1.1)$$

and,

$$O_2 + 4H^{+} + 4e^{-} \rightarrow 2H_2O \quad (1.2)$$

Ferrous ions are then further oxidised precipitating as a variety of oxides or oxyhydroxides including magnetite (Fe_3O_4), haematite (Fe_2O_3) and lepidocrocite (γ-FeOOH).

Becher *et al.* [5] investigated the effect of pulp density, temperature, type and concentration of catalyst, and pressure on the aeration of reduced ilmenite. They found that successful aerations were obtained for weight ratios of water to reduced ilmenite of between 10:1 and 2:1. At a total pressure of 791 kPa, aeration went five times faster than at atmospheric pressure. Also, at these elevated pressures the aeration rate was constant between 50 and 150°C. Importantly, in addition to oxidation by dissolved oxygen, some acid oxidation of metallic iron was noticed at high temperatures. For aerations at atmospheric pressure, it was observed that temperatures around 55°C were ideal and that nothing is gained by increasing the temperature to 75°C. Typical aerations took 6.5 hours.

In situ rusting refers to the process where iron oxides precipitate within the pores of the reduced ilmenite grain resulting in high total iron levels in the synthetic rutile product. In extreme circumstances, *in situ* oxide can stop the oxidation reaction prematurely. *In situ* rusting was encountered under the following conditions [5]:

a) aerations conducted below 10°C
b) poor stirring conditions during aeration
c) continuous removal of oxide during aeration
d) sodium salts in aeration liquor
e) aeration with steam

Mandyczewsky [19] investigated the oxidation of iron powder by dissolved oxygen in dilute NaCl and NH_4Cl solutions. The buffering action of NH_4^{+} was recognised as important in preventing passivation. He concluded that oxidation proceeds in two stages:

a) electrochemical oxidation of metallic iron to ferrous ions
b) oxidation of ferrous ions to hydrated ferric oxide

Farrow *et al.* investigated various aspects of aeration and the corrosion of pure iron [20, 21]. Corrosion potential measurements of both pure iron and reduced ilmenite electrodes at different electrode rotation speeds (in acetic acid/acetate buffered 0.1 M NH_4Cl) gave Levich plots indicating that iron corrosion is under oxygen diffusion control. Initial aeration rates for reduced ilmenite were found to peak at 70°C which contrasts with the results of Becher *et al.* [5] where no difference in the *total* aeration time was observed between 53 and 75°C. After adding reduced ilmenite to the liquor, the pH jumped to 7.5 and then quickly stabilised between pH 4.5 and pH 3.5. Addition of HCl to the liquor at the start resulted in a consistently lower pH throughout the aeration however the aeration rate did not increase which indicates that acid corrosion was not occurring.

Farrow *et al.* [20, 21] also conducted aerations using 0.1 M NaCl, $ZnCl_2$ and $MgCl_2$. These metal chlorides were chosen in order to investigate:

a) NH_4^+ as a buffer (since Zn^{2+} and Mg^{2+} have lower and higher pK_a values respectively) and,
b) the importance of ferrous-ammine complex formation in assisting the aeration reaction

In situ rusting resulted in residual total iron levels (Fe_T) of 4.2, 8.8 and 13% for $ZnCl_2$, $MgCl_2$ and NaCl aerations respectively, compared with 0.5% for NH_4Cl aerations. All of the metallic iron was oxidised but it was trapped as hydrated iron oxide in the pores. NH_4Cl aerations took only about 4.5 hours compared with 7-8 hours for the other salts. Thus, the rate of Fe_T removal was much faster in NH_4Cl. However, no definite comparisons about the metallic iron (Fe_M) removal rate were made since only Fe_T, and not Fe_M values were reported. The higher residual Fe_T values in NaCl and $MgCl_2$ are consistent with Na^+ and Mg^{2+} being significantly poorer buffers against OH^- than NH_4^+. However the residual high Fe_T value for $ZnCl_2$ aerations is not consistent since $pK_a(Zn^{2+}) < pK_a(NH_4^+)$, which means that Zn^{2+} should be a better buffer against OH^- than NH_4^+.

Farrow *et al.* [21] explained that the $ZnCl_2$ aeration was probably inferior to the NH_4Cl aeration due to the precipitation of $Zn(OH)_2$ in the high pH regions "*close to the cathodic sites*" (despite $pK_a(Zn^{2+}) < pK_a(NH_4^+)$):

"Apart from the fact that such a compound (that is, $Zn(OH)_2$) *would certainly be unstable at pH 3* (the bulk pH), *this explanation does not account for the occurrence of* in situ *rusting in zinc chloride solution, but not in ammonium chloride solution. A*

second and more likely explanation is to suppose that the iron(II) ions generated during the reaction are stabilized by the formation of an iron(II)-ammonia complex."

Higher Fe_T levels for $ZnCl_2$ aerations compared with NH_4Cl aerations suggests that iron hydroxide/oxide precipitation is more facile in the absence of NH_4^+. However, in the absence of Zn analyses for the synthetic rutile, it is not possible to completely rule out that $Zn(OH)_2$ precipitation may have contributed to the poor $ZnCl_2$ aerations thus weakening the explanation that ferrous-ammine complexation is responsible for the good aerations in NH_4Cl . However, higher $Fe(OH)_2$ solubilities measured in 0.1 M NH_4Cl, over that predicted by the solubility product, provide evidence that ferrous-ammine complexes may form and possibly explain the effectiveness of NH_4Cl aerations [20, 21].

Linear Fe_T removal rates are expected for oxygen diffusion controlled corrosion. However non-linear Fe_M removal rates were observed during aerations and Bax and Ritchie suggested that "*…complications are caused by diffusion down the pores of the ilmenite particles*" [22]. A typical (0.1 M) NH_4Cl aeration in their inverted cone reactor took about 4.2 hours using air. Aerations carried at oxygen partial pressures below 21 kPa gave significantly lower iron removal rates. For example after 4 hours at 0.42 kPa oxygen partial pressure, more than half of the metallic iron was left. As the oxygen partial pressure was increased, the percentage of haematite also increased. The total aeration time did not decrease any further at temperatures above 40°C which is in agreement with the results of Becher *et al.*[4]. However the percentage of haematite that formed did increase with increasing temperatures and was the exclusive product from aerations conducted at 90°C.

Aerations were also performed in $(NH_4)_2SO_4$, sea water and $(NH_4)_2SO_4$-sea water mixtures [22]. The sea water aeration rate was a little lower than for the other electrolytes which the authors suggested is due to the absence of NH_4^+ rather than passive oxide film formation. The absence of *in situ* rusting, even in sea water, was suggested to be the result of the high degree of agitation achieved in the inverted cone reactor. Only mixtures of lepidocrocite (γ-FeOOH) and haematite (α-Fe_2O_3) were observed which is indicative of a low oxygen utilisation typical of low pulp density aerations [22] such as these. Bax and Ritchie surmised that for plant aerations, where much higher pulp densities are used and agitation is much less vigorous, NH_4Cl prevents *in situ* rusting.

Ward's investigation of the aeration reaction focused on understanding the factors controlling oxide formation and precipitation [23]. The corrosion potential of reduced ilmenite strongly depended upon the degree of metallisation: the lower the percentage metallisation, the more positive the corrosion potential. So the degree of metallisation could affect the solution potential during aeration and thus may be an important factor controlling what type of oxide will form [23]. Laboratory scale aerations focused on using Eh and pH in order to control magnetite and haematite formation. Magnetite could be produced at pH > 5 and red haematite could be formed at pH < 3 and at potentials above 0.200 V (*she*). During one experiment [Fe^{2+}] reached as high as 0.0176 M [23]. Plant scale aerations were conducted in order to investigate the effect of different of air flow regimes on the temperature, pH, [Fe^{2+}] and Eh profiles. The following air flow regimes were tested:

a) moderate aeration at 5200 $m^3\ h^{-1}$
b) extreme aeration at 7000$m^3\ h^{-1}$
c) graduated aeration at 3000$m^3\ h^{-1}$ for the first 5 hours followed by air flow rates at 6000 $m^3\ h^{-1}$ for the next 7 hours

Interestingly, [Fe^{2+}] was quite high throughout aeration and ranged between 1×10^{-3} and 8.8×10^{-3} M. The pH usually varied within a single pH unit range around pH 6. Little difference between the aeration rates of the three regimes was observed [23]. The data were interpreted in terms of pH changes resulting from competition between the acid consuming rusting reaction (equations (1.1) and (1.2)) and acid generating oxyhydrolysis of Fe^{2+}:

$$2Fe^{2+} + ½O_2 + 3H_2O \rightarrow 2FeOOH + 4H^+ \qquad (1.3)$$

Reid [24] investigated the effect of removing carbon dioxide from the sparge air, substituting NaCl for NH_4Cl, pulp density and temperature on the aeration of reduced ilmenite using a fluidised bed reactor. At 80°C a typical (1.3%) NH_4Cl aeration took between 9 and 10 hours. He found that at 40°C removing CO_2 from air made little difference for NH_4Cl aerations. However, the addition of $NaHCO_3$ (0.0025 M) decreased the aeration rate at 50°C and changed the oxide by-product from magnetite to lepidocrocite and the leaching kinetics were no longer linear. The cause of this inhibition was not discussed, however one possible explanation is that CO_3^{2-}, formed from the

buffering reaction of HCO_3^-, could precipitate as $FeCO_3$ or $FeHCO_3$ passivating iron [25, 26].

Aeration rates in NaCl and NH_4Cl (pulp density = 250 g L^{-1}) were the same between 60 and 80°C; linear aeration kinetics were observed in both cases. However, in NaCl at 50°C, the initial aeration rate was much lower and stopped for a period of 4 hours – which is indicative of passivation – before starting up again, which could have been caused by the attritioning of particles. A magnetite by-product formed in both liquors. Reducing the pulp density to 150 g L^{-1} in NaCl at 70°C also resulted in passivation which was considered to be caused by higher oxygen concentrations expected in lower pulp density liquors [24]. Microscopic investigation of reduced ilmenite particles at various stages during aeration showed that higher porosity particles leached more quickly [24].

Avraamides *et al.* investigated the effect of air flow rate at "high" and "low" pulp densities and also investigated the effect of NH_4Cl concentration [27]. Air flow rates above 0.3 L min^{-1} at low pulp density and, 0.5 L min^{-1} at the higher pulp density, did not further increase the aeration rate. Typical aerations took 5-7 hours to complete. Aeration was faster at higher pulp density and oxygen utilisation also increased. Magnetite formed at high pulp density while haematite formed at low pulp density [27]. NH_4Cl concentrations of 0.5-1.0% (w/v) produced similar aeration times and residual iron levels. However, above 1.0%, the aeration rate slowed slightly, possibly due to lower dissolved oxygen levels at higher salt concentrations. Below 0.5% the aeration rate was also a little lower indicating that NH_4Cl does directly influence the corrosion of iron in reduced ilmenite [27].

Ward *et al.* investigated the influence of citric and tartaric acids on the aeration of reduced ilmenite [28]. Tartaric acid had little effect on aeration while in citric acid/citrate buffer solution aeration was much faster (4 hours) compared with NH_4Cl (7 hours). The highest aeration rate was obtained in the 1:1 citric acid/citrate buffer, with similar residual iron levels to NH_4Cl aerations being achieved. This result highlights the importance of the effective buffering for good aerations.

Jayasekera *et al.* investigated the effect of high temperatures and high oxygen partial pressures on the aeration reaction [29]. Aerations conducted using air at 75°C took about 7 hours to reduce Fe_M to 1.7%. At 75°C and 101 kPa oxygen partial pressure Fe_M was reduced to 2.2% after about 140 minutes aeration. Further increases in the

oxygen partial pressure resulted in a further acceleration of the aeration rate with Fe_M down to 5% within 40 minutes. However at 300 kPa oxygen partial pressure, Fe_M remained at 5%. Raising the temperature to 130°C not only further increased the aeration rate but also reduced the residual metallic level to about 2% after 40 minutes at 300 kPa oxygen partial pressure. *In situ* rusting was a significant problem at high oxygen partial pressures with Fe_T levels as high as 14% obtained. However, subsequent sulphuric acid leaching reduced Fe_T to 3%.

1.3 THERMODYNAMICS FOR THE IRON-WATER AND IRON-WATER-AMMONIA SYSTEM

An understanding of the thermodynamics of the Becher process is important to help interpret leaching and electrochemical results. In the first of the following two sections the thermodynamics of the iron-water system is reviewed using Eh-pH diagrams. In the second section the thermodynamic data for ferrous-ammine complexes are reviewed and a new Eh-pH diagram for the iron-water-ammonia system will be presented.

1.3.1 The iron-water system

Ever since the first Eh-pH diagrams for the iron-water system were published by Pourbaix [30], scientists have continued to publish new diagrams using revised thermodynamic data, including additional elements or species and extending them to elevated temperatures and pressures. Eh-pH diagrams have proved useful in a diverse spectrum of sciences ranging from corrosion science [30-32] and hydrometallurgy [33] to geochemistry [34, 35]. However the major limitation of Eh-pH diagrams is that they say nothing about the kinetics of a reaction. So even though a reaction may be thermodynamically favourable it may in reality proceed at a very slow or undetectable rate.

A variety of Eh-pH diagrams was constructed by Misawa [36] using different combinations of iron hydroxides, oxides and oxyhydroxides in addition to activity-pH and predominance diagrams for dissolved iron species in equilibrium with various oxides and hydroxides. Figure 1.2 shows the Eh-pH diagram considering γ-FeOOH.

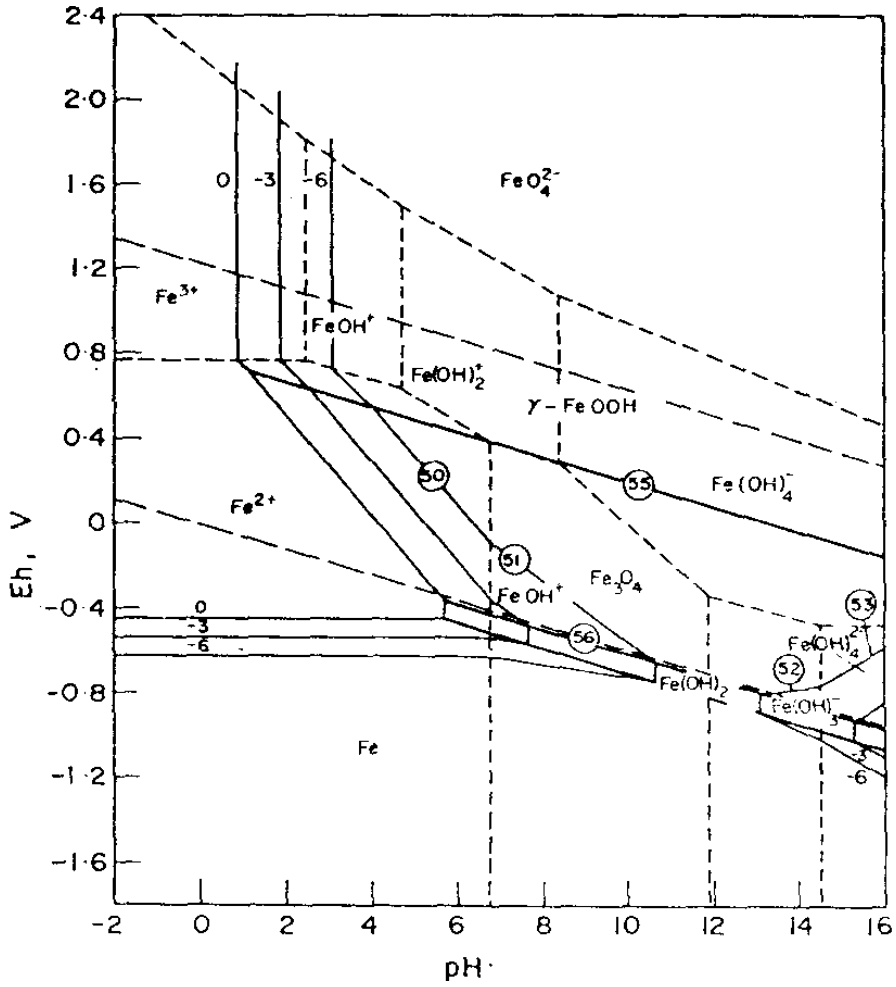

Figure 1.2 Eh-pH diagram for the iron-water system at 25°C considering Fe, $Fe(OH)_2$ and γ-FeOOH, from Misawa [36].

Figure 1.3 shows the Eh-pH diagram for the iron-water system at 80°C and at a high soluble iron activity of 0.5 M [37]. These values were chosen to more accurately reflect actual Becher process conditions. Biernat and Robins [38] reported a series of diagrams for the iron-water system between 25 and 300°C. Figure 1.4 shows one of their diagrams at 150°C. This diagram shows that at high temperatures $Fe(OH)_2$ is now replaced by magnetite (Fe_3O_4).

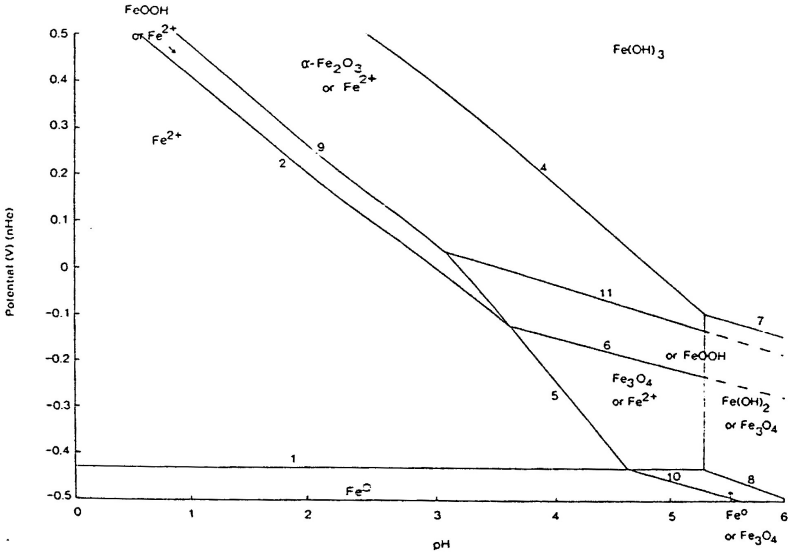

Figure 1.3 Eh-pH diagram for the iron-water system at 80°C with iron activity of 0.5 M, from Ward [37].

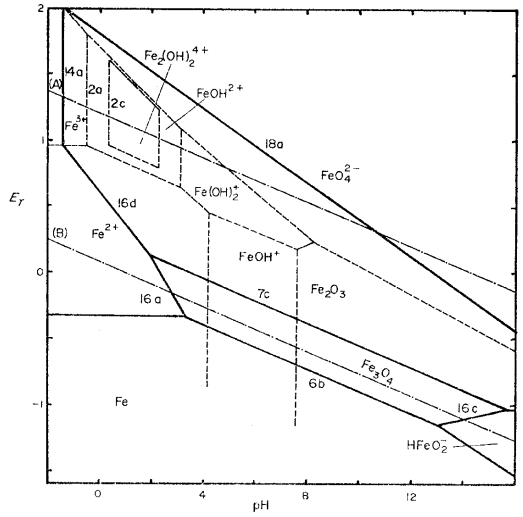

Figure 1.4 Eh-pH diagram for the iron-water system at 150°C, from Biernat and Robins [38].

1.3.2 The iron-water-ammonia system at 25°C

Cotton and Wilkinson [39] state that ferrous halides can combine with gaseous ammonia to form ammoniates and add that "*The ammine complexes are not stable in water, however, except in saturated aqueous ammonia*". Weitz and Müller [40] provided early evidence of ferrous hexa-ammine complex formation:

$$Fe^{2+} + 6NH_3 \rightarrow Fe(NH_3)_6^{2+} \quad (1.4)$$

Leussing and Kolthoff [41] suggested the increased solubility of $Fe(OH)_2$ in 0.1 M NH_4Cl compared with NaCl solution is due to the formation of a tetra-ammine complex and estimated a stability constant for this complex (see Table 1.1). Farrow *et al.* [20, 21] also observed higher $Fe(OH)_2$ solubility in 0.1 M NH_4Cl which they also attributed to ferrous-ammine formation. Yatsimirskii [42, 43] gave the stability constants for the mono- and di-ammine complexes. Klocke and Hixon [44] measured the solubility of ferrous ion in concentrated (300-500 g L^{-1}) HCl and NH_4OH solutions and provided experimental evidence that a cationic hexa-ammine complex formed. However, Isaev *et al.* [45] found the hexa-ammine complex unstable and only reported the stepwise formation constants for the mono- to penta-ammine complexes. Table 1.1 lists the logarithm of the cumulative formation constant, β, for ferrous ammine complexes reported in the literature.

β	Equilibrium reaction	log β [45]	log β [41]	log β [43]
β_1	$Fe^{2+} + NH_3 \rightarrow Fe(NH_3)^{2+}$	1.4		1.4
β_2	$Fe^{2+} + 2NH_3 \rightarrow Fe(NH_3)_2^{2+}$	2.25		2.2
β_3	$Fe^{2+} + 3NH_3 \rightarrow Fe(NH_3)_3^{2+}$	2.68		
β_4	$Fe^{2+} + 4NH_3 \rightarrow Fe(NH_3)_4^{2+}$	2.75	3.7	
β_5	$Fe^{2+} + 5NH_3 \rightarrow Fe(NH_3)_5^{2+}$	2.35		

Table 1.1 Cumulative formation constants for ferrous-ammine complexes at 25°C.

Some Eh-pH diagrams for this system have been published in order to help understand the hydrometallurgy of nickeliferous ore processing [46, 47]. For example, Queneau and Weir [47] presented some Eh-pH diagrams for the iron-water-ammonia system where $[NH_4^+] + [NH_3] = 5$ M and showed that a stable ferrous tetra-ammine region exists between pH 8 and 11. Unfortunately however, these workers did not report the source of thermodynamic data used to construct their diagram. Osseo-Asare [46] presented Eh-pH and activity-pH diagrams for the iron-water-ammonia system. He included the ferrous di-ammine and tetra-ammine complexes in his diagrams and referenced a compilation [42] as the source of his data. This compilation lists the

stability constants from Yatsimirskii [43] and Leussing and Kolthoff [41] for the di-ammine and tetra-ammine respectively. These data are also listed in Table 1.1. Osseo-Asare's Eh-pH diagram and activity-pH diagram are reproduced in Figure 1.5. From pH 7.8 to 8.4, $Fe(NH_3)_2^{2+}$ (Note the typographical error in Figure 1.5 where $Fe(NH_3)^{2+}$ is implied) predominates and from pH 8.4 to 10.8, $Fe(NH_3)_4^{2+}$ predominates.

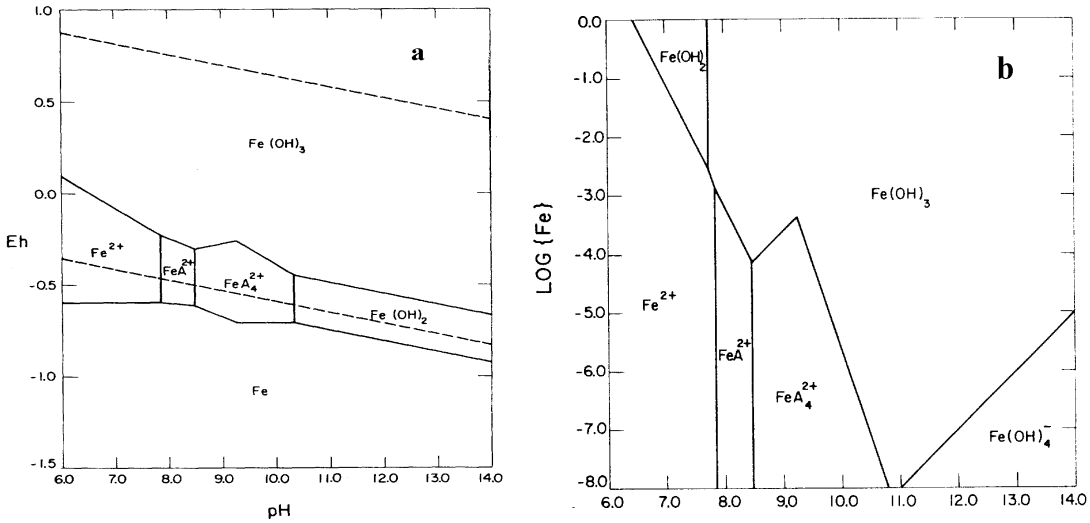

Figure 1.5 a) Eh-pH diagram for the iron-water-ammonia system where $[Fe^{2+}] = 10^{-4}$ M and $[NH_4^+] + [NH_3] = 1.0$ M and, b) Activity-pH diagram where $[NH_4^+] + [NH_3] = 1.0$ M and E = -0.3 V (*she*) at 25°C, from reference [46].

Figure 1.6 shows an ammonia activity-pH diagram also from reference [46].

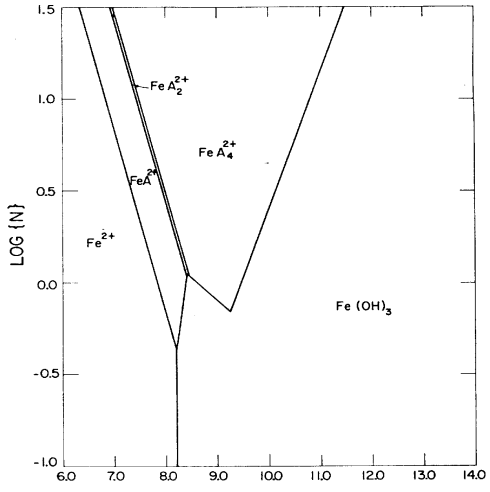

Figure 1.6 Ammonia activity-pH diagram for iron-water-ammonia system where $[Fe] = 10^{-4}$ M and Eh = -0.3 V at 25°C, from reference [46].

According to this diagram, above pH 8.2 and for ammonia concentrations less than 0.5 M, $Fe(OH)_3$ precipitates.

1.3.2.1 New activity-pH and Eh-pH diagrams for the iron-water-ammonia system at 25 °C

Table 1.2 lists the Gibbs free energy of formation values for the iron-water-ammonia

Species	$G°_{f\ 25°C}$ / kJ mol^{-1}	Reference
Fe^{2+}	-78.9	[48]
$FeOH^{+}$	-277.4	[48]
$Fe(OH)_{2(aq)}$	-449	[49]
$Fe(OH)_3^{-}$	-614.9	[48]
$Fe(OH)_4^{2-}$	-769.7	[48]
$Fe(NH_3)^{2+}$	-113.4	Calc. from β_1 in Table 1.1 [45]
$Fe(NH_3)_2^{2+}$	-144.7	Calc. from β_2 in Table 1.1 [45]
$Fe(NH_3)_3^{2+}$	-173.7	Calc. from β_3 in Table 1.1 [45]
$Fe(NH_3)_4^{2+}$	-200.6[a]; -163.8[b]	Calc. from β_4 in Table 1.1, a = [45]; b = [41]
$Fe(NH_3)_5^{2+}$	-224.8	Calc. from β_5 in Table 1.1 [45]
$Fe(OH)_2$	-486.5	[48]
Fe^{3+}	-4.7	[48]
$FeOH^{2+}$	-229.4	[48]
$Fe(OH)_2^{+}$	-438	[48]
$Fe(OH)_{3(aq)}$	-659.3	[48]
$Fe(OH)_3$	-714	[50]
$Fe(OH)_4^{-}$	-842	[51]
$Fe_2(OH)_2^{4+}$	-467.3	[48]
Fe_3O_4	-1015.4	[48]
FeOOH	-490	[50]
Fe_2O_3	-742.2	[48]
$NH_{3(aq)}$	-26.5	[48]
NH_4^{+}	-79.3	[48]

Table 1.2 Gibbs free energy of formation ($G°_{f\ 25°C}$) for the iron-water-ammonia system at 25°C.

system at 25°C. Ferrous-ammine Gibbs free energy values were calculated using the reaction stability constants from Isaev *et al.* [45] and Leussing and Kolthoff [41].

Figure 1.7 shows the Fe^{II} activity-pH diagram with a total ammonia activity of 0.2 M, calculated using only the ferrous-ammine data from Isaev *et al.* [45] which are

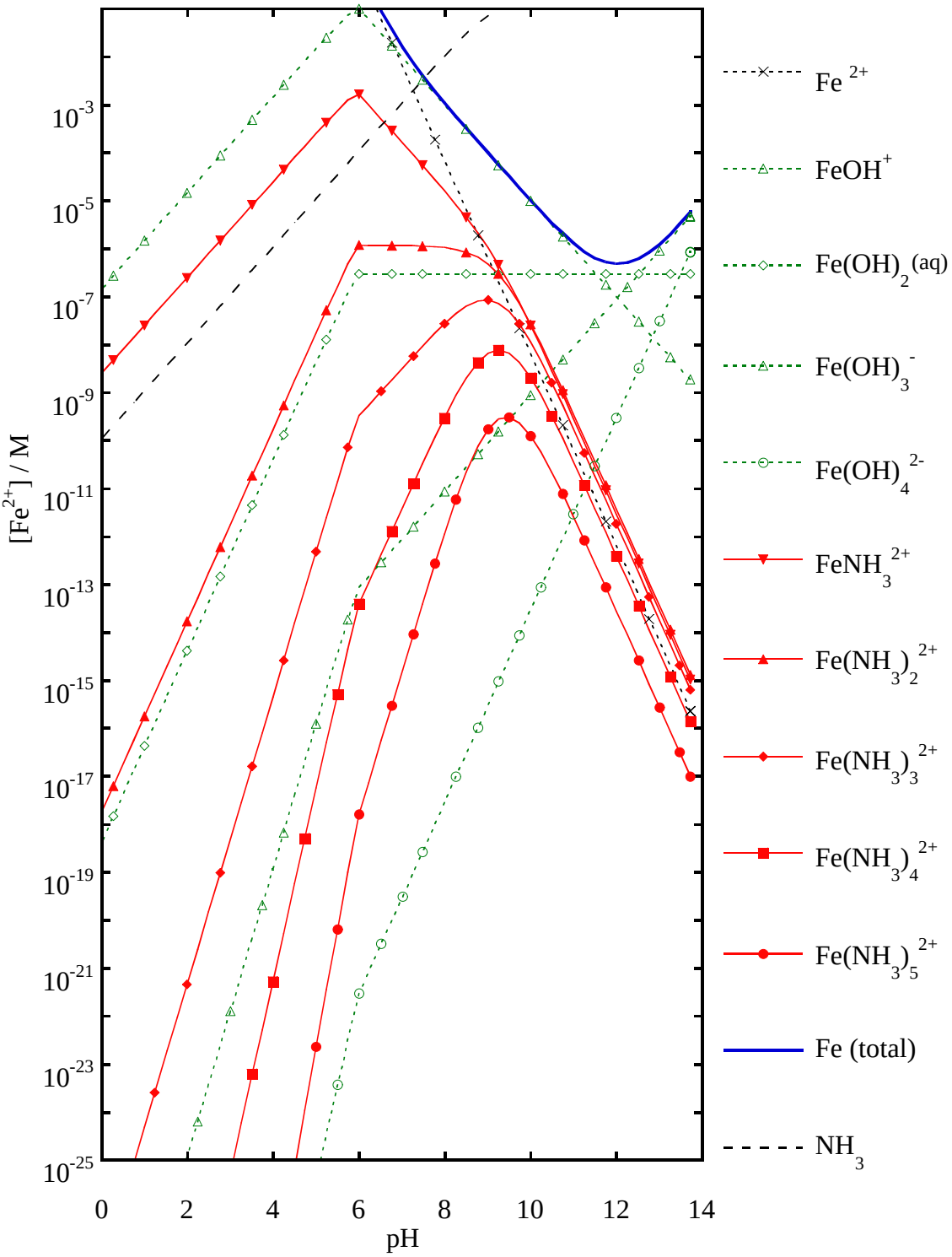

Figure 1.7 Activity-pH diagram for the Fe^{II} speciation and solubility for a saturated $Fe(OH)_2$ solution at 25°C. Ferrous-ammine thermodynamic data from reference [45]. $[NH_4^+] + [NH_3] = 0.2$ M.

listed in Table 1.2. The mono-ammine complex is the most abundant of all the ammine complexes. This is to be expected since the mono-ammine complex has the highest stability constant (Table 1.1).

Figure 1.8 shows the Fe^{II} activity-pH diagram calculated using only the data from Leussing and Kolthoff [41] which are also listed in Table 1.2. It is obvious that the concentration of tetra-ammine complex is significantly lower in Figure 1.8, calculated using the thermodynamic data derived from Leussing and Kolthoff's experimental β_4 value ([41] and Table 1.1). The most likely reason for this difference is that the stability constant calculated by Leussing and Kolthoff [41] assumed that only a tetra-ammine complex forms. However, Isaev *et al.* have shown that the mono-ammine complex is in fact the most stable of the series of complexes that extends up to penta-ammine [45].

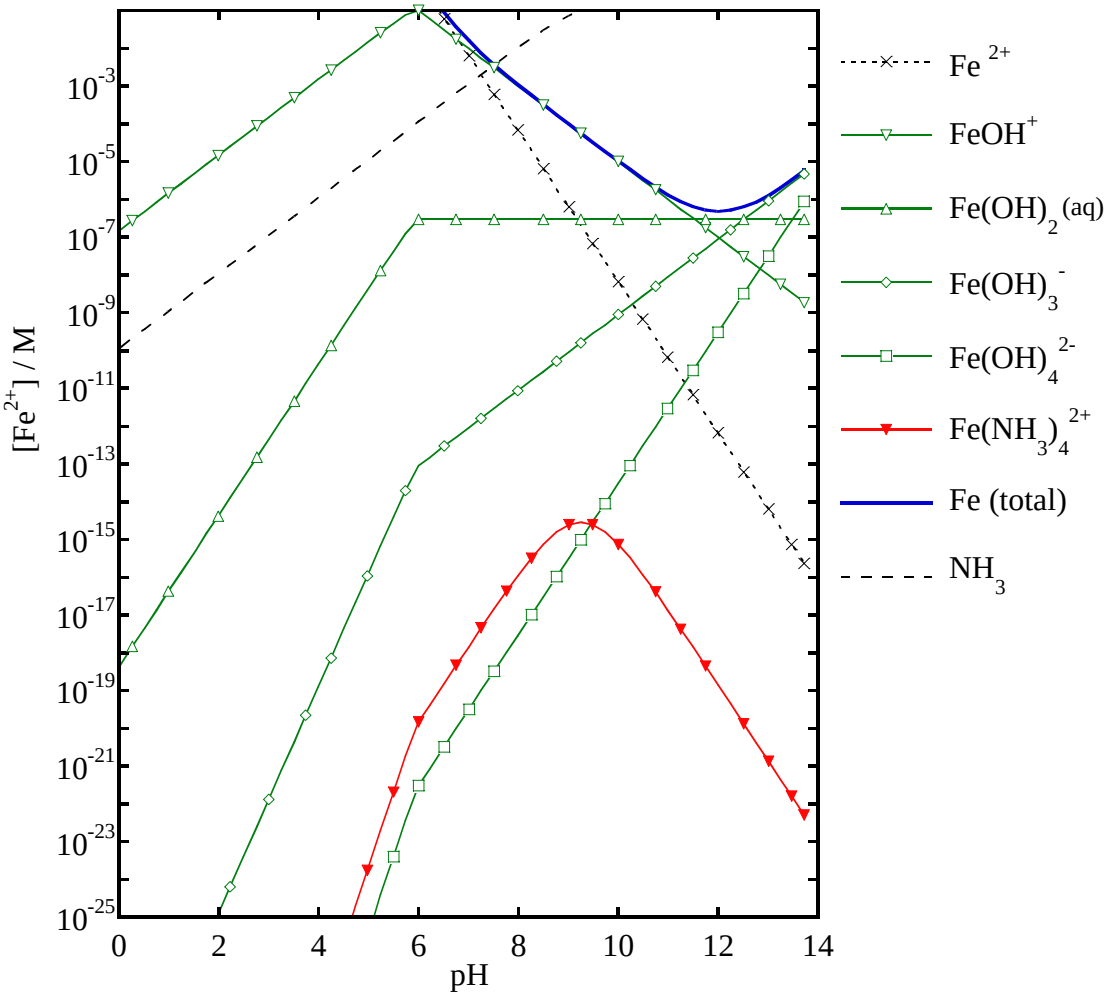

Figure 1.8 Activity-pH diagram showing Fe^{II} speciation and solubility for a saturated $Fe(OH)_2$ solution at 25°C. Ferrous-ammine thermodynamic data from reference [41]. $[NH_4^+] + [NH_3] = 0.2$ M.

Figure 1.9 overlays the total Fe^{II} solubility curves (from Figure 1.7) in the presence and absence of ammonia with the experimental solubility from Farrow and Ritchie [20, 21] and Leussing and Kolthoff [41]. Even though ferrous-ammine complexes are predicted to form, their activity is significantly lower than for the ferrous-hydoxo species. As a result, the total iron solubility is not predicted to increase in the presence of ammonia. Figure 1.9 shows that the experimental solubility is higher than the calculated solubility, and the difference between them increases with increasing pH. This difference indicates that the thermodynamic data does not accurately model the system. This difference may be due to still inaccurate thermodynamic values or perhaps due to the existence of other species, such as iron-ammine-chloro complexes, that have not been considered. To the authors knowledge data supporting the existence of such complexes has not been reported.

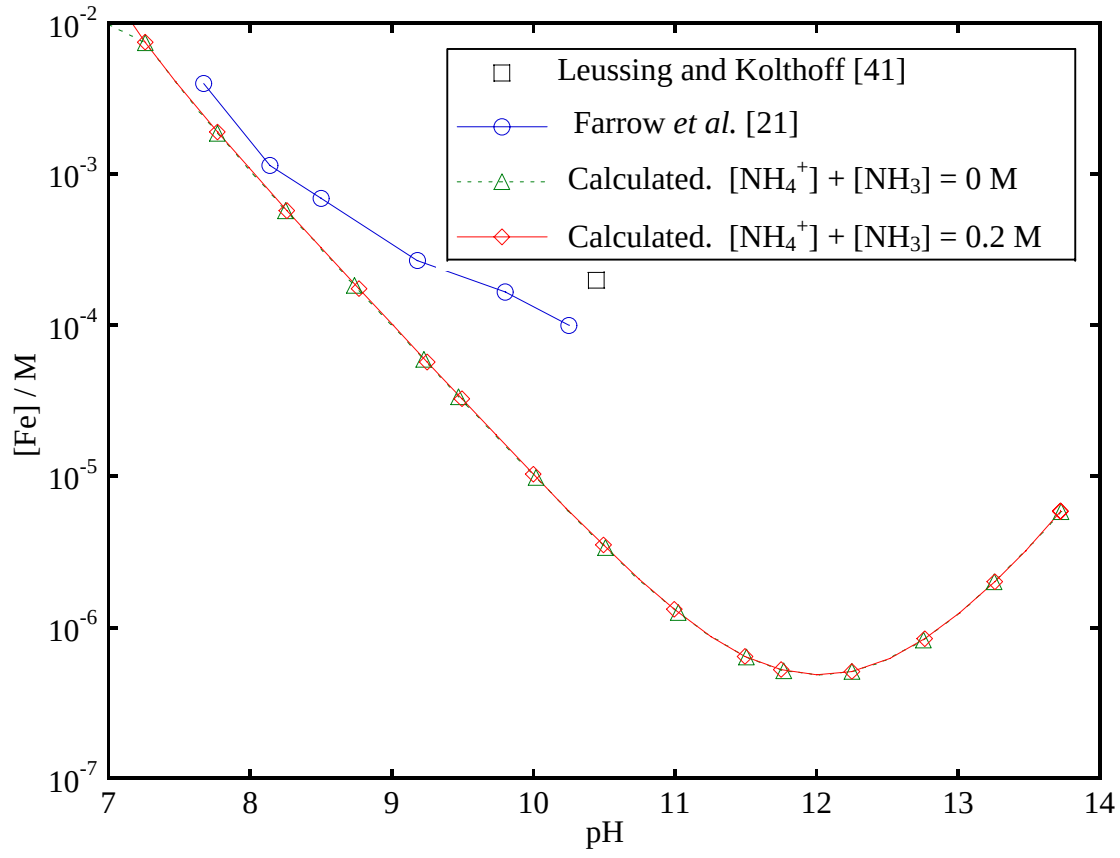

Figure 1.9 Measured and calculated total Fe^{II} solubilities at 25°C. Calculated from the thermodynamic data in Table 1.2.

Figure 1.10 shows the new Eh-pH diagram for the iron-water-ammonia system with a total ammonia activity of 1 and 5 M at 25°C. A large ferrous penta-ammine

region is predicted between pH 8 and 12 that cuts across the magnetite stability region. Eh-pH diagrams were also constructed for ammonia activities between 0.1 and 4 M. The ferrous-ammine stability area shrinks as the ammonia activity decreases. For an ammonia activity of 1 M, the penta-ammine area is about 10% of that at 5 M ammonia activity. For an ammonia activity of 0.2 M, a stable ferrous-ammine area is not predicted. Penta-ammine was always the predominant ferrous-ammine complex of the series.

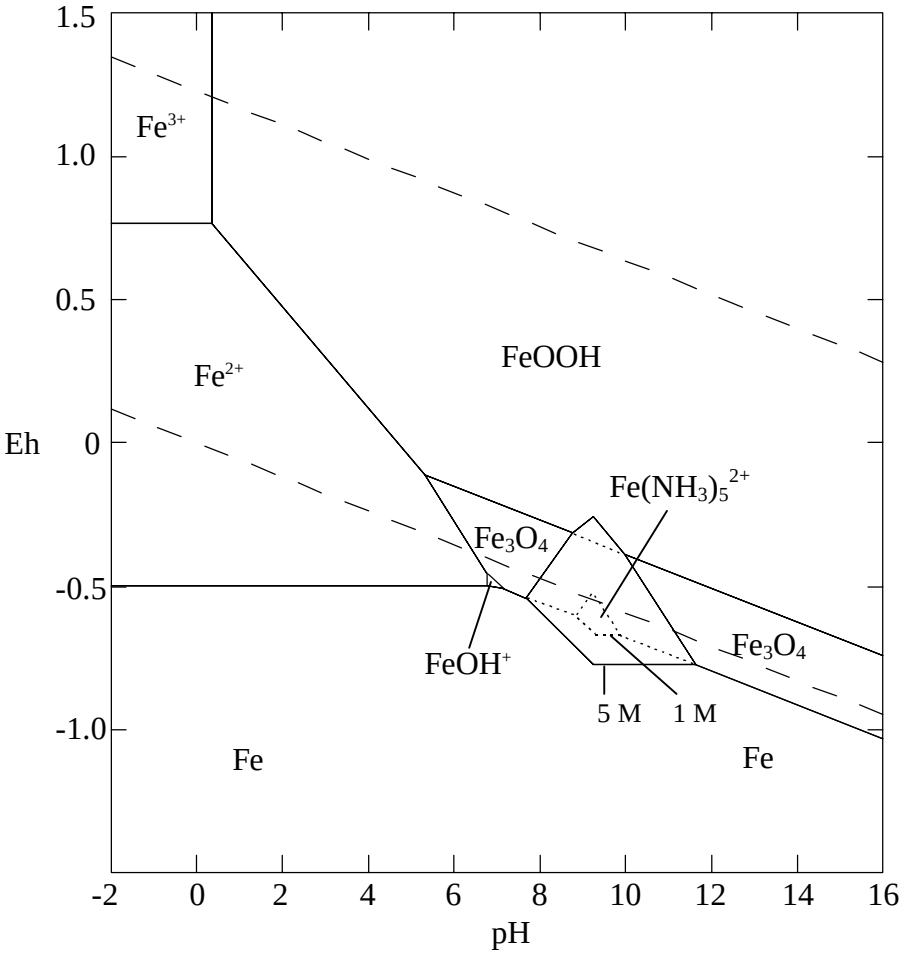

Figure 1.10 Calculated Eh-pH diagram for the iron-water-ammonia system. [Fe] = 1×10^{-3} M. $[NH_4^+] + [NH_3]$ = 1 M and $[NH_4^+] + [NH_3]$ = 5 M. The area of difference for $[NH_4^+] + [NH_3]$ = 1 M is shown as a dotted line. The dashed lines represent the limits of stability for water.

1.4 AIMS OF THIS WORK

The aim of this work is to understand the electrochemistry of the aeration step of the Becher process. The following limitations of the Becher process will be considered:

1. the variability of aeration time
2. intrinsic slowness of the aeration
3. the poor understanding of the action of ammonium chloride

The thesis will attempt to address the above points by investigating the following electrochemical aspects of aeration:

(i) Anodic dissolution of pure iron (Chapter 3). Iron dissolution will be investigated at ambient temperatures and pressures in a number of selected electrolytes including ammonium chloride, with the objective of improving the understanding of the action of ammonium chloride. The pH and temperature dependence of dissolution will also be characterised.

(ii) Oxygen reduction on iron and gold (Chapter 4). Polarisation curves will be measured on a rotating disk electrode using linear sweep voltammetry and potentiostatic methods. These curves can be used to determine the mechanism of reduction on iron and gold at ambient temperatures and pressures. Polarisation curves for oxygen reduction on gold at high temperatures and pressures will provide important quantitative information about reduction under these conditions.

(iii) Oxygen corrosion of pure iron (Chapter 5). Using iron as a model system for iron in reduced ilmenite, the effect of various parameters including temperature, pH, electrolyte composition and oxygen partial pressure will be investigated providing invaluable information about the most important factors influencing aeration.

(iv) Anodic iron dissolution from reduced ilmenite (Chapter 6). Cyclic voltammetry of reduced ilmenite, using carbon paste electrodes in selected electrolyte solutions and at different temperatures, will provide new insights into the variability of aeration. To help interpret the results, this technique will also be used to characterise the electrochemistry of Fe^{III}/Fe^{II}, iron powder and iron oxides.

2 Experimental

2.1 AMBIENT PRESSURE ELECTROCHEMISTRY

2.1.1 Electrodes

Pure polycrystalline iron (99.99% Johnson Matthey) was used to make several disc electrodes with accurately measured radii ranging between 2 and 2.5 mm. A gold disc electrode was also used (r = 1.41 mm). An epoxy resin was used to insulate the electrodes [52]. The electrodes were polished on successively finer grades of SiC paper to a final grade of 1200 or 2400.

2.1.2 Equipment

A conventional three-electrode cell was used, with a basal port added to accept a Luggin capillary via a Quickfit screw joint. The platinum wire loop counter electrode was separated from the cell using a glass tube that dipped into the electrolyte. A glass frit was located at the bottom of the tube in order to maintain electrical contact. All potentials are reported against 3 M KCl Ag/AgCl (E = 0.208 V *vs. she*). A water jacketed cell was used to thermostat the solution at temperatures up to 90 ± 0.5°C. A Pine Model AFASRE Analytical rotator was used to rotate the electrode.

A PAR model 173 potentiostat/galvanostat and model 175 universal programmer were used to generate the polarisation curves. Data acquisition was assumed by a personal computer using a DAPA A/D converter and DAPA software [53] to record the curves.

2.1.3 Solutions

Solutions were made by dissolving the solid (Univar, AR grade) in Milli-Q water. Where necessary, the pH was adjusted with the addition of aqueous NaOH. Humidified air or nitrogen was bubbled through the solutions for 30 minutes prior to immersion of

the electrode. The pH of the solutions was checked (after the voltammetry experiment) to ensure that bubbling did not significantly decrease the solution pH through ammonia removal.

2.2 HIGH PRESSURE ELECTROCHEMISTRY

2.2.1 Electrodes

Pure polycrystalline iron (99.99% Johnson Matthey) was used to make several disc electrodes with accurately measured radii ranging between 2 and 2.5 mm. A gold disc electrode was also used (r = 1.37 mm). The electrodes were insulated using a ceramic filled epoxy (Devcon Pump Repair Liquid, Maxwell Chemicals Pty. Ltd.). The electrodes were polished on successively finer grades of SiC paper to a final grade of 2400. The iron electrode was attached to the cell and then cathodically polarised at -0.78 V prior to immersion into the solution. The gold electrode was immersed into the solution without polarisation.

2.2.2 Equipment

Figure 2.1 shows a schematic diagram of the high temperature high pressure rotating disc electrode system used in this work. The system was developed at the Mineral Processing Laboratory, Department of Minerals and Energy WA. The cell is similar in design to commercial non-electrochemical autoclaves. The lower ¾ of the stainless steel vessel sits snugly in a hole in the tabletop of the apparatus. Supporting the vessel beneath the tabletop is an electrical band heater. The autoclave head and attached motor can be raised and lowered onto the top of the vessel using hydraulics. The vessel is attached onto the autoclave head using a split clamping ring with a Teflon® gasket (affixed in the head) providing the seal.

The electrodes are screwed onto the shaft that comes down through the top of the autoclave head. The seal around the shaft works by water being pumped under pressure into the chamber around the seal. The pump pressure is regulated manually and was always maintained at least 100 kPa above the working pressure inside the vessel in order to ensure the integrity of the seal. The pump and the container for the recirculated water for the pressure seal are located beneath the tabletop of the apparatus. Above pressure seal unit on the shaft are two slip rings that provide electrical contact for the disk and

ring electrodes via contacting brushes. Solutions were insulated from the stainless steel using a glass beaker that fits inside the vessel thus preventing any chance of grounding problems between the electrode and the apparatus.

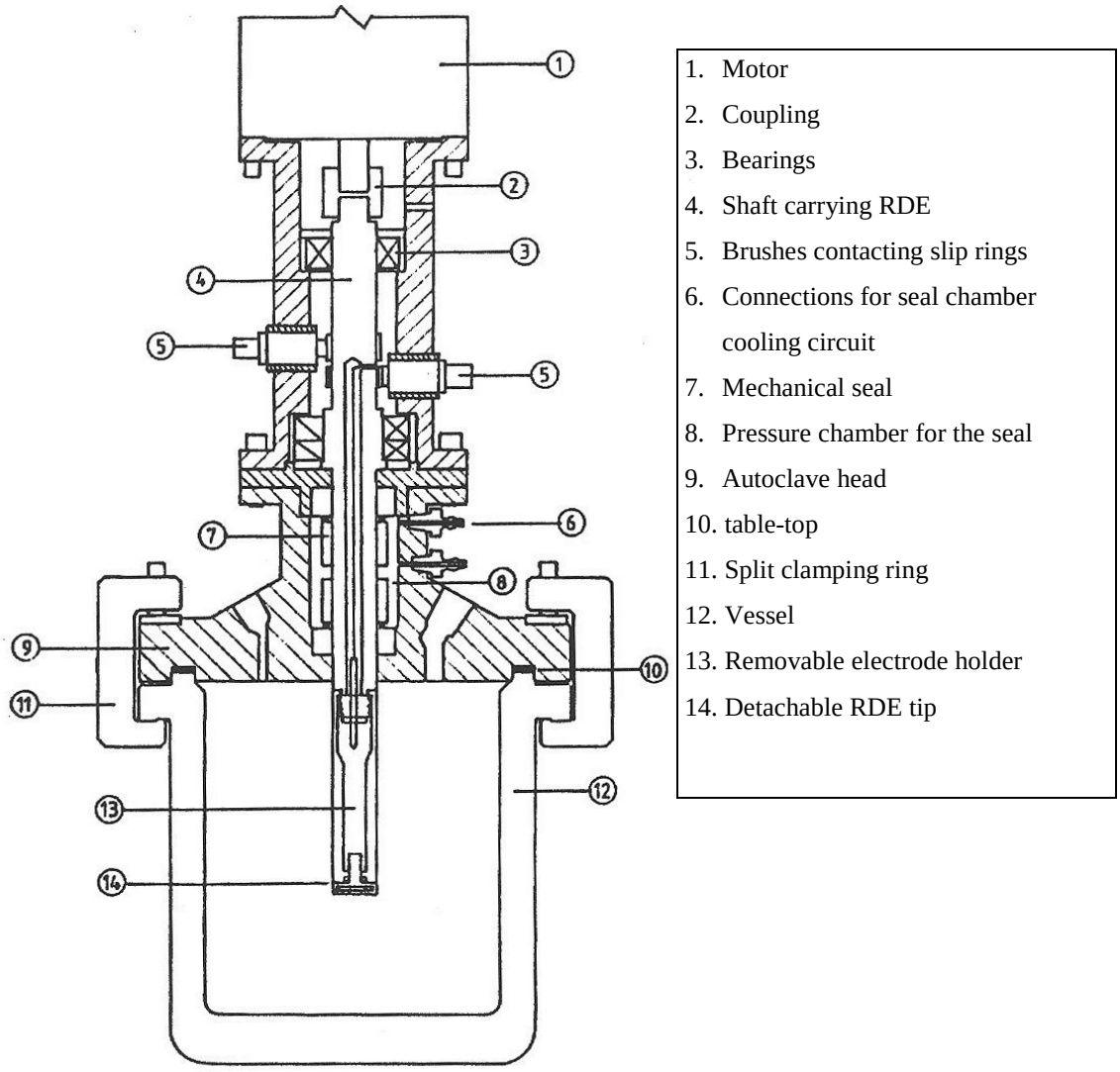

Figure 2.1 Schematic diagram of the high pressure high temperature rotating disc electrode assembly.

The autoclave head has ports to allow access into the sealed vessel for a) pressurising the cell and/or sparging the solution (via a titanium tube), b) depressurising, c) a pressure gauge d) a cooling water coil (also made of titanium) and e) a reference electrode.

A 0.1 M KCl Ag/AgCl external pressure balanced reference electrode (E = 0.279 V *vs. she*) was used and connected to the cell via Teflon® tubing and a Luggin capillary

placed 2-5 mm below the disc working electrode. The electrode was a simpler version of the electrode described by MacDonald *et al.* [54] and included a copper coil around the reference electrode compartment through which water was pumped, ensuring the electrode remained at a constant temperature. However, all potentials are reported against 3 M KCl Ag/AgCl (E = 0.208 V *vs. she*) after correction for the thermal cell potential (-0.00104 V/K) which arises from the temperature differential between the cell and the external reference electrode [54]. The cell was thermostatted at temperatures up to 150 ± 3°C via automatic microprocessor control of the band heater and cooling coil water valve. Another description of the system is also given elsewhere [55].

A PAR model 173 potentiostat/galvanostat and model 175 universal programmer were used to generate the polarisation curves. Data acquisition was assumed by a personal computer using a DAPA A/D converter and DAPA [53] or DAPA-EIT software [56] to record the curves.

2.2.3 Solutions

Ammonium chloride solutions were made by dissolving the solid (BDH AR grade) in distilled water. No pH adjustment was made to any of the solutions. The solution was heated while bubbling with the appropriate gas. After the desired temperature was reached the gas outlet valve was closed and the required partial pressure of gas attained. Pressure and temperature equilibration of the cell took approximately 1 hour.

3 The Anodic Dissolution of Pure Iron

3.1 INTRODUCTION

This Chapter describes the anodic dissolution of pure iron in dilute electrolyte solution. The effect of the pH, temperature and electrolyte composition on this oxidation reaction have been investigated.

The anodic dissolution of iron in acidic solutions has been extensively studied, however, the anodic dissolution of iron in slightly acidic solution has received much less attention and a brief review of the literature is presented below. The effect of ammonium ion and chloride on the dissolution reaction is, of course, particularly relevant to the Becher process and thus a second review of the effect of these species on the electrochemistry of iron is also presented.

3.1.1 Electrochemistry of iron in slightly acid solutions

Anderson and Debnath [57] summarised the processes that occur as the potential of iron is scanned from -0.66 to 1.1 V (3M KCl Ag/AgCl) in weakly acidic solutions:

(i) -0.66 to -0.56 V, rapidly rising current: the active range
(ii) -0.56 to -0.46 V, relatively constant current: the transition range
(iii) -0.46 to -0.01 V, slowly rising current: the prepassive range
(iv) -0.01 to 0.04 V, sharp drop in current: the beginning of the passive range
(v) 0.04 to 1.1 V, constant low level current up to oxygen evolution: the passive range

It is generally agreed that oxidation occurs via $(FeOH)_{(ad)}$ and the iron dissolves as $FeOH^{+}_{(aq)}$ throughout the active and prepassive ranges in a series of single electron transfers [58]. In the transition range, $Fe(OH)_{2(ad)}$ forms and slows the dissolution of $FeOH^{+}_{(aq)}$. Sato presented a very general mechanism for metal dissolution to the divalent cation [58] which is presented below in modified form for iron.

$$Fe + H_2O \rightarrow FeOH_{(ad)} + H^+ + e^- \quad (3.1)$$

$$FeOH_{(ad)} \rightarrow FeOH^+_{(aq)} + e^- \quad (3.2)$$

$$FeOH^+_{(aq)} \rightarrow Fe^{2+}_{(aq)} + OH^- \quad (3.3)$$

Numerous detailed mechanisms for iron dissolution have been postulated in the literature and considerable debate about which is the correct mechanism has ensued [59]. These mechanisms have been recently reviewed by Heusler [60], Drazic [61] and Plonski [59]. It is beyond the scope of this work to review these mechanisms here, however, an example of a detailed mechanism for iron dissolution from Lorenz and co-workers is shown below [62-64]. This scheme falls within the category of branching mechanisms that were proposed in the early 1980's in order to account for the active, transition and prepassive ranges of the overall active state [59].

1. Active range

$$Fe + H_2O \leftrightarrow (FeOH)_{(ad)} + H^+ + e^- \quad (3.4)$$

$$(FeOH)_{(ad)} \rightarrow FeOH^+_{(aq)} + e^- \quad \text{rate determining step} \quad (3.5)$$

$$FeOH^+_{(aq)} + H^+ \leftrightarrow Fe^{2+}_{(aq)} + H_2O \quad (3.6)$$

2. Transition range

$$(FeOH)_{(ad)} + H_2O \leftrightarrow [Fe(OH)_2]_{(ad)} + H^+ + e^- \quad (3.7)$$

$$Fe[Fe(OH)_2]_{(aq)} \rightarrow FeOH^+_{(aq)} + (FeOH)_{(ad)} + e^- \quad \text{rate determining} \qquad (3.8)$$

3. Prepassive range

$$[Fe(OH)_2]_{(ad)} + H_2O \leftrightarrow [Fe(OH)_3]\text{-oxide phase} + H^+ + e^- \qquad (3.9)$$

4. Passive layer formation

$$2[Fe(OH)_3]\text{-oxide phase} \leftrightarrow \gamma\text{-}Fe_2O_3 + 3H_2O \qquad (3.10)$$

$$[Fe(OH)_2]_{(ad)} + Fe_2O_3 \leftrightarrow Fe_3O_4 + H_2O \qquad (3.11)$$

In summarising the results from many workers, Plonski [59] concluded that the transition and prepassive current density increases with increasing solution pH. In sulphate solutions a typical reaction order with respect to hydroxide is 1 between pH 0.97 and 3.3 with an anodic Tafel slope of 0.040 V dec^{-1}. Between pH 1 and 6 the polarisation curve for iron shows at least two peaks (I and II). The current density between the two peaks (*ie.* prepassive) increases with increasing electrode rotation speed, decreasing pH and decreasing potential scan rate. As a result, above pH 3 peak I degenerates into a plateau and below pH 2 becomes an inflection point. Below pH 1, peak I is not detectable.

At sufficiently high anodic potential the anodic dissolution rate reaches a second maximum, and then starts to decrease due to the formation of solid phases (equation (3.9)) and finally decreases to very low values due to the formation of oxides directly on the surface (equations (3.10) and (3.11)). Passive iron is covered with a pore-free γ-Fe_2O_3 or Fe_3O_4 film 20-40 Å thick [65]. The anodic current density in the passive region is limited by one more of the following processes [66]:

a) movement of cations from the metal into the oxide
b) movement of cations and/or oxide ions through the oxide
c) movement of cations from the oxide into solution

Discussion of the various theories of iron passivity is beyond the scope of this work. However, Uhlig provides a good introduction to this area [67]. A passive air-formed film

also occurs on iron which has been exposed to air [60]. Heusler added that the air-formed film can be removed by cathodic polarisation leaving an active iron surface [60].

3.1.2 Influence of ammonia and chloride on iron electrochemistry

3.1.2.1 Ammonia

Various workers have investigated the corrosion of iron and steel in concentrated NH_4NO_3-NH_3-H_2O mixtures [68-70]. Very high corrosion rates are observed and it was postulated that a ferrous hexa-ammine complex forms [69] and prevents the precipitation of Fe_3O_4 which would decrease the corrosion rate. A linear region in the Tafel plot was not observed, however, a Tafel value of 0.07 ± 0.01 V dec^{-1} was estimated in any case [69].

Tsinman *et al.* [71] measured the anodic polarisation curves for iron and steel in ammoniacal solutions between pH 9 and pH 14. Typical active-passive behaviour was observed with a transpassive region spanning a wide potential range. Meshcheryakova [72] measured the polarisation curve for carbon steel in concentrated mixtures (30% $CO(NH_2)_2$, 25% NH_4Cl, 25% H_2O and 20% NH_3) and active-passive behaviour was observed. The peak passivation potential and current density strongly depended on whether the electrode was stationary or rotating, but only increased slightly with increasing in rotation speed. Between 0.2 and 1.0 V (*she*) the electrode was passive.

Osseo-Asare and co-workers have investigated the anodic dissolution and corrosion of iron in ammoniacal carbonate solutions over a period of many years [46, 73-76]. Tafel slopes of 0.080 and 0.150 V dec^{-1} at low and high current densities respectively, were obtained in mixtures containing 2 M NH_4OH + 1 M $(NH_4)_2CO_3$ (pH = 9.8). Passivation was observed at higher potentials [76]. The following equation was suggested in order to interpret the results:

$$Fe + nNH_3 \rightarrow Fe(NH_3)_n^{2+} \qquad (3.12)$$

Kim *et al.* investigated the anodic dissolution of sintered iron powder in pH = 9.8 2 M NH_4OH + 1 M $(NH_4)_2CO_3$ solution [74] and provided a theoretical analysis of the results [75]. Sintered iron displayed active-passive behaviour and active dissolution was mass transport dependent. In their theoretical treatment of the results, it was assumed that iron was oxidised to aqueous ferrous ion which quickly complexes with ammonia and is then transported out of the pores.

Bech-Nielsen and Reeve investigated anodic iron dissolution in a variety of pure and mixed electrolytes including NH_4ClO_4 and NH_4Cl [77, 78]. To the authors knowledge, Bech-Nielsen *et al.* are the only workers who have provided quantitative evidence for the direct participation of ammonia on anodic iron dissolution in ammonium ion-containing solution. In NaCl and NH_4Cl mixtures at pH 4.5, chloride ion was found to dominate the adsorption equilibrium in NH_4Cl from 0.1 to 0.9 M. However in 0.9 M NH_4Cl the results deviated in the direction expected for increasing ammonia concentration in the NH_4^+/NH_3 buffer system. Bech-Nielsen commented, "*As in the chloride experiments, a low constant concentration of* NH_4^+ *seemed advantageous, although the halide ion completely dominated the adsorption equilibrium in this range of pH. Kinetically, however, the presence of* NH_4^+ *still had an effect*" [77]. The experiments indicated that 2 electrons were involved in the electron transfer. A general equation valid for both charged and uncharged ligands is presented below for ammonia:

$$Fe^0(NH_3)_a + 3H_2O \leftrightarrow Fe^{II}(OH^-)_3(NH_3)_{a-1}^- + 3H^+ + NH_3 + 2e^- \qquad (3.13)$$

Bech-Nielsen suggested that for systems dominated by ammonia, the order of the active iron dissolution with respect to pH is between 0.7 and 0.8.

Some further qualitative evidence that ammonia molecules interact directly with iron atoms comes from the corrosion inhibition field. Organic amine compounds have received considerable attention with the aim of correlating inhibitive efficiency with the molecular weight, the length of the hydrocarbon chain, the degree of branching and the presence of functional groups. The inhibitive power of these amines is considered to be primarily determined by the electron density on the nitrogen atom of the amine, which provides an electron bond between the inhibitor molecule and the metal surface [79].

3.1.2.2 Chloride ion

Drazic [61] has recently reviewed the influence of halide ions on the anodic dissolution of iron. He wrote "When attempting to summarize the previously given, large number of works on the effects of anions, in particular halide ions, one finds that most authors have found inhibitive effects of these ions when their concentrations are less than ca. 1M in mixtures of sulfate or perchlorate ions". Chloride adsorption at low chloride concentration inhibits anodic iron dissolution via the "hydroxide" mechanism (equations (3.1)-(3.3)) while the "chloride" mechanism – where chloride ion accelerates anodic dissolution – prevails at high chloride activity and high acidity [58]. Thus there will be a

change from hydroxide to chloride mechanisms according to the relative values of chloride activity and acidity [58].

Chloride breakdown of passive films at high anodic potential is well known [60, 66] and leads to pitting dissolution [58, 80]. Many theories exist to the mechanism of the chloride breakdown of passive films [81] however, briefly, the effect is that the anodic current density increases rapidly with potential where normally iron is passive.

3.2 EXPERIMENTAL

The experimental method and equipment used have been described in Chapter 2 (p. 23). In this Chapter all the solutions were deaerated by bubbling with nitrogen gas. All potentials are reported against 3 M KCl Ag/AgCl (E = 0.208 V *vs. she*).

3.3 RESULTS AND DISCUSSION

3.3.1 Influence of electrolyte composition on iron electrochemistry at 30°C

In this section the electrochemistry of iron in different electrolyte solutions is studied using cyclic voltammetry. First, the results from experiments in $NaClO_4$ are discussed since it is a non-complexing electrolyte and thus provides a good baseline for comparison with other electrolytes. Second, NaCl was chosen to show the effect of chloride ion and third, NH_4ClO_4 to show the effect of ammonium ion. NH_4NO_3 was included in order to help explain some of the results observed in NH_4ClO_4. Finally, results from the most complicated electrolyte, NH_4Cl, will be described.

3.3.1.1 $NaClO_4$

The open circuit potential for iron in this solution (pH 6.5) was -0.366 ± 0.008 V and was independent of the electrode rotation speed. Figure 3.1 shows the cyclic voltammogram for an iron rotating disc electrode in 0.2 M $NaClO_4$. Peak labels are usually assigned according to when they appear in the cyclic voltammogram. Therefore, depending upon scan conditions, the same electrochemical feature may be labelled differently. Scanning anodically from the open circuit potential, a very small broad peak (I) was observed at 0.35 V (I_{pI} = 0.0003 A cm^{-2}). The relatively noble open circuit potential and very small anodic current density clearly shows that iron is in the passive state prior to commencing

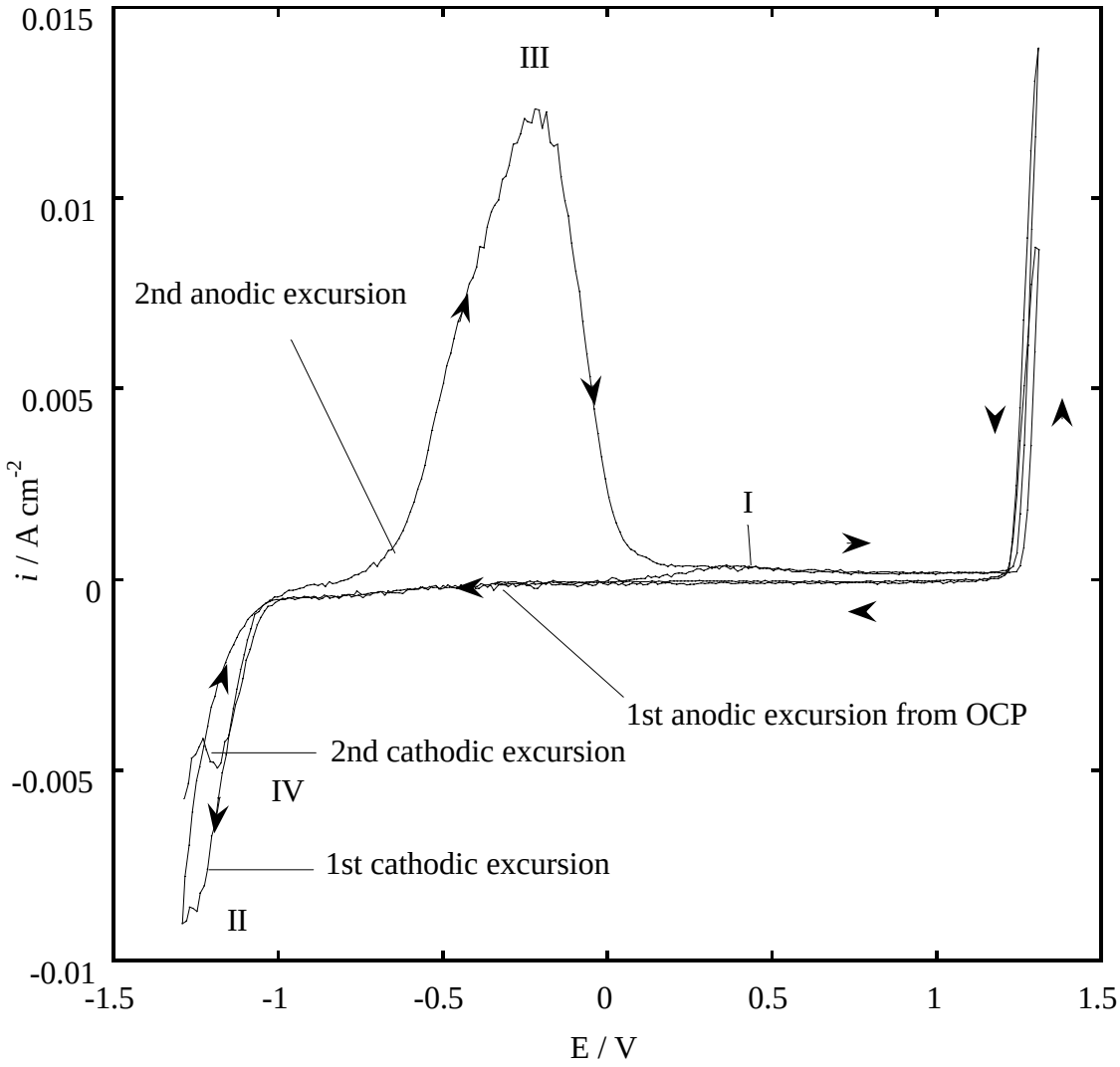

Figure 3.1 Cyclic voltammograms for an iron rotating disc electrode (1000 rpm) in 0.2 M $NaClO_4$ at 50 mV s^{-1}. Anodic scan started from the open circuit potential (OCP). Cycle number indicated. T = 30.0°C. pH = 6.5.

the scan. On the reverse cathodic scan a reduction wave (II) was observed around -1.2 V as a shoulder against the hydrogen evolution current density. However on the following anodic scan a large peak (III) was observed at -0.20 V (I_{pIII} = 0.012 A cm^{-2}). This large oxidation-passivation peak was also observed after the potential was initially scanned in the cathodic direction from the open circuit potential. Regardless of which of these initial scan programs was used, on the cathodic scan following peak III, a smaller but more clearly resolved reduction peak (IV) was observed at -1.20 V (I_{pIV} = 0.0048 A cm^{-2}). The shape of the cyclic voltammogram then changed little further on subsequent potential cycles. Pits were not observed on the surface of the electrode after the run.

Heusler described that due to an air-formed film, iron is passive when it is transferred to a neutral, oxygen-free borate solution [60]. Heusler added that the air-formed film can be removed by cathodic polarisation leaving an active iron surface [60, 81].

These results maybe interpreted as follows.

It is likely that an invisibly thin air-formed film passivates iron and accounts for the noble open circuit potential after immersion and the very low anodic current density during the first anodic scan. Upon scanning cathodically, this air-formed film is reduced leaving a bare iron surface. This results in fast active dissolution on the subsequent anodic sweep, eventually resulting in peak III. Above 0.2 V the anodic current density is very small presumably due to an anodically-formed film. This film is then reduced at -1.2 V (IV).

The cathodic charge under peak IV(Q_{cIV}) corresponds to the amount of anodically-formed film while the anodic charge under peak III (Q_{aIII}) represents the total amount of iron oxidised. The ratio Q_{cIV}/Q_{aIII} is 0.07 which means that most of the iron oxidised at peak III is lost to the solution and only a small amount goes into passive film formation. The amount of charge passed at peak IV was 0.0026 C cm^{-2} assuming that the roughness factor (real surface area/geometric surface area) is 1 . The amount of charge required for a single monolayer, assuming that the oxide present is Fe_3O_4, is 0.00195 C cm^{-2}. If only one monolayer of Fe_3O_4 does form, the roughness factor for the surface would be 1.3.

Figure 3.2 shows the cyclic voltammogram for a stationary iron disc electrode in 0.2 M $NaClO_4$. The first anodic and cathodic potential scans were similar to that observed for the iron rotating disc electrode discussed above. That is, during the first cathodic sweep reduction of the air-formed film occurred around -1.2 V overlapping with

the hydrogen evolution reaction. However, after reduction of the air-formed film, the subsequent anodic scan was very different from that for the iron rotating disc electrode since three small anodic peaks (III, IV, and V) were observed. On the following cathodic scan a clearly resolved peak (VI) at -1.20 V was observed which is most probably due to reduction of an anodically formed film. The reduction of the anodically-formed film (peak IV in Figure 3.1 and peak VI in Figure 3.2) does not depend upon electrode rotation which confirms that this process is a solid state transformation. The shape of the cyclic voltammogram then changed little further on subsequent potential cycles.

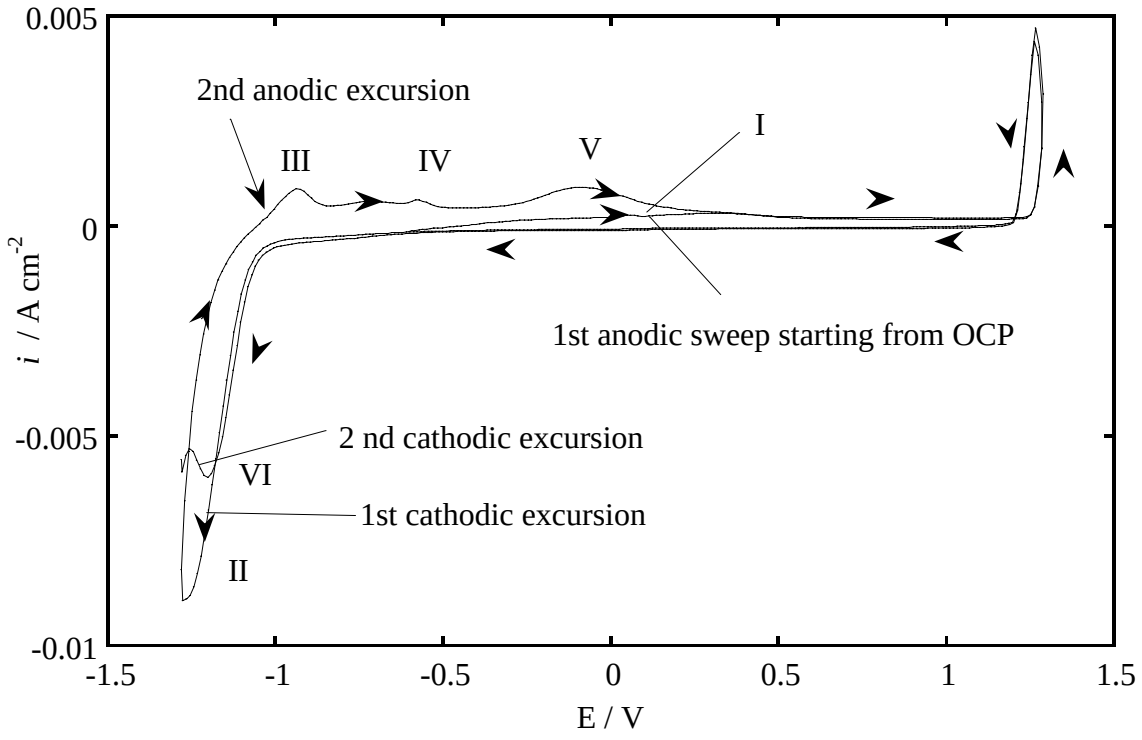

Figure 3.2 Cyclic voltammograms for a stationary iron disc electrode in 0.2 M $NaClO_4$ at 50 mV s^{-1}. Anodic scan started from the open circuit potential (OCP). Cycle number indicated. T = 30.0°C. pH = 6.5.

It is unlikely that the oxidation at peak III is due to iron oxidation since its peak potential of -0.933 V is much lower than the equilibrium potential for the iron couple (Fe/Fe^{II} = -0.648 V). It is more likely however that this peak corresponds to the oxidation of adsorbed hydrogen formed below -1.0 V [76, 82]. Therefore only peaks IV and V can be attributed to iron oxidation. Peak IV probably corresponds to the initial stages of iron oxidation encompassing the active (equations (3.4) to (3.6)) and the transition ranges (equation (3.7) and (3.8)). Peak V is the prepassive range represented

by equation (3.9). The formation of the anodically-formed passive film can be represented by equations (3.10) and (3.11).

Both the active and transition ranges include reactions that involve the solution species $FeOH^{+}_{(aq)}$ (equations (3.5) and (3.8) respectively) and it is most likely that the cyclic voltammograms for active iron are affected by electrode rotation through this species. For example, when the electrode is stationary, the solution near the iron surface very quickly saturates with $FeOH^{+}_{(aq)}$ and iron would be more quickly passivated by $Fe(OH)_{2(ad)}$ (Figure 3.2, peaks IV and V) than when the electrode is rotated since $FeOH^{+}_{(aq)}$ would be swept away to the bulk solution, requiring much higher current densities in order to passivate the iron (Figure 3.1, peak III). Moreover, the absence of a reduction peak at -0.96 V for $FeOH^{+}_{(aq)}$ reduction indicates that all of the iron oxidised goes into passive film formation.

3.3.1.2 NaCl

The open circuit potential for iron in this solution (pH 6.6) was -0.41 ± 0.02 V and was independent of the electrode rotation speed. Figure 3.3 shows the cyclic voltammogram for an iron rotating disc electrode in 0.2 M NaCl. On the first anodic scan iron oxidation only started at approximately -0.15 V and then increased rapidly above this potential (I). This suggests that an air-formed film also passivates iron in NaCl, however, unlike $NaClO_4$, the passive film rapidly breaks down above -0.15 V in NaCl resulting in pitting dissolution. On the reverse cathodic scan the current density during pitting was always higher than on the previous anodic scan. However iron was once again passive below -0.30 V. At more negative potentials a reduction peak (II) was observed at -1.19 V (Ip_{II} = 0.0072 A cm^{-2}). On the following anodic scan, oxidation started at approximately -0.60 V eventually forming a peak (III) at -0.19 V (I_{pIII} = 0.014 A cm^{-2}) undoubtedly corresponding to the formation of an anodically-formed film. Pitting of this film started at -0.07 V. On the following cathodic scan the anodically-formed film also re-passivated as the potential was made more negative and was followed by a reduction peak (IV) at -1.08 V (I_{pIV} = -0.0031 A cm^{-2}). After the experiment, pits were observed on the iron surface. Scans above 0.2 V resulted in catastrophic pitting of the electrode. Integrating the current beneath peaks III and IV reveals that only about 4% of the iron oxidised at peak III is then reduced at IV – the balance must be lost to the bulk solution. The shape of the cyclic voltammogram then changed little further on subsequent potential cycles.

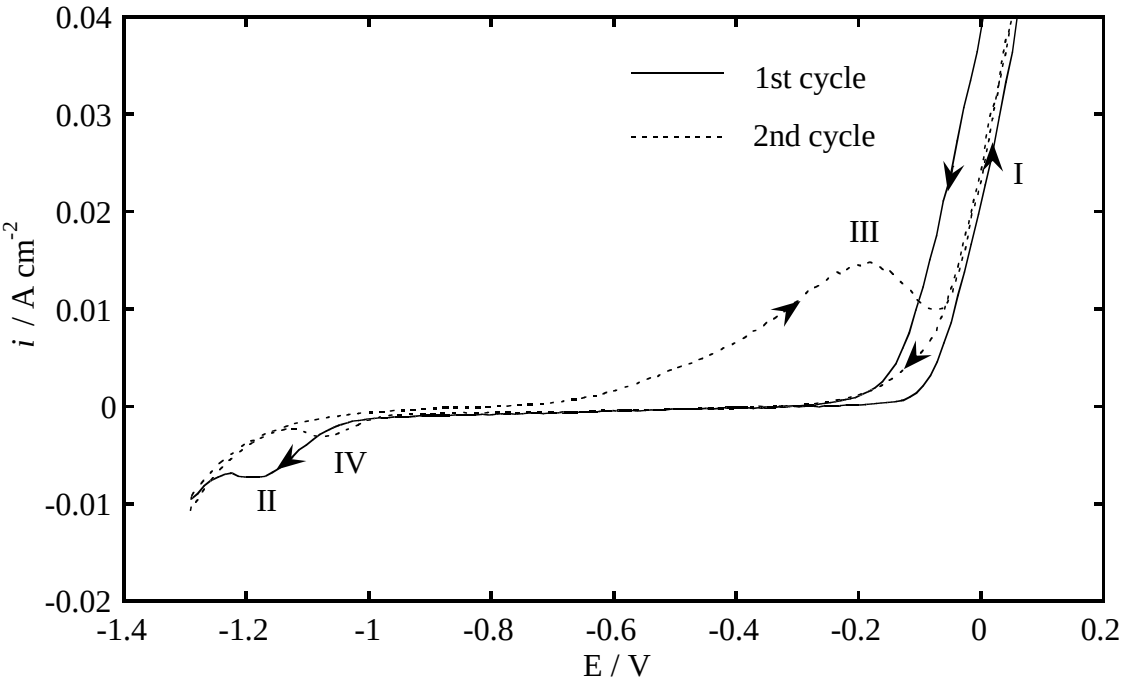

Figure 3.3 Cyclic voltammograms for an iron rotating disc electrode (1000 rpm) in 0.2 M NaCl at 50 mV s^{-1}. Anodic scan started from the open circuit potential. T = 30.0° C. pH = 6.6.

Figure 3.4 shows the cyclic voltammogram for a stationary iron disc electrode in 0.2 M NaCl. The scan commenced in the cathodic direction in order to observe the reduction of the virginal air-formed film. A peak (I) corresponding to the reduction this film was observed at -1.190, (I_{pI} = -0.0059 A cm^{-2}). The close coincidence of peak I with peak II in Figure 3.3 shows that the properties of the air-formed film are not significantly altered despite being first subjected to pitting and then re-forming. On the following anodic scan small oxidation peaks (II, III and IV) were observed between -0.94 and -0.56 V (as shown in the inset of Figure 3.4) followed by a sharp rise in current density due to the onset of anodically-formed-film breakdown, and pitting at more positive potentials. On the subsequent cathodic scan a new peak (V) at -0.960 V appeared which overlaps with the reduction of the anodically-formed film (VI). The origin of this new peak will be discussed below.

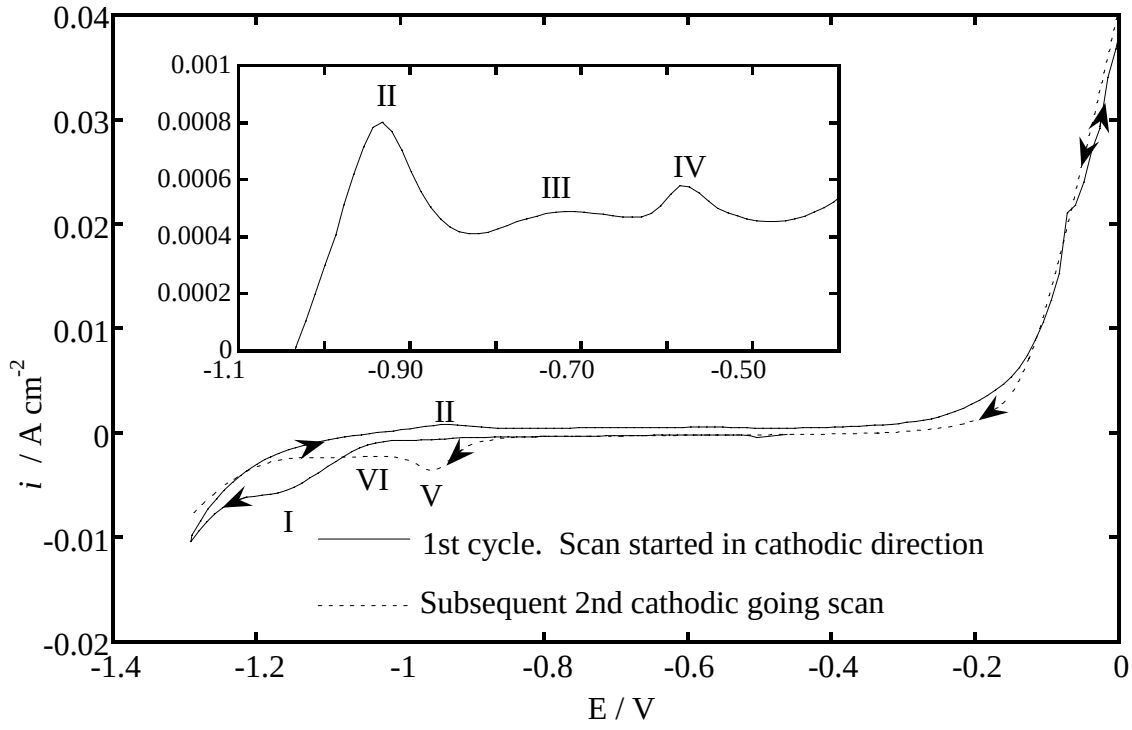

Figure 3.4 Cyclic voltammograms for a stationary iron disc in 0.2 M NaCl at 50 mV s^{-1}. Cathodic scan started from the open circuit potential. Cycle number indicated; (·····) = second cathodic going scan after sweep reversal at E_{Ra} = 0.1 V. T = 30.0°C. pH = 6.6. Inset: 1st anodic scan with expanded current scale.

The active dissolution curve shown in the inset of Figure 3.4 is very similar to the active dissolution curve for stationary iron in $NaClO_4$ (Figure 3.2). Peak IV at -0.577 V is believed to be due to active dissolution forming $Fe(OH)_2$ and peak II is the oxidation of adsorbed hydrogen [76, 82]. Figure 3.5 also shows the cyclic voltammogram for a stationary iron disc electrode in 0.2 M NaCl but with the scan having been initiated in the anodic direction first. Iron pitted on the anodic and following cathodic scan above -0.30 V (I) but was passive below this potential. At more negative potentials two consecutive reduction processes were observed at -0.966 V (II) and at -1.18 V (III). At peak III the air-formed (but anodically pitted and re-passivated) film is reduced. Peak II was observed at the same potential as peak V in Figure 3.4 and in both cases the reduction peak was only observed for a stationary electrode and only when the previous anodic scan extended into the pitting region. This shows that the species reduced at these two peaks is soluble and was formed during pitting dissolution above -0.3 V and therefore most probably corresponds to the reduction of $FeOH^+_{(aq)}$ to metallic iron.

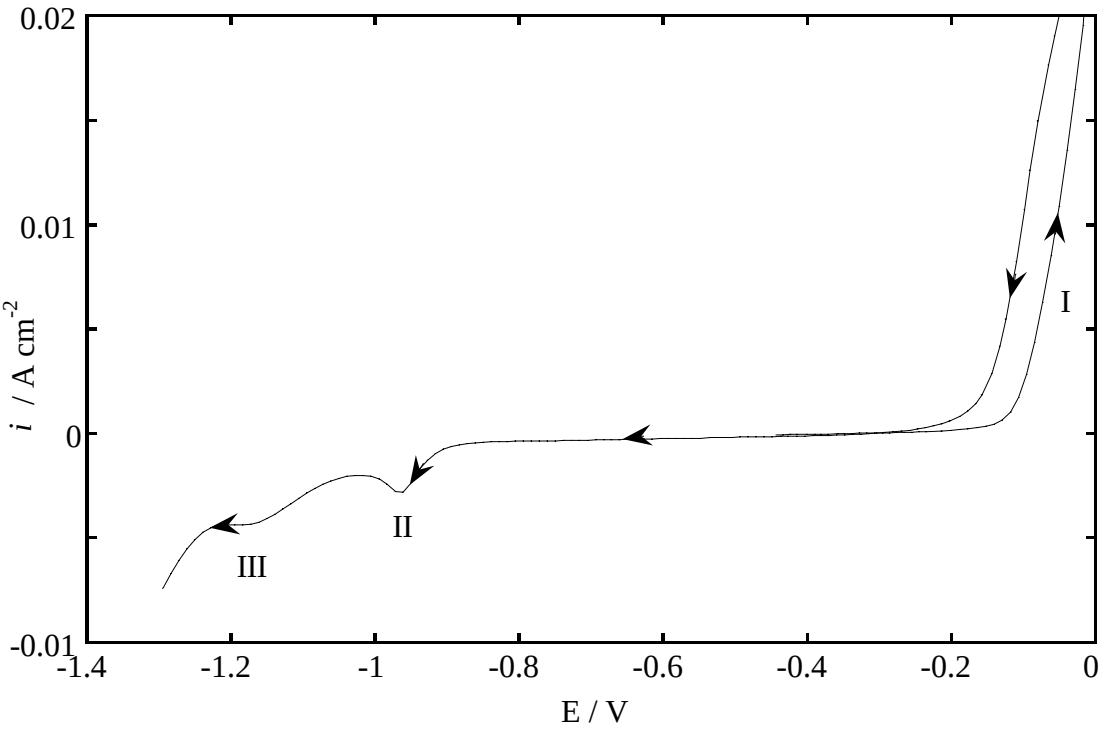

Figure 3.5 Cyclic voltammogram for a stationary iron disc in 0.2 M NaCl at 50 mV s^{-1}. Anodic scan started from the open circuit potential. T = 30.0°C. pH = 6.6.

Both the air-formed and anodically-formed films are most probably conducting since $FeOH^{+}_{(aq)}$ reduction occurred prior to the reduction of the films. This suggests that the anodically-formed and air-formed films consist of magnetite since it is a relatively conducting oxide [39].

3.3.1.3 NH_4ClO_4

The open circuit potential for iron in this solution (pH 5.3) was -0.711 ± 0.005 V and was independent of the electrode rotation speed. Figure 3.6 shows the cyclic voltammogram for an iron rotating disc electrode in 0.2 M NH_4ClO_4 when the scan was initiated in the anodic direction from the open circuit potential. The oxidation peak (I) at -0.05 V (I_{pI} = 0.056 - 0.064 A cm^{-2}) was also observed when scan was initiated in the cathodic direction first. This fact and the relatively negative open circuit potential proves that the air-formed passive film was removed during immersion prior to commencing the scan. Thus the shape of the cyclic voltammogram in NH_4ClO_4 did not depend on the initial scan direction as was observed for iron in $NaClO_4$ (Section 3.3.1.1) and in NaCl (Section 3.3.1.2). Very large anodic current densities were observed before iron started to passivate at approximately -0.05 V. Above this potential the current density decreased rapidly, and between 0.1 and 1.3 V, iron was passive. The inset in Figure 3.6 shows a

portion of the same cyclic voltammogram with an expanded current density scale. This reveals that on the cathodic scan, a small reduction peak (II) at -0.345 V is followed by an overlapping oxidation peak at -0.590 V (III). The relatively large reduction current density below -1.0 V is most likely due to the enhanced rate of the hydrogen evolution reaction in this more acidic electrolyte solution.

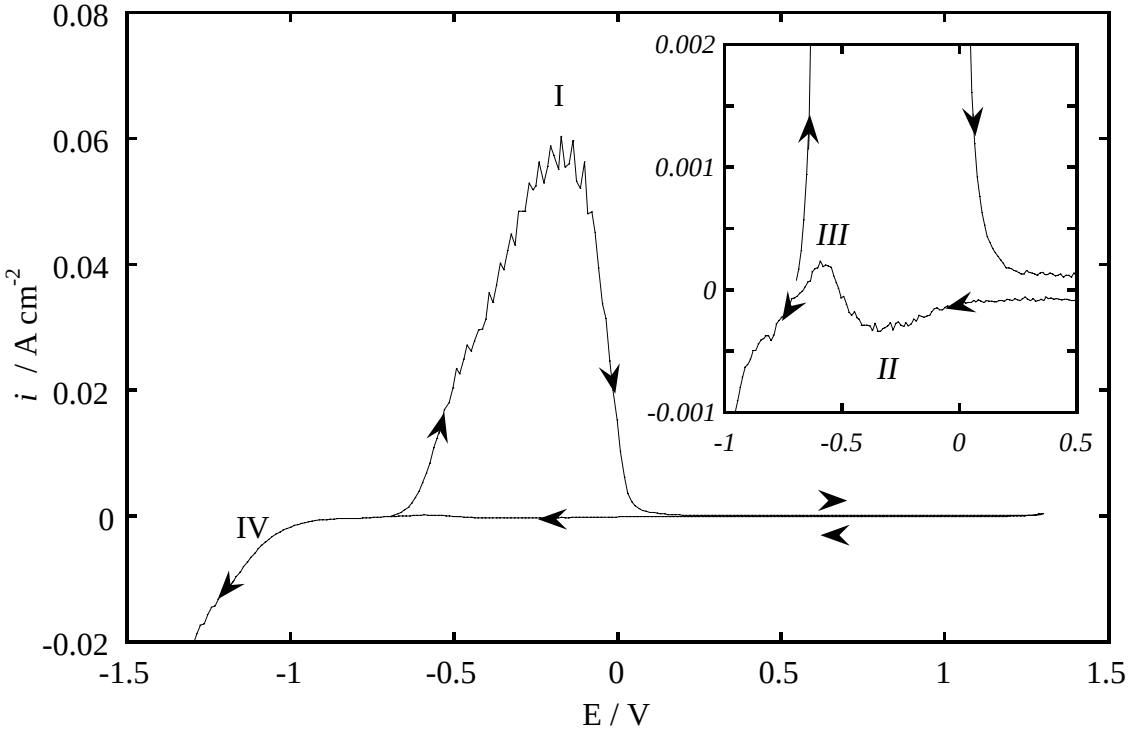

Figure 3.6 Cyclic voltammogram for an iron rotating disc electrode (1000 rpm) in 0.2 M NH_4ClO_4 at 50 mV s^{-1}. Anodic scan started from the open circuit potential (OCP). T = 30.0°C. pH = 5.3.

The air-formed film is obviously not very stable in NH_4ClO_4 solution since rapid oxidation occurs upon anodic polarisation. The anodically-formed film produced at I, which passivates the surface at potentials above 0.1 V, is possibly reduced at peak II via a reductive dissolution mechanism [83-85]:

$$Fe_3O_4 + 8H^+ + 2e^- \rightarrow 3Fe^{2+} + 4H_2O \qquad (3.14)$$

leaving a bare metal surface which starts to re-oxidise under active dissolution at peak II.

Figure 3.7 shows two cyclic voltammograms for a stationary iron disc electrode in 0.2 M NH_4ClO_4, each having a different cathodic reversal potential (E_{Rc}). When the scan was initiated in the cathodic direction, as shown in Figure 3.7, the current density on

the following anodic sweep was relatively small. For E_{Rc} = -1.3 V, two small oxidation peaks (I and II) were observed at -0.72 and -0.52 V. However as E_{Rc} was made more positive, peaks I and II increased in size and a third peak (III) was observed at -0.1 V (Figure 3.7, E_{Rc} = -1.1). For $E_{Rc} \geq$ -1.0 V, only a single large oxidation peak, similar in size and shape to peak I in Figure 3.6, was observed at about -0.1 V on the following anodic scan. Scanning in the anodic direction first on a stationary iron electrode also resulted in a peak similar in size and shape to peak I in Figure 3.6. Pits were not observed on the surface of the electrode after the run.

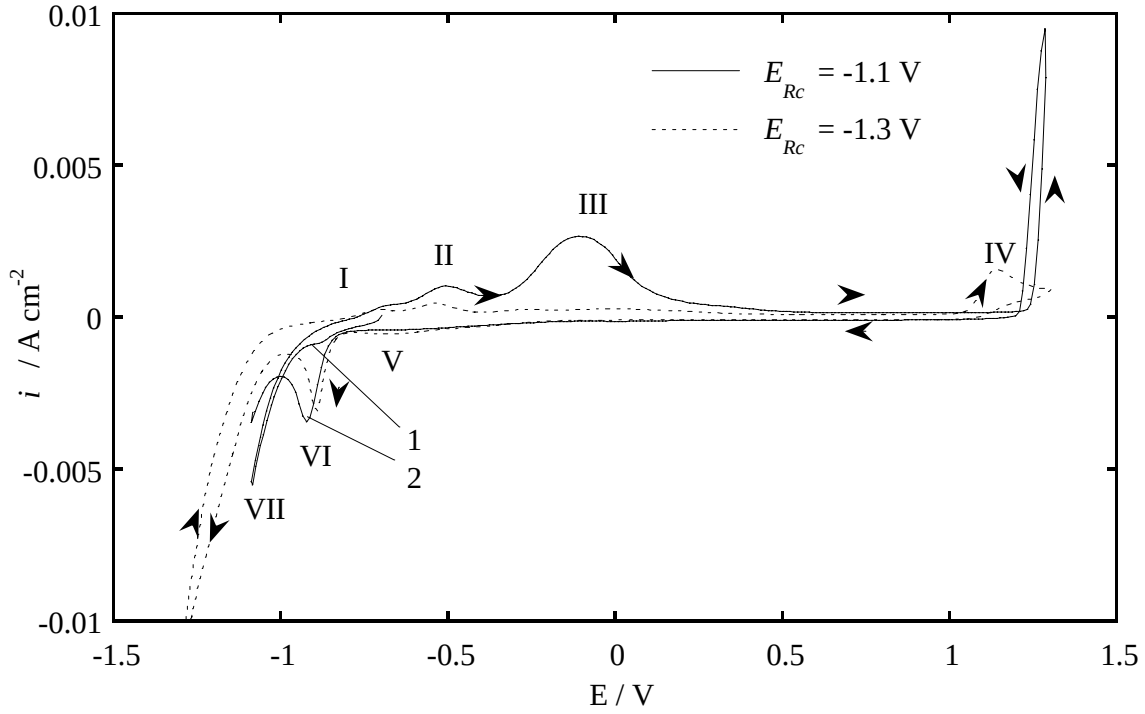

Figure 3.7 Cyclic voltammograms for a stationary iron disc electrode in 0.2 M NH_4ClO_4 at 50 mV s^{-1} showing the effect of cathodic reversal potential (E_{Rc}). Cycle number indicated. T = 30.0°C. pH = 5.3.

A new oxidation peak (IV) was observed at 1.14 V only when the reversal potential on the previous cathodic scan extended to -1.2 V or more negative. On the following cathodic scan reduction peaks (V and VI) were observed at -0.683 and -0.90 V. Peak V appears to correspond to the reduction of the product of the oxidation at 1.14 V (IV) during the previous anodic scan – this will be addressed further in Section 3.3.1.4. Peak VI is most likely to correspond to the reduction of $FeOH^+_{(aq)}$ to metallic iron.

3.3.1.4 NH_4NO_3

The open circuit potential for iron in this solution (pH 5.6) was -0.566 ± 0.009 V and was independent of the electrode rotation speed. Figure 3.8 shows the cyclic voltammogram for an iron rotating disc electrode in 0.2 M NH_4NO_3. Upon initiating a cathodic scan reduction (I) occurred immediately at potentials negative of the open circuit potential. On the following anodic scan the current density retraced the previous cathodic scan until the open circuit potential was reached and an oxidation peak (II) was observed at 0.18 V (I_{pI} = 0.033 A cm^{-2}). Between 0.0 V and 1.3 V iron was passive. The shape of the cyclic voltammogram was independent of the initial scan direction or the number of potential cycles.

Figure 3.9 shows the cyclic voltammogram for a stationary iron disc electrode in 0.2 M NH_4NO_3. The reduction at I was similar to that observed at 1000 rpm (Figure 3.8). The inset Figure 3.9 shows that on the following anodic scan a very small oxidation peak (II) was observed at -0.55 V (I_{pII} = 0.38 mA cm^{-2}). A second larger oxidation peak (III) was then observed at 1.10 V (I_{pIII} = 0.013 A cm^{-2}) followed by a reduction peak (IV) at -0.44 V (I_{pIV} = 0.002 A cm^{-2}) on the following cathodic scan. Both the oxidation (III)

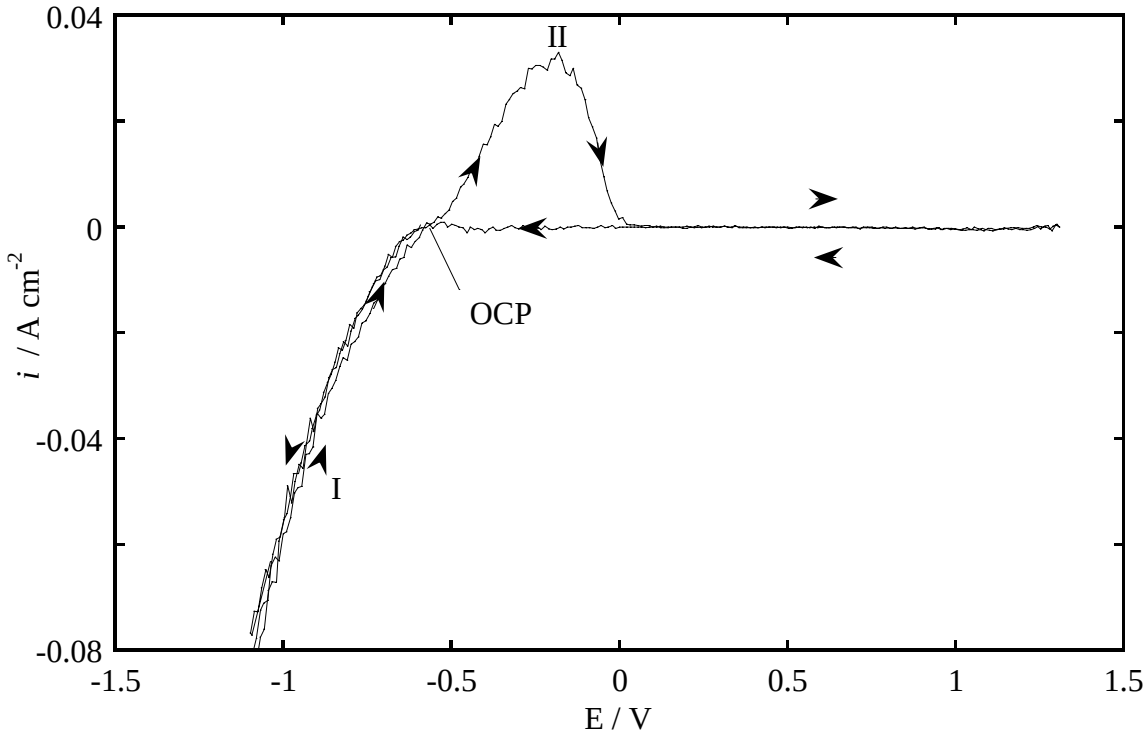

Figure 3.8 Cyclic voltammogram for an iron rotating disc electrode (1000 rpm) in 0.2 M NH_4NO_3 at 50 mV s^{-1}. Cathodic scan started from the open circuit potential (OCP). T = 30.0°C. pH = 5.6.

and reduction (IV) peaks were not observed when the scan was initiated in the anodic direction.

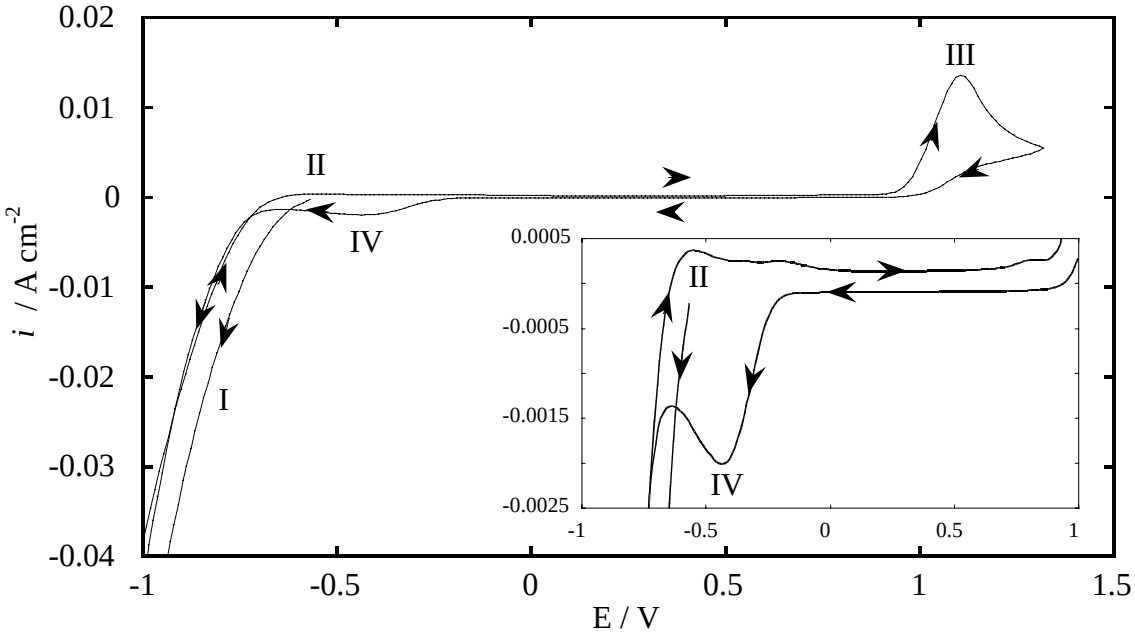

Figure 3.9 Cyclic voltammograms for a stationary rotating disc electrode in 0.2 M NH_4NO_3 at 50 mV s^{-1}. Cathodic scan started from the open circuit potential. T = 30.0° C. pH = 5.6. Inset: Expanded current scale.

These results maybe interpreted as follows.

The large reduction at wave (I) below -0.6 V in Figure 3.8 and Figure 3.9 was only observed in NH_4NO_3 solution and therefore most probably corresponds to the reduction of nitrate to nitrous acid [86]:

$$NO_3^- + 3H^+ + 2e^- \rightarrow HNO_2 + H_2O \quad E° = 0.94\ V \qquad (3.15)$$

The magnitude of the current density at I was independent of the electrode rotation speed showing that nitrate reduction is activation controlled. Nitrous acid is a weak acid (pK_a = 5.22) and can behave as an oxidant toward Fe^{2+} [39]. Thus it is possible that HNO_2 accumulates near the surface during the reduction of NO_3^- (I) on a stationary iron electrode and oxidises $FeOH^+_{(aq)}$ as soon as it is generated on the following anodic scan (peak II) forming a passive film. On a rotating iron electrode HNO_2 is swept into the bulk solution allowing active iron dissolution to occur on the following anodic scan (peak II, Figure 3.8). However even at 1000 rpm, the oxidation peak in NH_4NO_3 (II, Figure 3.8) is less than half of the height of the oxidation peak in NH_4ClO_4 solution (I,

Figure 3.6). This indicates that passive film formation on iron is still more favourable in NH_4NO_3 compared with NH_4ClO_4 solution.

Both the oxidation (III) and reduction (IV) peaks in Figure 3.9 involve solution species since they were absent at 1000 rpm (*cf* Figure 3.8). HNO_2 produced from the reduction at I is possibly oxidised at peak III and the product of this oxidation is then reduced at peak IV since both peaks III and IV were absent if the scan was initiated in the anodic direction first. Further experiments are required to elucidate the nature of the reactions occurring at these peaks but both electrochemical and chemical transformations of species such as NO, N_2O, N_2O_4 and NH_4^+ may be possible. However, the significance of these experiments is that they suggest the species produced from the reduction of nitrate (I, Figure 3.9) may also be produced from the reduction of NH_4^+ at more negative potentials in NH_4ClO_4 since the oxidation peak at 1.10 V was observed in both solutions (IV, Figure 3.7 and III, Figure 3.9).

3.3.1.5 NH_4Cl

The open circuit potential for iron in this solution (pH 4.8-5.0) was -0.735 ± 0.003 V and was independent of the electrode rotation speed. Figure 3.10 shows the cyclic voltammograms for a rotating iron disc electrode in 0.2 M NH_4Cl. Oxidation started as soon as the scan was commenced in the anodic direction and a peak (I) was observed at -0.33 V. The current density decreased between -0.33 V and -0.10 V, but then increased rapidly at more positive potentials (II). On the following cathodic scan the current density retraced the previous anodic scan to -0.10 V and then decreased to very low values below -0.4 V. An oxidation peak (III) was then observed at -0.54 V followed by a reduction wave (IV) below -1.0 V. On the following anodic scan a small oxidation peak (V) was observed at -0.703 V. The rest of the second anodic scan was essentially the same as the first. Peak V did appear on the first anodic scan following an initial cathodic scan, however, the shape of the remainder of the scan was similar to an anodically initiated cyclic voltammogram.

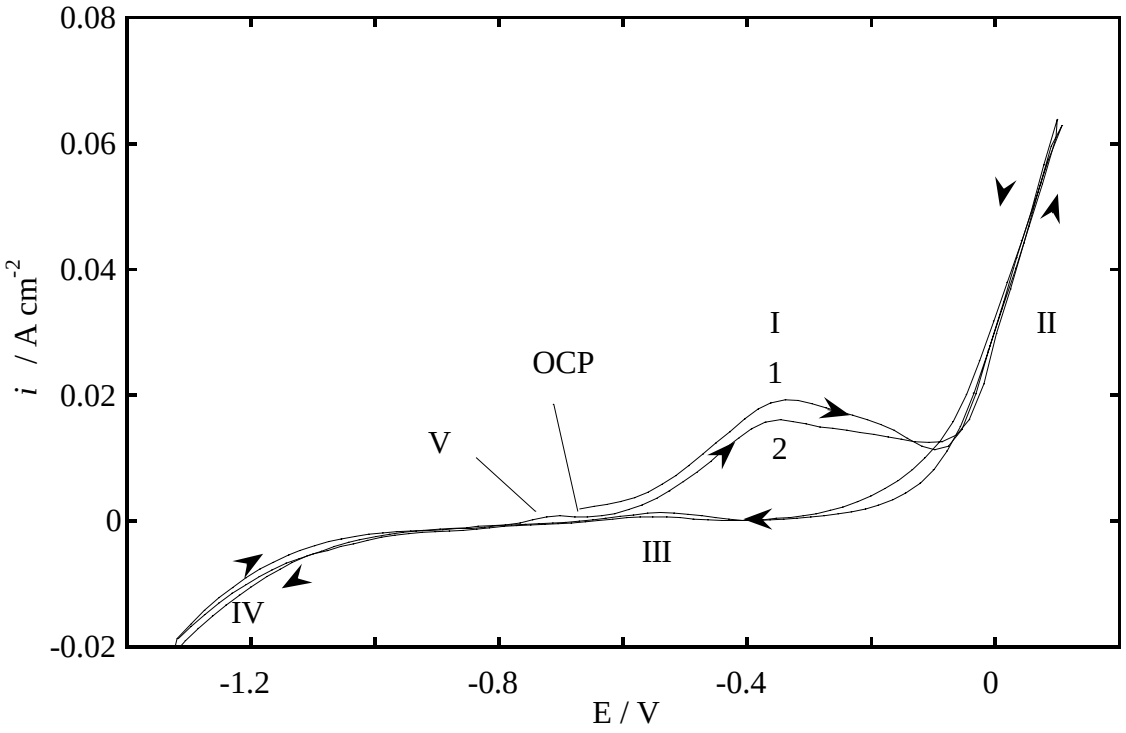

Figure 3.10 Cyclic voltammogram for an iron rotating disc electrode (1000 rpm) in 0.2 M NH_4Cl at 50 mV s^{-1}. Anodic scan started from the open circuit potential (OCP). T = 30.0°C. pH = 4.8.

Figure 3.11 shows the cyclic voltammograms for a stationary iron disc electrode

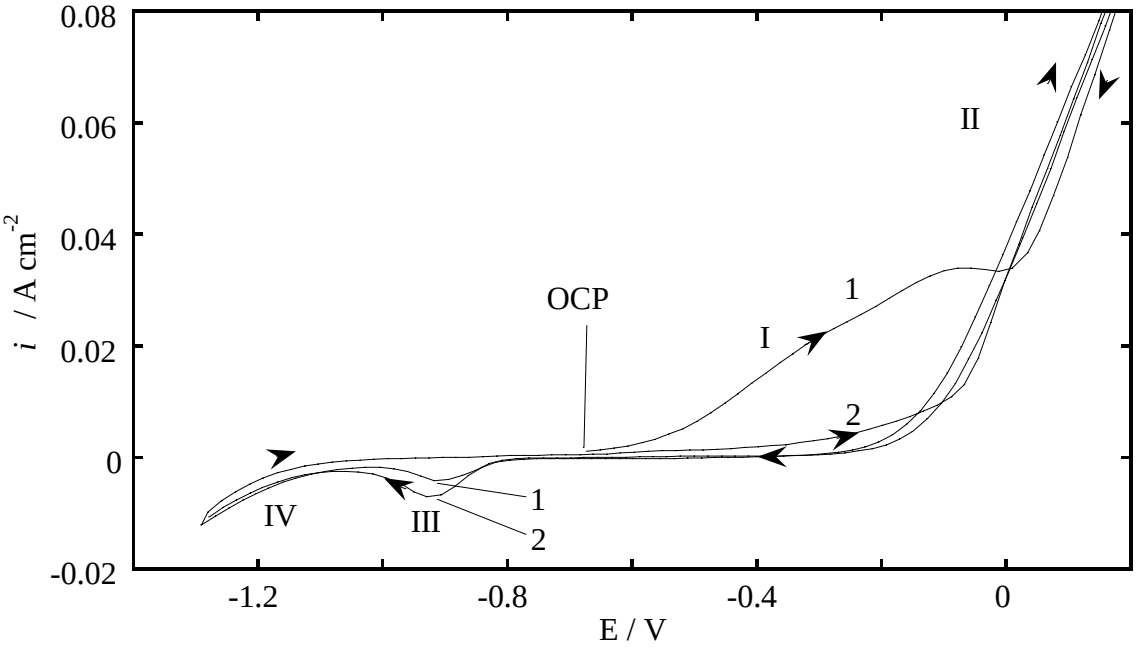

Figure 3.11 Cyclic voltammograms for a stationary iron disc electrode in 0.2 M NH_4Cl at 50 mV s^{-1}. Anodic scan started from the open circuit potential (OCP). Cycle number indicated. T = 30.0°C. pH = 4.8.

in 0.2 M NH_4Cl. Scanning anodically, oxidation commenced immediately and the current density increased steadily with potential (I), levelled off at around -0.06 V for a short period before it rapidly increased above -0.01 V (II). On the following cathodic scan the current density decreased rapidly reaching very low values by -0.3 V. A reduction peak (III) was observed at -0.91 V only after iron oxidation had occurred on the previous anodic scan. On the following (second) anodic scan the current density increased only very gradually with potential up to -0.01 V and then increased rapidly with potential above this value as observed on the previous scan (II). The following (second) cathodic scan was similar to the first. After the experiment, pits were observed on the iron surface.

The following experiments were designed to elucidate the nature of the passivation that was observed after scanning the electrode to -1.3 V (second cycle, Figure 3.11).

Figure 3.12a shows the cyclic voltammograms for a stationary iron disc electrode cycled between the open circuit and the anodic reversal potential (E_{Ra} = 0.2 V). The current density on the second anodic scan was significantly less than observed on the first anodic scan. Figure 3.12b shows the cyclic voltammograms for a stationary iron disc electrode cycled between the open circuit potential and 0.2 V, however, after the first anodic cycle was completed, 22 seconds elapsed at the open circuit potential before the

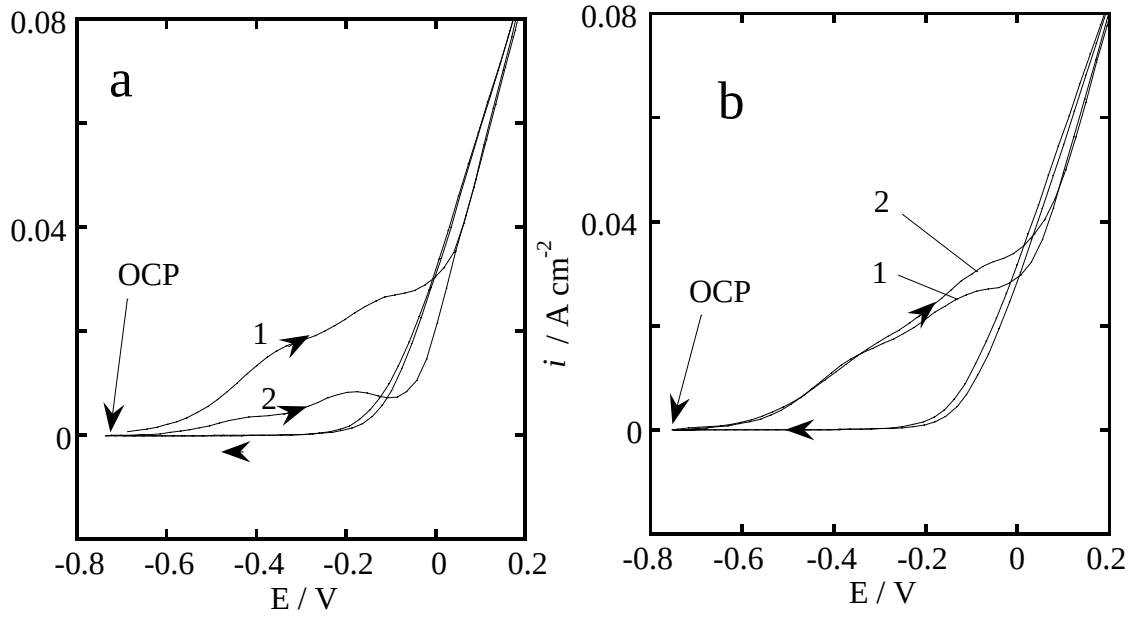

Figure 3.12 Cyclic voltammograms for a stationary iron disc electrode in 0.2 M NH_4Cl at 50 mV s^{-1}. Anodic scan started from the open circuit potential (OCP). (a) 0 s wait time at OCP and (b) 22 s wait time at OCP after the first potential cycle. Cycle number indicated. T = 30.0°C. pH = 4.8.

second anodic scan was initiated. The 22 second wait time was chosen since it is the time taken to scan from the open circuit potential to -1.3 V and back. Figure 3.12b shows that the anodic current density on the second anodic scan was nearly the same as on the first anodic scan. This clearly shows that there are two unrelated processes responsible for the low anodic current depending on whether the electrode scan is initiated in the anodic or cathodic direction first.

The reduction peak at -0.91 V (III, Figure 3.11) is most probably due the reduction of $FeOH^{+}_{(aq)}$ to metallic iron. To confirm this, Fe^{2+} was added to the electrolyte as $FeCl_2.4H_2O$ (~4.5 mM). The cyclic voltammogram for a stationary iron disc electrode in this solution is shown in Figure 3.13. A reduction peak (I) at -0.87 V

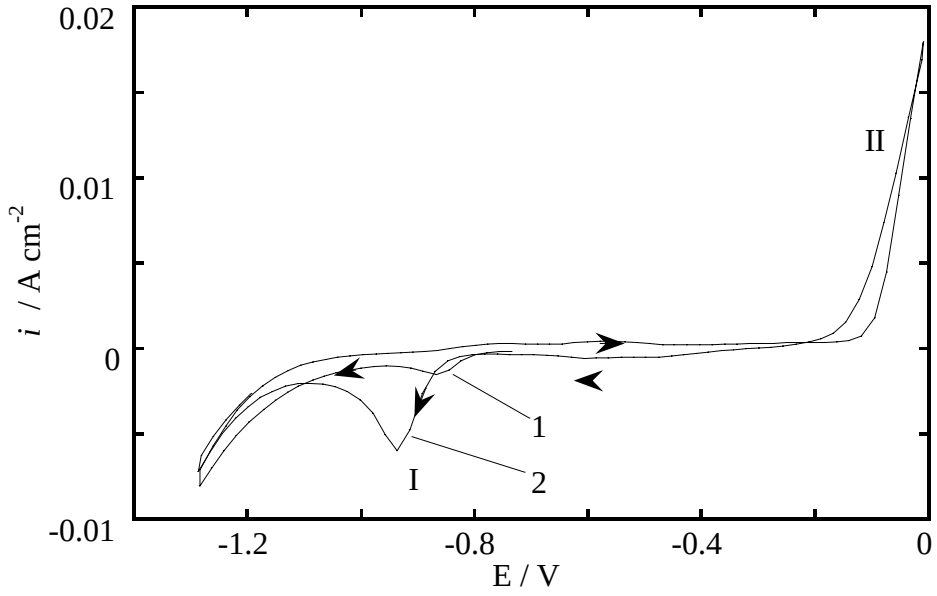

Figure 3.13 Cyclic voltammogram for a stationary iron disc electrode in 0.2 M NH_4Cl containing 4.5 mM Fe^{2+} at 50 mV s^{-1}. Cathodic scan initiated from the open circuit potential. Cycle number indicated. T = 30.0°C.

was observed on the first cathodic sweep (I_{pI} = 0.0015 A cm^{-2}) and corresponds to the reduction of Fe^{2+} in the bulk solution, to metallic iron. After iron oxidation above -0.2 V (II), a larger reduction peak at -0.91 V was observed on the following cathodic sweep. The more negative peak potential is probably a result of the higher concentration of $FeOH^{+}_{(aq)}$.

These results may be interpreted as follows.

The very negative open circuit potential and the large anodic current densities on the first anodic scan, indicate that the air-formed film is removed during immersion prior to commencing the scan.

Between the open circuit potential and -0.10 V, active (equations (3.4)-(3.6)), transition (equations (3.7) and (3.8)) and prepassive dissolution (equation (3.9)) occurs. The reason why passivation occurred at more negative potentials and to a greater extent at 1000 rpm compared with 0 rpm is not clearly understood.

The sharp increase in the current density above -0.10 V is most likely due to anodic pitting dissolution. The apparent linear dependence of the current density on the potential and its independence from electrode rotation, are characteristics of anodic pitting processes [58, 80].

The soluble oxidation product of the iron dissolution reaction was reduced at a single reduction peak at -0.91 V which strongly suggests that a single Fe^{II} species, most probably $FeOH^{+}_{(aq)}$, is the only soluble Fe^{II} iron oxidation product in NH_4Cl solution.

The low anodic current densities observed for stationary electrodes after cathodic potential excursions may be due to one or more of the following:

a) the adsorption of hydrogen and/or FeH formation that inhibits anodic dissolution [76, 87]
b) the high interfacial pH, a result of the hydrogen evolution reaction, results in the formation of a stable $Fe(OH)_2$ film

The low anodic current densities observed between -0.01 and -0.60 V on the cathodic scan after anodic pitting is most likely a result of the fast re-passivation of the pits, completing the anodically formed film. However, like the air-formed film, the anodically-formed film is unstable in NH_4Cl solution. This film is removed over a period of only a few seconds allowing iron oxidation to once again occur uninhibited. This is most clearly demonstrated in Figure 3.12a and Figure 3.12b. The instability of the anodically formed film also explains the oxidation peak (III) at -0.54 V observed on the cathodic sweep in Figure 3.10.

3.3.1.6 Effect of Ammonium and Chloride Ions

Figure 3.14 shows the cyclic voltammograms for iron rotating disc electrodes in each of the electrolyte solutions discussed above. For $NaClO_4$ and NaCl, where the air-formed film was stable and passivated the electrode, the second cycle of the voltammograms are shown so that the active dissolution region can be seen.

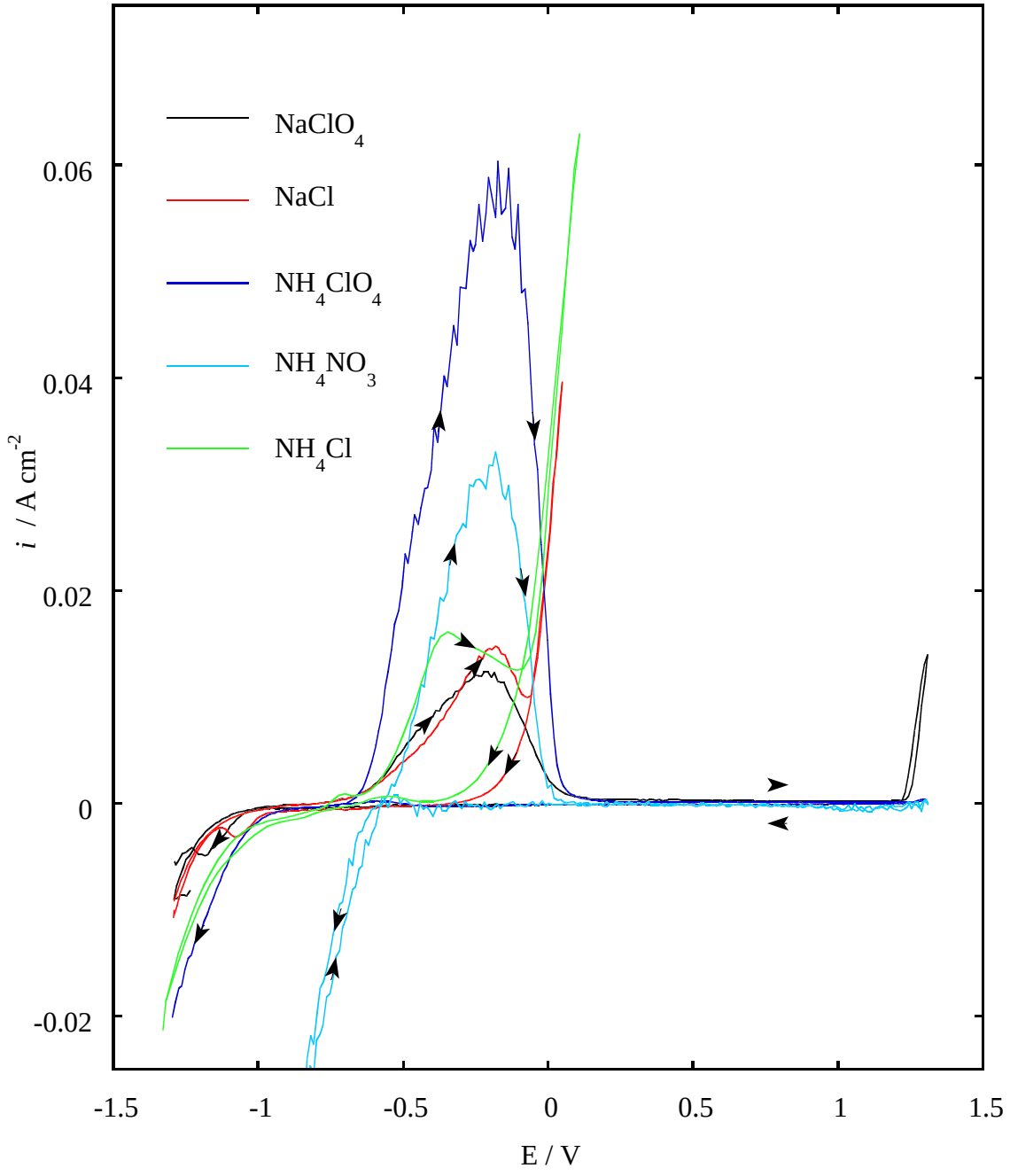

Figure 3.14 Cyclic voltammograms for an iron rotating disc electrode in various 0.2 M electrolyte solutions at 50 mV s^{-1}. T = 30.0°C.

In the presence of chloride, the anodically-formed and air-formed films break down above -0.1 V resulting in pitting dissolution. Below -0.1 V, films are stable even in the presence of chloride but only if ammonium ion is absent.

In the ammonium electrolyte solutions, the anodically formed film appears stable but this is only true over the short time frame of a single voltammogram (tens of

seconds). At longer times the anodically-formed film is removed just like the air-formed film is removed during immersion, prior to polarisation.

The active anodic current density is higher in the absence of chloride and in the presence of ammonium ion.

3.3.2 The pH dependence of anodic iron dissolution in 0.2 M NH_4Cl at 30°C

Figure 3.15 shows the effect of pH on the open circuit potential for an iron rotating disc electrode in 0.2 M NH_4Cl, 5 minutes after immersion. The open circuit potential decreased from -0.56 V to -0.710 V between pH 3.0 and 4.0, was constant between pH 4.0 and 6.0, increased slightly at pH 6.5 and 7.0 and then increased to -0.3 V at pH 8.0.

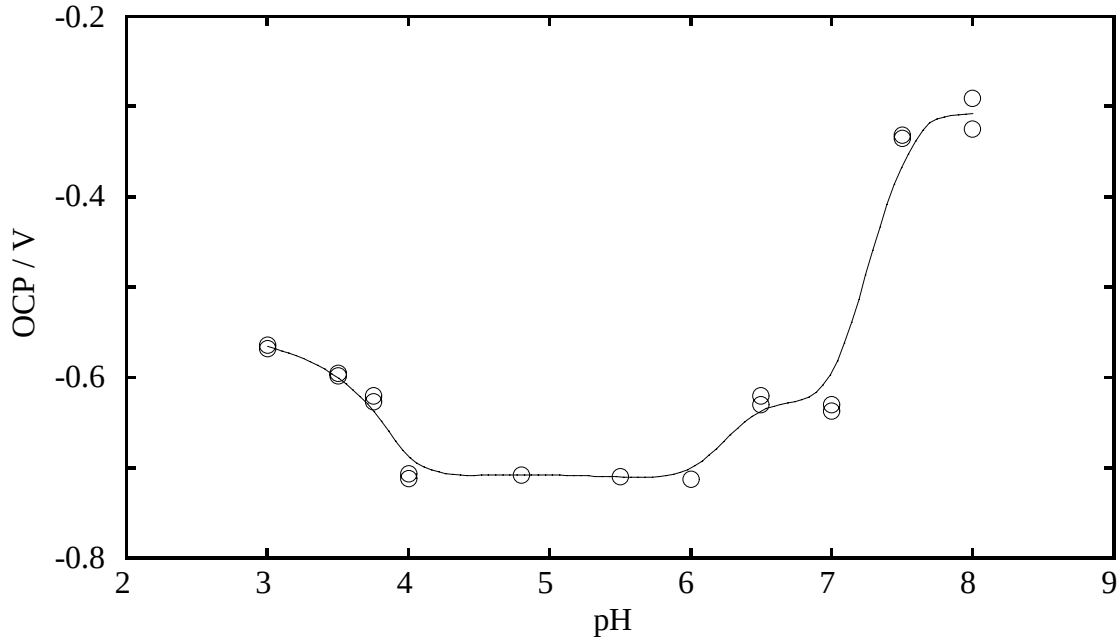

Figure 3.15 The open circuit potential (OCP) for an iron rotating disc electrode (1000 rpm) in 0.2 M NH_4Cl as a function of pH. T = 30.0°C. Immersion time = 5 minutes.

In acidic solutions it is well known that the open circuit potential shifts in the negative direction with an increase in the pH [59, 61]. The slope, dOCP/dpH, was between -40 and -62 mV in acidic sulphate solutions (pH 0-4) [59]. Figure 3.15 shows a non-linear decrease in the open circuit potential between pH 3.0 and 4.0. However, dOCP/dpH was more negative than -100 mV. Between pH 4.0 and 6.0 the open circuit potential was constant and was at its lowest value of -0.71 V. The very positive open circuit potential at pH 7.5 and 8.0 indicates that the iron is passive, most probably due to the stability of the air-formed film at high pH.

Figure 3.16 shows anodic polarisation curves for an iron rotating disc electrode in

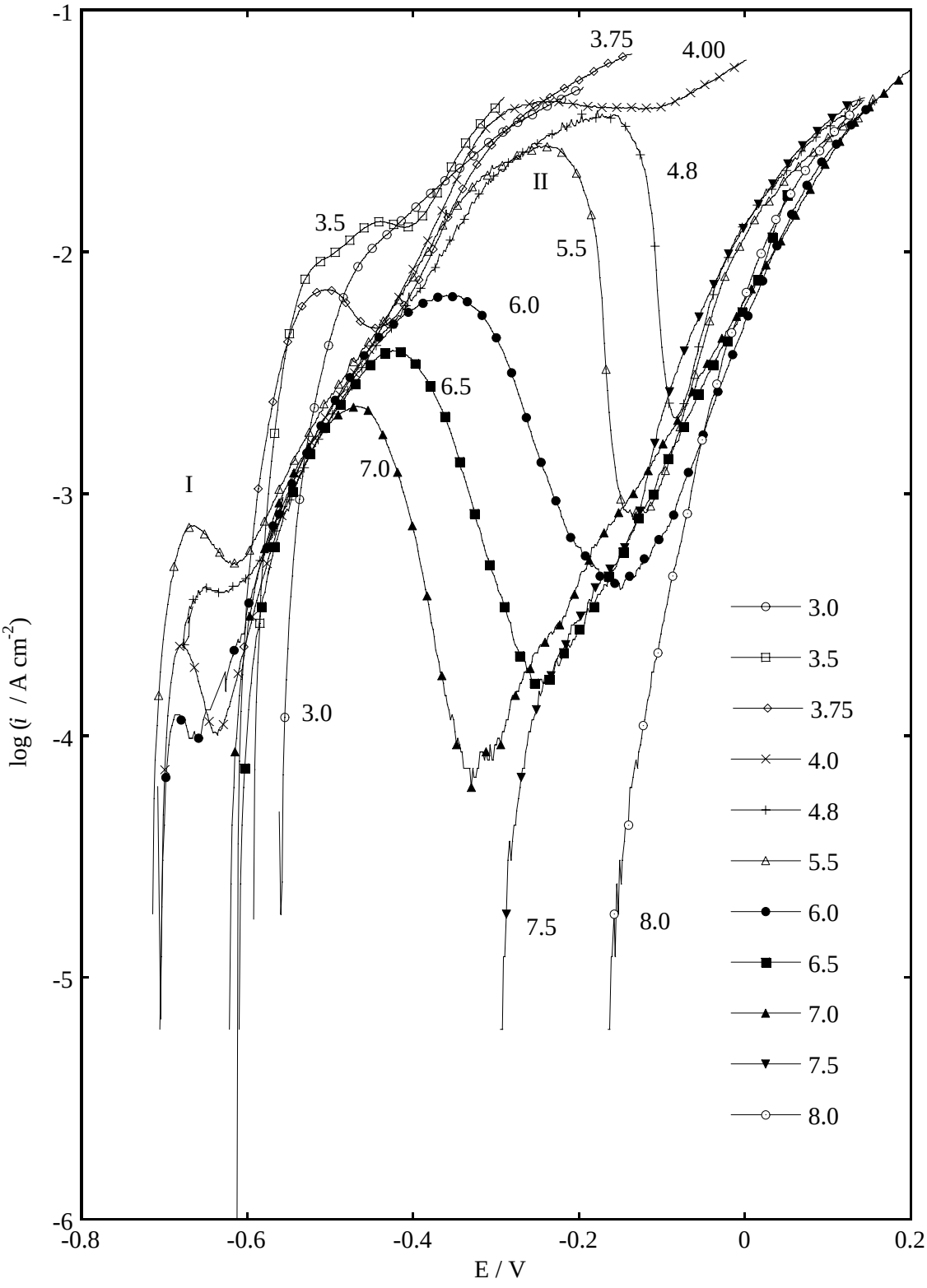

Figure 3.16 Anodic polarisation curves for an iron rotating disc electrode (1000 rpm) in 0.2 M NH_4Cl as a function of pH at 1 mV s^{-1}. T = 30.0°C.

0.2 M NH_4Cl between pH 3.0 and 8.0. The polarisation behaviour of iron over this pH range can be separated into four distinct regions as follows:

1. pH 3.0-3.75; Active and/or prepassive dissolution
2. pH 4.0-6.0; Active dissolution, transition, prepassive dissolution, onset of passivation and pitting dissolution
3. pH 6.5-7.0; Prepassive dissolution, onset of passivation and pitting dissolution
4. pH 7.5-8.0; Pitting dissolution only

For the potential range -0.60 to -0.40 V, the highest current densities were observed between pH 3.0 and 3.75. The shapes of the polarisation curves at the these pH values are quite different. At pH 3.0 there are two Tafel regions. At pH 3.5 there also appears to be two Tafel regions: a transition or an arrest in the increase of current density with potential, followed by a third Tafel region. And at pH 3.75, after the first Tafel region, passivation starts and is followed by a second Tafel region at more positive potentials. Microscopic inspection of the electrode after the experiment confirmed that iron dissolution was uniform.

Between pH 4.0 and 6.0 the polarisation behaviour is well defined and is almost typical of iron behaviour in mildly acidic solutions [64]. The first increase in the current density corresponds to the active dissolution region. Peak I marks the start of the transition region where the current density is relatively constant. The next increase in current density is the prepassive region. Table 3.1 lists the Tafel slopes of the prepassive region. Peak II, at around -0.15 V, is followed by a region of decreasing current density and marks the beginning of the passive range. Significantly, an extended passive range was not observed, due to the presence of chloride ion. Instead the current increased monotonously from -0.18 V (at pH 4.8) indicating that pitting dissolution is operative which was confirmed by microscopic examination of the surface the after the experiment.

pH	Tafel Slope / V dec^{-1}	Potential Range / V
4.8	0.212 ± 0.007	$-0.50 \rightarrow -0.35$
5.5	0.18 ± 0.02	$-0.60 \rightarrow -0.35$
6.0	0.10 ± 0.015	$-0.65 \rightarrow -0.55$
6.5	0.169 ± 0.002	$-0.55 \rightarrow -0.45$

Table 3.1 Tafel slope for iron in the prepassive range at different pH values, from Figure 3.16. The error bars indicate twice the standard error in the mean.

The peak potential for peak II (E_{pII}) shifted steadily to more negative potentials with increasing pH and the peak current density (I_{pII}) decreased between pH 4.8 and 7.0. The significance of these trends is discussed in more detail later. The transition from passivation to pitting dissolution also steadily decreased to more negative potentials with increasing pH and the current density at this transition point also decreased with increasing pH. This is an indication of the increasing stability of the anodically-formed film at higher pH. At pH 7.5 and 8.0 only pitting dissolution was observed. The pits were about 0.05 to 0.2 mm in diameter and often had a dark coloured oxide streaming from them across the surface.

Lorbeer and Lorenz [64] derived equations relating the peak current density and potential with pH based on their mechanism for iron dissolution (equations (3.4) to (3.11)). The equations for the prepassive region and for peak II are reproduced below.

$$\left(\frac{\partial \log i_{+}}{\partial pH}\right)_{E} = 0 \tag{3.16}$$

$$\left(\frac{\partial E_{pII}}{\partial pH}\right) = -\frac{2.303RT}{F} \tag{3.17}$$

$$\left(\frac{\partial \log I_{pII}}{\partial pH}\right) = -\alpha \tag{3.18}$$

$$\left(\frac{\partial E}{\partial \log i}\right) = \frac{2.303RT}{\alpha F} \tag{3.19}$$

Figure 3.17a shows the peak II peak potential as a function of pH and Figure 3.17b shows the logarithm of the peak II peak current density as a function of pH. The slope of the least squares line through the data points in Figure 3.17a (dE_{pII}/dpH) (see

equation (3.17)) is -0.123 V. Equation (3.17) is derived from the following more general equation:

$$\left(\frac{\partial E}{\partial pH}\right) = -\frac{-m2.303RT}{nF} \tag{3.20}$$

where *m* and *n* are the numbers of hydrogen ions and electrons respectively, involved in the reaction. For equation (3.9) both *m* and *n* are equal to one and thus equation (3.17) predicts a slope of -0.060 V. The experimental slope -0.123 V means that *m* = 2 (since it is most unlikely that *n* = 0.5). This is a significant difference between experiment and theory and further work needs to be to eleucidate the exact nature of the reaction occuring in the pre-passive range. The slope of the least squares line through the data points in Figure 3.17b ($d\log I_{pII}/dpH$) is -0.54. This value can then be substituted into equation (3.18) giving a value for the charge transfer coefficient, α, of 0.54.

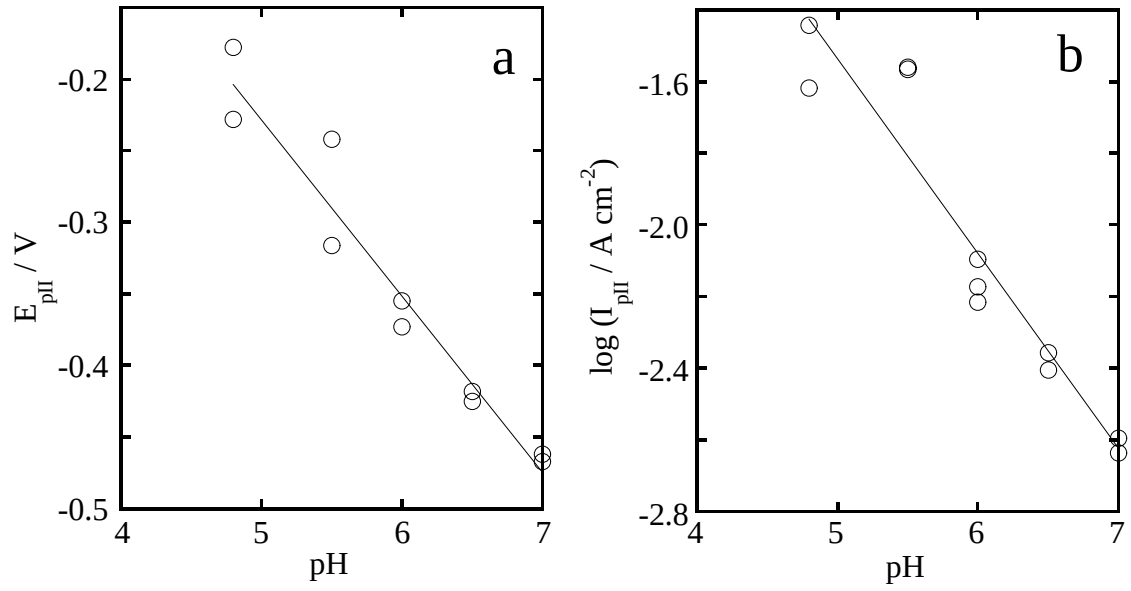

Figure 3.17 a) Peak potential (E_{pII}) and b) the logarithm of the peak current (I_{pII}) as a function of pH, from Figure 3.16.

3.3.3 Temperature dependence of anodic iron dissolution in 0.2 NH_4Cl

Figure 3.18 shows the polarisation curves for an iron rotating disc electrode at various

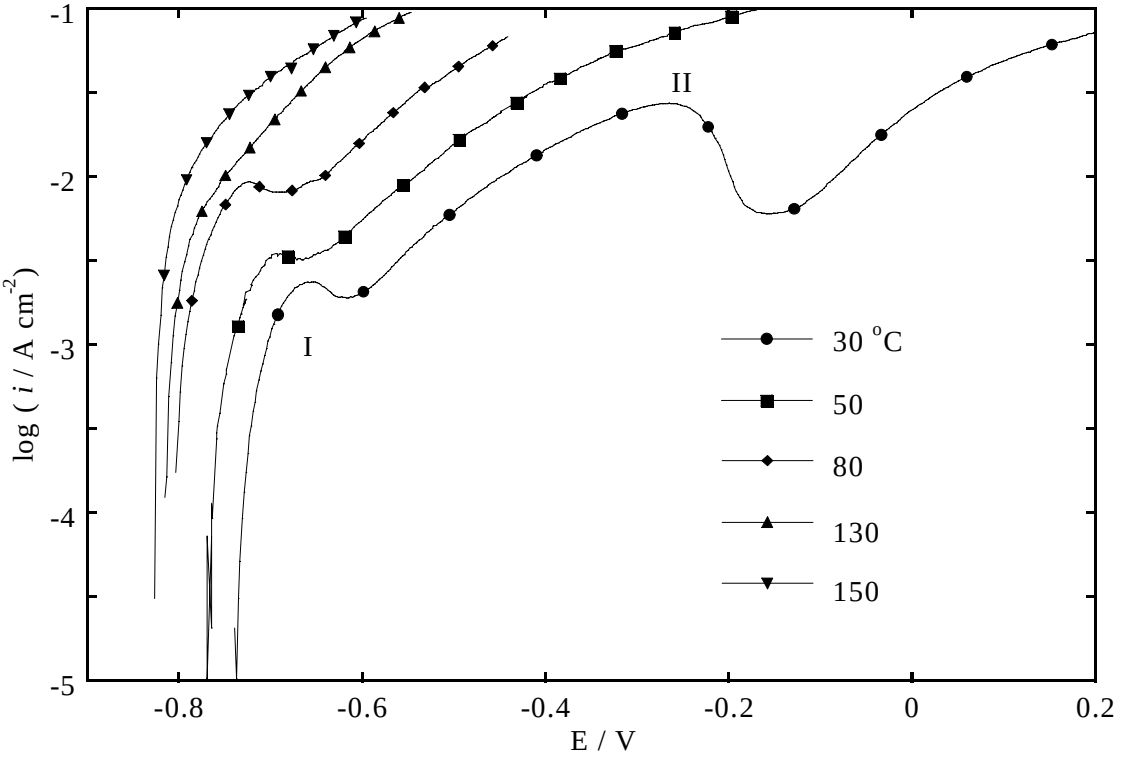

Figure 3.18 Anodic polarisation curves for an iron rotating disc electrode (1000 rpm) in 0.2 M NH_4Cl at various temperatures at 1 mV s^{-1}. pN_2 = 300 kPa.

temperatures between 30 and 150°C [29]. As the temperature was increased from 30 to 80°C, peak I increased steadily in size. However, the peak was absent from the polarisation curve at 130 and 150°C. Peak II was observed only at 30°C.

Table 3.2 lists the Tafel slopes in the prepassive range between 30 and 80°C and in the single active region at 130 and 150°C. The Tafel slope was a constant 0.24 V dec^{-1} up to 80°C. At 130°C the Tafel slope decreased to 0.16 V dec^{-1} and then increased again to 0.26 V dec^{-1} at 150°C degrees. The constancy of the Tafel slope between 30 and 80°C indicates that the mechanism for iron dissolution is most likely to also be constant over this temperature range, and only the overall dissolution rate increased with increasing temperature. The absence of peak II above 30°C may be explained by the combined effects of increased iron hydroxide/oxide solubility with increasing temperatures [38] and a decrease in the pH of ammonium chloride solutions with increasing temperatures [88]. The change in the shape of the polarisation curve at 130°C is also accompanied by a

large decrease in the Tafel slope to 0.16 V dec^{-1}, indicating that the dissolution mechanism may have changed.

temperature / °C	Tafel Slope / V dec^{-1}	Potential Range / V
30	0.24	-0.53 → -0.40
50	0.24	-0.60 → -0.40
80	0.24	-0.60 → -0.40
130	0.16	-0.65 → -0.55
150	0.26	-0.60 → -0.50

Table 3.2 Tafel slope for iron in the prepassive range at various temperatures, from Figure 3.18.

Figure 3.19 shows the Arrhenius plot constructed from Figure 3.18 at -0.60 V However, dOCP/dpH was more negative than -100 mV. This potential was chosen for it is near the corrosion potential for iron in air-saturated solutions (see Chapter 5). A good linear relationship was obtained up to 150°C giving an activation energy (E_a) of 33 kJ mol^{-1}, assuming a single electron transfer. Keddam *et al.* reported an activation energy of 63 kJ mol^{-1} for the passive dissolution of iron in 1 M $HClO_4$ between 30 and 50°C [89]. Heusler *et al.* reported an activation enthalpy for iron in the passive region of 41 kJ

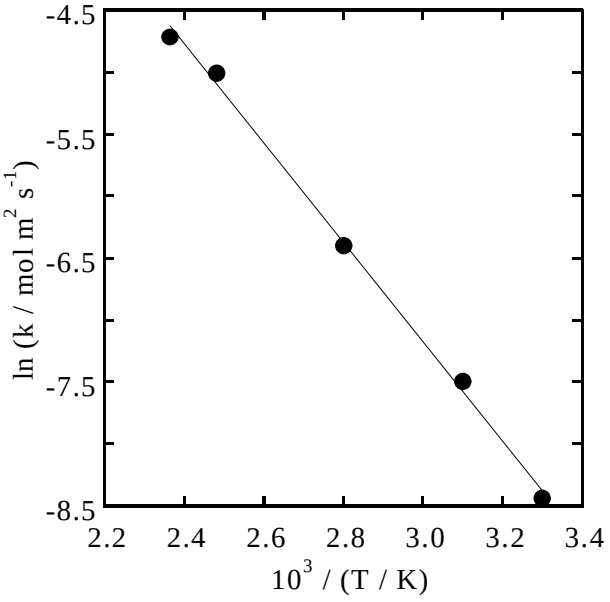

Figure 3.19 Arrhenius plot for anodic iron dissolution at -0.60 V, from Figure 3.18.

mol^{-1} in weakly basic solutions at temperatures up to 300°C [90]. Park and Macdonald reported activation energies for carbon steel in 0.001 M $FeCl_3$ + 0.997 M NaCl + 35 ppb O_2 (between 200 and 270°C) of 30 and 75 kJ mol^{-1} after 20 and 200 hours exposure respectively [91].

3.4 CONCLUSIONS

The following conclusions can be drawn from this work.

(i) a 1-2 monolayer thick air-formed film, possibly consisting of magnetite, is present on iron after electrode preparation (by abrasion using SiC paper)

(ii) in NH_4Cl and NH_4ClO_4 at the open circuit potential, the air-formed film is removed shortly after immersion. However the film is stable and passivates iron in NaCl and $NaClO_4$

(iii) in NH_4Cl at the open circuit potential, the air-formed film is removed from iron even up to pH 7.0

(iv) in pH 7.5 and 8.0 NH_4Cl, the air-formed film is stable and results in pitting dissolution upon polarisation.

(v) a single monolayer (9Å) oxide film forms on iron during anodic polarisation and is reduced at -1.2 V concurrently with hydrogen evolution

(vi) the active iron oxidation current density was increased by ammonium ion and inhibited by chloride ion

(vii) in NH_4Cl the activation energy up to 150°C for active iron oxidation at -0.60 V is 33 kJ mol^{-1}

(viii) iron is passivated in NH_4Cl and NH_4ClO_4 by adsorbed hydrogen and/or $Fe(OH)_2$ after cathodic excursions below -1.2 V

(ix) in NH_4Cl the prepassive current density is constant (at constant potential) in the range from pH 4.8 to 7.0 and a single electron transfer is operative which is consistent with theory.

4 The Electrochemical Reduction of Oxygen

4.1 INTRODUCTION

Oxygen reduction is an integral part of the Becher process and deserves individual attention. Therefore this Chapter describes a rotating disk study of the reduction of dissolved oxygen on iron and gold at ambient and high oxygen partial pressures in 0.2 M NH_4Cl. A brief literature review concerning the mechanism and kinetics of oxygen reduction will be presented followed by a review of oxygen solubility in aqueous solutions. Finally, the experimental results will be presented and discussed.

Oxygen reduction can proceed via the "direct 4-electron" or, the "peroxide" pathway as shown below [92].

A. Direct 4-electron Pathway

Alkaline Solutions.

$$O_2 + 2H_2O + 4e^- \rightarrow 4OH^- \quad E^\circ = 0.401 \text{ V} \tag{4.1}$$

Acid Solutions.

$$O_2 + 4H^+ + 4e^- \rightarrow 2H_2O \quad E^\circ = 1.229 \text{ V} \tag{4.2}$$

B. Peroxide Pathway

Alkaline Solutions.

$$O_2 + H_2O + 2e^- \rightarrow HO_2^- + OH^- \quad E^\circ = -0.065 \text{ V} \tag{4.3}$$

followed by either the reduction of peroxide:

(i) $$HO_2^- + H_2O + 2e^- \rightarrow 3OH^- \quad E^\circ = 0.867 \text{ V} \tag{4.4}$$

or the decomposition of peroxide:

(ii) $$2HO_2^- \rightarrow 2OH^- + O_2 \qquad (4.5)$$

Acid Solutions.

$$O_2 + 2H^+ + 2e^- \rightarrow H_2O_2 \quad E^\circ = 0.67\ V \qquad (4.6)$$

followed by either the reduction of peroxide:

(i) $$H_2O_2 + 2H^+ + 2e^- \rightarrow 2H_2O \quad E^\circ = 1.77\ V \qquad (4.7)$$

or the catalytic decomposition of peroxide:

(ii) $$2H_2O_2 \rightarrow 2H_2O + O_2 \qquad (4.8)$$

When only the peroxide pathway B is operative (*ie.* rate of pathway A is zero) oxygen reduction is said to occur via a series mechanism. In alkaline solution the sum of the two series equations (4.3) and (4.4) or equations (4.3) and (4.5) is a 4-electron reduction equivalent to equation (4.1). In acid solution, the sum of equations (4.6) and (4.7) or equations (4.6) and (4.8) is a 4-electron reaction equivalent to equation (4.2). So in order to distinguish the extent of pathway A or B on a particular electrode, a rotating ring-disc electrode is used to detect peroxide.

The activation controlled current density (i_k) for oxygen reduction is given by:

$$i_k = nFkC_b \qquad (4.9)$$

where k is the rate constant. The mass transport or diffusion controlled oxygen reduction current density (i_l) is given by the Levich equation:

$$i_l = 0.62nFC_bD^{2/3}\nu^{-1/6}\omega^{1/2} \qquad (4.10)$$

where C_b (mol cm^{-3}) is the bulk dissolved oxygen concentration, D ($cm^2\ s^{-1}$) is the diffusion coefficient, ν ($cm^2\ s^{-1}$) is the kinematic viscosity and ω (rad s^{-1}) is the angular velocity of the electrode. Under mixed control the following equation describes the total current density (i):

$$\frac{1}{i} = \frac{1}{i_k} + \frac{1}{i_l} = \frac{1}{i_k} + \frac{1}{B\omega^{1/2}} \qquad (4.11)$$

where B is the Levich constant which includes all of the components in equation (4.10) except for the electrode angular frequency (ω). A Koutecky-Levich plot ($1/i$ against $\omega^{1/2}$) should give a straight line where the slope equals $1/B$ and the intercept equals i_k. For a first order reaction, plots constructed at various potentials will give linear and parallel lines allowing the kinetic current, i_k, to be determined [93, 94]. Equation (4.12) can also be used to calculate i_k – however knowledge of the limiting current, i_l, is required and can be obtained from the plot of $1/i$ against $\omega^{-1/2}$ as the kinetic current density tends to zero ($i_k \rightarrow 0$). This is equivalent to the Koutecky-Levich plot described above and likewise is valid for first order reactions only [95, 96].

$$i_k = \frac{i_l i}{(i_l - i)} \tag{4.12}$$

4.1.1 Oxygen reduction on iron and steel

The literature concerning the reduction of oxygen on pure iron has been recently reviewed by Drazic [61]. The work that was reviewed focused on determining the mechanism of oxygen reduction on iron. Drazic stressed that in neutral or alkaline solutions analysis of the reduction mechanism is difficult due to changes in the state of the electrode surface arising from the formation of hydrated iron oxide corrosion products [61]. Most of the work to date has been conducted at room temperature and at oxygen partial pressures up to 101 kPa so there is considerable scope for the elucidation of the mechanism and kinetics of oxygen reduction on iron at higher temperatures and oxygen partial pressures.

In acid solutions a 4-electron pathway operates with a H_2O_2 intermediate (equations (4.6) and (4.7)). However, direct reduction without peroxide formation (equation (4.2)) was also considered possible [97]. For oxygen reduction on stainless steel in 0.5 M NaCl [94], cathodic polarisation curves were very similar between pH 4 and 10 and exhibited activation-diffusion control type behaviour. The polarisation curves did not depend significantly on the scan rate or the scan direction. The limiting current agreed with the Levich equation and the calculated (using published values for C_b, D, ν and assuming $n = 4$) and experimental Levich slopes compared well, indicating that the 4-electron path is most likely. Tafel slopes from reduction curves measured using anodic scans (-0.115 to -0.120 V dec^{-1}) were always lower than Tafel slopes from

polarisation curves measured using cathodic scans. This was attributed to potential dependent changes in the iron surface. Plots of $1/i$ against $\omega^{-1/2}$ (equation (4.12)) gave lines that were linear and parallel confirming that the reaction order with respect to oxygen is 1.

A 4-electron reduction operates on a clean carbon steel surface in oxygen saturated 3% NaCl [98]. Delahay observed the appearance of H_2O_2 in a potential region that encompassed the corrosion potential (-0.54 V *she*) and the number of electrons ranged from 2.4 at -0.2 V to 4 at -0.6 V [99].

By comparing the calculated and experimental *B* values from equation (4.11) it was shown that a 4-electron reduction is operative between pH 7 and 9.4 in borate buffer [100]. It took 1-2 minutes to reach a steady state current during potentiostatic polarisation. For oxygen partial pressures up to 101 kPa, the apparent reaction order with respect to pH and oxygen was 0 and 1 respectively. Hydrogen peroxide is an intermediate in the series 4-electron pathway (equations (4.3) and (4.4)) but it accounts for less than 1% of the total reduction current. Hydrogen peroxide forms as an adsorbed peroxide or superoxide and does not lead to a solution species [100].

At pH = 9.8 in oxygen saturated borate buffer, a 4-electron pathway is operative at potentials below -0.45 V (*sce*) [101]. However, above -0.45 V, reduction is activation controlled and thus a Levich plot could not be obtained. A 4 electron transfer was also observed on (potentiostatically-formed) passive surfaces. Tafel plots (constructed using equation (4.12)) were dependent on the scan direction. Scans in the anodic direction gave a single Tafel value of -0.150 V dec^{-1} while scans in the cathodic direction gave Tafel values of -0.080 and -0.110 V dec^{-1} in the low and high current density regions respectively. Hysteresis of the oxygen reduction curve was observed after the anodic potential scan was reversed at potentials above -0.5 V and this was attributed to passive film formation. Reduction to OH^- occurs without catalytic decomposition of H_2O_2 (equation (4.8)). On oxide-free iron very little H_2O_2 is formed so a reliable distinction between the series and parallel mechanism could not be made [101].

4.1.2 Oxygen reduction on gold

Genshaw concluded that oxygen reduction on gold occurs by two parallel pathways in acid solutions, that is, via equations (4.2) and (4.6) [102]. Štrbac and coworkers investigated oxygen reduction on Au(111) and Au(332) in 0.05 M H_2SO_4 and 0.1 M NaOH [95]. In acidic solution reduction proceeds via 1.7 and 1.9 electrons on Au(111)

and Au(332) respectively. These workers suggested that the peroxide formed blocks the surface resulting in the average number of electrons exchanged per oxygen molecule being less than 2.

In air-saturated 0.2 M NH_4Cl, oxygen reduction on polycrystalline gold proceeds via the peroxide pathway equation (4.6) [103]. Results from voltammetry experiments in solutions containing both dissolved oxygen and H_2O_2 indicate that peroxide may inhibit the oxygen reduction reaction.

4.1.3 Oxygen solubility as a function of temperature and partial pressure

Henry's law states the concentration of a gas in an ideal solution at constant temperature is proportional to the partial pressure:

$$p_g = x_g H \tag{4.13}$$

where p_g is the partial pressure of the gas, x_g is the mole fraction of gas dissolved in the solvent and H is the Henry's law proportionality constant. Briefly, Henry's Law constant can be evaluated by any one of the following methods [104].

a) the slope of experimental values of p_g *vs.* x_g up to a certain partial pressure (*eg.* 101 kPa)
b) from the ratio p_g/x_g for a single value of p_g
c) extrapolation of p_g/x_g data to zero pressure

Fogg and William [104] suggest that Henry's law is satisfactory for predicting oxygen solubility at 25°C and at partial pressures up to 202 kPa. However, for higher temperatures and pressures, it is safer to measure the solubility rather than use Henry's law since authors may not state the temperature and pressure range used to calculate their H values [104]. However, other workers have found that oxygen solubility in pure water obeys Henry's law between 0 and 300°C when the maximum oxygen partial pressure ranged from 4300 kPa at the lowest temperatures to 5200 kPa at the highest temperatures [105-107]. Cramer [107] provides a good summary of the literature concerning oxygen solubility in both pure water and brine solutions.

The "Solubility Data Series" [108] includes an extensive review of oxygen solubility including a section for oxygen partial pressures above 200 kPa. Equation (4.14), from reference [108], fits through the oxygen solubility data provided by Broden

and Simonson [109] which was obtained at oxygen partial pressures between 1000 and 5000 kPa and at temperatures between 50 and 150°C.

$$[O_2](\text{mM}) = 5.351 - 1.252 \times 10^{-2}\,(\text{T/K}) - 79.54(p/\text{MPa}) + 2.135 \times 10^{-4}\,(p/\text{MPa})\,(\text{T/K})^2 + 2.125 \times 10^{4}\,(p/\text{MPa})/(\text{T/K}) \quad (4.14)$$

Benson *et al.* [110] calculated equation (4.15) which gives Henry's constant, *H*, as a function of temperature. This was done by analysing their own very accurate solubility data between 0 and 60°C, together with high temperature and pressure data from Stephan *et al.* [111].

$$\ln H = -4.1741 + 1.3104 \times 10^{4}/(\text{T/K}) - 3.4170 \times 10^{6}/(\text{T/K})^2 + 2.4749 \times 10^{8}/(\text{T/K})^3 \quad (4.15)$$

Figure 4.1 shows the oxygen solubility in pure water as a function of temperature

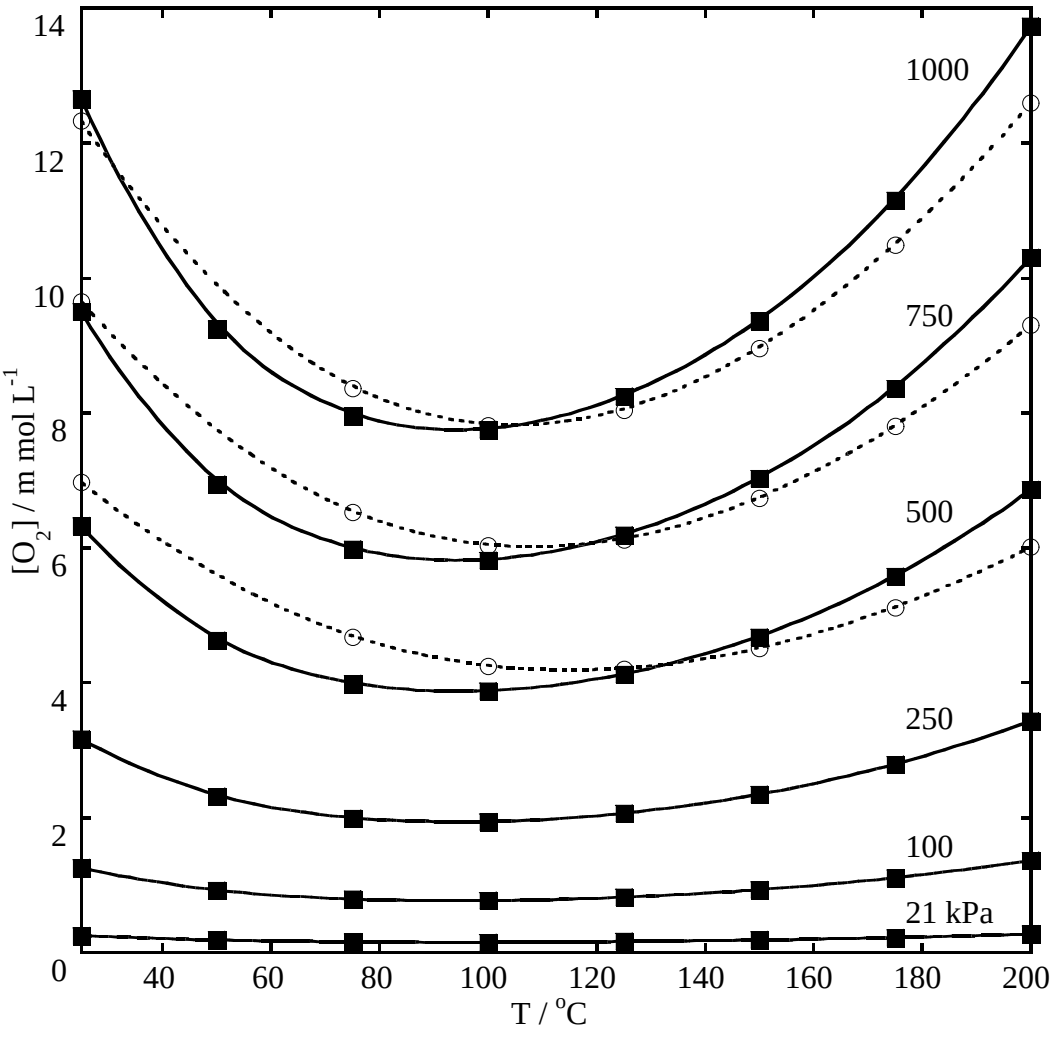

Figure 4.1 Solubility of oxygen in pure water as a function of temperature, and at various oxygen partial pressures, calculated using equation (4.14) (----○----) and equation (4.15) (—■—).

calculated at different oxygen partial pressures using both equations (4.14) and (4.15). For equation (4.15), in converting Henry's constants at each temperature to concentrations at various pressures, it was assumed that the molar volume of the solution was the same as the molar volume of pure water [110]. Good agreement between the two sets of data confirms the general validity of Benson's equation (equation (4.15)) even at very high pressures. However, it must be noted that oxygen solubilities calculated using Broden and Simonson's equation (4.14) were significantly in error below 500 kPa – which is not surprising, since this is outside the range of their original measurements [109].

A colorimetric method was used to determine oxygen solubility in aqueous ammonium chloride as a function of electrolyte concentration (up to 5 M) and at temperatures up to 75°C [112]. For 2 M NH_4Cl solution, Henry's law was strictly obeyed at 25 and 50°C. These workers derived the following empirical relationship between the oxygen solubility and the electrolyte concentration:

$$\log \frac{S}{S_0} = -\sum K_i C_i \qquad (4.16)$$

where K_i is the solubility constant for each species i, C_i is the molarity of species i, S_0 is the solubility of oxygen in pure water and S is the solubility in the electrolyte solution. Substituting into equation (4.16) K_i values for NH_4^+ and Cl^- from reference [112] and $S_0 = 2.35 \times 10^{-4}$ M at 30°C from Figure 4.1, gives the following expression for the oxygen solubility in 0.2 M NH_4Cl:

$$S = 0.9718\, S_o \qquad (4.17)$$

Using equation (4.17) the solubility of oxygen in air-saturated (pO_2 = 21 kPa) 0.2 M NH_4Cl at 30°C was calculated to be 2.28×10^{-4} M.

4.2 EXPERIMENTAL

The experimental method and equipment used are described in Chapter 2. All potentials are reported against 3 M KCl Ag/AgCl (E = 0.208 V *vs. she*).

4.3 RESULTS AND DISCUSSION

4.3.1 Oxygen reduction on pure iron

In this section an investigation of the reduction of oxygen in 0.2 M NH_4Cl using linear sweep voltammetry with a pure iron disc electrode will be discussed.

4.3.1.1 Air-saturated 0.2 M NH_4Cl at 30°C

Figure 4.2 shows the potentiodynamic and potentiostatic polarisation curves for oxygen reduction on iron in air-saturated 0.2 M NH_4Cl at 30°C. Both sets of polarisation curves were measured by increasing the potential in the anodic direction. The potentiostatic current densities were measured 1 to 2 minutes after polarisation, when the rate of change of the current density with time was not significant.

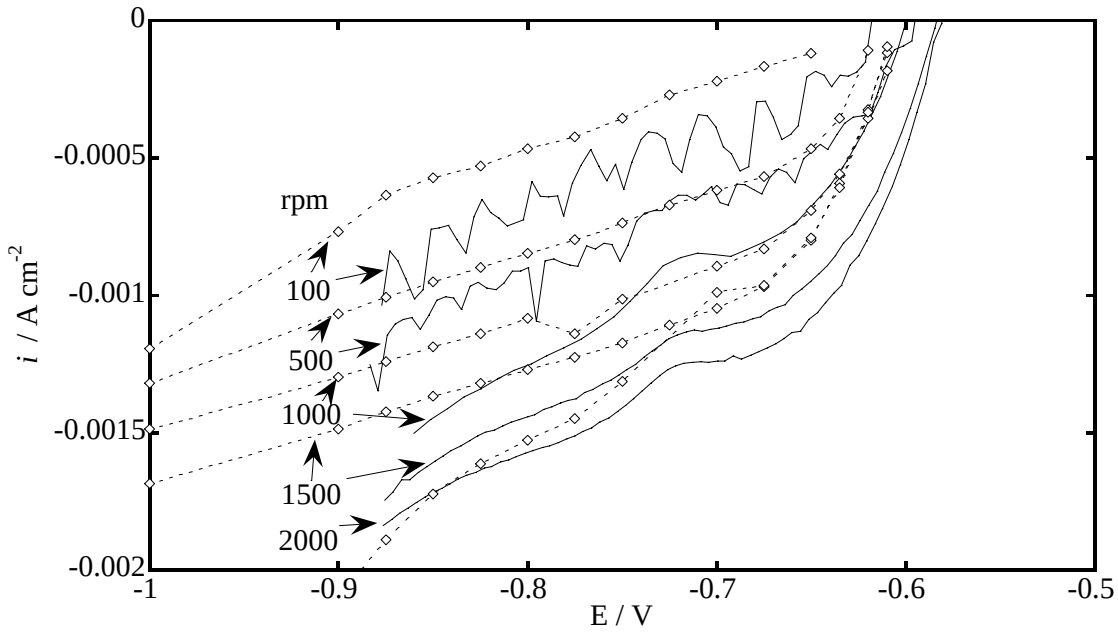

Figure 4.2 Potentiodynamic (————, 10 mV s^{-1}) and potentiostatic (- - - ◇ - - -) polarisation curves for oxygen reduction on iron in air-saturated 0.2 M NH_4Cl at various electrode rotation speeds. T = 30.0°C.

The potentiodynamic curves at 100 and 500 rpm had quite regular current density oscillations however the curves were smooth at 1000 rpm and above. These oscillations may be a result of poor solution hydrodynamics at low rotation speeds. At 1000 rpm and above, the potentiodynamic polarisation curves exhibit a distinct decrease in cathodic current density at - 0.75 V followed by a short plateau prior to decreasing rapidly near

the corrosion potential. For the potentiostatic curve this dip at -0.75 V was only observed at 2000 rpm.

Figure 4.3 shows the Levich plot for potentiostatic and potentiodynamic oxygen reduction at -0.8 V. Potentiodynamic oxygen reduction current densities were 1.1×10^{-5} A cm^{-2} larger than potentiostatic current densities at all rotation speeds. This demonstrates the importance of performing steady state measurements. Consistently lower potentiostatic cathodic current densities and the dip in the potentiostatic polarisation curve around -0.75 V are most likely to be the result of the formation of an $Fe(OH)_2$ film that blocks the surface (Section 3.3.2). This decreases the real oxygen reduction current density by both physically blocking the surface and by the contribution of an anodic current density. The non-zero intercept in Figure 4.3 indicates that H^+ reduction is making a small contribution to the cathodic current density.

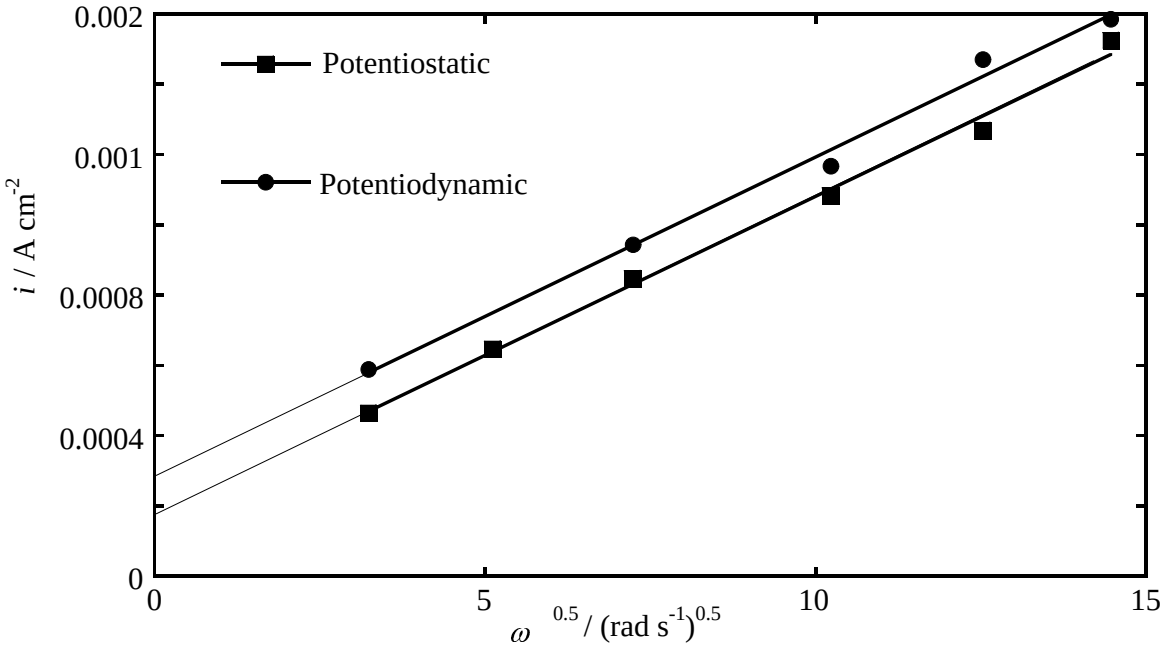

Figure 4.3 Levich plot for oxygen reduction on iron in air-saturated 0.2 M NH_4Cl at -0.8 V from Figure 4.2.

Substituting the potentiostatic Levich slope (8.89×10^{-5}) and the following set of values (at 30°C) into equation (4.10): $C_b = 2.3 \times 10^{-7}$ mol cm^{-3}; $D = 2 \times 10^{-5}$ cm^{-2} s^{-1}; $\nu = 1 \times 10^{-2}$ cm^{-2} s^{-1}, gives a value for n of 4.1. D and ν were chosen after comparing values for various electrolyte solutions [94, 95, 98]. This shows that the 4-electron pathway is operative for oxygen reduction on iron. Calculations of n were performed at other

potentials and indicate that the 4-electron pathway is operative over a large potential range probably including the corrosion potential. This is consistent with previous reports in the literature for oxygen reduction on iron in near neutral solutions [98, 100, 101, 108]. However it is not possible to conclude from these experiments whether oxygen reduction proceeds via a direct 4-electron mechanism (equation (4.2)) or a series mechanism (equations (4.6) and (4.7)).

Figure 4.4 and Figure 4.5 show the Koutecky-Levich plots for oxygen reduction on iron obtained from the potentiostatic and potentiodynamic polarisation curves (Figure 4.2). As discussed in Section 4.1, linear and parallel lines in these plots would indicate that oxygen reduction is first order with respect to oxygen. However in the present work the plots obtained are linear, but not parallel, which indicates that oxygen reduction on iron may not be first order with respect oxygen. For potentiostatic reduction, as shown in Figure 4.4, the lines converge at a single point at high rotation speeds while the degree of convergence is less for potentiostatic reduction as shown in Figure 4.5.

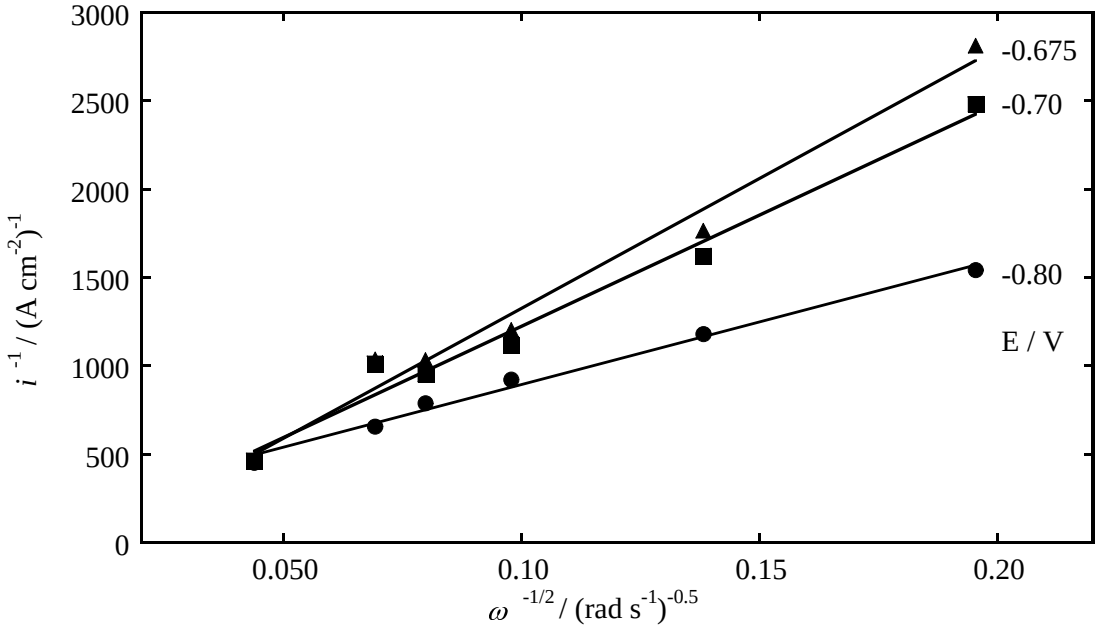

Figure 4.4 Dependence of i^{-1} against $\omega^{-1/2}$ for potentiostatic oxygen reduction on iron in air-saturated 0.2 M NH_4Cl at different potentials. T = 30.0°C.

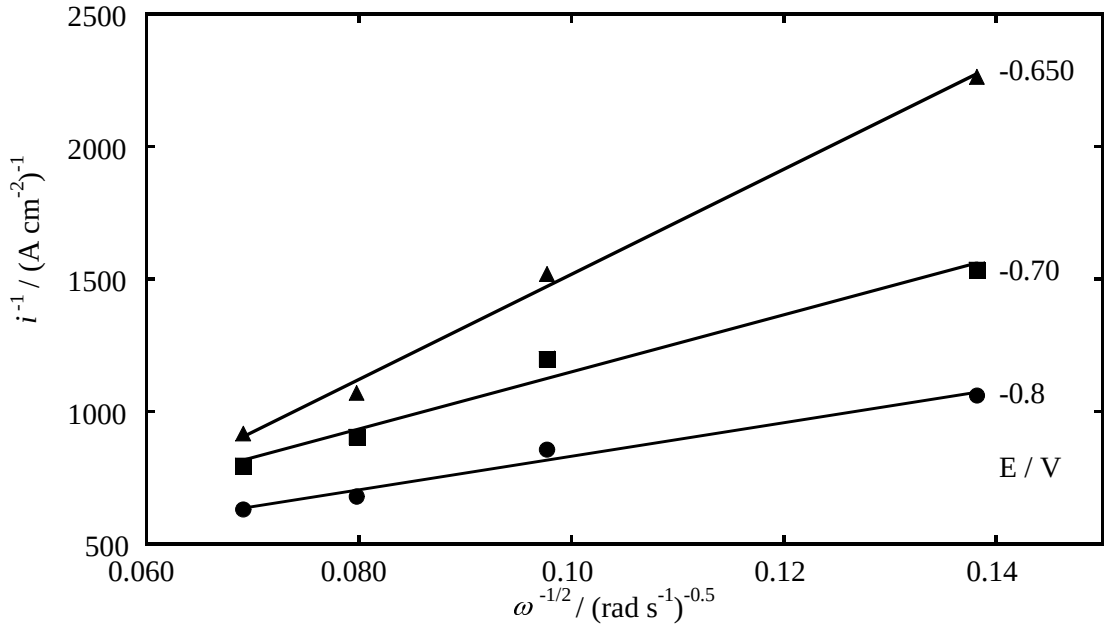

Figure 4.5 Dependence of i^{-1} against $\omega^{-1/2}$ for potentiodynamic oxygen reduction on iron in air-saturated 0.2 M NH_4Cl at different potentials. T = 30.0°C.

4.3.1.2 The effect of pH

Figure 4.6 shows the potentiodynamic polarisation curves for oxygen reduction in air-saturated 0.2 M NH_4Cl at various pH values. Between pH 5.0 and 6.5 the curves have a similar shape and have a distinct plateau at -0.75 V. The polarisation curve does not show any clear dependence on the pH. For example, the magnitude of cathodic current density in the plateau region was lower at pH 5.0 than at pH 6.5, however, the current density at pH 6.0 was greater than at pH 5.5. At pH 7.0 the plateau region was much less distinct but the cathodic current density was similar to that at pH 5.0. And at pH 7.5 very erratic curves were obtained. At pH 8.0 the distinct plateau at -0.75 V disappeared and the current density below -0.80 V was significantly lower.

Since the scans used to measure the oxygen reduction curves were initiated at -0.9 V, it is most likely that the air-formed film (Section 3.3.1) was reduced and oxygen reduction occurred on a film-free iron surface. The air-formed film would even have been reduced in pH 8 solutions since the corrosion potential (*ie.* the potential at zero current density) was always less than -0.60 V. When the air-formed film passivates iron, the open circuit potential is significantly higher (Section 3.3.2). The changes in the oxygen reduction curve with pH are believed to be due to the influence of the iron oxidation reaction. In fact, the variation in the plateau region exactly reflects the changes in the anodic polarisation curve in deaerated solution (Figure 3.16). For example,

between pH 4.8 and 6.0 the oxidation peak (I, -0.66 V, Figure 3.16) decreased from pH 4.0 to 4.8 and to pH 6.0 but the highest anodic current density was observed at pH 5.5 which is consistent with the observed cathodic current density at pH 6.0 being greater than at pH 5.5 in Figure 4.6. Moreover, the distinct change in shape of the oxygen reduction curve between pH 6.5 and 7.0 coincides with the disappearance of the oxidation peak (I, -0.66 V, Figure 3.16) in the anodic polarisation curve. The very noisy polarisation curve at pH 7.5 is probably related to the transition from active to passive (and pitting) dissolution for iron at this pH (Figure 3.16).

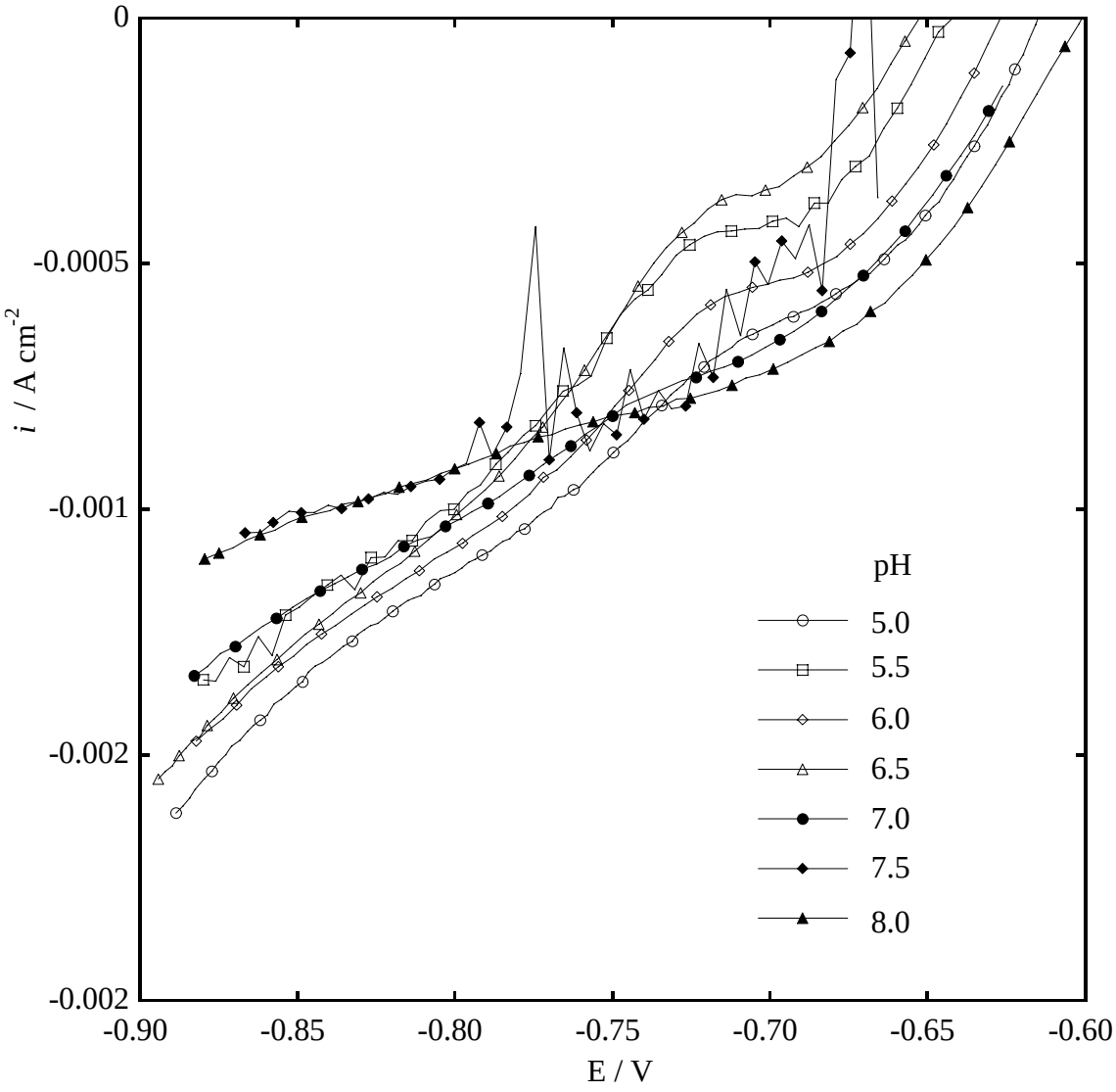

Figure 4.6 Potentiodynamic polarisation curves for oxygen reduction on an iron rotating disc electrode (1000 rpm) in air-saturated 0.2 M NH_4Cl at various pH values. T = 30.0°C.

4.3.2 Oxygen reduction on pure gold

In this section an investigation of the reduction of oxygen at a pure gold disc electrode in 0.2 M NH_4Cl, using linear sweep voltammetry at ambient and elevated temperatures and pressures, will be discussed.

4.3.2.1 Air-saturated 0.2 M NH_4Cl at 30°C

Figure 4.7 shows the potentiodynamic and potentiostatic polarisation curves for oxygen reduction on gold at different electrode rotation speeds in 0.2 M NH_4Cl. The shape of the polarisation curves depends strongly upon the type of potential control used. The reduction current density below -0.8 V was much higher for the potentiodynamic curves compared with the potentiostatic curves. The pH of the solutions was much the same when measured before and after the volatammetric runs. This may indicate that the hydrogen evolution reaction on gold is highly sensitive to the sweep rate. Unfortunately time constraints prevented an investigation into the effect of potential sweep rate on the reduction reaction. At more positive potentials the difference between the potentiostatic and potentiodynamic curves was not so great. Potential dependent surface reconstruction

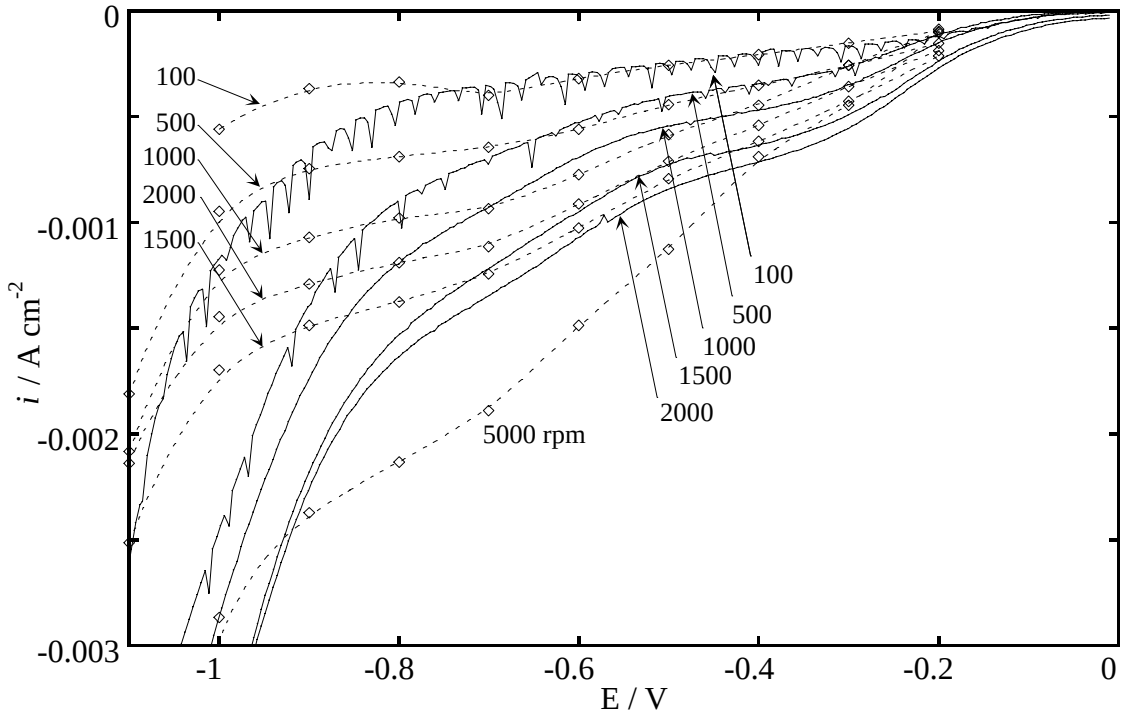

Figure 4.7 Potentiodynamic (———, 10 mV s^{-1}) and potentiostatic (·····◇·····) polarisation curves for oxygen reduction on gold in air-saturated 0.2 M NH_4Cl at various rotation speeds. T = 30.0°C.

for Au(111) [95] can occur and, if reconstruction is also time dependent, different sweep rates may be expected to affect the reduction.

Figure 4.8 and Figure 4.9 show the potentiostatic and potentiodynamic Levich plots respectively for oxygen reduction on gold. For both sets of data the Levich slope increased as the potential was made more negative. This means the number of electrons involved in oxygen reduction also increases as the potential is made more negative. Table 4.1 lists the number of electrons involved in oxygen reduction at different potentials. The differences between the potentiostatic and potentiodynamic polarisation curves in Figure 4.7 are also reflected in the *n* values shown in Table 4.1. The *n* values for were calculated in the same way as shown for iron in Section 4.3.1.1. The *n* values for oxygen reduction were greater for potentiodynamic scans compared with potentiostatic scans at all potentials except at -0.6 V, where they were approximately the

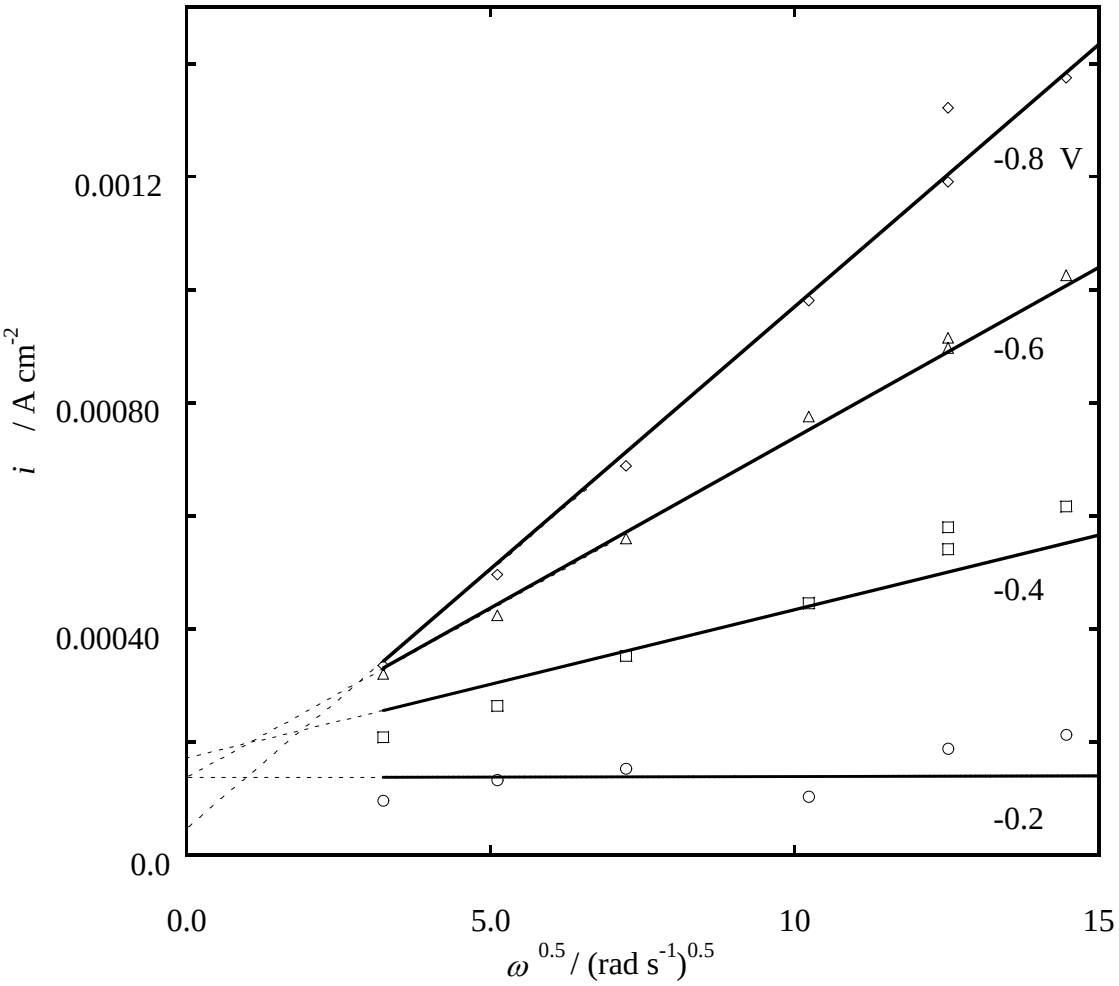

Figure 4.8 Levich plots for potentiostatic oxygen reduction on gold in air-saturated 0.2 M NH_4Cl at different potentials. T = 30.0°C.

same. The number of electrons increased from near zero at -0.2 V to 4 at -0.8 V. As described in Section 4.1.2, Štrbac *et al.* [95] also reported unusual *n* values. These authors reported *n* values of 1.7 and 1.9 for different Au faces and suggested that the H_2O_2 blocks the surface for O_2 reduction which results in the average number of electrons exchanged per O_2 molecule being less than two. So the overall reactions are still the same, ie. a 2 electron reduction at more positive potentials and a 4 electron series reduction at more negative potentials. Obviously, the mechanism of oxygen reduction on gold is potential dependent.

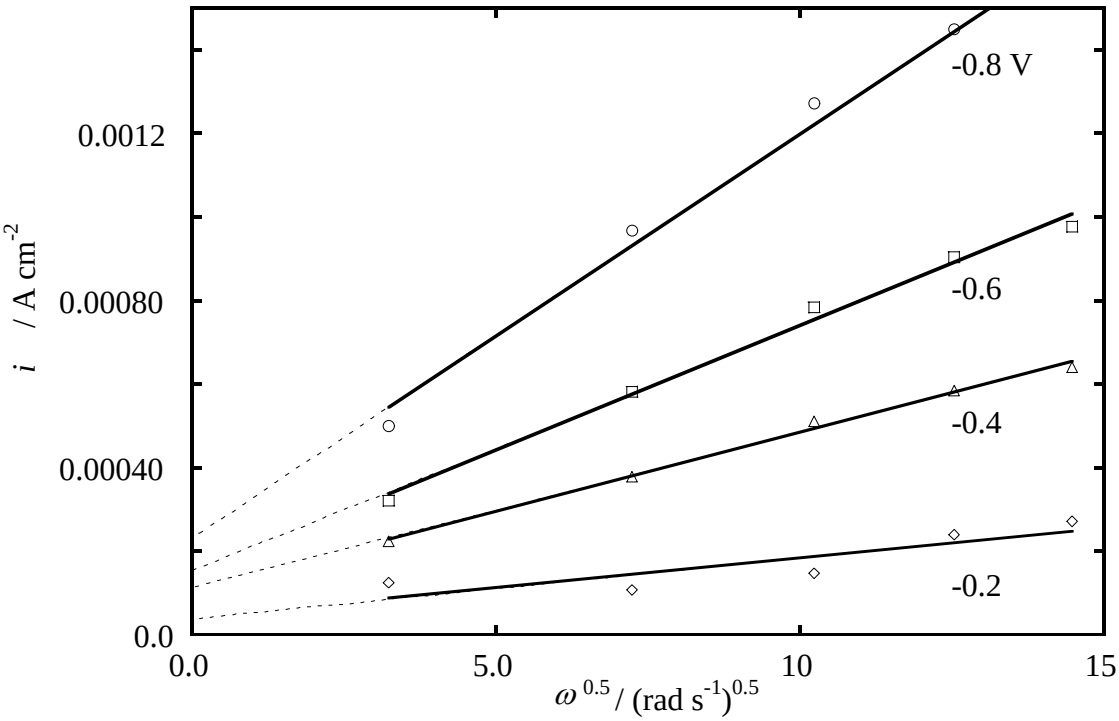

Figure 4.9 Levich plot for potentiodynamic oxygen reduction on gold in air-saturated 0.2 M NH_4Cl at different potentials. T = 30.0°C.

E / V	*n* (potentiostatic)	*n* (potentiodynamic)
-0.2	0.0	0.6
-0.4	1.2	1.7
-0.6	2.8	2.7
-0.8	4.2	4.4

Table 4.1 Number of electrons (*n*) for oxygen reduction on gold at various potentials, from Figure 4.8 and Figure 4.9.

The Levich lines in Figure 4.8 and Figure 4.9 do not decrease to zero current density as the electrode rotation speed approaches 0 rpm. As discussed in the previous section for iron, some H^+ reduction does contribute to the total cathodic current density. For potentiostatic measurements the intercept varied somewhat erratically between 2.5×10^{-5} and 1.7×10^{-4} A cm^{-2} while for potentiodynamic measurements the intercepts increased from 4.2×10^{-5} A cm^{-2} at - 0.2 V to 2.3×10^{-4} A cm^{-2} at -0.8 V.

Figure 4.10 and Figure 4.11 show the Koutecky-Levich plots for oxygen reduction on gold. The lines are very straight and almost parallel indicating that the order of the reduction with respect to oxygen is very close to one [95].

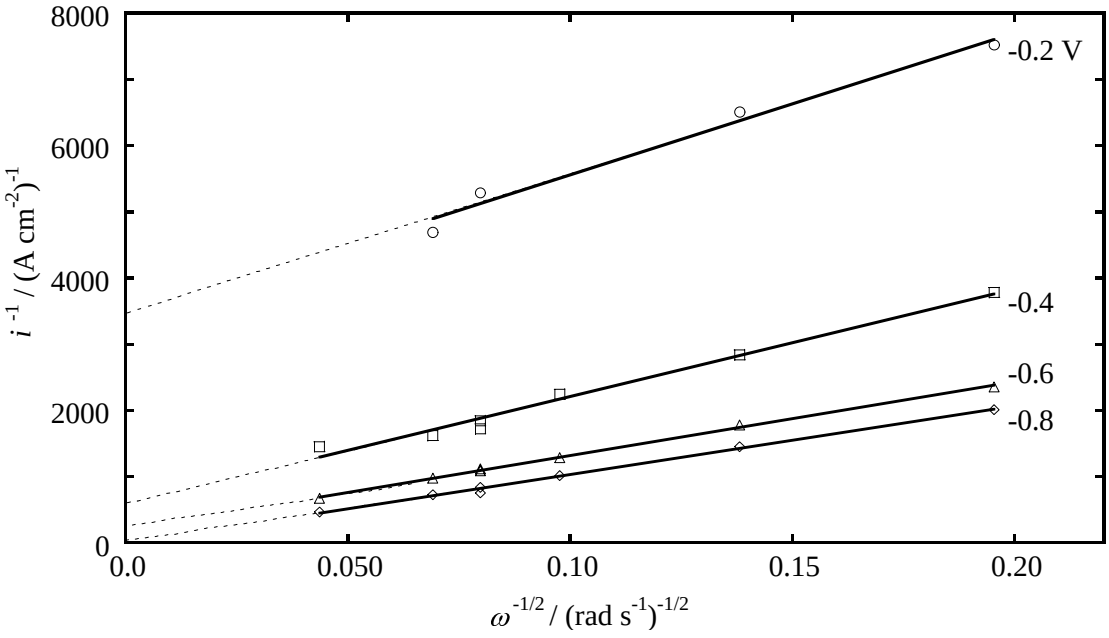

Figure 4.10 Koutecky-Levich plot for potentiostatic oxygen reduction on gold in air-saturated 0.2 M NH_4Cl at various potentials. T = 30.0°C.

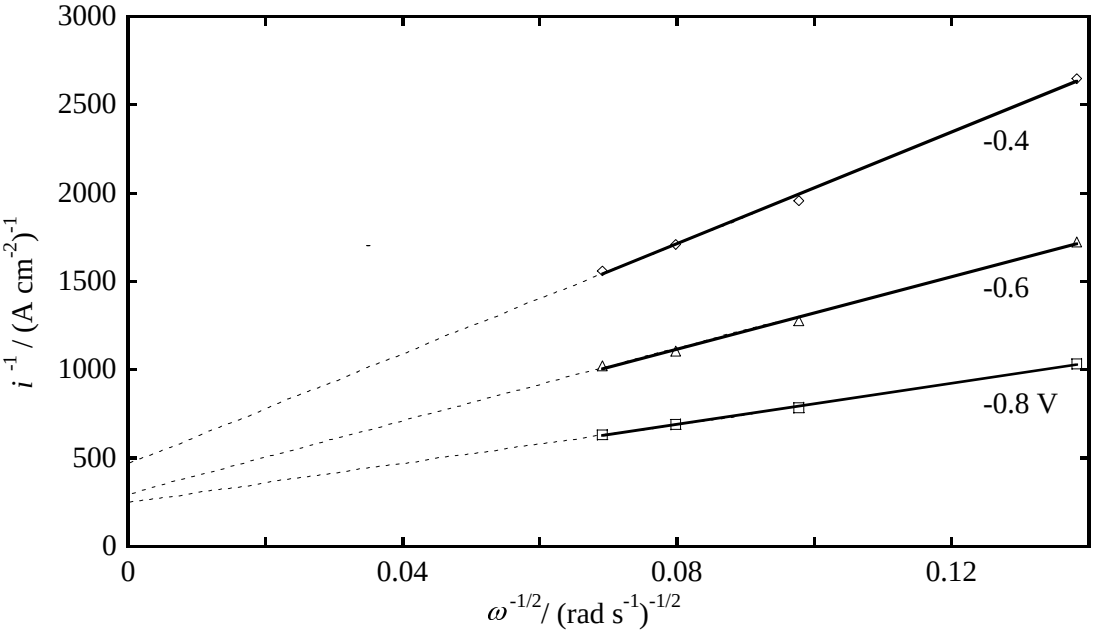

Figure 4.11 Koutecky-Levich plot for potentiodynamic oxygen reduction on gold in air-saturated 0.2 M NH_4Cl at different potentials. T = 30.0°C.

4.3.2.2 Oxygen reduction at high temperature and pressure

Figure 4.12 shows the potentiodynamic polarisation curves for oxygen reduction on gold as a function of temperature at 300 kPa oxygen partial pressure [29]. The cathodic current density below -1.0 V increased dramatically with temperature which is consistent with the H^+ reduction reaction being activation controlled. At 30 and 50°C oxygen reduction on gold is activation-diffusion controlled between 0 and -0.8 V. The cathodic current density in the mixed-control region is significantly greater at 50°C than at 30°C. However, in the diffusion controlled region – between -0.80 and -1.10 V – the cathodic current densities are the same. Between 50 and 80°C the current density increased in both the diffusion (by about 0.0036 A cm^{-2} at -0.80 V) and the activation controlled regions. Between 80 and 130°C a very large increase in the cathodic current density was observed over the entire potential range.

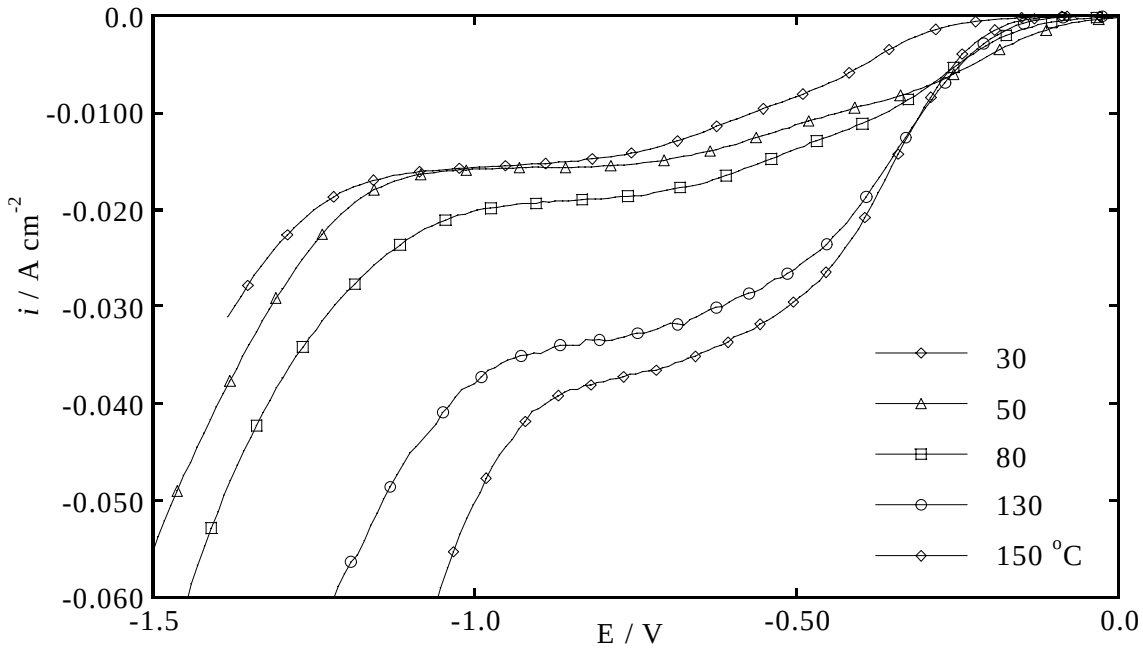

Figure 4.12 Potentiodynamic (10 mV s^{-1}) polarisation curves for oxygen reduction (pO_2 = 300 kPa) on a gold rotating disc electrode (1000 rpm) in 0.2 M NH_4Cl at various temperatures.

Figure 4.1 shows the oxygen solubility decreases with increasing temperature, reaching a minimum value at around 95°C and then steadily increases thereafter. The small increase in the oxygen reduction current density between 30 and 80°C, despite the decrease in the oxygen concentration, is most probably a result of an increase in the oxygen diffusion coefficient [113] and a decrease in the viscosity at higher temperatures [114, 115]. Both of these effects result in an overall increase in the oxygen flux to the electrode surface and hence an increase in the reduction current density. The large increase in the reduction current density between 80 and 130°C is most probably due to the combined effects of increasing oxygen solubility above 95°C (Figure 4.1), an increase in the diffusion co-efficient, and a further decrease in the viscosity.

Figure 4.13 shows the effect of oxygen partial pressure on the polarisation curve at 80°C in 0.2 M NH_4Cl. The cathodic current density in both the mixed and diffusion controlled regions increased with increasing oxygen partial pressure.

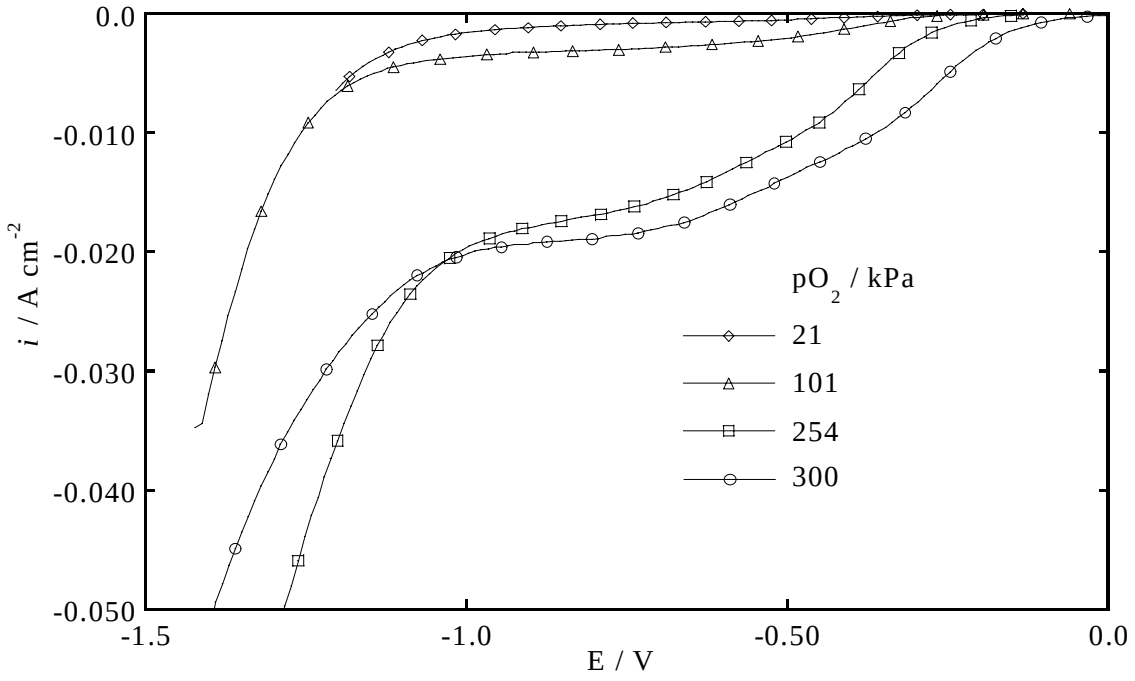

Figure 4.13 Potentiodynamic polarisation curves (10 mV s^{-1}) for a gold rotating disc electrode (1000 rpm) in 0.2 M NH_4Cl at different oxygen partial pressures. T = 80°C.

Figure 4.14 that the limiting current density at -0.73 V is essentially a linear function of the oxygen partial pressure. This relationship is consistent with the limiting

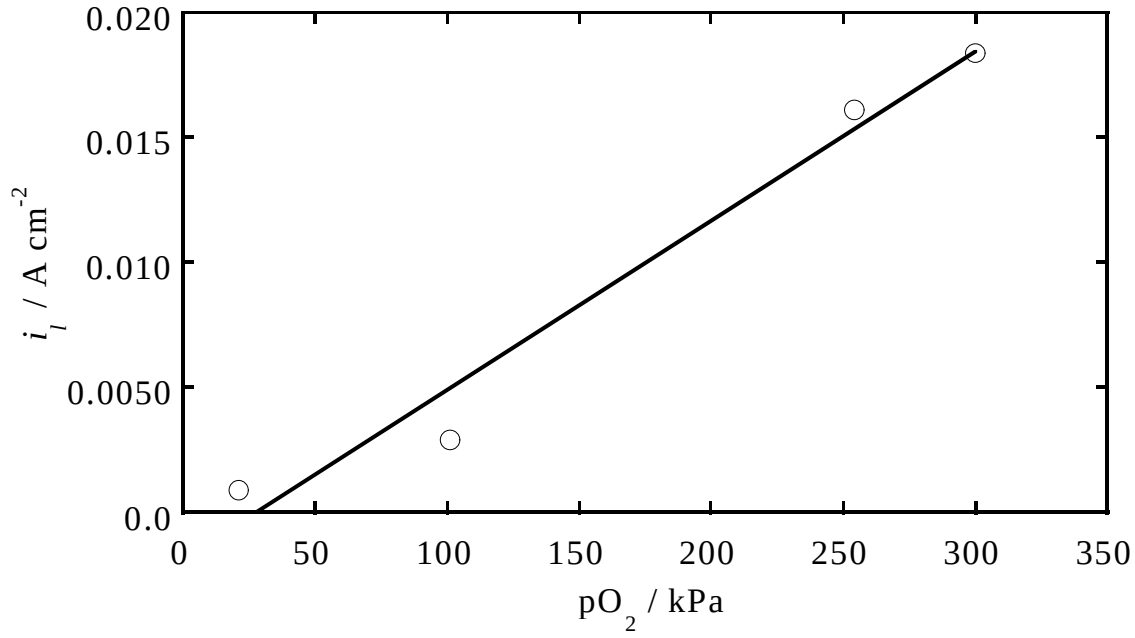

Figure 4.14 Diffusion limited current density (i_l) at -0.73 V on a gold rotating disc electrode (1000 rpm) in 0.2 M NH_4Cl as a function of the oxygen partial pressure. T = 80°C.

current density being proportional to the dissolved oxygen concentration which is in turn proportional to the oxygen partial pressure as described by Henry's law (equation (4.13)).

Figure 4.15 shows the potentiodynamic oxygen reduction curves on gold at 285 kPa oxygen partial pressure and at a temperature of 150°C in 0.2 M NH_4Cl [29]. Above -0.4 V oxygen reduction is largely activation controlled while below this potential diffusion control is predominant. Figure 4.16 shows the Levich plot for oxygen reduction at -0.63 V from Figure 4.15.

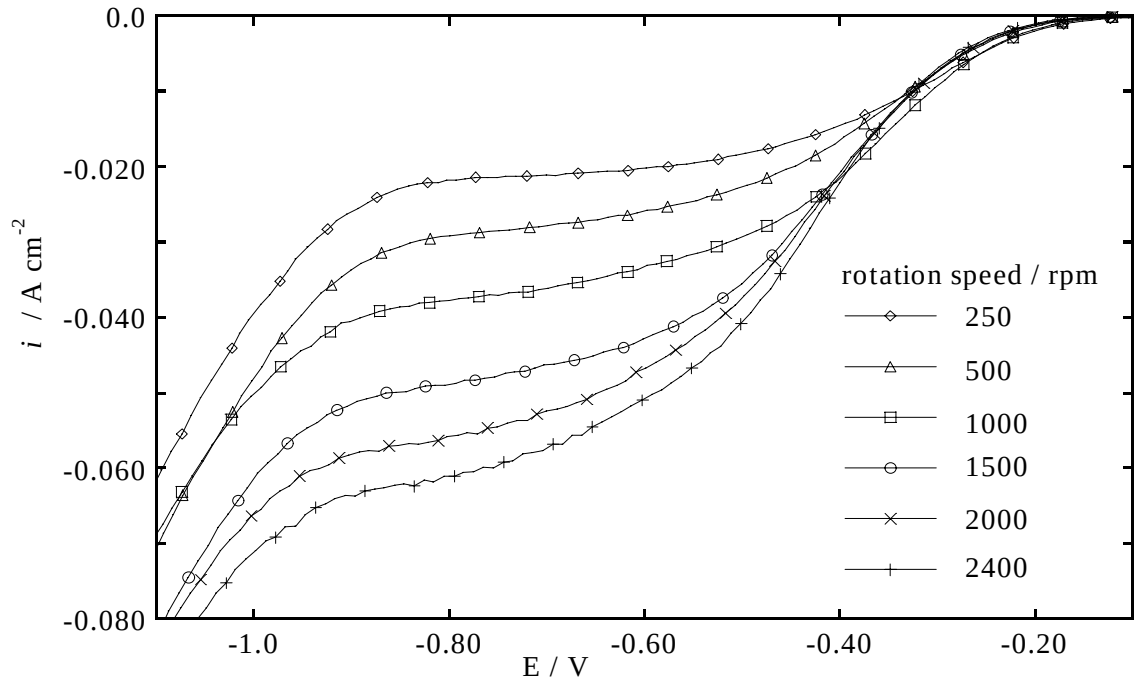

Figure 4.15 Potentiodynamic polarisation curves (10 mV s^{-1}) for oxygen reduction on gold in 0.2 M NH_4Cl at various electrode rotation speeds. pO_2 = 285 kPa. T = 150°C.

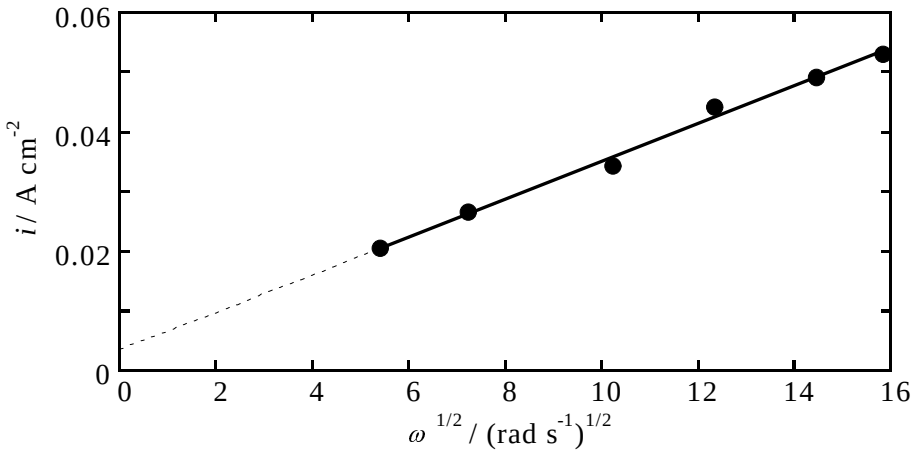

Figure 4.16 Levich plot for oxygen reduction on gold in oxygen saturated 0.2 M NH_4Cl at -0.63 V. pO_2 = 285 kPa. T = 150°C.

4.4 CONCLUSIONS

In 0.2 M NH_4Cl:

(i) oxygen reduction on iron proceeds via a 4-electron pathway but a distinction between the direct (equation (4.2)) and series (equations (4.6) and (4.7)) pathways could not be made

(ii) oxygen reduction on iron is diffusion controlled at -0.8 V

(iii) significant differences between potentiodynamic and potentiostatic oxygen reduction curves on iron are thought to be due to more extensive $Fe(OH)_2$ formation at long potentiostatic polarisation times

(iv) oxygen reduction on iron is not greatly influenced by pH between pH 4.8 and pH 8.0. However, the shape of the cathodic polarisation curve near the corrosion potential is influenced by pH through the iron oxidation reaction

(v) the oxygen reduction mechanism on gold is highly potential dependent with the number of electrons involved varying between nearly zero at -0.2 V and four at -0.8 V

(vi) oxygen reduction on gold is first order with respect to oxygen

(vii) significant differences observed between potentiodynamic and potentiostatic oxygen reduction curves on gold are possibly due to facile potential and time dependent reconstruction of Miller-index faces of gold

(viii) at 300 kPa oxygen partial pressure the oxygen reduction current density on gold nearly doubled between 80 and 130°C – the largest increase observed over a 50°C range

5 Aqueous Corrosion of Pure Iron by Dissolved Oxygen

5.1 INTRODUCTION

In Chapter 3 it was demonstrated that ammonium ion was able to remove the air-formed passive film on iron. It was also shown that the anodic current density was higher in the presence of ammonium ion, and that chloride ion inhibited active iron dissolution. In Chapter 4 it was shown that oxygen reduction is diffusion controlled and a 4-electron pathway is operative.

In this Chapter an electrochemical study of iron corrosion by dissolved oxygen in NH_4Cl and other electrolyte solutions will be described. First, the characteristics of uniform and localised corrosion will be introduced. Second, a review of the electrochemical techniques used in this Chapter to measure the corrosion current density will be given. This will include a critical discussion of the meaning, and the practical use of the polarisation resistance (R_p) – the most commonly measured quantity used to estimate the corrosion rate of metals. Third, a literature review of iron corrosion by oxygen will be presented.

The aim of this work is to understand the important factors affecting the aeration step of the Becher Process. A pure iron electrode will be used as a model system for iron in reduced ilmenite. The effect of the following variables on the corrosion of iron by dissolved oxygen will be investigated.

(i) immersion time
(ii) pH
(iii) temperature
(iv) electrode rotation speed
(v) electrolyte composition
(vi) polarisation
(vii) oxygen partial pressure

5.1.1 Corrosion mechanisms

Uniform or general corrosion occurs when the surface areas of both the anodic and the cathodic partial reactions are the same, resulting, on average, in a uniform corrosion rate all over the surface. On the other hand, localised corrosion occurs when the surface areas of the anodic and cathodic reactions are unequal, resulting in a different corrosion rates over parts of the surface. Usually, the anodic area is very small compared with the cathodic area resulting in localised areas of intense metal dissolution.

5.1.2 Corrosion rates

5.1.2.1 The meaning of the polarisation resistance (R_p) and the calculation of a corrosion rate

R_p is the most commonly measured electrochemical parameter used to estimate corrosion rates of metals. R_p is defined as the slope of the steady state polarisation curve at the corrosion potential (E_{corr}):

$$R_p = \left(\frac{dE}{di}\right)_{E=E_{corr}} \tag{5.1}$$

For an alternating potential perturbation, R_p is the in-phase component (Z') of the impedance (Z_f) at E_{corr} in the limit of zero frequency ($f \rightarrow 0$):

$$R_p = \lim_{f \rightarrow 0} \{Z'\}_{E=E_{corr}} \tag{5.2}$$

Equation (5.2) is mathematically equivalent to equation (5.1). Z' is also often referred to as the real component of Z_f.

Stern and Geary [116] and Stern [117] proposed that i_{corr} could be determined from R_p:

$$i_{corr} = \frac{b_a . b_c}{2.303 R_p (b_a + b_c)} \tag{5.3}$$

Where b_a and b_c are the anodic and cathodic Tafel constants respectively, and i_{corr} is the net corrosion current density. In order to calculate i_{corr} from the measured R_p value, the Tafel constants need to be obtained by some other method.

Equation (5.4) combines the Tafel constants into a single term, B. In this form it is clear that i_{corr} is inversely proportional to R_p.

$$i_{corr} = \frac{\mathrm{B}}{2.303R_p} \text{ where } \mathrm{B} = \frac{b_a . b_c}{(b_a + b_c)} \tag{5.4}$$

In the past, experimental determination of B was not often done since it required relatively time consuming anodic and cathodic polarisation curves to be measured separately. However corrosion rates were still estimated in a variety of ways. First, tables of B values have been constructed for a variety of systems [118] and can be used in equation (5.4) to estimate i_{corr}. Second, a reasonable value of B can be guessed and since B varies relatively little in magnitude with changes in b_a or b_c, i_{corr} can be still be estimated within a factor of say, two [119]. Third, in many cases, changes in the value of R_p are sufficient to indicate approximate changes in the corrosion rate with respect to particular variables in the corrosive environment [120] so that a B value is not necessary at all. In these cases sometimes only the reciprocal of R_p (*ie.* R_p^{-1}) is used (for example in references [121] and [122]) since the i_{corr} is proportional to R_p^{-1} (equation (5.4)).

The charge transfer resistance (R_t) is a term that is often used in the corrosion literature together and, in certain instances, interchangeably with R_p. R_p and R_t can be used interchangeably in the Stern-Geary (equation (5.3)) only when both the anodic and cathodic reactions are one step, Tafel electron transfers [87]. That is, when each reaction involved can be described by the Butler-Volmer equation [123]. Interestingly, although both iron dissolution and cathodic oxygen reduction reactions go through multiple steps (Chapters 3 and 4), this is not a fundamental problem since one of the steps is usually rate determining.

The most important instances (relevant to iron corrosion by oxygen) where R_p and R_t are not the same is when the cathodic reaction is under pure diffusion control ($i_{corr}/i_l \approx 1$) and partial diffusion or mixed control ($0 < i_{corr}/i_l < 1$). In both of these instances the relationship between R_t and i_{corr} is still given by equation (5.3) (by substituting R_t for R_p). However, this is not the case for R_p. When the cathodic reaction is under pure diffusion control the following equation relates i_{corr} and R_p [117, 124]:

$$i_{corr} = \frac{b_a}{R_p} \tag{5.5}$$

When the cathodic reaction is under partial diffusion control the expression linking R_p and i_{corr} is complicated, depending on the degree of diffusion control [87, 120]. Nagy described a completely general polarisation equation that can accommodate this partial diffusion condition with only the additional knowledge of the limiting current density (i_l) being required [123].

The two main limitations for practical use of the Stern-Geary equation (equation (5.3)) to calculate i_{corr} are [61]:

a) the approximations made in the linearisation of the polarisation equation (*ie.* assuming the current density is directly proportional to the polarising voltage)
b) requirement of the Tafel values b_a and b_c

Other important factors that can influence i_{corr} calculated using the Stern-Geary equation include the double layer effect, uncompensated solution resistance and reverse reactions [123].

The following sections will describe in some detail the experimental techniques used in this Chapter to estimate the corrosion rate, namely linear polarisation, electrochemical impedance spectroscopy and potentiodynamic polarisation. Practical considerations and the limitations of each technique will be discussed.

5.1.2.2 Linear Polarisation (LP)

This method for determining i_{corr} using the Stern-Geary equation (equation (5.3)) is so named because it really represents a linear approximation of the Butler-Volmer equation applied to the Wagner-Traud concept of corrosion processes [61]. That is, the current near E_{corr} is assumed to vary linearly with potential. It is known however, that the polarisation curve is never exactly linear but this assumption only introduces a small error. Nagy provided an expression to calculate the error associated with this approximation [123]. Methods including curve fitting, and the three point technique, have been devised to address problems associated with assuming linear behaviour [123].

LP curves are most commonly measured by scanning the potential 2-10 mV either side of E_{corr}. Another variation of this approach is the small amplitude cyclic voltammetry (SACV) technique where the potential is repetitively scanned through E_{corr} [125]. Another, less common approach is to control the current (statically [126, 127] or dynamically) and measure the potential near zero current density.

Mansfeld and Kendig [128] gave a theoretical basis for the choice of appropriate scan rate and Rocchini [129] quantitatively described the dependence of the measured R_p

value on the scan rate. The higher the R_p value the lower the scan rate that must be used in order to get an accurate estimate of R_p [129, 130]. Scan rates between 0.1 and 1 mVs^{-1} are suitable for most systems. Rocchini [129] highlighted the fact that as the scan rate is increased, a competition between R_p and the double layer capacitance (C_{dl}) produces a distortion in the polarisation curve.

A major disadvantage of the linear polarisation technique is that the R_p value measured includes contributions from mass transport resistance, uncompensated solution resistance (R_s) and resistances from passive films. These additional resistances add together and hence the corrosion rate can be significantly underestimated (since i_{corr} is inversely proportional to R_p). The error in i_{corr} due to uncompensated solution resistance has been treated quantitatively by Nagy [123]. Walter also considered the uncompensated resistance (attributed to both solution and/or a film) in his error calculations [126, 131].

For the ideal linear polarisation technique, the error in i_{corr} increases markedly with an increase in the ratio R_s/R_p. For a maximum error of 20%, it was calculated that R_p must be 4 times larger than R_s [123]. However, this is still an underestimation of the error since it also neglects the error in b_a and b_c due to the uncompensated resistance.

The qualitative detection of localised and uniform corrosion is also possible. For example, linear polarisation curves that have a lot of noise or scatter in the current are indicative of localised corrosion while smooth curves are indicative of uniform corrosion [132].

5.1.2.3 Potentiodynamic polarisation or the Tafel technique

Polarisation curves measured using this technique have various uses. First, they can simply provide signatures of corrosion behaviour for metals in a given environment. Second, Tafel slopes, b_a and b_c, determined from the slope of the polarisation curve at moderate overpotentials (*eg.* $E_{corr} \pm 75$ mV), can be used in equation (5.3) to give i_{corr}. Third, i_{corr} can be calculated by extrapolating the anodic and cathodic Tafel slopes back to the corrosion potential. However, this is only valid if the Tafel regions are far away enough from E_{corr} and also only if other spurious reactions are negligible.

The polarisation curve is often measured by scanning the voltage and measuring the current, hence the name "Potentiodynamic Polarisation". Anodic or positive current indicates that electrons are leaving the surface and a cathodic or negative current

indicates electrons collecting on the surface. There are significant disadvantages to this technique including:

a) rapid oxidation at large positive overpotentials usually results in a surface significantly different from that at E_{corr}; this not only introduces some uncertainty into the results, but also the sample is effectively destroyed after a single measurement
b) at very negative overpotentials, hydrogen adsorption or oxide film reduction can occur, further changing the surface
c) large currents will also increase the risk of current distortion due to uncompensated solution resistance and, the mass transport of products to and from the metal surface may be limiting which will also affect the results
d) the potential dependent adsorption of species will of course be affected by large overpotentials, which can cause further uncertainty in the results

The choice of scan rate is also important – this should be low enough to ensure that approximate steady state conditions are achieved. The potentiodynamic polarisation curve can be measured in a number of ways. For example, by pulsing the electrode to negative potentials and then scanning in a positive direction through E_{corr} or, alternatively, the potential can be scanned in the cathodic direction first and then the scan reversed in order to detect any hysteresis in the cathodic process, pausing for some time at E_{corr} for equilibration before continuing the scan in the anodic direction.

5.1.2.4 Electrochemical Impedance Spectroscopy (EIS)

The theoretical foundation of this technique in the study of electrochemical reactions is that the response or impedance of an electrochemical interface to an applied sinusoidal excitation voltage (ΔE) is considered to be equivalent to the response of an appropriate electrical circuit. A simple electrochemical interface can be represented by the equivalent circuit shown in Figure 5.1. Each component represents a useful electrochemical parameter and by applying alternating current theory to the response of the equivalent circuit, the value of each parameter can be determined.

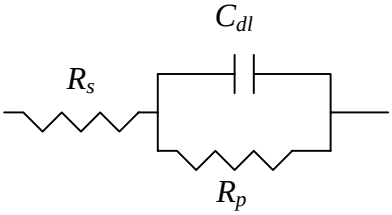

Figure 5.1 A simple equivalent circuit.

Macdonald and McKubre [133] reviewed methods for the measurement of the interfacial impedance and Macdonald also reviewed the use of EIS for investigating the mechanism of electrode reactions [134]. Numerous reviews on the application of EIS to corrosion science have been published [87, 125, 134-138]. The review below is concerned with the use EIS for the determination of corrosion rates and simple corrosion mechanisms.

The response of any conductive system to an electrical perturbation can be described by a transfer function which can be identified as an impedance, Z_f, when the input perturbation and output response are linearly related [134]. Linearity between input and output is necessary for valid EIS results. The impedance of the equivalent circuit in Figure 5.1 in response to an applied sinusoidal voltage of varying frequency, f, is given by the following equation:

$$Z_f = R_s + \frac{R_t}{1 + j2\pi f R_t C_{dl}} \tag{5.6}$$

where $j = \sqrt{-1}$. The angular frequency, ω (rad s^{-1}) = $2\pi f$ (Hz). Sometimes the product $R_t \times C_{dl} = \tau$ is used, where τ (seconds) is the time constant for the RC couple.

Impedance data from corrosion experiments are often graphically presented, usually in one or more of the following three formats:

a) the Nyquist plot (Figure 5.2a): Z'' (the out-of-phase component of Z_f) is plotted against Z', giving a semicircle for the simple circuit Figure 5.1. C_{dl} can be extracted using equation (5.7) and the frequency of the impedance at the top of the semicircle (f_{max}).

$$C_{dl} = \frac{1}{R_t 2\pi f_{max}} \tag{5.7}$$

b) Bode phase angle plot (Figure 5.2b): the phase angle of Z_f in degrees (θ) is plotted against log f. The advantage of this plot is that electrochemical reactions with different time constants, τ, can be visually identified as peaks.

c) The Bode |Z| (modulus) plot (Figure 5.2c): |Z| is the magnitude of the impedance vector Z_f and is plotted against log f. Sometimes Z' is plotted instead of |Z|.

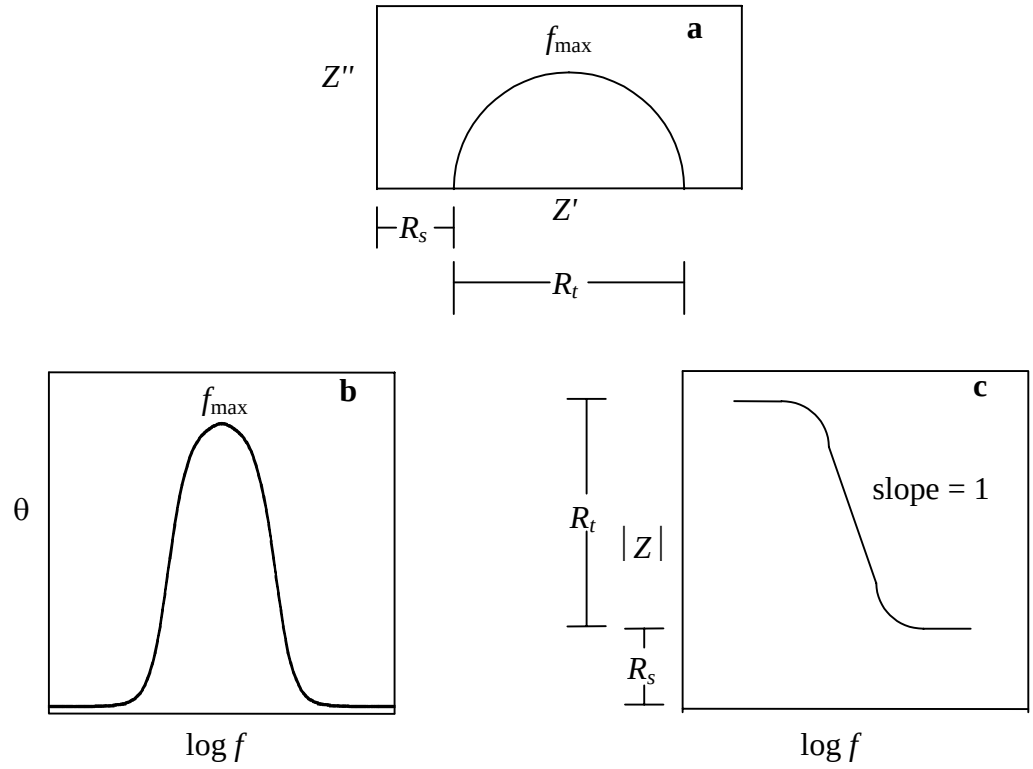

Figure 5.2 Commonly used graphical representations of corrosion impedance data. Schematic plots for the impedance response of the equivalent circuit in Figure 5.1 a) Nyquist plot, b) Bode phase angle plot and c) Bode |Z| plot.

The impedance response of corroding systems is, however, often more complicated than described above. For example, the center of the semicircle is located below, rather than on the Z' axis (which is also often referred to as the real axis) – this deviation is termed the depression angle. In the Bode |Z| diagram the depression angle is manifested as a slope less than 1 [139]. As with the depression angle, mass transfer control is also common and affects the impedance response in ways that cannot be modelled using the simple equivalent circuit in Figure 5.1. Also, more than one loop may be observed in the Nyquist plot for iron and these distortions from the ideal impedance response must be incorporated into the equivalent circuit in order to obtain meaningful R_p values. These common distortions from the ideal impedance response for iron are described in more detail below.

"Frequency dispersion" of the impedance response is often used to explain the depression angle. However different explanations have been offered to account for this phenomenon:

a) incorrect placement of the reference probe; the reference probe should be placed in between the working and counter electrodes where the current lines are parallel [133, 140]
b) surface roughness; recently, the magnitude of the depression angle has been correlated with the degree of pitting and pit depth [121, 141, 142]

Silverman [139] believes that the depression angle has little useful mechanistic information since it may result from more than one type of phenomenon as described above. The depression angle is mathematically incorporated into the equivalent circuit with the addition of the exponent α (a constant phase element, CPE) into equation (5.6):

$$Z_f = R_s + \frac{R_t}{1 + j2\pi f\left(R_t C_{dl}\right)^{\alpha}} \tag{5.8}$$

Mansfeld and Lorenz state that the physical meaning of α is not entirely clear [143]. The exponent α can be calculated using numerical curve fitting procedures or measured from the depression angle (ϕ in radians) using equation (5.9) [141].

$$\alpha = 1 - \frac{2\phi}{\pi} \tag{5.9}$$

Note that in reference [141] the unit for ϕ is incorrectly stated to be degrees rather than radians. As suggested by the term, constant phase impedances are independent of the frequency. Other electrochemical phenomena that give rise to constant phase impedances include semi-infinite diffusion (Warburg, α = 0.5) and pore diffusion (α = 0.25) [136].

Figure 5.3 shows a schematic Nyquist plot exhibiting an additional inductive

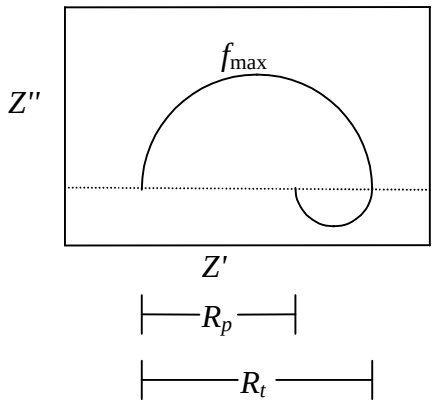

Figure 5.3 A schematic diagram of a Nyquist plot exhibiting a capacitive and an inductive loop. Modified from Epelboin *et al.* [87].

impedance response which manifests itself as a loop below the in-phase axis at low frequencies.

The inductive loop in Figure 5.3 can be caused by problems such as non-linearity or electroactive adsorbed intermediates such as hydrogen on the surface [139]. Non-linearity can also be caused by the application of an excessive excitation voltage (ΔE) to the system. The inductive loop is probably not an experimental artefact if the magnitude of the inductive loop does not decrease with decreasing ΔE [140]. The inductive loops for iron have also been attributed to the iron dissolution process itself and were shown to originate from the potential dependence of the surface coverages of hydrogen and $FeOH_{(ad)}$ [82, 122, 144].

Calculation of the corrosion rate for iron exhibiting an inductive loop in its Nyquist plot has attracted considerable attention and also generated some controversy in the literature. Figure 5.3 shows that R_t corresponds to the first intersection of the impedance loop with the real axis while R_p corresponds with the second intersection of the loop with real axis. Epelboin *et al.* concluded that R_t is more intimately related to i_{corr} than R_p [87]. On the other hand, Lorenz and Mansfeld state that this assertion is only valid if the capacitive part does not contain any Faradaic impedance which is considered to be located in the inductive loop [122]. They calculated R_t by subtracting the capacitive contribution to the impedance response, resulting in a smaller Nyquist plot where R_t is smaller than R_p. These workers found that after this treatment, R_p correlated much better with i_{corr} than R_t. Schweickert *et al.* also calculated R_t in this way for their investigation of iron dissolution in acidic sulphate solutions [144]. These examples illustrate that when more than one time constant is observed in the impedance response, determination of the corrosion rate can be complicated.

The Warburg diffusion impedance, Z_W *or* W, models the contribution to the impedance from semi-infinite linear diffusion [133, 145]:

$$W = Z_W = \sigma\omega^{-0.5} - j\sigma\omega^{-0.5} \qquad (5.10)$$

where σ is the Warburg diffusion coefficient ($\Omega\ s^{-0.5}$) and the other symbols have their usual meaning. The equivalent circuit incorporating the Warburg term is shown in Figure 5.4.

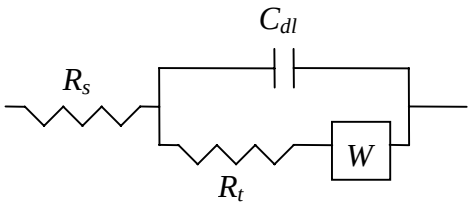

Figure 5.4 An equivalent circuit including a Warburg semi-infinite diffusion impedance component (*W*).

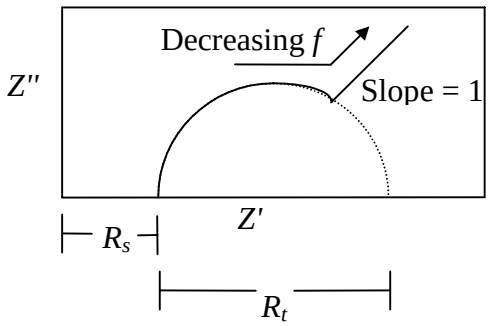

Figure 5.5 Schematic Nyquist plot showing the impedance response of the Warburg equivalent circuit in Figure 5.4.

By using the equivalent circuit in Figure 5.4, contributions to the Faradaic impedance, Z_f, by the charge transfer resistance R_t and the Warburg impedance, Z_W, can be separated and therefore a more accurate estimate of the corrosion rate can be made [113].

5.1.3 Corrosion of iron by dissolved oxygen in mildly acidic and neutral aqueous solutions – a literature review.

The aim of this work is to understand the important factors affecting the aeration step of the Becher Process by using pure iron as a model system for iron in reduced ilmenite. Therefore it is important to review the literature concerning oxygen corrosion of iron in other mildly acidic and neutral solutions in order to provide a comparison of iron corrosion rates and behaviour with results presented in this Chapter.

Juttner, Lorenz, Mansfeld and co-workers have published several articles discussing the corrosion of pure iron in air-saturated 0.5 M Na_2SO_4 [137, 143, 146, 147]. Their work has involved analysis of EIS data to obtain quantitative corrosion rate and mechanistic information. They proposed an impedance model that takes into account the complications in the corrosion mechanism arising from the formation of a three

dimensional (3-D) inhomogeneous layer of corrosion product. Their experiments were conducted over periods of up to 72 hours. Aspects of this work are summarised below.

A large deviation from the Levich equation was observed for dissolved oxygen reduction on iron covered with corrosion product. The cathodic current density was always less than that predicted by the Levich equation and decreased with increasing immersion time – a consequence of corrosion product build-up. This supports the theory that oxygen reduction occurs on exposed metal sites within the pores of the corrosion product layer. Potentiodynamic polarisation curves also showed that the anodic current density increased with immersion time. This was accounted for by the formation of local aeration cells that lead to localised corrosion occurring and a net increase in the anodic current.

Nyquist plots were characterised by partial semicircles and diffusion tails at lower frequencies. As a result, R_p defined by equation (5.2) (*ie*. by the impedance in the limit of zero frequency) could not be determined since even dc measurements would give the wrong R_p value and hence the wrong corrosion current density. However by fitting the experimental data to their equivalent circuit – which accounted for linear diffusion and diffusion through the pores of the corrosion product layer – they extracted R_{Me}, the resistance of the metal dissolution reaction. Using equation (5.5), valid when the cathodic reaction is under mass transport control, they calculated a corrosion rate that correlated well with weight loss data. Table 5.1 shows the R_{Me} values obtained at different rotation speeds and corrosion rates calculated using b_a = 0.04 V dec^{-1}. From a weight loss measurement at 960 rpm an i_{corr} value of 6 × 10^{-5} A cm^{-2} was calculated which compares quite well with the electrochemically determined value shown in Table 5.1, confirming the general validity of their approach.

Rotation speed / rpm	E_{corr} / V	t_{corr} / hours	R_{Me} / Ω cm^2	i_{corr} / A cm^{-2}	C_{dl} / μF cm^{-2}
0	-0.531	22	20000	8.7×10^{-7}	40
240	-0.492	26	1400	1.2×10^{-5}	78
960	-0.479	29	480	3.6×10^{-5}	105

Table 5.1 Corrosion data from Juttner *et al.* [147] for an iron disc electrode in air-saturated 0.5 M Na_2SO_4. pH = 6. T = 25°C. b_a = 0.040 V dec^{-1}. The type of reference electrode was not stated in the original paper.

You *et al.* investigated the corrosion of iron in air-saturated 0.5 M NaCl at 30°C [148]. These workers also investigated the oxygen reduction reaction using DC techniques and used EIS to investigate the corrosion reaction. EIS curves were characterised by two time constants, giving rise to two partial semicircles on the Nyquist plots. Corrosion products emanating from pits formed an inhomogeneous layer on the electrode surface. The corrosion product was characterised by a "first zone" and a "second zone" which was composed of a more adherent layer. For short immersion times oxygen reduction occurred on the bare surface and the anodic reaction was highly localised. However at longer immersion times the pits became less active and the corrosion more uniform. Qualitative correlations between the nature of the corroding surface and features on the EIS spectrum were made. You *et al.* surmised that the low frequency loop corresponds to diffusion across the corrosion product layer and the medium frequency loop is corresponds to diffusion to the bare iron surface. It was suggested that these two processes occur simultaneously but at various rates depending on both the rotation speed and the immersion time. These workers concluded that quantitative determination of the corrosion rate seems dubious. They also reiterate the comments made by Jovancicevic [149] that the resistance due to oxygen diffusion through the pores of the corrosion product layer calculated by Juttner *et al.* [147] could also be due to diffusion within the pits.

Lorenz and Mansfeld [122] discussed the problems associated with measuring a corrosion rate for iron in air-saturated 0.5 M H_2SO_4, 0.5 M Na_2SO_4 and 1 M HCl solutions. They compared corrosion rates calculated from potentiodynamic polarisation, LP and EIS experiments. In 0.5 M Na_2SO_4 (pH = 7) iron corrodes forming a porous oxide layer of limited conductivity. This layer decreases the area available for reduction, explaining why the oxygen reduction current density on corroded iron is always less than that predicted by the Levich equation. In 0.5 M H_2SO_4 over a period of 24 hours, b_a increased from 0.03 to 0.08 V dec^{-1} while no clear trend was observed for b_c, which varied between -0.08 and -0.11 V dec^{-1}. B increased from around 0.010 to 0.018 V in 2 hours and then essentially remained constant up to 24 hours. The corrosion current density, i_{corr} was calculated by fitting equation (5.3) to polarisation data even though the cathodic current involves both oxygen and proton reduction. i_{corr} increased sharply after 6-7 hours from an initial value of 5×10^{-4} A cm^2 to 5×10^{-3} A cm^2 and then remained constant up to 24 hours.

Cox and Lyon [150] studied oxygen reduction on non-corroded and atmospherically corroded iron covered by very thin (300 μm) solutions of air-saturated 0.2 M Na_2SO_4. Orange lepidocrocite (γ-FeOOH) formed after exposure to air. Potentiodynamic polarisation curves showed that the cathodic reduction current density on 30 day exposed iron was about an order of magnitude greater than for clean iron. The anodic current density and Tafel slope (0.110 V) however, were about the same for both specimens. For oxygen reduction, $i_l \approx 6.0 \times 10^{-5}$ A cm^{-2}. However, corrosion rates (calculated by the extrapolation of anodic and cathodic Tafel curves) are 8.0×10^{-5} and 2.4×10^{-4} A cm^{-2} for 3 and 30 day exposed specimens respectively. These workers considered that oxygen reduction on the corroded samples appeared to be activation controlled even though the Tafel slope was extremely high (380 V dec^{-1}). Cox and Lyon [150] showed that the enhanced cathodic current was due to the reduction of γ-FeOOH to Fe^{2+} or $Fe(OH)_2$ thus further increasing i_{corr}.

Roberge *et al.* investigated the corrosion of mild steel electrodes in deaerated and aerated 3% NaCl in order to then gauge the effectiveness of different inhibitors [121, 142]. In this work no attempt was made to calculate the corrosion rate, rather changes in R_p and the depression angle were used to semi-quantitatively assess changes in the corrosion rate and pit depth respectively. After 20 days immersion the following results were obtained: E_{corr} = -0.65 ± 0.03 V (*sce*), R_p = 500 ± 100 Ω cm^{-2} and the depression angle was -18 ± 2°.

Silverman and Carrico [151] used EIS to investigate the corrosion of carbon steel in water containing a dilute mixture of salts at 32°C. In stagnant solution a partial semicircle and a small diffusion tail at low frequencies were observed in the Nyquist plot. After about 48 hours a constant R_p value was obtained. The composition of a gelatinous orange-brown oxide deposit that formed was not reported, however it is most likely to be γ-FeOOH. The EIS data were analysed by fitting the impedance response to the equivalent circuit shown in Figure 5.4. This mechanism was chosen for it was assumed that oxygen diffusion is the rate controlling step. This was still considered to be a reasonable assumption even though b_c was not much larger than b_a (b_c = -0.105 V dec^{-1}; b_a = 0.06 to 0.10 V dec^{-1}). An R_p value of 1000 Ω cm^2 was estimated. Interestingly, the diffusional component disappeared with rotation and two time constants appeared instead. However, these workers did not actually show their EIS spectra under stirred conditions. By comparison with corrosion rates determined from weight loss

experiments, it was determined that the lower frequency time constant (τ) represented the charge transfer process. For stirred solutions the impedance response was modelled using a circuit containing a second *RC* couple in series with R_t. R_p decreased to 475 Ω cm^2 at 1000 rpm. Table 5.2 lists some their data.

rotation speed / rpm	R_p / Ω cm^2	mass loss	EIS
		i_{corr} / A cm^{-2}	i_{corr} / A cm^{-2}
0	1000	6.5×10^{-7}	1.0×10^{-6}
1000	475	3.3×10^{-6}	2.2×10^{-6}

Table 5.2 Corrosion data from Silverman and Carrico [151] for mild steel in air-saturated water at different electrode rotation speeds. T = 32°C.

Yang *et al.* investigated the corrosion of iron microelectrodes (diameter = 50 and 250 μm) in a series of low conductivity air-saturated electrolytes (pH = 7.2-8.5) using the LP, potentiodynamic polarisation and EIS techniques [152]. Corrosion rates were about half that expected if oxygen diffusion was considered limiting ($i_l = 6.45\times10^{-6}$ A cm^{-2}, 50 μm diameter. electrode) and also the cathodic Tafel slopes were indicative of mixed control (-0.2 to -0.3 V dec^{-1}). Uniform corrosion was observed and an orange-brown porous and loosely adhering corrosion product formed. Due to the presence of these oxides, the authors considered the assumption that the cathodic and anodic reactions occur on the same site was unlikely to be correct. Nevertheless, they concluded this assumption was reasonable, at least to a first approximation, since i_{corr} calculated by polarisation resistance (LP), cathodic and anodic Tafel extrapolation techniques, did not differ significantly as shown in Table 5.3.

t_{corr}/hr	E_{corr}/V	R_p / Ω cm^2	b_a / V dec^{-1}	b_c / V dec^{-1}	$i_{corr,\,Rp}$ / A cm^{-2}	$i_{corr,\,c}$ / A cm^{-2}	$i_{corr,\,a}$ / A cm^{-2}
20	-0.651	81	0.041	-0.742	3.5×10^{-4}	5.1×10^{-4}	2.0×10^{-4}

Table 5.3 Corrosion current density (i_{corr}) for iron in air-saturated low conductivity water (solution E, pH = 7.2~7.5) calculated using polarisation resistance (R_p), cathodic (*c*) and anodic (*a*) Tafel extrapolation techniques. From Yang *et al.* [152]. T = 29.4°C. *sce* reference.

In one of the low conductivity solutions (E, pH = 7.2~7.5) it was found that the corrosion rate increased at rotation speeds from 0 to 250 rpm but then decreased as the rotation speed was further increased from 500 to 1000 rpm [152]. They explained that at low rotation speeds the corrosion product is very porous and provides no protection so at a higher rotation speed the supply of oxygen increases and thus i_{corr} increases. However, as the rotation speed increases still further, the loose deposit is swept away leaving a thinner, more compact layer that provides some protection and thus i_{corr} decreases.

Farrow *et al.* [21] found that E_{corr} varied linearly with the square root of the electrode rotation speed for iron in 0.2 M NH_4Cl proving [52] that the corrosion reaction was under oxygen diffusion control. Mandyczewsky investigated the corrosion of coarse and fine iron powders in air and oxygen saturated 10% (by weight) NH_4Cl and NaCl solutions [19]. He recognised that that the buffering action of NH_4^+ was important in preventing passivation and concluded that oxidation proceeds first by the electrochemical oxidation of metallic iron to ferrous ions followed by oxidation of ferrous ions to hydrated ferric oxide.

Bonnel *et al.* studied the corrosion of carbon steel in air-saturated 3% NaCl [98]. Pitting corrosion occurred with spirals of corrosion product covering some of the non-corroded areas. The Nyquist plot consisted of two partial semicircles or loops. The high frequency loop was attributed to iron dissolution while the low frequency loop was attributed to mass transfer of oxygen with some influence from the anodic reaction as well. They concluded that that some of the dissolved oxygen was consumed in oxidising Fe^{2+} to Fe^{3+}. This resulted in a lower effective oxygen concentration. Mansfeld *et al.* [153] doubted some of the work by Bonnel *et al.* [98] since these workers only observed a single loop in the same solution. The discrepancy can probably be explained by the differences in immersion time. Bonnel *et al.* [98] reported that at shorter immersion times a single loop is observed while after 2-3 hours a second loop is observed at lower frequencies. Mansfeld *et al.* only reported their results measured after about 1 hour of immersion [153].

Table 5.4 lists the corrosion rate data for iron in 3.5% NaCl at different oxygen partial pressures from Laque and Hobson [154] (reference 67 in [119]). The corrosion rate is linearly dependent on the pressure up to 10 atmospheres only. At 60 atmospheres the corrosion rate is less than that expected from the trend up to 10 atmospheres. The reason for this is not known but may be due to effects of poor oxygen transfer from the gas to the solution phase and/or passivation.

pO_2 / kPa	Corrosion rate / mpy	i_{corr} / A cm^{-2}
0.21	2.2	4.8×10^{-6}
101	9.3	2.0×10^{-5}
1000	86.4	1.9×10^{-4}
6000	300	6.5×10^{-4}

Table 5.4 Corrosion current densities (i_{corr}) calculated from weight loss for iron in 3.5% NaCl at various oxygen partial pressures. From reference No. 67 in [119].

5.2 EXPERIMENTAL

The experimental method and equipment used were described in Chapter 2.

5.2.1 Ambient pressure electrochemistry

5.2.1.1 Solutions

Humidified air was bubbled through the solutions for 30 minutes prior to immersion of the electrode.

5.2.1.2 Equipment

A PAR model 273 potentiostat and model 5120 lock-in amplifier were used to measure impedance spectra. Experiment control and data acquisition was assumed by a personal computer running PAR model 398 EIS software [155]. Frequencies were chosen in the range from 100 kHz to 10 mHz with an applied excitation voltage of 5 mV. In most cases, the impedance measurements were performed at E_{corr} however, some experiments were done at anodic and cathodic overpotentials as well. All potentials are reported against 3 M KCl Ag/AgCl (E = 0.208 V *vs. she*).

A Perkin Elmer Infrared Fourier Transform Spectrometer was used to measure FTIR spectra of corrosion products using KBr discs.

5.2.2 High pressure electrochemistry

5.2.2.1 Solutions

Air or pure oxygen was bubbled through the solutions as described in Chapter 2.

5.3 RESULTS AND DISCUSSION

5.3.1 Corrosion of pure iron in air-saturated 0.2 M NH_4Cl

5.3.1.1 The effect of immersion time

Figure 5.6 shows typical trends in R_p and E_{corr} as a function of immersion time for an iron rotating disc electrode in air-saturated 0.2 M NH_4Cl at 30°C. Immediately after immersion E_{corr} decreased (negative dE_{corr}/dt) reaching a minimum value after about 2 minutes and then increased (positive dE_{corr}/dt = 1) reaching a maximum value around 20 minutes after immersion and then decreased slowly (and approximately linearly) with time thereafter. R_p decreased sharply between 10 and 20 minutes after immersion and decreased at a slower rate thereafter (Figure 5.6).

In Section 3.3.1 it was shown that the air-formed oxide film on iron can inhibit iron oxidation. The initial low corrosion rate is most likely due to the inhibitive effects of this film on the corrosion reaction and the corrosion rate increase with time reflects the removal of this film from the iron surface.

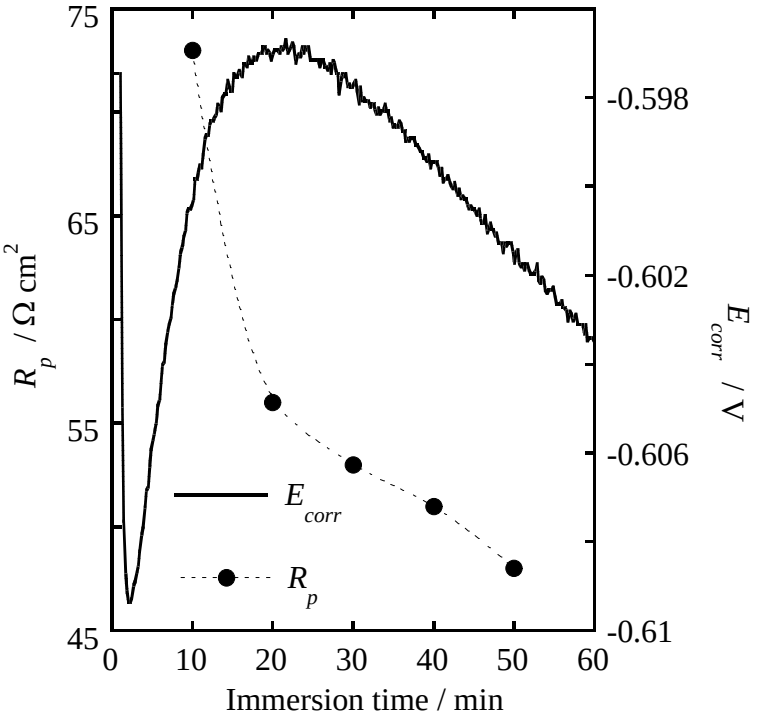

Figure 5.6 Typical trends in R_p (from LP) and E_{corr} as a function of immersion time for an iron rotating disc electrode (1000 rpm) in air-saturated 0.2 M NH_4Cl. T = 30.0°C.

According to Plonski [59], a negative slope in the E_{corr} versus time plot indicates an increase in the predominance of electron source reactions, in this case iron oxidation. A positive slope indicates the predominance of electron sink reactions, in this case oxygen reduction. When the electron source and electron sink intensities balance each other $dE_{corr}/dt = 0$.

Removal of the electrode from the solution after 1 hour immersion revealed a loosely adhering yellow-orange film on the iron surface. This film could be easily wiped off with a tissue, revealing a uniformly etched surface where the polycrystalline grain structure was visible. This type of surface is indicative of an active uniform corrosion mechanism. The FTIR spectrum of the dry corrosion product in Figure 5.7 shows that the film is lepidocrocite, γ-FeOOH.

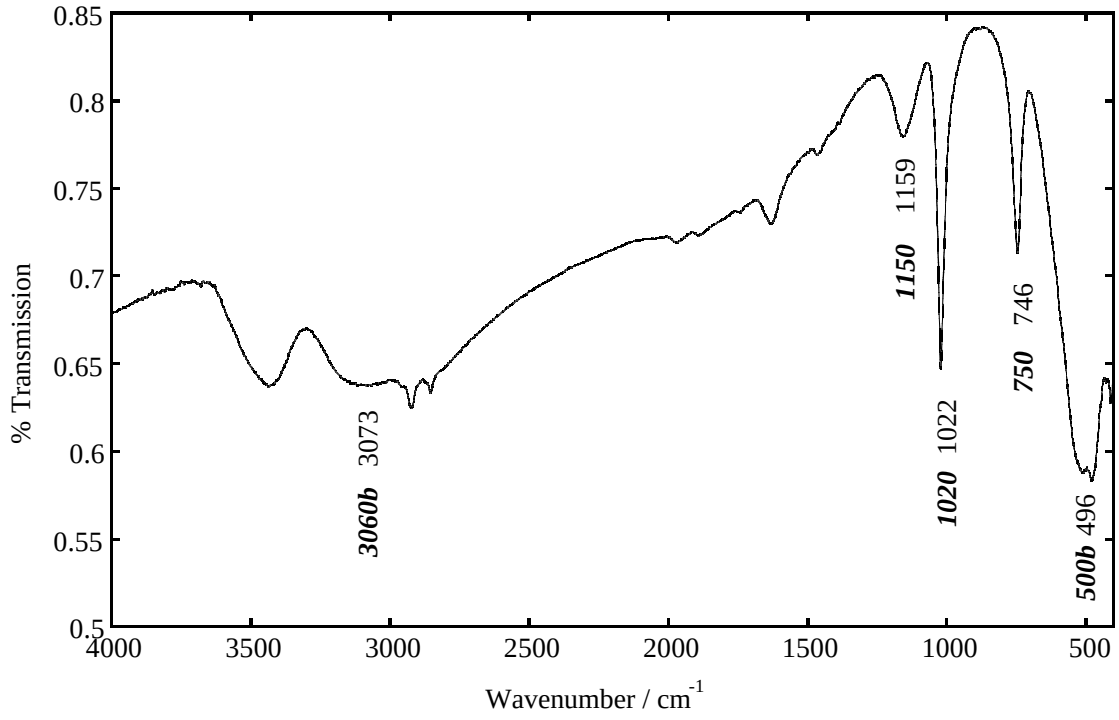

Figure 5.7 FTIR spectrum of the corrosion product from an iron rotating disc electrode in air-saturated 0.2 M NH_4Cl. Italicised bold numbers are infrared bands for γ-FeOOH [156]. Note: ***b*** = broad.

Figure 5.8 shows the Nyquist plot for an iron rotating disc electrode at various immersion times. After the initial sharp decrease in R_p within 30 minutes of immersion, R_p remained essentially constant (between 50 and 60 Ω cm^2) for at least 3 hours after immersion. Obviously the γ-FeOOH film does not affect the corrosion rate any further

despite its continual growth. This indicates that the film is most probably very porous. However after 7 hours immersion, R_p had increased to 200 Ω cm^2. After this time it was observed that a more compact and adherent γ-FeOOH had formed beneath the porous layer. This compact film is most probably a more effective barrier to oxygen diffusion to the iron surface. The iron surface beneath the compact γ-FeOOH film was bright and considerably roughened, perhaps indicating that some localised corrosion may have been occurring as a result of the film. Similar observations of localised corrosion occurring beneath films have been reported by others [98, 147].

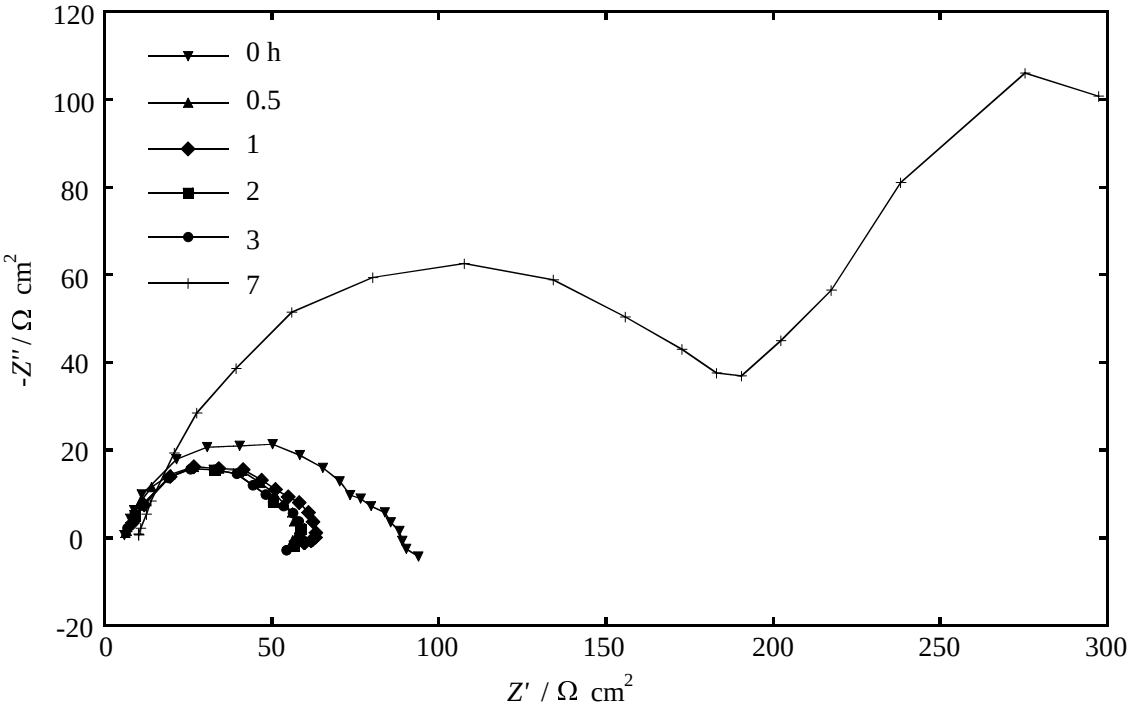

Figure 5.8 Nyquist EIS plots for an iron rotating disc electrode (1000 rpm) in air-saturated 0.2 M NH_4Cl at various immersion times. T = 30.0°C.

The results above show that the maximum corrosion rate was achieved between 30 minutes and 3 hours after immersion. An immersion time of 50 minutes was therefore chosen to assess the corrosion behaviour of iron. Thus, after 50 minutes immersion, the corrosion current density was $8.4 \times 10^{-4} \pm 0.7$ A cm^{-2}. This value was obtained by substituting a R_p value of 53.4 ± 4.5 Ω cm^2 and a B value of 0.045 V dec^{-1} into equation (5.3). The corrosion potential after 50 minutes immersion was -0.603 ± 0.008 V.

5.3.1.2 The effect of pH

In this section the effect of pH on the corrosion behaviour of iron in air-saturated NH_4Cl will be described. It has been suggested that localised high pH conditions arise within the reduced ilmenite grain during aeration [20-22] and in NH_4Cl solution the ammonia formed at high pH complexes with Fe^{2+} assisting in the removal of iron from the grain. In Section 1.3.2.1 the conditions for ferrous-ammine formation have been discussed. To the author's knowledge, this is the first study of the effect of pH on the corrosion behaviour of pure iron in any concentration of air-saturated NH_4Cl solution.

Figure 5.9 shows R_p and E_{corr} for an iron rotating disc electrode as a function of pH after 20 minutes immersion. A shorter immersion time was chosen (rather than 50 minutes) in order to minimise the loss of ammonia from solutions above pH 7. From pH 4.8 to 5.5 R_p was constant. At pH 6.0 R_p dipped slightly before increasing to around 80 Ω cm^2 between pH 6.5 and 7.0. Above pH 7.0, R_p rose rapidly to a maximum value of 176 Ω cm^2 at pH 8.14. The strong correlation between E_{corr} and R_p is clear, with both parameters increasing sharply between pH 7.0 and 8.0. The dip in R_p at pH 6.0 coincides with a shift in E_{corr} to slightly more positive values.

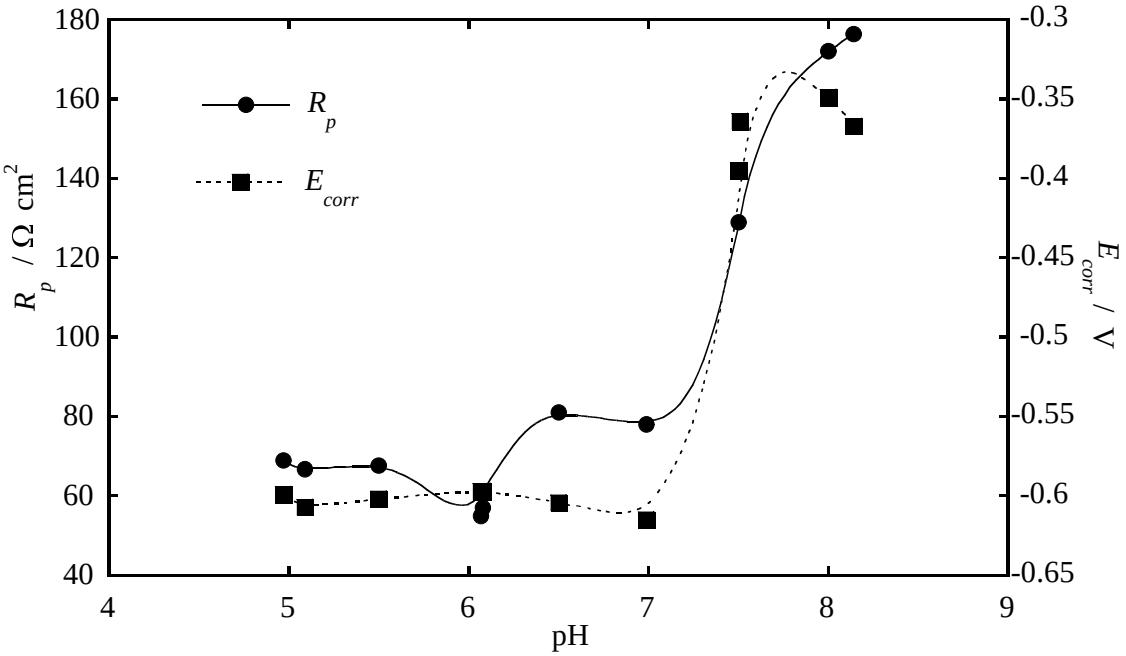

Figure 5.9 R_p (from LP, 20 minutes after immersion) for an iron rotating disc electrode (1000 rpm) as a function of pH in air-saturated 0.2 M NH_4Cl. At pH 8.14, R_p was measured using EIS. T = 30.0°C.

In the previous section it was shown that a lepidocrocite film formed on iron corroding in ammonium chloride solution at its natural pH (Section 5.3.1.1). Lepidocrocite films also formed at higher pH, but some important differences were observed. For example, below pH 6.0 the γ-FeOOH film was thin and not very adherent while between pH 6.5 and 7.0 the film was observed to be more compact. The iron surface beneath this film appeared uniformly corroded. At pH 7.5 corrosion was highly localised at pits and crevices while most of the surface appeared completely unaffected. A mixture of voluminous yellow-orange (γ-FeOOH) and brown oxide (possibly Fe_2O_3 or finely divided γ-FeOOH) spread out across the surface from these localised points.

These results maybe interpreted as follows.

In Section 3.3.2 it was shown that the air-formed oxide film on iron was stable at pH 7.5 and above in deaerated 0.2 M NH_4Cl. The very positive open circuit potentials and high R_p values for iron at pH 7.5 and above in air-saturated solutions are most likely to be due to the presence of the air-formed film. In the presence of chloride, the air-formed film breaks down at isolated points leading to pitting and crevice corrosion. At pH 7.0 and below, the air-formed film is removed, leaving a bare iron surface. This results in uniform corrosion, and more negative corrosion potentials and lower R_p values compared with the results at pH 7.5 and above. The smaller variations in R_p observed between pH 4.8 and 7.0 are also believed to be significant. For example, the higher R_p values observed at pH 6.5 and 7.0 are believed to result from the either a compact γ-FeOOH film, or some residual air-formed film, blocking oxygen transport to the iron surface. However, the lower R_p value observed at pH 6.0 compared with the results between pH 4.8 and 5.5, is more difficult to explain, especially since both oxygen reduction and iron oxidation current densities are constant within this pH and potential range (see sections 3.3.2, p. 50 and 4.3.1.2, p. 68). Figure 1.7 predicts a peak in the concentration of both $FeOH^+_{(aq)}$ and $FeNH_3^{2+}$ at precisely pH 6.0 and provides circumstantial evidence that ammonia is exerting an influence on iron corrosion, most likely by increasing the solubility of Fe^{2+}, resulting in faster removal of the air-formed film.

5.3.1.3 The effect of temperature

Figure 5.10 and Figure 5.11 show R_p and E_{corr} respectively, for an iron rotating disc electrode in air-saturated 0.2 M NH_4Cl as a function of temperature. In Figure 5.10 the points are average R_p values from both EIS and LP experiments. Between 30 and 50°C

R_p was constant but then decreased with increasing temperature reaching its minimum value between 70 and 80°C before increasing again at 90°C. The corrosion potential followed a similar trend where a minimum value of -0.71 V was observed at 70°C before it shifted to more positive values at 90°C. The reason for this peak in corrosion rate between 70 and 80°C is known to be due to the balance between the opposing effects of decreasing oxygen solubility and an increase in oxygen diffusivity coupled with a decrease in viscosity with increasing temperatures [103, 157]. At 90°C the decrease in dissolved oxygen concentration [108] becomes more important than the other two effects that increase the oxygen transport rate, resulting in a net decrease in the oxygen flux to the iron surface and thus a decrease in the corrosion rate (seen as an increase in R_p).

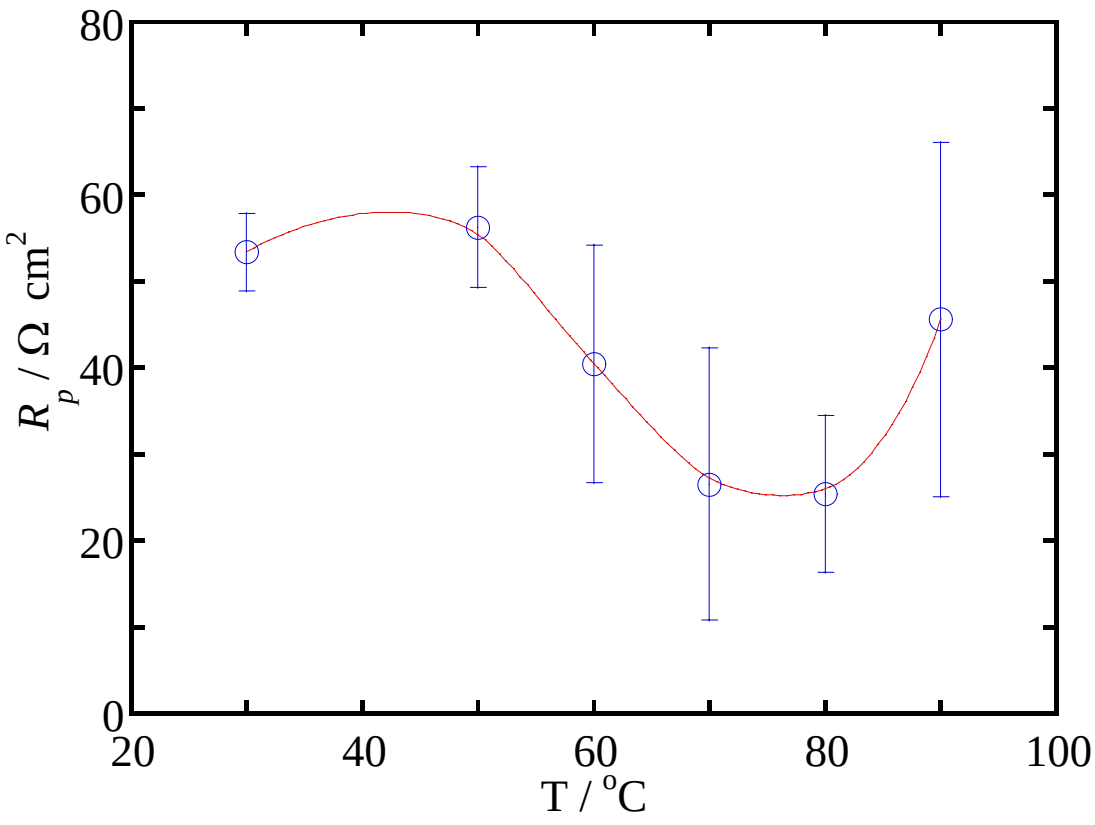

Figure 5.10 Polarisation resistance (R_p) (from LP and EIS, 50 minutes after immersion) for an iron rotating disc electrode (1000 rpm) in air-saturated 0.2 M NH_4Cl as a function of temperature. The error bars indicate twice the standard error in the mean.

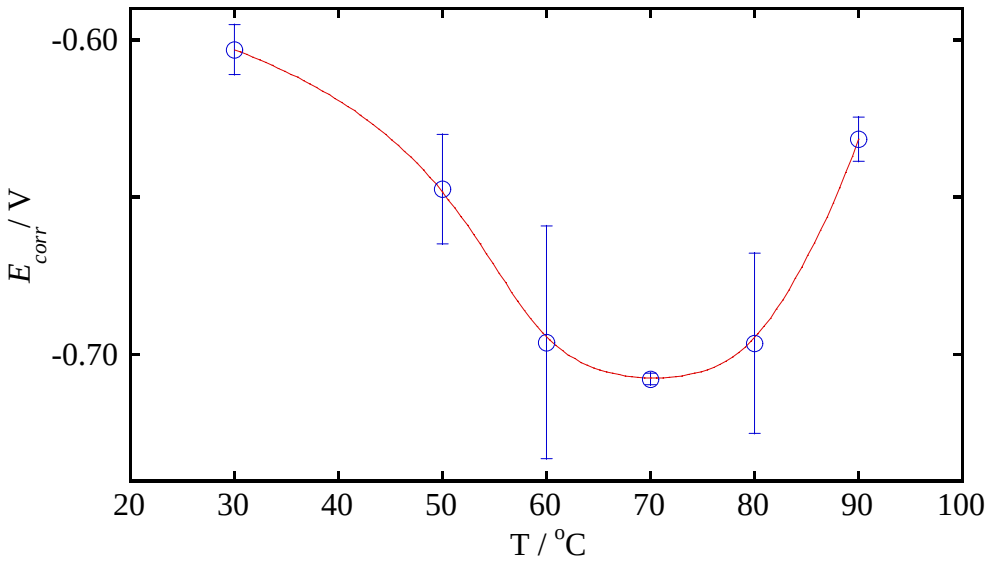

Figure 5.11 Corrosion potential (E_{corr}) for an iron rotating disc electrode (1000 rpm) in air-saturated 0.2 M NH_4Cl as a function of temperature. The error bars indicate twice the standard error in the mean.

At all temperatures only uniform corrosion was observed. Above 50°C, corrosion products were not observed on the electrode surface, which is most likely to be a result of higher Fe^{3+} solubility with increasing temperature [38].

Figure 5.12 shows the potentiodynamic polarisation curves for an iron rotating disc electrode in air-saturated 0.2 M NH_4Cl between 30 and 90°C. The anodic current density increased significantly with temperature up to 80°C but decreased at 90°C. In Section 3.3.3 it was shown that iron prepassive dissolution at -0.58 V (3M KCl Ag/AgCl) is activation controlled up to 150°C in deaerated 0.2 M NH_4Cl. Between 30 and 90°C the pH decreased (approximately linearly) by about one pH unit which agrees with the pH change calculated for 0.001 molal NH_4Cl over a similar temperature range [88]. The disappearance of the passivation peak above 50°C shows that the solubility of Fe^{3+} most probably does increase, preventing anodic film formation and passivation.

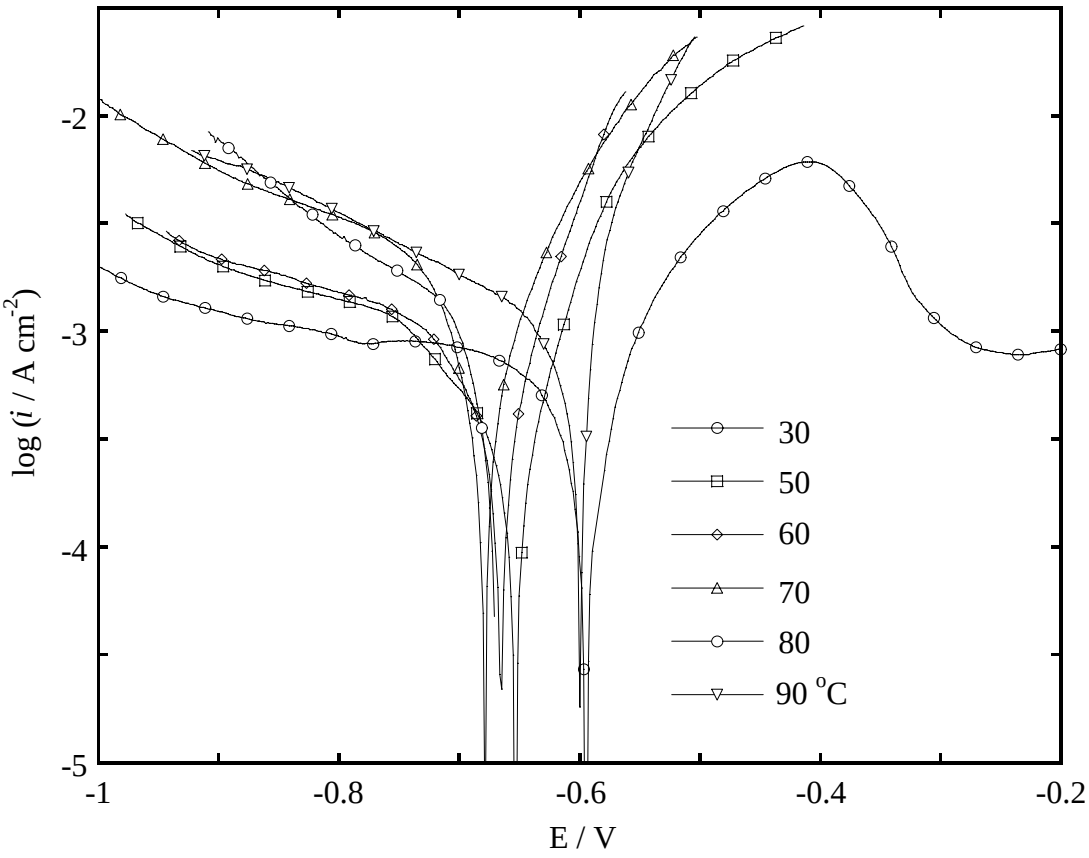

Figure 5.12 Polarisation curves for an iron rotating disc electrode (1000 rpm) in air-saturated 0.2 M NH_4Cl at various temperatures at 10 mV s^{-1}. 75 minutes after immersion.

The oxygen reduction current density increased between 30 and 50°C; however only a slight increase was observed after further increasing the temperature to 60°C. Between 60 and 70°C the current density increased by almost an order of magnitude. However little change was observed between 70 and 90°C. The polarisation curves in Figure 5.12 exhibit the same dependence of the corrosion potential with temperature as shown in Figure 5.11, which indicates that the large potential polarisation did not significantly perturb the corrosion behaviour of the system.

5.3.1.4 The effect of electrode rotation speed

Figure 5.13 shows R_p values for an iron disc electrode in air-saturated 0.2 M NH_4Cl as a function of electrode rotation speed. Between 0 and 500 rpm R_p decreased sharply and then decreased at a slower rate up to 2000 rpm. This result clearly shows the corrosion rate is oxygen diffusion controlled.

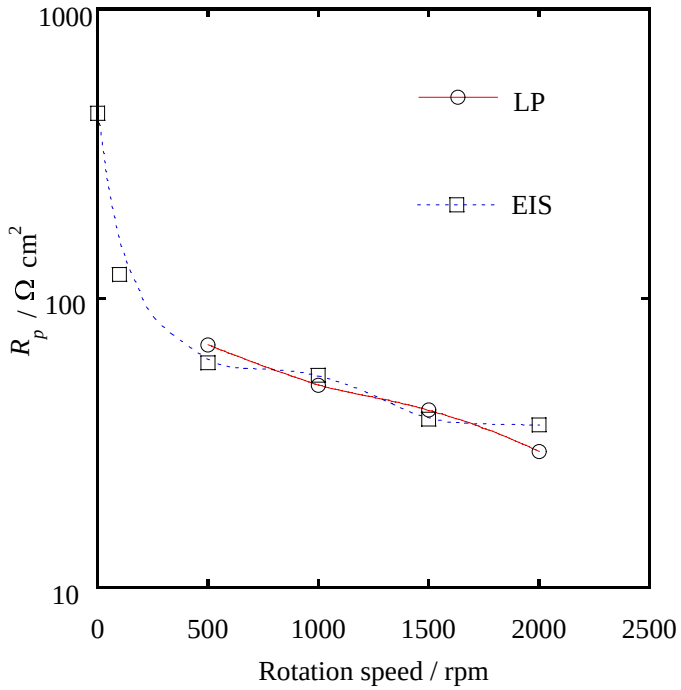

Figure 5.13 Polarisation resistance (R_p) for an iron disc electrode in air-saturated 0.2 M NH_4Cl (from LP and EIS) as a function of electrode rotation speed. T = 30.0°C.

Good agreement between R_p values from EIS and LP measurements was obtained. As the rotation speed was increased, it was observed the γ-FeOOH film became more adherent and compact. A similar observation was made by Yang *et al.* [152]. Beneath the corrosion product film the iron surface appeared finely etched and uniformly corroded.

Figure 5.14 and Figure 5.15 show the Nyquist and Bode Z' plots respectively for iron at various electrode rotation speeds. The markers are the experimental data points while the solid line is the calculated impedance response [158]. At most rotation speeds the experimental impedance response was adequately modelled using the simple equivalent circuit shown in Figure 5.1; however, the impedance response at 0 rpm was more accurately modelled using the equivalent circuit shown in Figure 5.4 which incorporates the Warburg diffusion resistance element, *W*. As discussed in Section 5.1.2.4, a tail in the Nyquist plot at low frequencies is indicative of (semi-infinite) diffusion control. It is therefore surprising that even in stagnant solution, a perfect diffusion tail at 45° to the x-axis was not observed. Instead the tail is bent down towards the x-axis. After 2 hours immersion the distortion increased and the tail eventually reached the x-axis. This is most probably due to the influence of the thickening γ-FeOOH film.

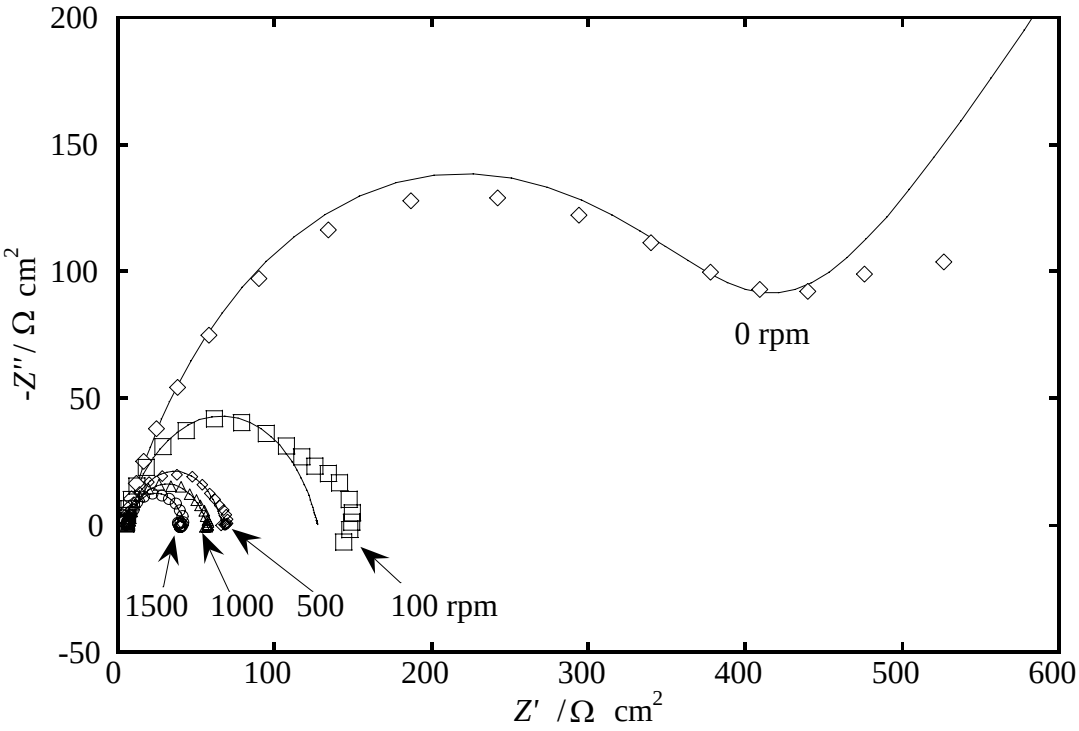

Figure 5.14 Experimental (hollow markers) and calculated (———) Nyquist plots for iron in air-saturated 0.2 M NH_4Cl at various electrode rotation speeds. T = 30.0°C.

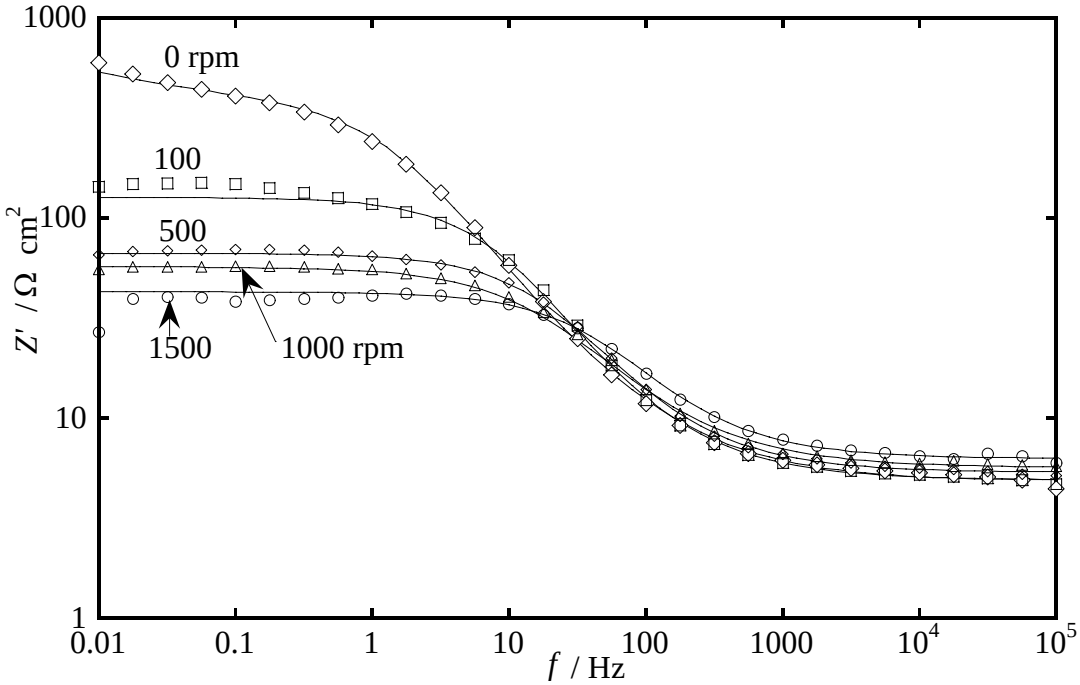

Figure 5.15 Experimental (hollow markers) and calculated (———) Bode Z′ plots for iron in air-saturated 0.2 M NH_4Cl at various electrode rotation speeds. T = 30.0°C.

Table 5.5 lists the equivalent circuit parameters extracted from the Nyquist plots in Figure 5.14. The double layer capacitance remained relatively static between 370 and 640 μF cm^{-2}. The depression angle (calculated using α and equation (5.9)) also did not show any systematic dependence upon the electrode rotation speed. Changes in the depression angle would only be expected if there were significant changes in the morphology of the surface such as during pitting corrosion [142]. The Warburg resistance at 0 rpm is 53 Ω cm^2. This value would be included in the resistance from a LP measurement under the same conditions, and would result in an underestimation of the corrosion rate by about 12%.

Rotation speed / rpm	R_p / Ω cm^2	W / Ω cm^2	C_{dl} / μF cm^{-2}	α *(dimensionless)*	Depression angle / °
0	398	53	450	0.747	22.8
100	123	0	368	0.779	19.9
500	62	0	407	0.767	21.0
1000	52	0	640	0.717	25.5
1500	37	0	376	0.761	21.5

Table 5.5 Fitted equivalent circuit parameters for the EIS data in Figure 5.14.

Figure 5.16 shows the potentiodynamic polarisation curve for an iron electrode at three different rotation speeds. The oxygen reduction current density increased with increasing electrode rotation speed while the anodic current density near the corrosion potential did not change significantly. However, at more anodic potentials, the current density increased slightly with increasing electrode rotation speed.

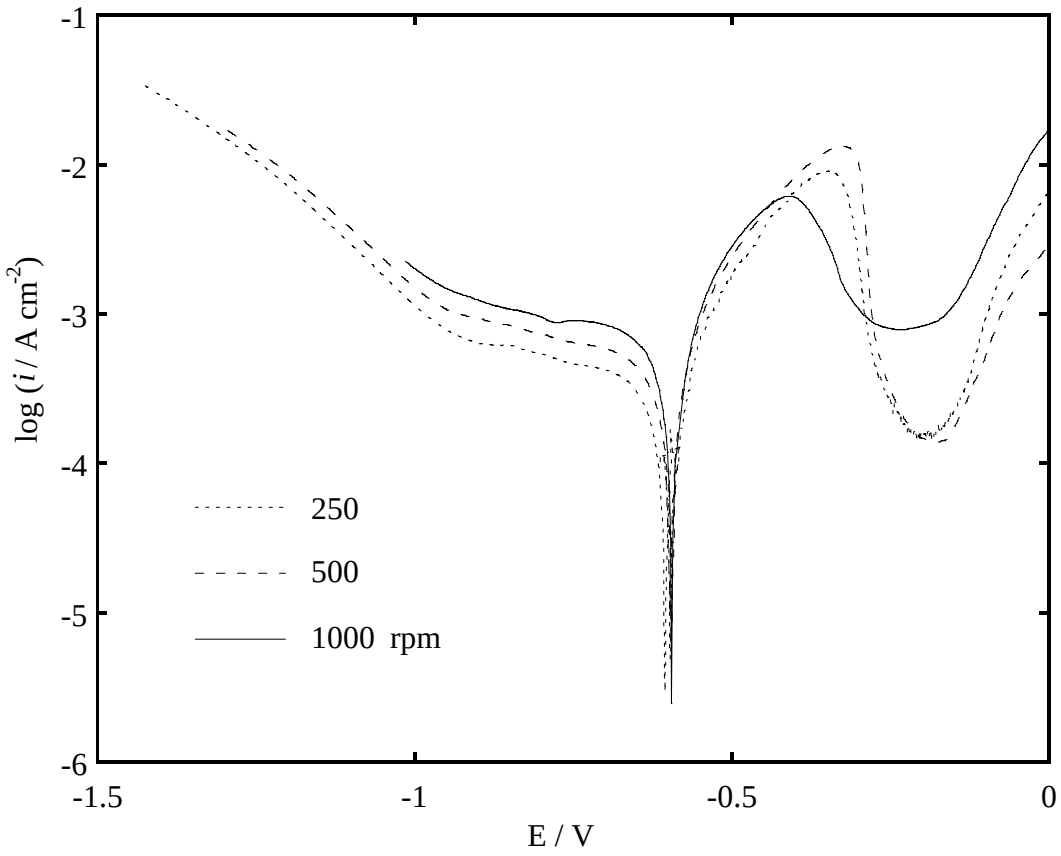

Figure 5.16 Potentiodynamic polarisation curves for iron in air-saturated 0.2 M NH_4Cl at different electrode rotation speeds. Scan rate = 1 mV s^{-1}. T = 28°C.

5.3.1.5 The effect of electrolyte composition

In this section the corrosion behaviour of iron in $NaClO_4$, NaCl and NH_4ClO_4 will be investigated and compared with NH_4Cl. The electrolytes were chosen in an attempt to isolate the influence of ammonium and chloride ions on iron corrosion. $NaClO_4$ was chosen since the perchlorate anion does not complex with cations and provides a good baseline for comparison with other electrolytes. NaCl was chosen to show the effect of chloride. Finally, NH_4ClO_4 was chosen to show the effect of ammonium ion.

Table 5.6 lists R_p values for an iron rotating disc electrode in all of the air-saturated electrolyte solutions investigated. The polarisation resistances for iron in NH_4ClO_4 and NH_4Cl were the same within experimental error. However the corrosion potential for iron in NH_4ClO_4 was about 40 mV more negative than in NH_4Cl. Uniform corrosion was observed in both of these electrolytes. In NaCl solution, pitting corrosion was observed and the polarisation resistance was slightly, but significantly higher than in NH_4Cl. In $NaClO_4$ solution, iron did not appear corroded at all; R_p was very high and the corrosion potential was also very positive compared with iron in the other electrolytes.

Electrolyte	R_p / Ω cm^2	E_{corr} / V
NH_4Cl	53 ± 4.5	-0.603 ± 0.008
NH_4ClO_4	54	-0.648
NaCl	65	-0.518
$NaClO_4$	594	-0.422

Table 5.6 Polarisation resistance (R_p) and corrosion potential (E_{corr}) for an iron rotating disc electrode (1000 rpm) in various 0.2 M electrolytes 50 minutes after immersion. T = 30.0°C except for NaCl, T = 28.7°C.

Figure 5.17 shows the potentiodynamic polarisation curves for an iron rotating disc electrode in each of the four different electrolyte solutions. The oxygen diffusion limited current (i_l) is the same in all solutions, indicating that the oxygen solubility is not

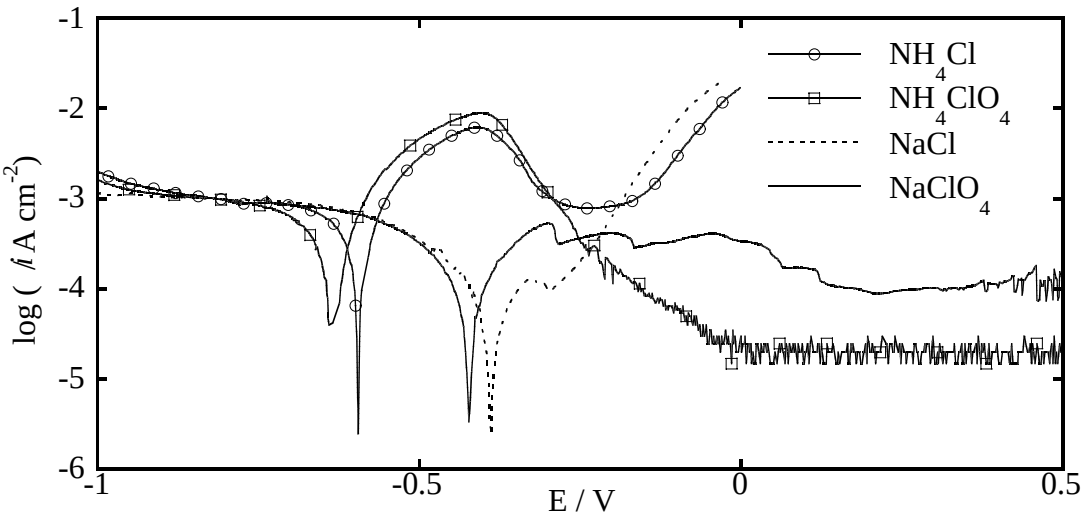

Figure 5.17 Potentiodynamic polarisation curves for an iron rotating disc electrode (1000 rpm) in air-saturated 0.2 M solutions of various electrolytes. T = 30.0°C. Scan rate = 1 mV s^{-1}.

affected by the compositions of the solutions. Since NH_4Cl and NH_4ClO_4 solutions are more acidic than the other two electrolytes (pH 5.0 compared with pH 6.5) this also confirms that oxygen reduction is not affected by the pH with this pH range. However the higher current densities below -0.9 V in the more acidic ammonium electrolyte solutions are consistent with the predominance of hydrogen evolution at negative potentials.

In ammonium electrolytes, intense active dissolution was observed, while in the sodium electrolytes the anodic current density was much smaller. This difference cannot be explained by the difference in pH between the two sets of solutions since it was shown in Section 3.3.2 that, between pH 4.0 and pH 7.0, the prepassive current density for iron in 0.2 M NH_4Cl was constant.

In both pairs of electrolyte solutions (ammonium and sodium) the anodic current density near the corrosion potential was lower in the chloride containing electrolyte. This shows that 0.2 M chloride does inhibit the anodic dissolution of iron to a small but significant extent. However above -0.2 V the anodic current density is much higher in the chloride electrolytes due to pitting dissolution, while in the perchlorate electrolytes iron was passive.

These results may be interpreted as follows.

In NH_4Cl and NH_4ClO_4 solutions the air-formed film is removed shortly after immersion. In NaCl and $NaClO_4$ solutions, the air-formed passive film is stable, resulting in the extremely low anodic current densities near the corrosion potential in Figure 5.17. The positive corrosion potential and high polarisation resistance for iron in $NaClO_4$ is consistent with the presence of a coherent passive film. In NaCl solution the corrosion potential was more negative than in $NaClO_4$ because of the chloride-induced localised active corrosion within pits, despite most of the surface being passive.

The instability of the air-formed film in the ammonium electrolytes cannot simply be due to the greater acidity of these electrolytes compared with the sodium electrolytes. The critical piece of evidence supporting this assertion is that the corrosion potential is constant at around -0.61 V between pH 4.0 and 7.0 which proves that the air-formed film was removed from iron even at pH 7.0 which is consistent with the observation for iron in deaerated solution (Section 3.3.2). This shows that ammonium ion has a unique ability to de-stabilise and remove that air-formed passive film on iron. Unfortunately the nature of this unique ability of ammonium ion cannot be determined from these experiments.

5.3.1.6 The effect of anodic and cathodic polarisation

The electrochemical behaviour of polarised passive and active iron electrodes has been previously investigated using EIS in deaerated solutions of various electrolytes [89, 144, 159] however studies in aerated solution have received less attention. Bonnel *et al.* measured impedance spectra for anodically and cathodically polarised carbon steel

electrodes in air-saturated 3% NaCl [98]. The aim of the present investigation is to use EIS to investigate the effect of small anodic and cathodic overpotentials on the corrosion behaviour of an iron rotating disc electrode in air-saturated 0.2 M NH_4Cl.

Figure 5.18 shows the Nyquist plot for an iron rotating disc electrode in air-saturated 0.2 M NH_4Cl at different anodic and cathodic overpotentials. The markers are the experimental data points while the solid line is the calculated impedance response [158]. The simple equivalent circuit shown in Figure 5.1 was used to calculate the impedance response. Table 5.7 lists the equivalent circuit parameters from the calculated data.

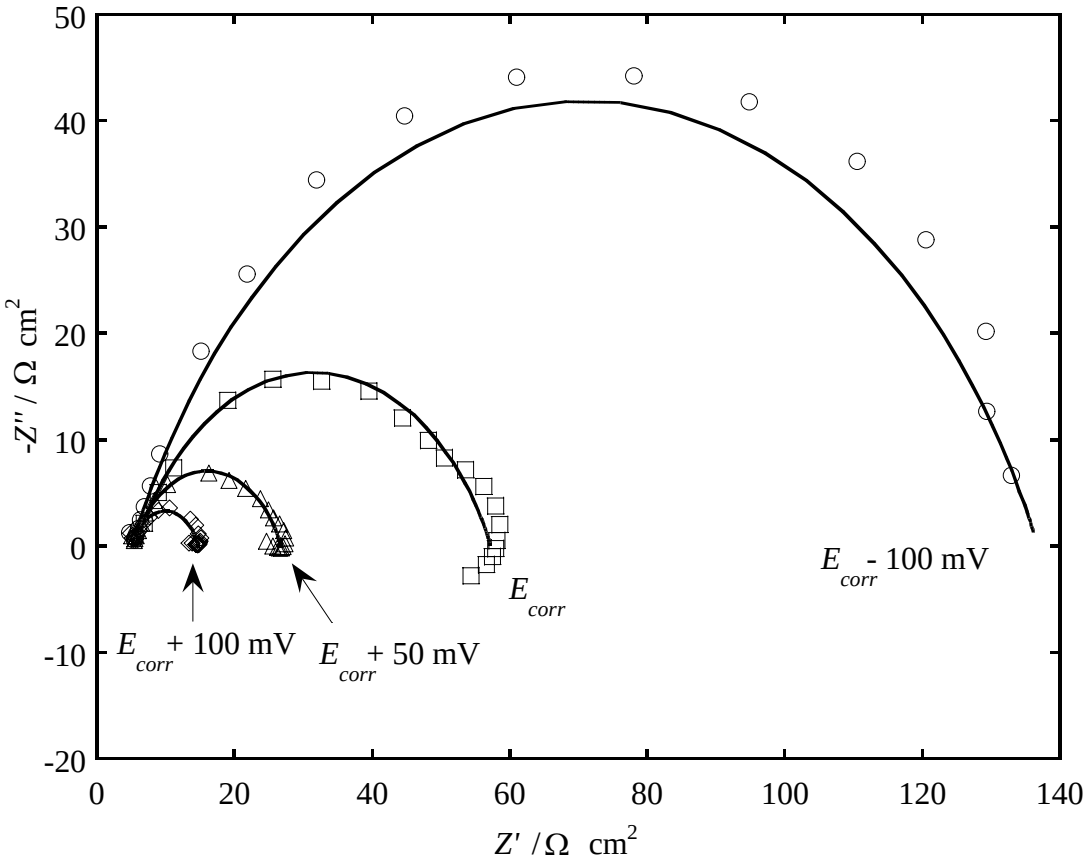

Figure 5.18 Experimental (hollow markers) and calculated (———) Nyquist EIS plots for an iron rotating disc electrode (1000 rpm) in air-saturated 0.2 M NH_4Cl at various overpotentials with respect to the corrosion potential (E_{corr}). T = 30.0°C. 30 minutes after immersion.

η / mV	R_p / Ω cm^2	C_{dl} / μF cm^{-2}	α (dimensionless)	Depression angle / °
-100	132	670	0.721	25.1
0	51	639	0.717	25.5
50	22	638	0.727	24.5
100	10	401	0.761	21.5

Table 5.7 Equivalent circuit parameters for iron at various overpotentials with respect to E_{corr}, from Figure 5.18. 30 minutes after immersion.

Figure 5.18 and Table 5.7 show that the polarisation resistance (R_p) decreased with increasing anodic overpotentials and increased at negative overpotentials. This indicates that the impedance of the corroding iron system is dominated by the charge transfer controlled iron oxidation. Park and Macdonald concluded that the corrosion rate for carbon steel in high temperature salt solutions was anodically controlled because it was observed that the corrosion rate increased after the application of a 30 mV anodic overpotential [160].

The application of anodic overpotentials accelerated the corrosion rate of iron in NH_4Cl solution. Not surprisingly, it was observed that the γ-FeOOH film was thicker on the electrode anodically polarised at 100 mV compared with the electrode polarised at only 50 mV. The thicker γ-FeOOH film at higher overpotentials started to impede the corrosion reaction since R_p increased from 10 to 30 Ω cm^2 between 30 and 60 minutes after immersion. Microscopic inspection of the electrode after the experiment revealed that it was roughened and that grain boundaries appeared to be preferentially oxidised.

The iron electrode polarised at -100 mV appeared bright and shiny, even after 60 minutes immersion, indicating that it was cathodically protected.

5.3.2 Corrosion of pure iron at elevated oxygen partial pressures in 0.2 M NH_4Cl.

5.3.2.1 The effect of oxygen partial pressure

Figure 5.19 shows the polarisation resistance (R_p) for an iron rotating disc electrode as a function of oxygen partial pressure in 0.2 M NH_4Cl at 30°C. R_p decreased sharply between 21 and 101 kPa and was then constant up to 300 kPa. Since iron corrosion is diffusion controlled, the corrosion rate should be directly proportional to the dissolved oxygen concentration which itself is proportional to the oxygen partial pressure. Obviously the corrosion rate is being inhibited. For example, the sharp drop in R_p

between 21 and 101 kPa is equal to a 3.5-fold increase in the corrosion rate which is only 70% of the increase in oxygen partial pressure. Laque and Hobson reported a 4.2-fold increase in the corrosion rate for iron between 21 and 101 kPa in 3% NaCl (Table 5.4).

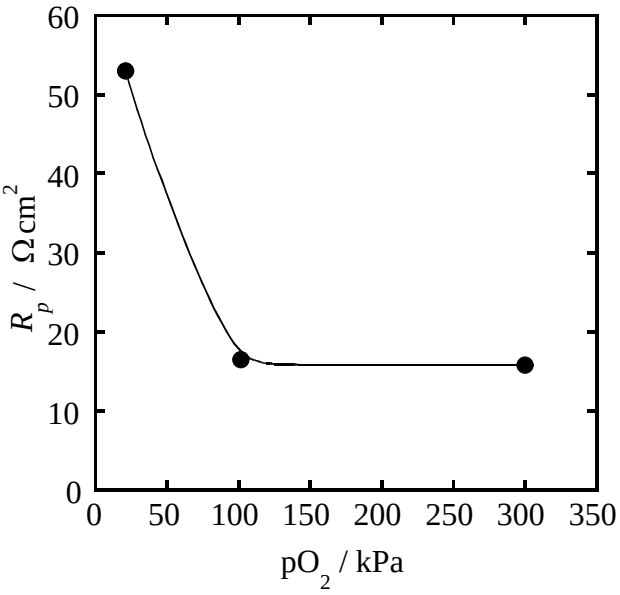

Figure 5.19 Polarisation resistance (R_p) for an iron rotating disc electrode (1000 rpm) in 0.2 M NH_4Cl as a function oxygen partial pressure. 60 minutes immersion. T = 30°C

Microscopic inspection of the electrode surface after the 300 kPa experiment revealed that the iron surface was covered by a porous γ-FeOOH film. To the naked eye however, the oxide appeared light brown indicating the γ-FeOOH particle size was in the order of 0.2 μm diameter compared with 1-2 μm for the yellow-orange γ-FeOOH film that forms at atmospheric pressure [161]. The decrease in oxide particle size with increasing pressure indicates that the γ-FeOOH precipitation rate also increased as a result of higher oxygen concentration as the oxygen partial pressure was increased [161]. It is most likely that the decrease in the γ-FeOOH particle size results in a more tightly packed protective layer that inhibits iron corrosion more effectively with increasing oxygen partial pressure.

Figure 5.20 shows the polarisation resistance (R_p) for an iron rotating disc electrode in 0.2 M NH_4Cl with 300 kPa oxygen partial pressure as a function of immersion time. Over a 1 hour period R_p increased from 8 to 18 Ω cm^2 which means that the corrosion rate decreased by a factor of 2. The increase in R_p reflects the growth of the γ-FeOOH film that inhibits the corrosion reaction. Areas of the electrode that were not

covered by oxide had a finely etched appearance while areas beneath the porous γ-FeOOH film were bright and severely corroded. This behaviour is indicative of the formation of aeration cells beneath the corrosion product film resulting in localised corrosion [147].

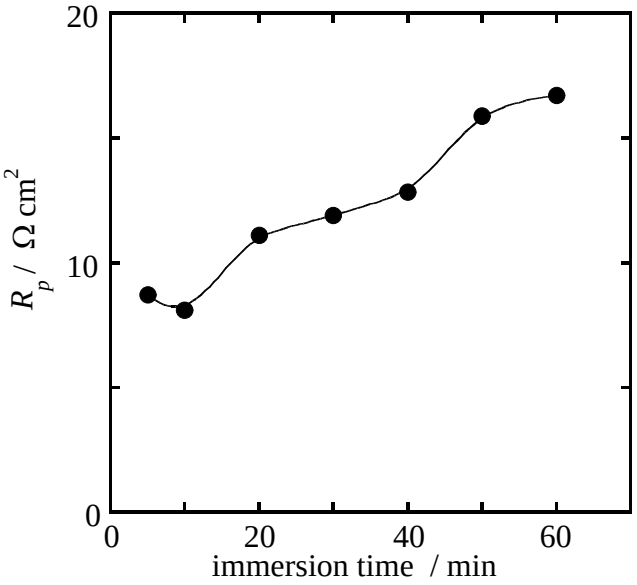

Figure 5.20 Polarisation resistance (R_p) for an iron rotating disc electrode (1000 rpm) in 0.2 M NH_4Cl as a function of immersion time at 300 kPa oxygen partial pressure. T = 30°C.

5.3.2.2 The effect of temperature at 300 kPa oxygen partial pressure

Figure 5.21 shows the polarisation resistance (R_p) for an iron rotating disc electrode as a function of temperature at 300 kPa oxygen partial pressure. R_p decreased quickly between 30 and 80°C and then remained constant up to 150°C. This corresponds to a 4-fold increase in the corrosion rate. Corrosion products were not observed on the surface above 50°C. This indicates the observed increase in the corrosion rate between 30 and 80°C is most likely a result of increases in Fe^{3+} solubility at elevated temperatures [38].

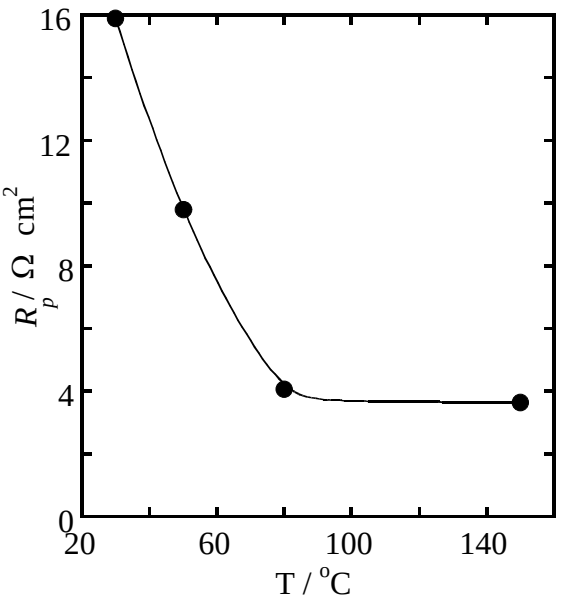

Figure 5.21 Polarisation resistance (R_p) for an rotating iron disc electrode (1000 rpm) in 0.2 M NH_4Cl as a function of temperature at 300 kPa oxygen partial pressure. T = 30°C.

5.4 CONCLUSIONS

The effects of immersion time, pH, temperature, electrode rotation speed, electrolyte composition, polarisation and oxygen partial pressure on the corrosion of iron have been investigated.

For an iron rotating disc electrode (1000 rpm) in air-saturated 0.2 M NH_4Cl at 30.0°C:

(i) an air-formed oxide film initially inhibits iron corrosion; however after approximately 30 minutes it is removed resulting in the maximum corrosion current of 0.84 ± 0.7 mA cm^{-2}

(ii) iron corrodes uniformly with the continual slow build up of a porous γ-FeOOH film which only inhibits the corrosion rate after more than 3 hours immersion

(iii) between pH 4.8 and 7 only uniform corrosion was observed. Between pH 7.5 and 8 localised breakdown of the film occurs leading to pitting corrosion

(iv) iron corrosion is oxygen diffusion limited

Other important conclusions include:

(v) a maximum corrosion current density of 1.8 mA cm^{-2} was observed in air-saturated solution at 80°C

(vi) ammonium ion was shown to be particularly efficient compared with sodium ion in removing the air-formed film, however the reason for this is still not understood

(vii) chloride inhibits the active dissolution of iron to a small extent. However, the corrosion rates in NH_4Cl and NH_4ClO_4 were still found to be identical within experimental error

(viii) a 3.3-fold increase in the corrosion rate was observed after increasing the oxygen partial pressure from 21 to 101 kPa at 30°C

(ix) fast γ-FeOOH precipitation at high oxygen partial pressure results in no change in the corrosion rate between 101 and 300 kPa oxygen partial pressure

6 The Electrochemistry of Reduced Ilmenite

6.1 INTRODUCTION

Reduced ilmenite is a unique mineral intermediate consisting of a heterogeneous agglomeration of a poorly conducting titanium oxide phase and a conducting metallic iron phase. Generally, in order to electrochemically characterise materials, they must be electrically conducting. However, reduced ilmenite pressed electrodes made at the beginning of this investigation had a very high resistance, which precluded their use as electrodes. Fortunately, the carbon paste electrode technique allows the electrochemistry of both conducting and poorly conducting minerals to be investigated [162].

The reduced ilmenite carbon paste electrode was used to study the mixed potential behaviour of the electrode in air-saturated ammonium chloride solutions as a function of electrode rotation speed [21] and as a function of the degree of metallisation of reduced ilmenite [23]. However, since the polarisation behaviour of this electrode has not been investigated, it was decided that a detailed study would be carried out.

This Chapter reports on a series of carbon paste electrode experiments of not only reduced ilmenite, but also of related systems including:

a) aqueous Fe^{II}/Fe^{III}
b) iron oxides
c) iron powder

The aim of this work is to investigate the factors influencing the anodic dissolution of iron from reduced ilmenite. This chapter is largely based on a previous publication [163].

6.1.1 Composition and morphology of reduced ilmenite

Ilmenite can be nominally regarded as $FeTiO_3$ [39]: where the TiO_3^{2-} anion is associated with Fe^{2+}. However natural ilmenite is often modified in a variety of ways. First, replacement of Fe^{2+} by Mn^{2+} and Mg^{2+} occurs frequently. Second, through weathering

ilmenite can undergo alteration where Fe^{2+} is oxidised to Fe^{3+}, which can then be leached out of the grain. Complete removal of iron in this way results in the formation of an amorphous material with a composition close to TiO_2 which is referred to as Leucoxene [164]. Partial weathering – which is common – results in an ilmenite grain of heterogeneous composition and structure. This is ultimately one factor that affects the composition and morphology of reduced ilmenite that in turn may affect its aeration characteristics.

The morphology of reduced ilmenite has been previously reported in the literature [164] and elsewhere [22] and is briefly summarised here. The formation of metallic iron during ilmenite reduction results in an increase in the specific gravity and the formation of numerous tiny voids within the titanium oxide matrix. In addition, cracks and fissures can occur throughout the grain. Iron morphology is quite strongly influenced by the temperature. For example at 1000°C iron tends to form along weathered regions of unaltered ilmenite while above 1000°C iron usually occurs as small globules distributed throughout the grain. At 1100°C the iron globules coalesce and tend to aggregate near the grain surface.

No data could be found in the literature to accurately describe the composition of metallic iron in reduced ilmenite; it is normally assumed to be pure. However at temperatures between 1000 and 1100°C, carbon has a small but finite solubility in iron: the main phase in the low carbon range (< 1% C) is austenite. When this material cools slowly, ferrite forms at the grain boundaries and, for higher carbon levels, pearlite forms (a mixture of cementite (Fe_3C) and ferrite) [165]. This may be an important factor affecting reduced ilmenite aeration since it is known that low levels of carbon can have a significant effect on the iron corrosion rate [166].

Reduced rutiles (Ti_nO_{2n-1} $n \geq 4$) also form during ilmenite reduction [167]. This is a problem for the Becher Process since Fe^{2+} incorporated into these phases cannot be removed by aeration.

6.2 EXPERIMENTAL

6.2.1 Electrodes

The carbon paste was tightly packed into a carbon paste holder electrode, which was equipped with a screw piston (length = 8-13 mm, diameter = 6.10 mm). The surface was smoothed and excess material removed using a sharp steel blade. The resistance of the paste was always less than 10 Ω.

6.2.1.1 Preparation of carbon pastes

Reduced ilmenite carbon paste was made by mixing a 1:4 weight ratio of reduced ilmenite (-600 μm magnetic fraction, local industrial source) and nujol carbon paste (2:1 graphite:nujol by weight; "ultracarbon" graphite, Ultra Carbon Corporation, Michigan USA). Preliminary tests were also conducted with 1:1 and 4:1 weight ratios using reduced ilmenite. In addition, single grains of reduced ilmenite were embedded into the surface of a carbon paste electrode by simply placing the grain on the paste surface then passing a sharp steel blade over it.

Iron oxide carbon paste was prepared by mixing iron oxide and carbon paste in a 1:19 weight ratio. Haematite iron ore was used as supplied (Mano-River haematite). Oxides containing mainly lepidocrocite and magnetite (as determined by X-ray diffraction analysis) were obtained from laboratory scale Becher process aeration of reduced ilmenite performed at different temperatures.

Iron powder from two sources was used (Koch Light, LR and Johnson Matthey, Puratronic) to prepare iron powder carbon paste. This was prepared by mixing iron powder with carbon paste in the following weight ratios: 1:80, 1:15 and 1:8. Iron powder-“additive” carbon paste was prepared by mixing the constituents in the following weight proportions: 0.104 g iron powder, 0.296 g “additive” and 1.6 g carbon paste. Additives used included: (a) Synthetic rutile; one was obtained from a laboratory scale Becher process aeration that was leached with dilute sulfuric acid, washed and dried and the second was an untreated synthetic rutile from a local industrial source (b) Natural rutile (Local industrial source) (c) TiO_2 pigment (from the chloride process, local industrial source) (d) Alumina (BDH Al_2O_3, AR grade). X-ray diffraction patterns and chemical compositions of selected materials used here can be found in Appendix A and Appendix B respectively. The 1:15 iron powder, and iron powder-“additive” paste

mixtures have the same weight proportion of iron as a 1:4 reduced ilmenite carbon paste, assuming the reduced ilmenite contains 26% metallic iron by weight.

6.2.2 Equipment

The electrochemical system has been described Chapter 2.

X-ray powder diffraction patterns were measured using Cuk_α radiation on a Siemens Model DACO-MP instrument. Patterns were recorded with 0.04°θ step size.

A Cambo still camera using Polaroid high contrast landscape film was used to measure contact angles of 0.2 M NH_4Cl solution on the carbon pastes using the sessile drop technique. Drops were formed using a capillary tube fed by a microsyringe that was controlled by a vernier.

All potentials are reported against 3 M KCl Ag/AgCl (E = 0.208 V *vs. she*).

6.2.3 Solutions

The electrolyte solutions were purged of oxygen by bubbling humidified N_2 for 30 minutes prior to immersion of the electrode. Approximately 1 mM ferrous solution and Fe(III) hydroxide-oxide sols [168] were made by adding appropriate amounts of solid $FeCl_2.4H_2O$ (BDH, AR grade) and $FeCl_3$ (BDH, LR grade) respectively to the above cell containing about 60 ml of deaerated electrolyte. The Fe(III) hydroxide-oxide sol was clear and orange in colour. The presence of colloidal particles was confirmed by filtering through a 0.22 μm membrane filter (Millipore) which removed most of the colour from the solution and left a smooth orange coloured deposit on the membrane.

6.3 RESULTS AND DISCUSSION

6.3.1 The Fe^{3+}/Fe^{2+} couple

It was considered important to investigate the electrochemistry of Fe^{2+} and Fe^{3+} using a carbon paste electrode since these species will likely be produced during iron oxidation from reduced ilmenite.

The cyclic voltammogram for Fe^{2+} in NH_4Cl solution with a carbon paste electrode is shown in Figure 6.1. The open circuit potential for this system was very stable and reproducible at 0.397 V. For a stationary electrode, the oxidation peak I which was observed at 1.01 V ($I_{pI} = 1.1 \times 10^{-4}$ A cm^{-2}) corresponds to the oxidation of Fe^{2+}. On

the following cathodic scan a reduction peak (II) was observed at 0.01 V (I_{pII} = 3.45 × 10^{-5} A cm^{-2}) and corresponds to the reduction of Fe^{3+} generated at peak I. A smaller reduction peak was still observed at 0.01 V before any oxidation occurred at I, which indicates that the $FeCl_2$ used to make the solution was contaminated with some Fe^{3+}.

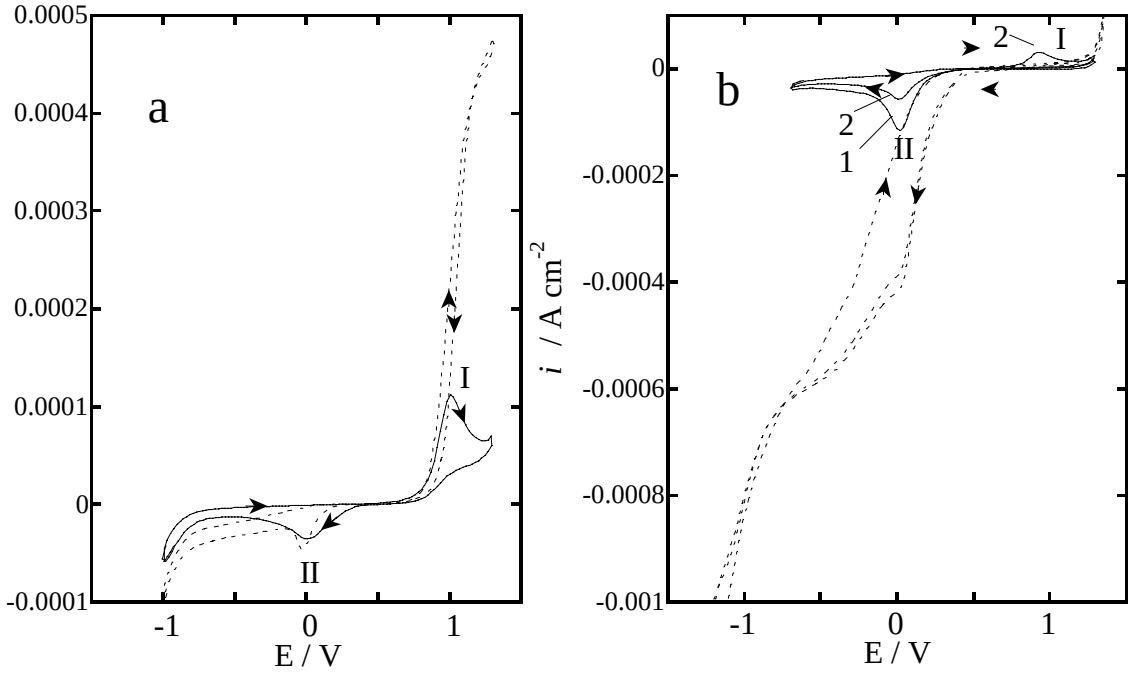

Figure 6.1 Cyclic voltammograms for (a) 1mM Fe^{2+} and (b) FeOOH sol (1 mM Fe^{3+}) in 0.2 M NH_4Cl solution with a stationary (———) and rotating (1000 rpm, ---------) carbon paste disc electrode at 50mV s^{-1}. Cycle number indicated. T = 30°C.

For a rotating electrode in Figure 6.1a, the anodic current density at 1.01 V (I) was much larger due to the constant supply of Fe^{2+} from the bulk solution. Interestingly however, the reduction peak (II) at 0.01 V was still observed on the reverse cathodic scan. This indicates that some of the Fe^{3+} generated at peak I precipitated as a solid film that adhered to the electrode surface. It is quite likely that the solid is γ-FeOOH since it also the product of iron corrosion in this solution at 30°C (Section 5.3.1.1). Formaro [169] and Ohtsuka *et al.* [170] found that oxidation of Fe^{2+} using gold electrodes in near neutral solutions occurred between -0.3 and 0 V. The precipitated film consisted of γ-FeOOH and amorphous FeOOH and was reduced at a potential 0.3 V cathodic to the oxidation. In this case the peak separation is 1.0 V, which is typical of the slow kinetics observed at carbon paste electrodes [171].

The height of peak II was approximately the same regardless of the amount of Fe^{2+} oxidised at I. This means only a limited amount of the FeOOH can be adsorbed onto the electrode surface (and the remainder was lost to the bulk solution) or only a fixed amount can be reduced at peak II. Both peaks I and II displayed an $I_p \propto \upsilon^{0.5}$ and peak $E_p \propto \log \upsilon$ relationship which is indicative of a fully irreversible electron transfer reaction [113].

The cyclic voltammogram for a FeOOH sol in deaerated NH_4Cl solution using a stationary and rotating carbon paste disc electrode is shown in Figure 6.1b. On the first anodic scan with a stationary electrode the anodic current density was very low indicating that the $FeCl_3$ used contained little contaminating Fe^{2+}. On the reverse cathodic scan a reduction peak (II) was observed at 0.17 V ($I_{pII} = -1.1 \times 10^{-3}$ A cm^{-2}) and must correspond to the reduction of FeOOH sol to Fe^{2+}. On the following anodic scan the cathodically generated Fe^{2+} is oxidised at 0.93 V (peak I). As shown in Figure 6.1b, an oxidation peak (I) was not observed at 0.97 V when the electrode was rotated which means that the electrochemically generated Fe^{2+} is soluble. At 1000 rpm the FeOOH sol reduction current density initially increased quickly as the potential was made more negative but then increased at a slower rate below 0 V. This shows that FeOOH is under mixed activation and diffusion control or perhaps cathodically formed Fe^{2+} hinders further reduction.

From the above observations we can conclude:

a) both anodically and chemically (oxide-sol) formed FeOOH were reduced to aqueous Fe^{2+} at about 0.00 V
b) aqueous Fe^{2+} was oxidised between -0.90 and 1.01 V precipitating FeOOH on the electrode surface

6.3.2 The iron oxide carbon paste electrode

In this section the electrochemistry of haematite, lepidocrocite and magnetite in NH_4Cl solution is studied using cyclic voltammetry with a carbon paste electrode. The electrochemistry for iron oxide carbon paste mixtures using acidic conducting binders has been reported previously with the aim of developing analytical techniques for the quantitative determination of oxide stoichiometry [172-176]. The use of an acidic conducting binder not only resulted in electron transfer occurring throughout the paste (rather than just at the paste/electrolyte interface) but also resulted in the oxide dissolving within the paste. Thus the previous studies have only limited relevance to this work

where a non-conducting binder was used. White *et. al.* [83] investigated the electrochemistry of solid magnetite electrodes.

The open circuit potential for haematite, lepidocrocite and magnetite carbon paste electrodes drifted erratically between 0.1 and 0.4 V. A stable and reproducible open circuit potential was not reached. This is undoubtedly a result of not having finite concentrations of Fe^{2+} and Fe^{3+} ions in solution. For this reason the voltammograms were measured by scanning the potential in the anodic or cathodic direction from an initial bias potential of 0.00 V.

The cyclic voltammogram of lepidocrocite in 0.2 M NH_4Cl is shown in Figure 6.2. Cyclic voltammograms for haematite and magnetite exhibited similar electrochemical features. The reduction (I) between -0.8 and -1.3 V probably involves

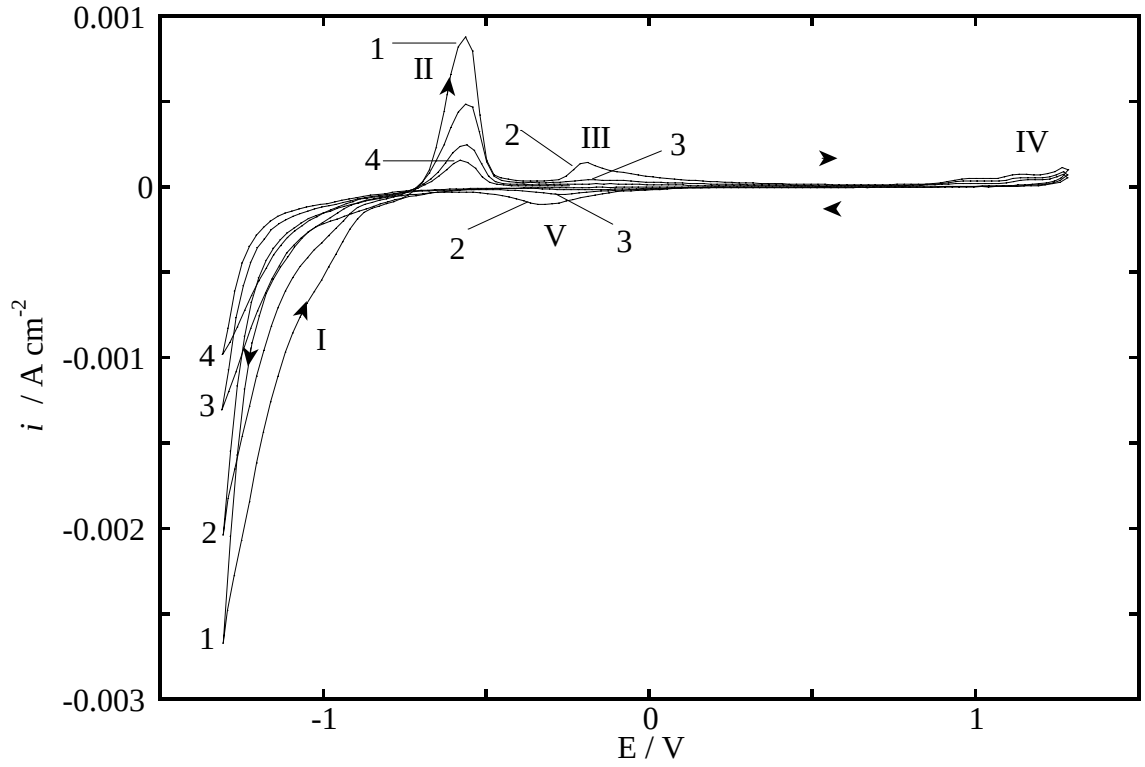

Figure 6.2 Cyclic voltammograms for a stationary lepidocrocite carbon paste disc electrode (1:19 γ-FeOOH:carbon paste by weight) in 0.2 M NH_4Cl at 50 mV s^{-1}. Cycle number indicated. T = 30.0°C.

not only the reduction of lepidocrocite, but also the reduction of hydrogen ions. A peak was resolved at -0.965 V for haematite reduction. For cathodic reversal potentials more negative than -1.00 V, an oxidation peak (II) was observed at -0.56 V ($I_{pII} = 8.7 \times 10^{-4}$ A cm^{-2}) on the reverse anodic sweep. Peak II increased in height the more negative the

cathodic reversal potential was on previous scan. This shows peak II corresponds to the oxidation of the lepidocrocite or oxide reduction product formed at I. It was also observed that peak II was not affected by electrode rotation, which indicates that the lepidocrocite or oxide reduction product adheres to the electrode surface.

The solid ferric species is reduced to $Fe(OH)_2$ below -1.00 V. For lepidocrocite, the reduction would proceed according to the following reaction [177]:

$$FeOOH_{(s)} + H^+_{(aq)} + e^- \rightarrow Fe(OH)_{2(aq)} \qquad (6.1)$$

The dissolution of $Fe(OH)_2$ is controlled by the pH near the paste/electrolyte interface – it will dissolve according to the following reaction:

$$Fe(OH)_{2(s)} + 2H^+_{(aq)} \rightarrow Fe^{2+}_{(aq)} + 2H_2O \qquad (6.2)$$

This must occur at a slow rate relative to the potential sweep rate used, since it is available for oxidation on the reverse anodic scan (peak II).

The reduction wave (I) between -0.8 and -1.3 V decreased with each successive potential cycle, indicating that FeOOH is being depleted from the electrode surface.

In Figure 6.2 the oxidation peaks at (IV) near 1.0 V were only observed after FeOOH reduction on a stationary electrode and possibly corresponds to the oxidation of aqueous Fe^{2+} ion (from the dissolution of $Fe(OH)_2$) to FeOOH. Voltammetric transitions of the iron oxides, similar to those described above, were also observed during the polarisation of iron electrodes in alkaline solutions [178, 179].

Peaks III and V were only observed for magnetite and lepidocrocite carbon paste electrodes. The species oxidised and reduced at these peaks were produced after FeOOH reduction had occurred and may correspond to the oxidation and reduction of iron hydroxides and oxides with different levels of hydration. In any case, no definite assignment of peaks III and V has been made.

6.3.3 Voltammetric study of anodic iron dissolution in model reduced ilmenite systems

In this section the anodic dissolution of iron powder in 0.2 M NH_4Cl solution is investigated using cyclic voltammetry with a carbon paste electrode. Iron powders from different sources were compared and the effect of different solid compounds on anodic iron dissolution will be discussed. Iron powder will be a model system for comparison with iron in reduced ilmenite.

6.3.3.1 Iron powder carbon paste electrode

The anodic dissolution of iron powder in various acidic electrolyte solutions was investigated previously by Freour using cyclic voltammetry with a conducting binder carbon paste electrode [176]. The cyclic voltammograms reported bear little resemblance to those generated in the present study. This difference can probably be attributed to the use of a conducting binder by Freour [176] while a non-conducting binder was used in this work.

The iron powders used in this section were not treated in order to remove the air-formed oxide film prior to commencing the experiments. This was considered appropriate since the reduced ilmenites – described in the following sections – were obtained from an industrial source where no special precautions were taken in preventing air oxidation of the product, other than keeping it clean and dry.

The cyclic voltammograms for different weight fractions of Koch Light iron powder in 0.2 M NH_4Cl are shown in Figure 6.3. The scans were initiated in the anodic direction from the iron open circuit potential which varied between -0.52 and -0.62 V,

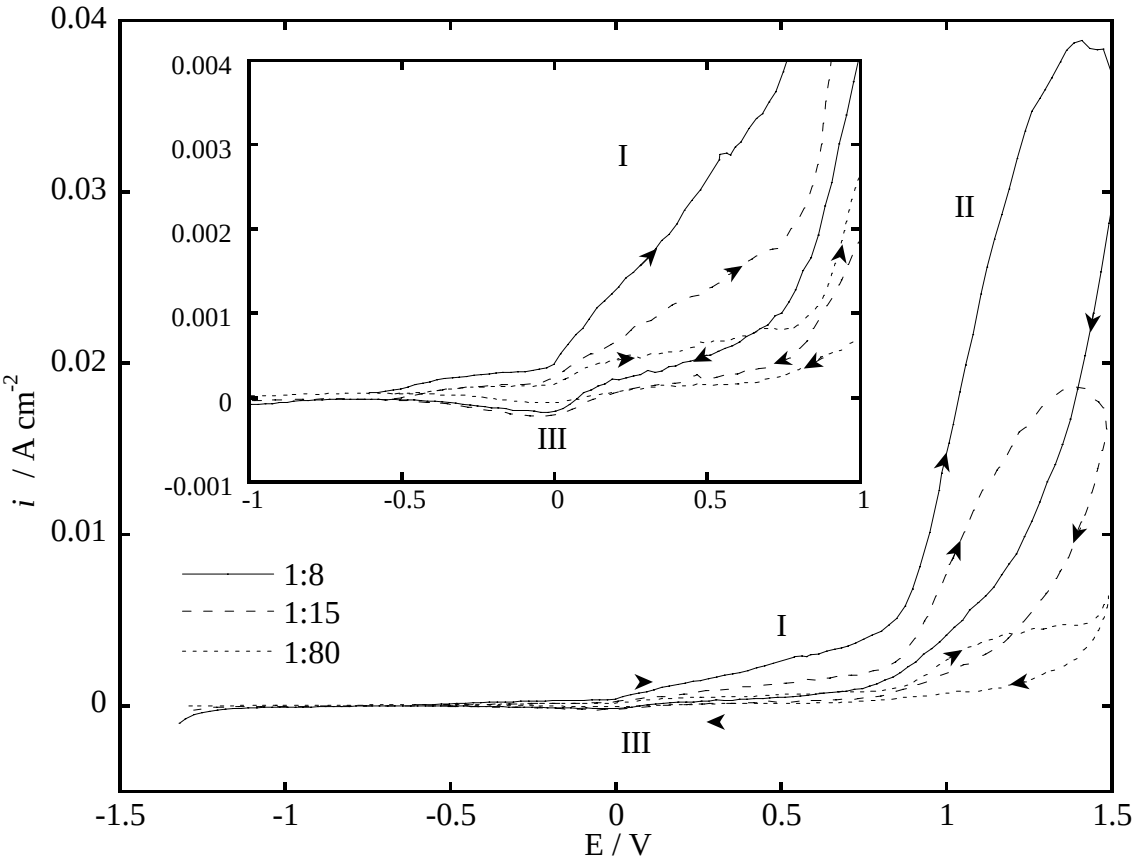

Figure 6.3 Cyclic voltammograms for Koch Light iron powder in 0.2 M NH_4Cl at 50 mV s^{-1}. The effect of different iron powder:carbon paste weight ratios. Inset: Cyclic voltammograms with expanded current density scale (First cycle only). T = 30.0°C.

but usually settled around -0.58 V. This is more than 0.130 V more positive than for a solid iron electrode (Section 3.3.1.5). This may indicate that an air-formed film is present on Koch Light iron powder.

The basic shape of the iron powder cyclic voltammograms in Figure 6.3 was similar for all the iron powder-carbon paste weight ratios investigated. The current density increased slowly (I) from the open circuit potential to about 0.7-0.8 V and then increased rapidly at more positive potentials giving rise to a peak (II) at around 1.0 V. Both the peak (II) current density and peak potential were proportional to the sweep rate. The current density at 1.5 V was directly proportional to weight ratio of iron in the carbon paste and was also independent of the electrode rotation speed. The anodic current density decreased on each successive potential cycle indicating that iron was being depleted at the electrode surface. The background current density, measured in the absence of iron, was less than 7.1×10^{-5} A cm^{-2} between -1.3 and 1.3 V but increased to 1×10^{-3} A cm^{-2} at 1.5 V. These results show that iron oxidation is the predominant anodic reaction.

The anodic current density on the following reverse scan was always less than on the previous forward scan. The reason for this hysteresis is still not certain, but it may be due to surface passivation by an anodically-formed FeOOH film. The inset in Figure 6.3 shows a reduction peak (III) was observed at 0.00 V which had a peak current density proportional to the scan rate, consistent with a surface or adsorption process [113]. However, this peak was not observed when the electrode was rotated at 1000 rpm, which is consistent with a solution process. This peak is probably is due to the reduction of anodically-formed FeOOH that precipitates as a sol near the electrode surface and/or as a weakly adhering film onto the iron/carbon paste surface.

Figure 6.4 shows the cyclic voltammograms for Johnson Matthey and Koch Light iron powders in 0.2 M NH_4Cl. The anodic dissolution current density for Johnson Matthey iron was much higher, and there was hardly any hysteresis between the anodic and cathodic scans, compared with Koch Light iron.

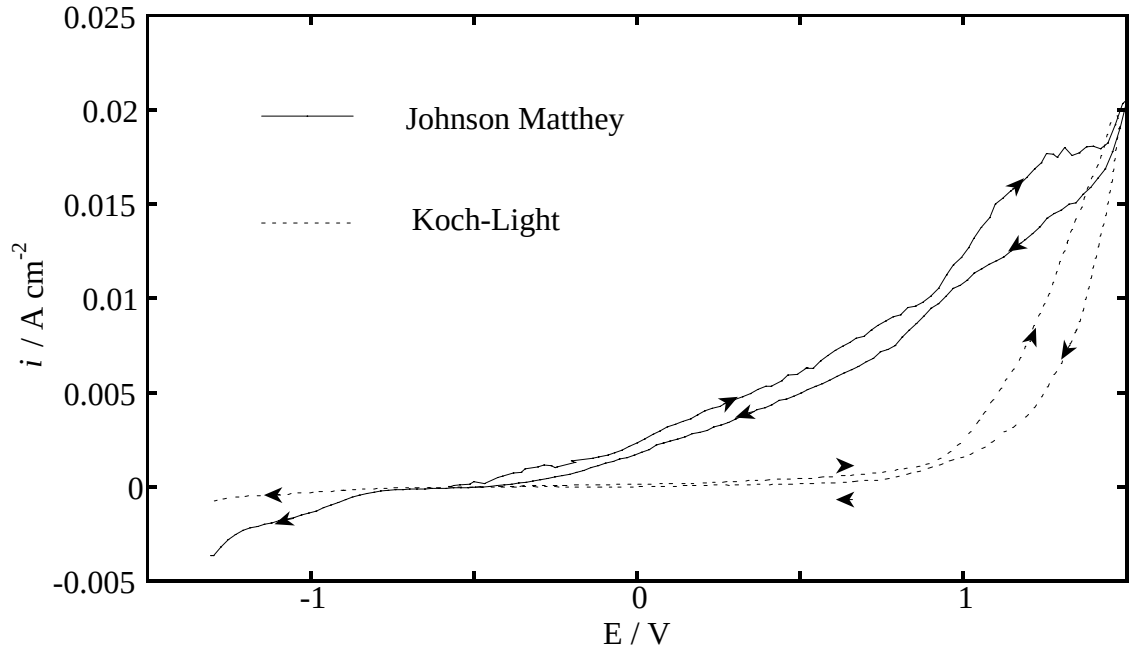

Figure 6.4 Cyclic voltammogram for Johnson Matthey (———) and Koch Light (----------) iron powders in 0.2 M NH_4Cl with a carbon paste (1:15, iron:carbon paste) electrode at 50 mV s^{-1}. Rotation speed = 1000 rpm. First cycle only. T = 30.0°C.

The Johnson Matthey iron powder was specially purchased for this study while the Koch Light material was taken from the laboratory shelf. It is therefore likely that the air-formed film is much thicker on the older Koch Light material. It is unlikely that the cause of the observed differences is the result of differences in the surface area of the two powders since the anodic current density at 1.5 V was the same for both. Thus it is most probable that the low anodic current density below 0.7 V for Koch Light iron powder is due to the presence of a passivating air-formed film. Therefore, the large increase in the current density above 0.7 V is probably due to breakdown of the air-formed passive film followed by pitting dissolution.

6.3.3.2 Iron powder-additive carbon paste electrode

In this section the effect of various solid compounds (or "additives") on the anodic dissolution of iron powder in NH_4Cl solution is studied using cyclic voltammetry with a carbon paste electrode. The five additives include two types of synthetic rutile, natural rutile, pigment grade TiO_2 and alumina. Synthetic rutile was chosen since it has same chemical composition, crystal structure (Appendix A), and morphology as the titanium oxide matrix of reduced ilmenite. Natural rutile grains are similar in size to reduced ilmenite but have much lower levels of reduced rutile, obviously a different crystal structure (Appendix A) and, a very smooth surface morphology compared with reduced

ilmenite. Pigment grade TiO_2 only has the basic chemical composition in common with reduced ilmenite while alumina was chosen as a control for it obviously does not contain TiO_2, although its surface morphology is highly irregular.

The cyclic voltammograms for Koch Light and Johnson Matthey iron powder with various additives in 0.2 M NH_4Cl are shown in Figure 6.5 and Figure 6.6 respectively. The open circuit potential for iron with all of the additives tested varied a little and was always between -0.57 and -0.59 V. This shows that none of the additives had significant galvanic interactions with iron.

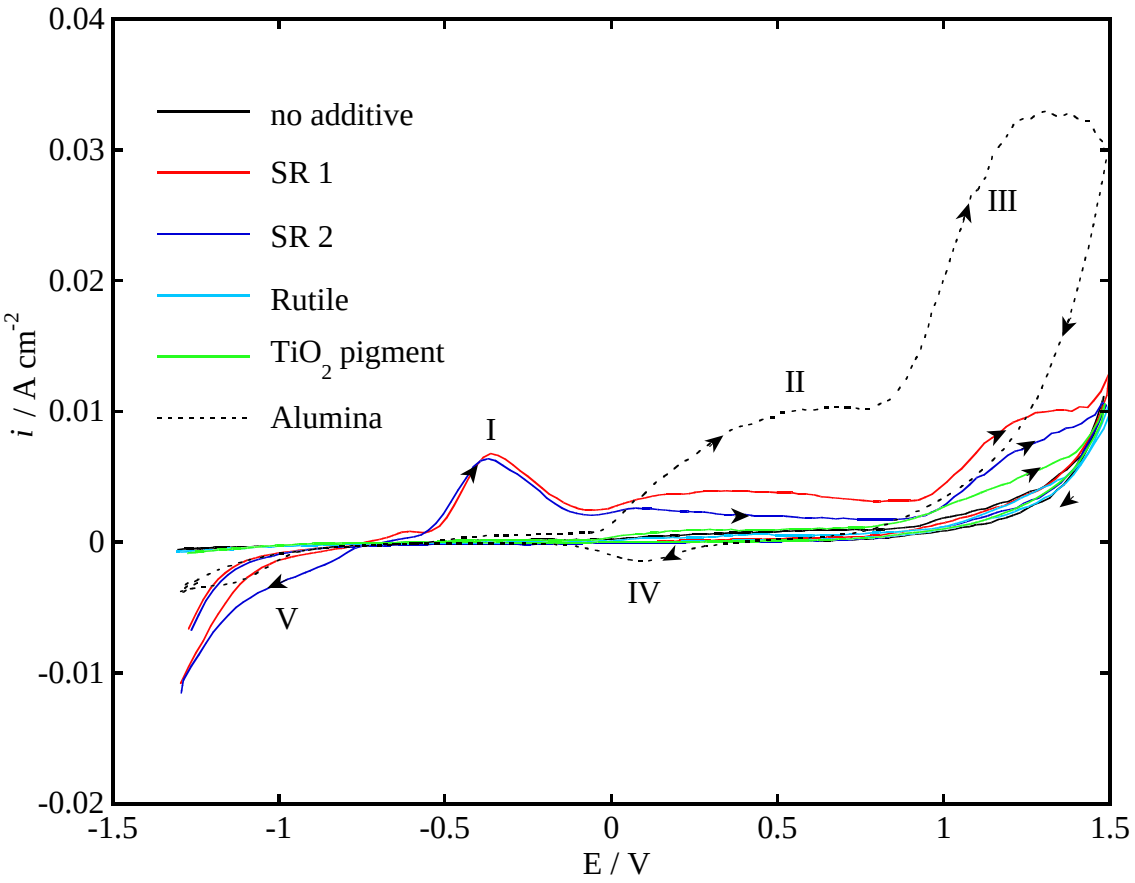

Figure 6.5 Cyclic voltammograms for Koch Light iron powder in 0.2 M NH_4Cl at 50 mV s^{-1}. The effect of different additives: No additive (iron powder only), synthetic rutile (SR 1 and SR 2), natural rutile (Rutile), TiO_2 pigment and alumina. Second cycle only. Rotation speed = 1000 rpm. T = 30.0°C.

Both synthetic rutiles greatly increased the anodic current density of both types of iron powder. However, the nature of the increased current was unique for each iron powder. For Koch Light iron the anodic current density increased by a very large amount near the open circuit potential and a peak (I) was observed at -0.37 V (I_{pI} = 6.7 ×

10^{-3} A cm^{-2}). The current density then decreased to about half the peak current density of peak I and remained quite constant up to 0.9 V (region II in Figure 6.5) before increasing rapidly at more positive potentials (III). A similar rapid increase in this potential range was observed for iron powder alone and was attributed to the onset of pitting dissolution (Section 6.3.3.1). The addition of synthetic rutile to Johnson Matthey iron powder also increased significantly the anodic current density near the open circuit potential, however, not to the same extent as observed for Koch Light iron. And above 0 V, the magnitude of the increased current density was approximately constant up to 1.5 V (Figure 6.6).

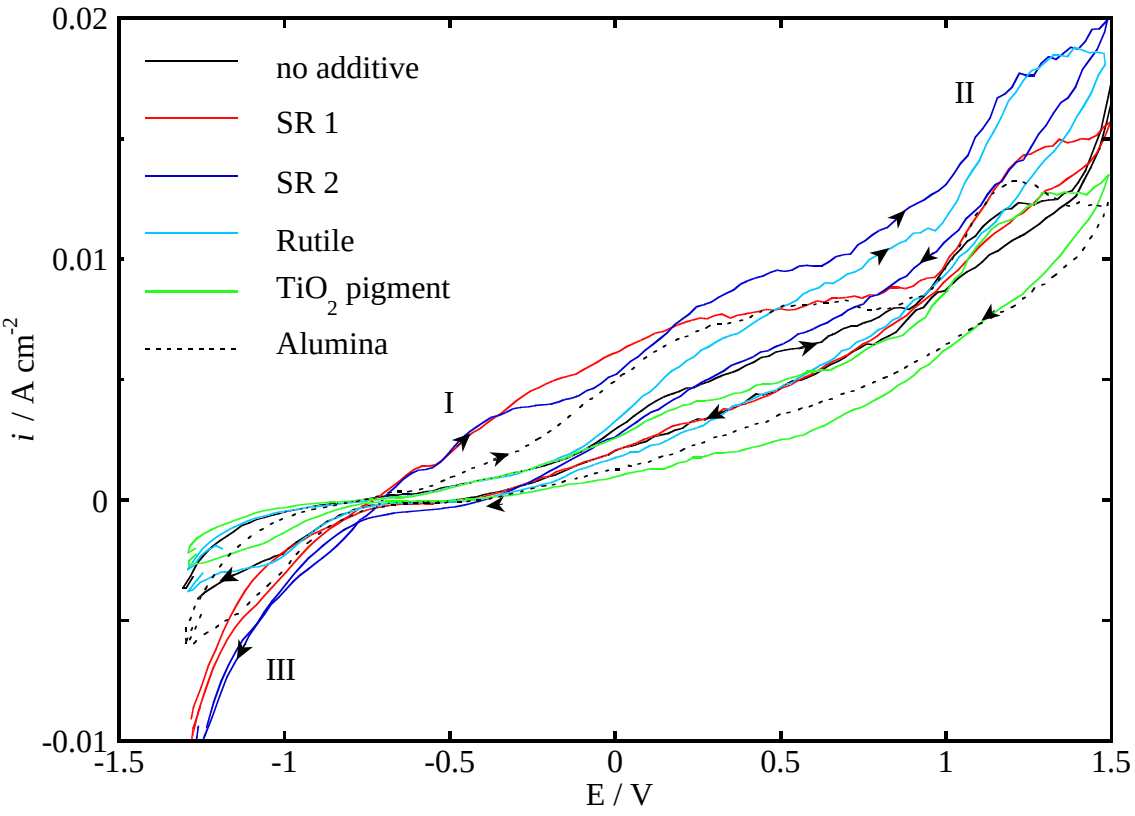

Figure 6.6 Cyclic voltammograms for Johnson Matthey iron powder in 0.2 M NH_4Cl at 50 mV s^{-1}. The effect of different additives: No additive (iron powder only), synthetic rutile (SR 1 and SR 2), natural rutile (Rutile), TiO_2 pigment and alumina. Second cycle only. Rotation speed = 1000 rpm. T = 30.0°C.

The addition of alumina also significantly increased the anodic current density of both types of iron powder (Figure 6.5 and Figure 6.6). Once again, the nature of the increased current density was not only unique for each iron powder, but also more complex than described above for iron with synthetic rutile. For example, a small but

significant increase in the current density was observed for the Koch Light iron up to about 0.0 V (region I, Figure 6.5) after which the current density increased rapidly then slowly levelled off near 0.8-0.9 V (II) before increasing rapidly again at more anodic potentials (III). For Johnson Matthey iron, alumina increased the anodic current density, from the open circuit potential up to 1.5 V in a similar manner to synthetic rutile however, not to the same extent. Natural rutile and TiO_2 pigment did not have a significant effect on the anodic current density of the iron powders.

Table 6.1 shows the effect of the different additives on the oxidation of iron powder at low (-0.5 V) and very high (1.3 V) current densities. With synthetic rutile, the anodic current density at -0.5 V increased 100-fold and 3.2-fold for Koch Light and Johnson Matthey iron respectively. However, the current density at 1.3 V increased by only 2-fold for Koch Light iron and even less for Johnson Matthey iron. Alumina increased the current density at -0.5 and 1.3 V by a factor of about 7 for Koch Light iron but only marginally increased the anodic current density for Johnson Matthey iron. Natural rutile decreased significantly the anodic current density at -0.5 V for Koch Light powder but hardly affected Johnson Matthey iron. TiO_2 pigment increased the anodic current density at -0.5 V by a factor of 3 for Koch Light iron but had only a marginal effect on Johnson Matthey iron.

Additive	Koch Light		Johnson Matthey	
	i at -0.5 V ($mA\ cm^{-2}$)	*i* at 1.3 V ($mA\ cm^{-2}$)	*i* at -0.5 V ($mA\ cm^{-2}$)	*i* at 1.3 V ($mA\ cm^{-2}$)
none	0.02	4.3	0.61	12.5
SR 1	1.8	9.9	1.9	14.6
SR 2	2.3	7.9	1.98	18.3
Rutile	0.004	4.2	0.51	18.2
TiO_2	0.07	2.7	0.51	12.7
Al_2O_3	0.15	32.9	0.94	12.7

Table 6.1 Anodic current densities for Koch Light and Johnson Matthey iron powder from, Figure 6.5 and Figure 6.6.

Figure 6.5 and Figure 6.6 show that the reduction current density, particularly below -1.0 V, increased with the addition of synthetic rutile and alumina. This may simply be due to the reduction of solid FeOOH formed during the previous anodic scan.

Receding, advancing and sessile drop contact angles were measured for all the carbon pastes used. The sessile drop contact angles were more reproducible than the mobile drop contact angles. The sessile drop contact angle for carbon paste was 51 ± 7°. Table 6.2 shows the effect of different additives on the sessile drop contact angles for 0.2 M NH_4Cl on Koch Light and Johnson Matthey iron powder carbon paste. Contact angles varied from 37° for Koch Light iron with TiO_2 pigment to 67° for Johnson Matthey iron with rutile. However, a systematic dependence of the anodic current density (measured at four potentials) on the contact angle was not observed. This clearly shows that factors other than the wettability of the surface are affecting iron dissolution.

Additive	Koch Light	Johnson Matthey
	Contact angle / °	Contact angle / °
none	55	63
SR 1	51	42
SR 2	55	44
Rutile	62	67
TiO_2	37	47
Al_2O_3	42	52

Table 6.2 Sessile drop contact angles for 0.2 M NH_4Cl on Koch Light and Johnson Matthey iron powder carbon paste containing different additives. T = 22°C.

The results maybe interpreted as follows.

In Figure 6.5 the reduction peak (IV) at 0.01 V can be attributed to the reduction of FeOOH (Section 6.3.1). The peak did not completely disappear when the electrode was rotated indicating that some FeOOH adsorbed onto the surface.

Since the amount of iron added to the carbon pastes is the same, synthetic rutile and alumina must be increasing the anodic current density by some mechanism. From the experiments conducted a number of possibilities can be ruled out as follows. First, the surface tension measurements rule out that the higher anodic current densities are caused by an increase the hydrophilicity of the paste surface. And second, it is unlikely that TiO_2 in synthetic rutile is exerting a photocatalytic effect [180] since TiO_2 pigment and natural rutile did not increase the dissolution rate at all. The XRD spectra (Appendix A) show that the crystal structure of synthetic rutiles is very different from both natural

rutile and TiO_2 pigment, so it is feasible that the photocatalytic properties are unique as well. However these experiments were conducted under ambient light conditions and experiments conducted under more controlled conditions with intense light sources would be required to definitively rule on a photocatalytic affect. Moreover, Al_2O_3 also increased iron oxidation.

It seems most likely that alumina and synthetic rutile increase the anodic iron dissolution rate by changing the morphology of the carbon paste/electrolyte interface. Synthetic rutile and alumina particles are rough and synthetic rutile also contains many voids and fissures. When added to the carbon paste, it is possible that the surface is opened up, exposing more iron to the solution and thereby increasing the anodic current. However, this explanation cannot account for the large variations in the magnitude of the increase with potential nor the difference in the magnitude of the increase between Koch Light and Johnson Matthey iron. This is because a simple increase in the surface area would effectively result in a displacement of the original cyclic voltammogram to higher current densities; the shape would not change. And the magnitude of the increase would also be expected to be the same for both types of iron powder. Clearly the results are not consistent with this explanation.

From the data presented here, a definite explanation cannot be determined. However, a number of tentative explanations can be suggested as follows. First, the voids and fissures created by the addition of rough and porous particles may create the conditions necessary for the development of numerous localised chemical environments (low in pH and high in chloride) to form during dissolution, resulting in very high current densities which are associated with pitting dissolution [58, 80]. Second, the 100-fold increase in the anodic current density when synthetic rutile is added to Koch Light iron compared with a 3.2-fold increase observed for the Johnson Matthey iron is a significant difference. In Section 6.3.3.1 it was suggested that an air-formed film on the older Koch Light material inhibited anodic dissolution. Then, it is conceivable that mixing together the abrasive synthetic rutile and alumina particles with iron powder to make the paste, damages the air-formed film resulting in active dissolution (peak I, Figure 6.5). However for Johnson Matthey iron, the air-formed film is obviously not as protective in the first place so the film damage would not result in a great increase in the anodic current density.

6.3.4 Voltammetric study of reduced ilmenite

6.3.4.1 Reduced ilmenite carbon paste electrode

Figure 6.7 shows the cyclic voltammogram for reduced ilmenite in 0.2 M NH_4Cl with a carbon paste electrode. On the first anodic potential scan the current density increased almost linearly with potential (I) and then increased more suddenly at about 0.8 V (II) and finally increased at a slower rate up to 1.5 V. At this potential, Fe^{2+} to Fe^{3+} oxidation was shown to occur (Section 6.3.1). Little hysteresis was observed on the following cathodic scan. On the second potential cycle the anodic current density substantially increased. This result shows that iron in reduced ilmenite has an air-formed film that inhibits iron oxidation on the first anodic scan. However, the air-formed film is reduced at negative potentials leaving a bare iron surface (see Section 3.3.1). This is consistent with previous work showing that a magnetite shell up to 2μm thick is present on iron in reduced ilmenite [181]. Potential cycling also increased the hysteresis between the

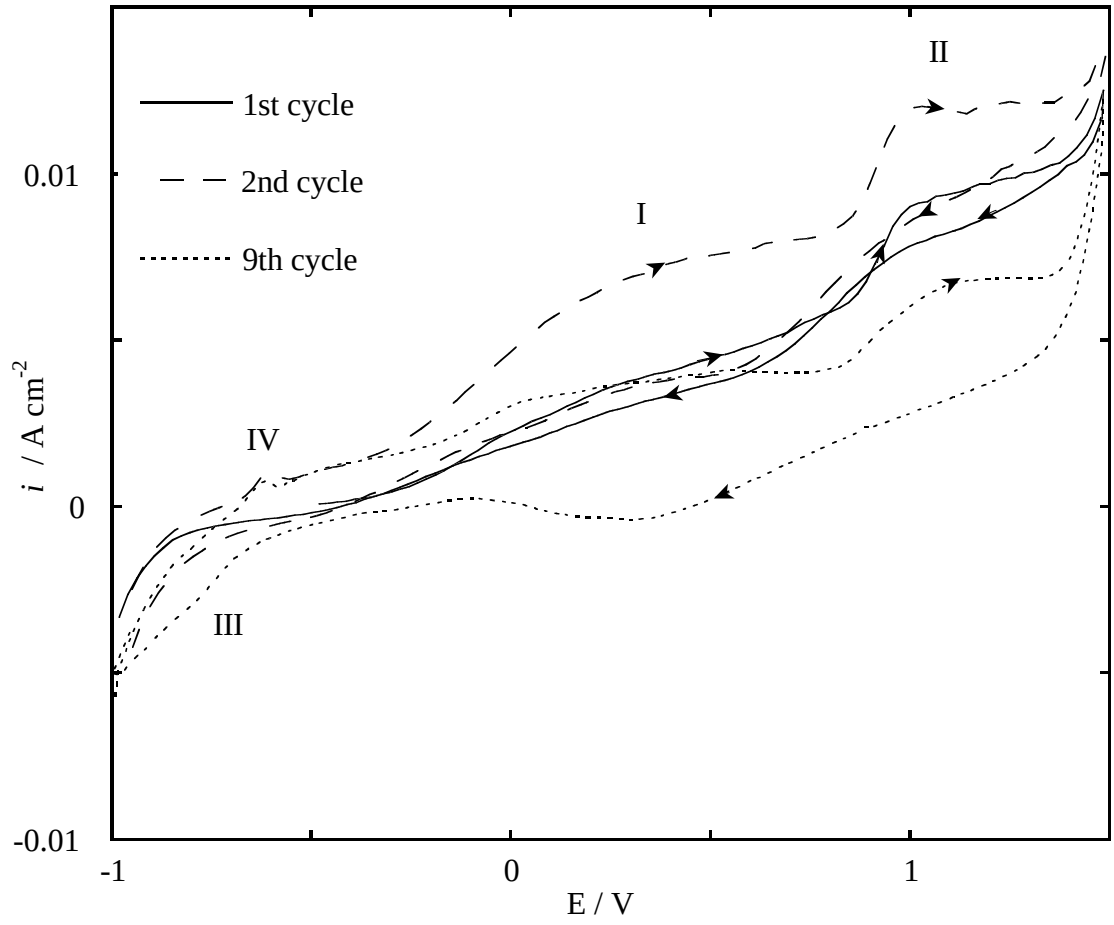

Figure 6.7 Cyclic voltammogram for reduced ilmenite in 0.2 M NH_4Cl at 50 mV s^{-1}. Cycle number indicated. T = 30.0°C.

anodic and cathodic scans; the shape of the curve during the forward scan did not change very much but the magnitude of the current density gradually decreased with each cycle. The wave below -0.7 V (III, Figure 6.7) increased with each successive potential cycle and probably corresponds to the reduction of FeOOH formed during the anodic scan. On the following anodic sweep a small peak (IV) at -0.61 V was observed and may correspond to the oxidation of $Fe(OH)_2$ formed at cathodic potentials.

Rotating the electrode at 1000 rpm had little effect on the cyclic voltammogram for reduced ilmenite. The independence of the anodic current density on the electrode rotation was confirmed by potentiostatic oxidation of reduced ilmenite at 0.5 V for 3

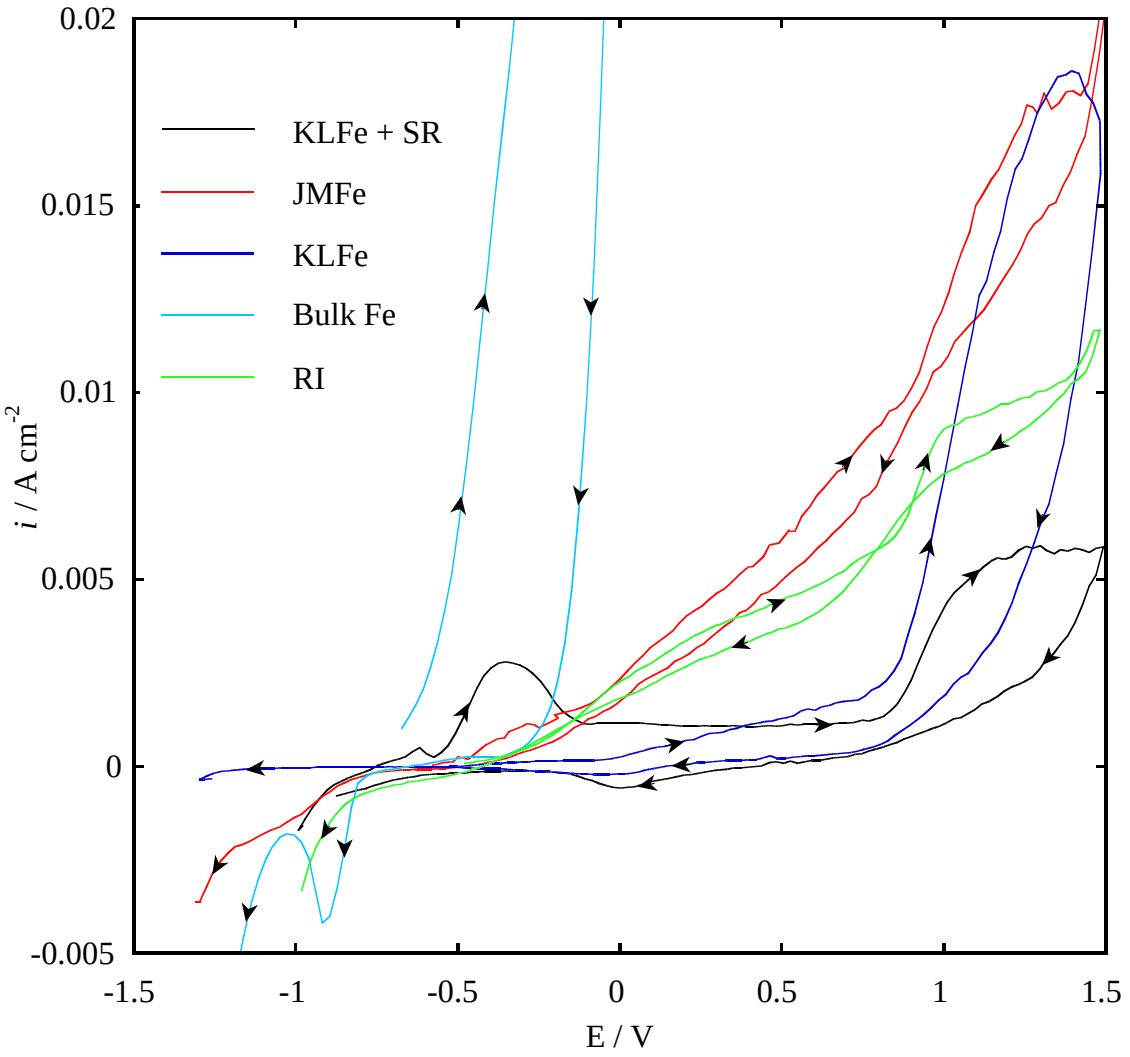

Figure 6.8 Cyclic voltammograms for various iron electrodes in 0.2 M NH_4Cl at 50 mV s^{-1}. Koch Light iron powder with synthetic rutile (KLFe+SR), Johnson Matthey iron powder (JMFe), Koch Light iron powder (KLFe), pure iron disc (Bulk Fe) and reduced ilmenite (RI) with a carbon paste electrode. Stationary electrode except for JMFe (1000 rpm).

minutes at various electrode rotation speeds. The current density at 0.5 V varied by only 1.4×10^{-4} A cm^{-2} between 0 and 2000 rpm. As expected however, the current density strongly depended upon the potential. For example, the current density at 0.5 and 1.4 V was 7×10^{-5} and 1.2×10^{-4} A cm^{-2} respectively, confirming that iron oxidation from reduced ilmenite is strongly dependent upon the potential.

Figure 6.8 overlays the cyclic voltammograms for various iron electrodes investigated. Also included in Figure 6.8 is the cyclic voltammogram for a pure iron disc electrode, from Figure 3.10.

6.3.4.2 Individual reduced ilmenite grains embedded in the surface of a carbon paste electrode

A single reduced ilmenite grain was placed on top of the carbon paste and pushed into the surface using a steel blade. A stable open circuit potential between -0.50 and -0.60 V was obtained for the single reduced ilmenite grain compared with an erratically varying potential between about 0.0-0.3 V for carbon paste only. This indicates that the measured potential is representative of the potential of iron in the single reduced ilmenite

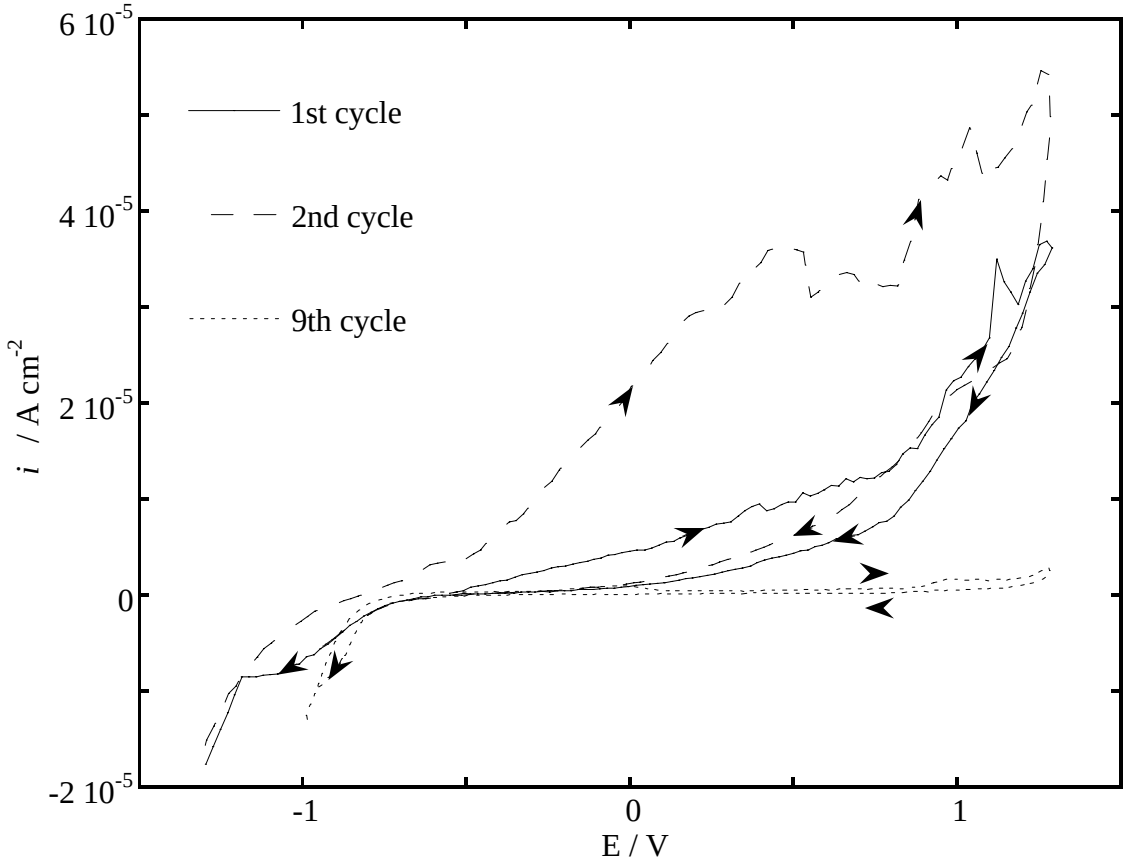

Figure 6.9 Cyclic voltammograms for a single reduced ilmenite grain embedded on the surface of a carbon paste electrode in 0.2 M NH_4Cl at 50 mV s^{-1}. Stationary electrode. Cycle number indicated. T = 30.0°C.

grain. Figure 6.9 shows the cyclic voltammogram of a single reduced ilmenite grain.

The size and shape of the cyclic voltammogram differed substantially between replicate measurements. This is not surprising considering the variability in size, iron content and iron distribution from grain to grain. The anodic current density increased gradually as the potential was made more positive on the first anodic scan and was only slightly lower on the following cathodic scan. On the second anodic cycle the current density had substantially increased compared to the first. This characteristic was also observed for reduced ilmenite carbon paste mixtures (Section 6.3.4.1) and is probably a result of reduction of the air-formed film during the negative part of the previous scan, leaving an activated surface. However, the current density on the following cathodic scan was much lower indicating that some passivation probably occurred. Thereafter the anodic current density decreased with each potential cycle eventually falling to very low values after about 9 cycles as shown in Figure 6.9. The open circuit potential of the electrode after 9 cycles increased to around 0.0 V, consistent with all of the available iron having been removed from the grain.

6.3.4.3 Comparison of different reduced ilmenites

In this section the electrochemistry of two other reduced ilmenites in 0.2 M NH_4Cl will be investigated using cyclic voltammetry with a carbon paste electrode. The reduced ilmenite discussed in the previous sections will be referred to as “X”. The other two reduced ilmenites were chosen according to their relative aeration behaviour: “Y” was found to give "good" aerations compared with “Z” which gave "bad" aerations. Good aerations are those that are complete within 8 to 10 hours and produce a magnetite by-product while poor aerations can take as long as 15 to 20 hours and produce undesirable lepidocrocite or haematite. Unfortunately, the relative aeration behaviour of X is not known. The compositions of the reduced ilmenites are listed in Appendix B.

Figure 6.10a shows the first cycle cyclic voltammogram for the three reduced ilmenites. Scanning from the open circuit potential, the anodic current density increased more quickly for Y and Z than for X. An oxidation peak (I, 0.0 V) was observed for both Y and Z while for X, the current density steadily increased with potential up to 1.5 V. Between 0.72 and 1.4 V the anodic current density for both X and Y was significantly higher than for Z. For example, the anodic current density for both X and Y was about 4.6 mA cm^{-2} at 0.72 V while for Z the current density was only 1.9 mA cm^{-2}. However the current density for Z increased rapidly, reaching similar values to X and Y at 1.5 V.

The current density on the following cathodic scan traced the entire previous forward scan only for X, while for Y and Z the current density below about 0.5 V was lower than on the forward anodic scan.

Figure 6.10b shows the fourth cycle cyclic voltammograms for the three reduced ilmenites. Surprisingly, the shapes of cyclic voltammograms were very similar, however the current density for X was significantly higher over the entire anodic range. Two oxidation peaks (I and II) were observed on the anodic scan: a broad anodic peak (I) at 0.4-0.5 V and a second anodic peak (II) at about 1.2 V. Significant hysteresis between the anodic and cathodic scans was observed. For all three reduced ilmenites the anodic current density on the subsequent cathodic scan was much lower than on the previous anodic scan. The reduction current at -0.9 V (III) also increased significantly between the first and fourth potential cycle.

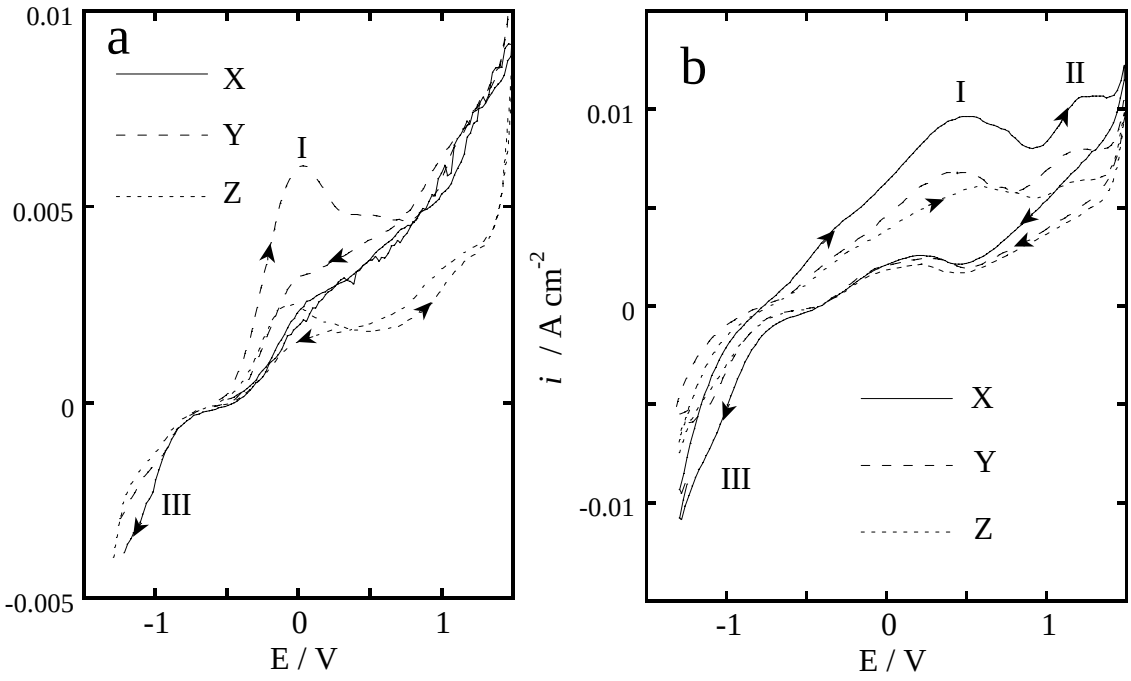

Figure 6.10 Cyclic voltammograms for reduced ilmenite X, Y and Z in 0.2 M NH_4Cl at 50 mV s^{-1}. a) first cycle b) fourth cycle. Rotating electrode (1000 rpm). T = 30.0°C.

Peak I is probably due to the formation of a $Fe(OH)_3$ film. Peak II is most probably due to the oxidation of Fe^{2+} to Fe^{3+}. The increase in the cathodic current at -0.9 V indicates that there is a continual build up of FeOOH with continued potential cycling.

The shape of the first cycle cyclic voltammogram of each type of reduced ilmenite appears to be unique and may provide useful information in characterising and comparing the properties of reduced ilmenites. Significantly higher anodic current

densities were obtained for the "good" reduced ilmenite, Y, compared with the "bad" reduced ilmenite, Z. This uniqueness, at least among the three reduced ilmenites investigated, is believed to originate from the different inhibitive properties of the air-formed film which controls the initial anodic dissolution rate of iron in reduced ilmenite. This suggests the variation in the aeration time may be due to the inhibitive properties of the air-formed passive film. Further work is required to confirm this postulate.

6.3.4.4 The effect of electrolyte composition

In this section the electrochemistry of reduced ilmenite in NH_4ClO_4, NaCl and $NaClO_4$ solution will be investigated using cyclic voltammetry with a carbon paste electrode.

Figure 6.11a and Figure 6.11b show the first cycle cyclic voltammogram for reduced ilmenite in chloride and perchlorate solutions respectively since the shape of the

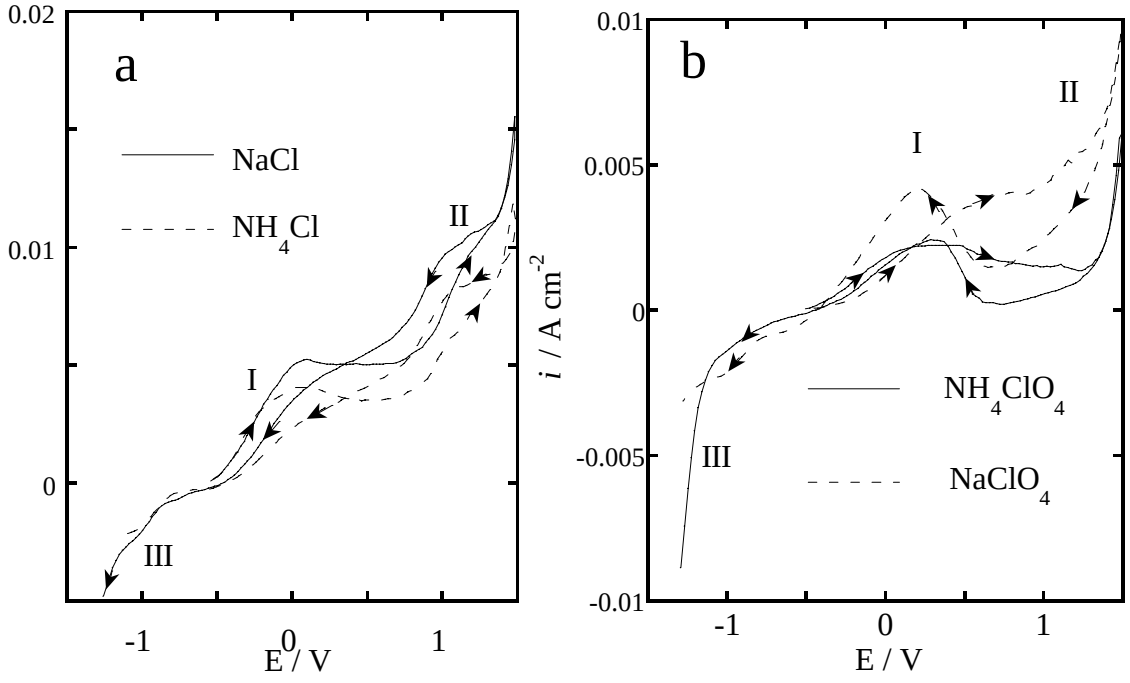

Figure 6.11 Cyclic voltammograms for reduced ilmenite in different 0.2 M electrolyte solutions at 50 mV s^{-1}. a) NaCl and NH_4Cl and b) NH_4ClO_4 and $NaClO_4$ solutions. Rotating (1000 rpm) carbon paste disc electrode. T= 30.0°C.

cyclic voltammograms for reduced ilmenite were most similar in electrolytes containing the same anion. The cyclic voltammograms in the two sets of solutions differed in two main ways:

a) the anodic current density over the entire anodic range was higher in chloride solutions compared with perchlorate solutions and,

b) in perchlorate solutions, an anodic peak (I) was observed between 0.2 and 0.4 V on the reverse cathodic scan

Figure 6.12 shows the fourth cycle cyclic voltammogram for reduced ilmenite in

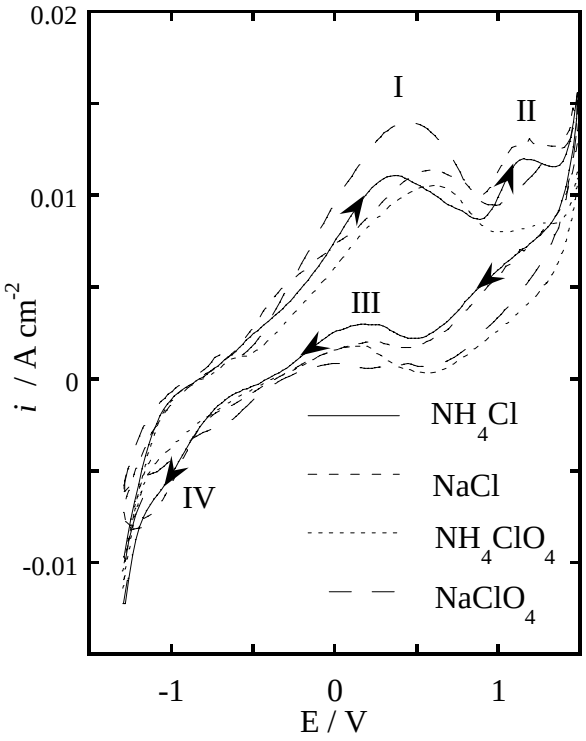

Figure 6.12 The fourth potential cycle cyclic voltammograms for a rotating (1000 rpm) reduced ilmenite carbon paste electrode in 0.2 M NH_4Cl, $NaClO_4$, NaCl and NH_4ClO_4 at 50 mV s^{-1}. T= 30.0°C.

all four electrolyte solutions. The most striking feature is the similarity in size and shape of the cyclic voltammograms in all the electrolyte solutions. This shows that chloride is only important in enhancing the dissolution rate of iron in reduced ilmenite during the first forward potential sweep as shown in Figure 6.11a.

The results may be interpreted as follows.

In Section 3.3.1 it was shown that the air-formed film on pure iron was not stable in NH_4Cl and NH_4ClO_4 which resulted in large anodic dissolution currents during the first anodic scan while in NaCl and $NaClO_4$ solution the anodic current density was very low until the air-formed film was removed by reduction at negative potentials. These results show that the air-formed film is present prior to starting the scan, even in the ammonium electrolytes, consistent with the results presented in the previous sections. Chloride ion increases the anodic current density on the forward scan by accelerating the breakdown of the air-formed passive film. However at the end of the first potential cycle

the air-formed passive film is removed by reduction in all of the electrolytes and thus the anodic current density on the reverse anodic sweep is approximately the same in all the electrolytes. It could not be determined from these results whether chloride ion inhibits active iron dissolution.

6.3.4.5 The effect of temperature

Figure 6.13a shows the first cycle cyclic voltammogram for reduced ilmenite in 0.2 M NH_4Cl at various temperatures. The anodic current increased slightly from 30 to 50°C and then sharply increased at 78°C. An increase in the anodic current density with temperature is expected since the anodic dissolution of iron in NH_4Cl solution is activation controlled (Section 3.3.3) [29]. At 78°C slight swelling of the paste was observed which may have created cracks or fissures in the paste exposing more reduced

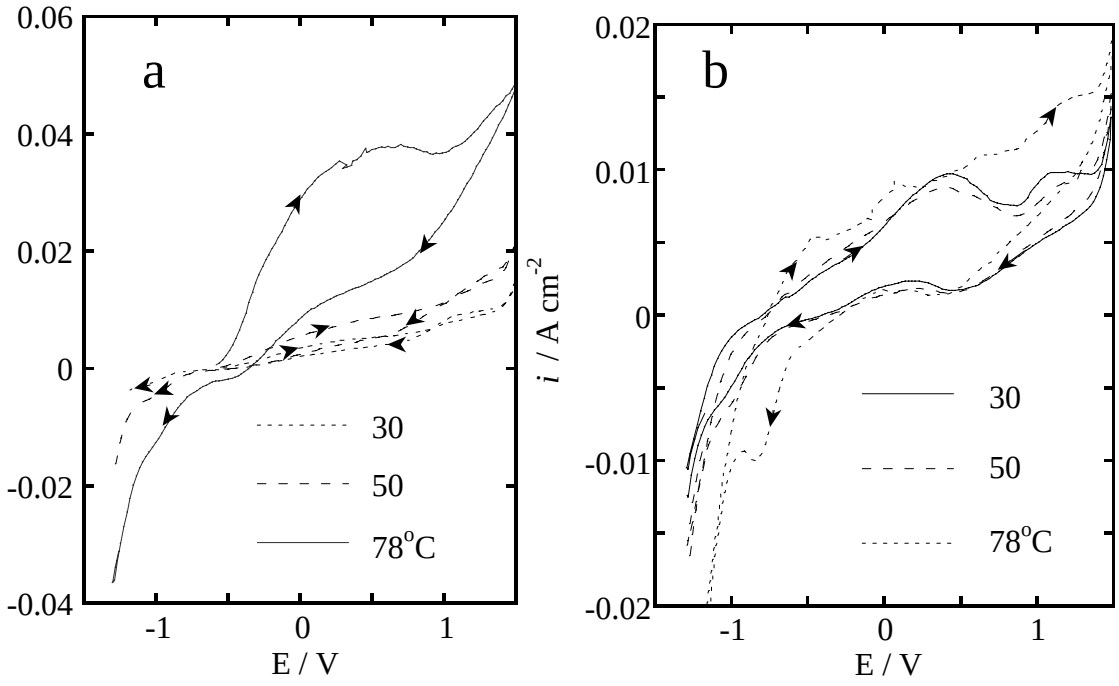

Figure 6.13 Cyclic voltammograms for reduced ilmenite in 0.2 M NH_4Cl at different temperatures. a) first cycle b) fourth cycle. Rotating carbon paste electrode (1000 rpm). Scan rate = 50 mV s^{-1}.

ilmenite to the solution and contributing to the increased anodic current density. However, this explanation is unlikely to be correct since, with repeated potential cycling, the anodic curve substantially decreased on each successive cycle until by the fourth cycle, the cyclic voltammogram almost superimposed over the cyclic voltammograms measured at 30 and 50°C (Figure 6.13b). This type of behaviour is not consistent with a larger exposed iron surface due to cracks in the paste. However, it is more likely that the

rapid decrease in the anodic current density with potential cycling is simply the result of rapid depletion of the iron from the within reduced ilmenite.

6.4 CONCLUSIONS

In 0.2 M NH_4Cl solution at 0.9 V, aqueous Fe^{2+} is oxidised to Fe^{3+} which precipitates as FeOOH that can adsorb onto the carbon paste as well as form a colloid. Both of these forms of FeOOH are reduced at 0.0 V. Reduction of colloidal FeOOH is under mixed activation-diffusion control. On the other hand, crystalline γ-FeOOH mixed into carbon paste is reduced at -1.0 V to $Fe(OH)_2$ that mostly precipitates onto the electrode surface. $Fe(OH)_2$ can then be subsequently oxidised at -0.60 V.

The electrochemistry of Koch Light and Johnson Matthey iron powder was investigated. Below 0.8 V anodic dissolution of Koch Light iron is significantly inhibited by the presence of an air-formed passive film. However above 0.8 V, due to the presence of chloride, the air-formed film breaks down, resulting in a large increase in the anodic current which is believed to be due to the onset of pitting dissolution. The air-formed film on Johnson Matthey iron must be quite thin or otherwise non-protective as facile oxidation occurred over the entire anodic range.

Synthetic rutile and alumina both increased the anodic current density for both types of iron powder. However, natural rutile and TiO_2 pigment had little effect. The most likely explanation of the observed catalytic effect is the porosity of reduced ilmenite and the rough surface morphology of alumina create a porous carbon paste surface where localised solution chemistry can develop. For example, localised pockets of solutions high in chloride and low in pH may form that lead to the high oxidation current densities observed during pitting dissolution.

Cyclic voltammetry experiments showed that an air-formed film on iron in reduced ilmenite inhibits anodic dissolution. This air-formed film is not removed during immersion in ammonium-containing electrolytes as was observed for pure iron (Section 3.3.1). However, the air-formed film is removed by reduction at negative potentials and as a result, the anodic current density substantially increases. Chloride ion increases the (reduced ilmenite) iron anodic current density by accelerating the breakdown of the air-formed film. Higher temperatures greatly accelerates anodic dissolution, probably by accelerating the breakdown of the air-formed passive film.

Cyclic voltammetry was also used to investigate the electrochemistry of two new reduced ilmenites; one that gave fast aerations and the second that aerated more slowly. Higher anodic current densities for the reduced ilmenite that also gave good aerations suggests that the characteristics of the air-formed film may be one of the factors controlling the aeration time. However, further experimental evidence is required to confirm this link. If this is true, aeration times may be minimised by maintaining an inert atmosphere (of CO_2 for example) over the reduced ilmenite as it cools after exiting the kiln – thereby reducing oxygen exposure. Another possibility is that higher concentrations of chloride ion in the aeration liquor may lead to the faster breakdown of the air-formed film.

7 Conclusions

7.1 CONCLUDING REMARKS

The aims of this thesis were to address the following limitations of the aeration step of the Becher process (Section 1.4):

(i) the variability of the aeration time

(ii) the intrinsic slowness of aeration

(iii) the poor understanding of the action of ammonium chloride

7.1.1 The variability of the aeration time

Cyclic voltammetry of reduced ilmenite using carbon paste electrodes showed that reduced ilmenite iron has an air-formed film that inhibits its initial anodic dissolution. The size and shape of the cyclic voltammogram was unique for each of the three different reduced ilmenites tested. The properties of the air-formed film are believed to be largely responsible for the uniqueness of each reduced ilmenite cyclic voltammogram. Importantly, the reduced ilmenite that was known to have a good aeration rate had the highest initial anodic dissolution current density. This is preliminary evidence that the variability of aeration may be due to the variability of the properties of the air-formed passive film that in turn controls the corrosion rate: the less stable the film, the shorter the aeration time.

The presence of synthetic rutile significantly increased the anodic dissolution rate of iron powder. It is believed that synthetic rutile increases the porosity of the carbon paste surface creating a morphology suitable for the development of highly localised solution chemistries necessary for pitting dissolution to occur. Thus the reduced ilmenite anodic iron dissolution reaction may be influenced by its morphology in a similar way.

Chloride initially increases the reduced ilmenite iron dissolution rate by assisting in the breakdown of the air-formed film. Higher temperatures also increased the dissolution rate mainly by accelerating the breakdown of the air-formed film.

7.1.2 The intrinsic slowness of aeration

The corrosion of rate of iron in air-saturated 0.2 M NH_4Cl solution at 80°C is 180×10^{-4} A cm^{-2} compared with 8.4×10^{-4} A cm^{-2} at 30°C. At ambient pressures the corrosion rate is controlled by oxygen diffusion and proceeds via a 4-electron reduction pathway. In this case, the corrosion rate should be significantly increased by increasing the flux of oxygen to the surface which can be achieved by increasing the oxygen partial pressure, increasing the rate of stirring and increasing the temperature. Indeed, the oxygen reduction current density was found to be proportional to the oxygen partial pressure up to 300 kPa. Especially large increases in the current density were observed between 80 and 130°C due to increasing oxygen solubility, increasing oxygen diffusion coefficient and decreasing viscosity. At 300 kPa oxygen partial pressure and at 130°C the oxygen reduction current density was as high as 0.03 A cm^{-2}. However, for the real corrosion system, the corrosion rate never reaches the oxygen current densities due to the precipitation of a thick γ-FeOOH film that impedes oxygen diffusion to the surface. A four-fold increase in the corrosion rate at elevated pressure was achieved by increasing the temperature from 30 to 80°C which increased the solubility of γ-FeOOH allowing oxygen greater access to the surface.

7.1.3 The poor understanding of the role of ammonium chloride

Even though the new Eh-pH diagram constructed for the iron-water-ammonia system showed that ammonia has no effect on the solubility of ferrous ions, ammonium ion did have the remarkable effect of rapidly removing the air-formed passive film on pure iron at the corrosion potential, resulting in fast active dissolution or uniform corrosion. In the absence of ammonium ion, the passive film is much more stable and chloride results in localised corrosion. Chloride does, however, inhibit the anodic dissolution of iron however the oxygen corrosion rate was not affected by chloride as long as ammonium ion was present. Ammonium ion itself increased the active current compared with sodium ion. Interestingly however, the anodic dissolution of reduced ilmenite iron was strongly affected by chloride through the acceleration of the breakdown of the air-formed passive film. Ammonium ion did not exhibit any special ability to remove the air-formed film from reduced ilmenite iron as it did for pure iron.

7.2 SUGGESTIONS FOR FUTURE WORK

7.2.1 Reduced ilmenite and the variability of aeration

An obvious limitation of the reduced ilmenite work is that there is not any direct physical evidence or characterisation of the air-formed film. High resolution scanning electron microscopy of whole grains and even carefully prepared grain cross-sections, should give information about the structure and morphology of the air-formed film and, coupled with EDAX, the composition of the film could be confirmed.

The observed relationship between the magnitude of the reduced ilmenite anodic iron dissolution current density and the aeration time requires further work in order to confirm the suggested link. In addition to quantitative aeration data, micro-porosity and iron surface area data would also need to be quantified and their influence characterised.

Another important question is that there is little known about the physical and the electrical interactions between the reduced ilmenite grains and the carbon paste. For example, SEM or optical microscopy of reduced ilmenite grains could confirm whether all of the iron is oxidised from a grain during voltammetry or only the iron available near the grain boundary. Knowledge of the mechanism and rate of removal throughout the grain would be invaluable.

A further valuable extension of this work would be to investigate the voltammetry of carefully selected size fractions of reduced ilmenite.

A useful improvement could be made to the iron powder dissolution work by determining the surface pH of the paste additives and characterising its effect, if any, on the dissolution of iron powder.

7.2.2 Oxygen corrosion of iron

As suggested for reduced ilmenite above, the physical properties of the air-formed and anodically-formed films need to be characterised to confirm the properties of the film alluded to in this work. Transmission electron microscopy of ultramicrotomed cross-sections should provide useful information.

Corrosion experiments in $NaClO_4$ and NaCl solution should be repeated at pH values closer to that of NH_4Cl solution (pH 4.8) to give further evidence that ammonium ion does indeed have special properties that result in the rapid removal of the air-formed film.

A difficult but worthwhile experiment would be the direct measurement of the localised pH, iron corrosion potential, ammonia and chloride ion concentration within a reduced ilmenite grain.

7.2.3 Anodic iron dissolution

A careful study is recommended to elucidate the mechanism of iron dissolution, to assess the degree of inhibition of iron dissolution by chloride and confirm the precise role of ammonium ion and ammonia.

7.2.4 Iron thermodynamics

Using the entropies and enthalpies of formation provided in the literature for the ferrous ammine complexes [182] Eh-pH and activity pH diagrams could be constructed at 80°C, a temperature closer to the actual aeration temperature and at higher temperatures relevant to pressure leaching.

Appendices

Appendix A: X-Ray diffraction patterns for iron powder and selected minerals used in this work.

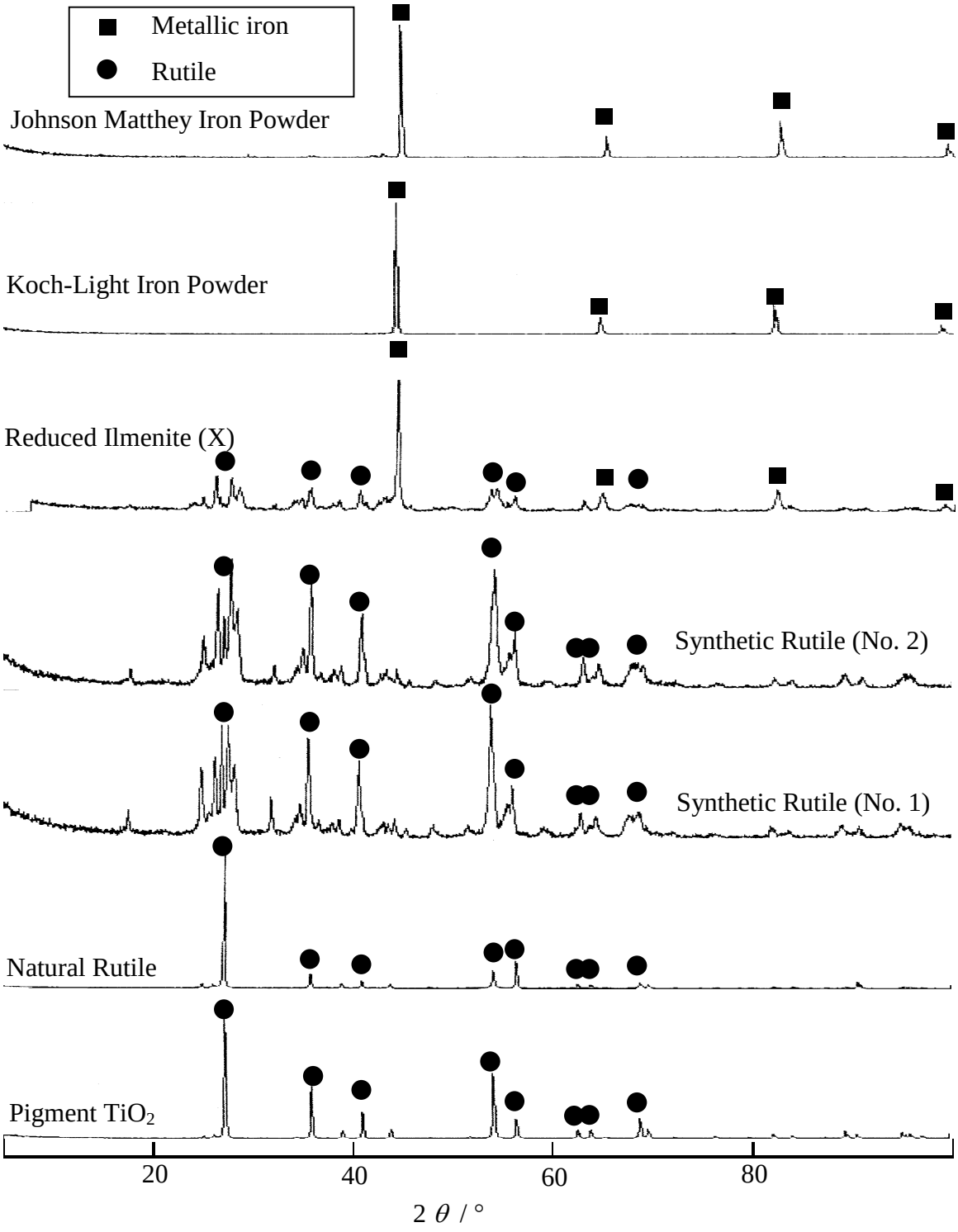

Appendix B: Chemical composition of selected minerals used in this work.

Analyte %	Reduced Ilmenite (X)	Reduced Ilmenite (Y)	Reduced Ilmenite (Z)	Synthetic Rutile (No. 1)	Synthetic Rutile (No. 2)	Natural Rutile
Fe_M	28.5	29.0	26.7	0.28	0.14	0.14
Fe_T	29.5	31.0	28.5	3.06	2.40	0.90
TiO_2	64.2	63.2	66.1	93.4	94.2	96.0
Al_2O_3	1.06	0.96	0.80	1.33	1.10	0.38
SiO_2	1.04	0.69	1.08	1.17	0.81	0.60
CaO	0.04	0.01	<0.01	0.02	0.03	0.02
Mn_3O_4	1.54	1.53	1.44	1.15	0.742	1.38
Cr_2O_3	0.09	0.08	0.14	0.09	0.13	0.17
P_2O_5	0.01	0.020	0.020	0.010	0.020	0.040
ZrO_2	0.13	0.06	0.08	0.11	0.08	0.81
ThO_2	0.030	0.030	0.040	0.020	0.020	<0.001
U_3O_8	<0.001	<0.001	<0.001	<0.001	<0.001	<0.001
LOI	-13.8	-13.2	-12.3	-1.04	-0.49	0.36

Bibliography

1. Digest of Mineral and Petroleum Statistics, Department of Minerals and Energy, Western Australia (1994).
2. R. Dullahide, Australian Commodities 3 (1996).
3. T. S. Mackey, JOM 46:59 (1994).
4. R. G. Becher (1963) Australian Patent, 247110.
5. R. G. Becher, R. G. Canning, B. A. Goodheart, and S. Uusna, AIMM Proc. 21:21 (1965).
6. Benelite Corporation of America (1974) United States Patent, 3825419.
7. H. N. Sinha, International Symposium on Research and Development in Extractive Metallurgy of Tin and Related Metals, Ipoh, Malaysia, 1988; p 375.
8. S. K. Ishihara (1970) DOS 2005832.
9. N. J. Welham, Minerals Engineering 9:1189 (1996).
10. N. J. Welham, Canadian Institute of Metallurgy Bulletin 90:64 (1997).
11. R. Heng, W. Koch, and A. N. Beyzavi (1992) Australian Patent, AY-B-59894/90.
12. V. G. Neurgaonkar, A. N. Gokarn, and K. Joseph, J. Chem. Tech. Biotech. 36:27 (1986).
13. H. N. Sinha and D. M. Waugh (1971) British Patent, 1255826.
14. C. D. Shiah (1966) United States Patent, 3252787.
15. G. Nakazawa and K. Terunuma (1958) Japanese Patent, 1117.
16. R. D. Pike (1959) United States Patent, 2903341.
17. L. George, F. Pretka, and C. J. Zelnik (1958) United States Patent, 2852452.
18. G. J. Dooley, Journal of Metals 27:8 (1975).
19. R. Mandyczewsky, Honours Thesis, University of Western Australia, 1964.
20. J. B. Farrow and I. M. Ritchie, Corrosion of Metallic Iron from Reduced Ilmenite, Report No. 19, West Australian Mining and Petroleum Research Institute (1985).
21. J. B. Farrow, I. M. Ritchie, and P. Mangano, Hydrometallurgy 18:21 (1987).
22. A. C. Bax and I. M. Ritchie, Final Report of the Research into the Aeration Process and Investigation of Production of Iron Oxide Pigments from Reduced Ilmenite, 15, Murdoch University and Associated Minerals Consolidated (1984).
23. C. B. Ward, Ph.D. Thesis, Murdoch University, 1990.

24. M. Reid, Investigation of the Aeration Stage of the Becher Process, Report No. 1, Murdoch University (1993).
25. G. Schmitt, in Advances in CO_2 Corrosion (R. H. Hausler and H. P. Godard, eds.), NACE, Houston, 1984, p. 10.
26. Z. Xia, K. C. Chou, and Z. Szklarska-Smilowska, Corrosion 45:636 (1989).
27. J. Avraamides, S. Bailey, T. O'Brien, and J. Ward, AIMM Proc. Conf., Brisbane, AIMM, 1994; p 167.
28. J. Ward, S. Bailey, and J. Avraamides, AIMM Proc. Conf., Perth, AIMM, 1996; p 231.
29. S. Jayasekera, Y. Marinovich, J. Avraamides, and S. Bailey, Hydrometallurgy 39:183 (1995).
30. M. Pourbaix, Atlas of Electrochemical Equilibria in Aqueous Solutions, Permagon Press, London, 1966.
31. M. Pourbaix, Lectures on Electrochemical Corrosion, Plenum Press, New York, 1973.
32. D. C. Silverman, Corrosion 38:453 (1982).
33. K. Osseo-Asare and T. H. Brown, Hydrometallurgy 4:217 (1979).
34. R. G. Robins, The application of potential-pH diagrams to the prediction of reactions in pressure hydrothermal processes, Report LR80(MST), Warren Spring Laboratory (Stenvenage U.K.) (1968).
35. R. M. Garrels, Mineral Equilibria at Low Temperatures and Pressures, Horper & Brothers, New York, 1960.
36. T. Misawa, Corros. Sci. 13:659 (1973).
37. C. B. Ward, S. L. Gibbons, I. M. Ritchie, and D. M. Muir, AIMM Proc.:209 (1989).
38. R. J. Biernat and R. G. Robins, Electrochim. Acta 17 (1972).
39. F. A. Cotton and G. Wilkinson, Advanced Inorganic Chemistry, 4th Edition, Wiley-Interscience, Oxford, 1980.
40. E. Weitz and H. Müller, Ber. 58:363 (1925).
41. D. L. Leussing and I. M. Kolthoff, J. Am. Chem. Soc. 75:2476 (1953).
42. L. G. Sillen and A. E. Martell, Stability Constants of Metal-ion Complexes, 2 Special Publication No. 17, The Chemical Society, London, 1964.
43. K. B. Yatsimirskii, Zhur Obshchei Khim 24:1498 (1954).

44. D. J. Klocke and A. N. Hixon, Ind. Eng. Process Des. Develop. 11:141 (1972).
45. I. Isaev, S. Tverdokhlebov, L. Novikov, and T. Padar, Russian Journal of Inorganic Chemistry 35:1162 (1990).
46. K. Osseo-Asare, Trans. Instn Min. Metall. C 90:159 (1981).
47. P. B. Queneau and D. R. Weir, in Iron Control in Hydrometallurgy (J. E. Dutrizac and A. J. Monhemius, eds.), Ellis Horwood Limited, Chichester, 1986.
48. A. G. Turnball and M. W. Wadsley, CSIRO - Monash Thermochemistry System, Ver. 1.0, CSIRO, Division of Mineral Products and Monash University, Department of Chemical Engineering (1992).
49. C. F. Baes and R. F. Mesmer, The Hydrolysis of Cations, Wiley, New York, 1976.
50. G. B. Naumov, B. N. Ryzhenko, and I. L. Khodavsky, Handbook of Thermodynamic Data, UGS-WRD-74-001, , 1974.
51. G. H. Kelsall and R. A. Williams, J. Electrochem. Soc. 138:931 (1991).
52. G. P. Power and I. M. Ritchie, Electrochim. Acta 26:1073 (1981).
53. P. N. Sheppard, Data Acquisition and Plotting Analysis, Ver. 1.43, DAPA Scientific Ltd (1992).
54. D. D. MacDonald, A. C. Scott, and P. Wentrcek, J. Electrochem. Soc. 126:908 (1979).
55. S. Jayasekera, J. Avraamides, S. Bailey, and L. Shaw, AIMM Proc. Conf., Brisbane, AIMM, 1995; p 123.
56. J. Zheng, DAPA-EIT, Ver. 1.00, (1994).
57. A. B. Anderson and N. C. Debnath, J. Am. Chem. Soc. 105:18 (1983).
58. N. Sato, Corrosion 45:354 (1989).
59. I. H. Plonski, in Modern Aspects of Electrochemistry, Vol. 29 (J. O. M. Bockris, B. E. Conway, and R. E. White, eds.), Plenum Press, New York, 1996, p. 203.
60. K. E. Heusler, in Encyclopedia of the Electrochemistry of the Elements (A. J. Bard, ed.), Marcel Dekker, New York, 1982.
61. D. M. Drazic, in Modern Aspects of Electrochemistry, Vol. 19, Plenum Press, New York, 1989, p. 69.
62. A. A. Miligy, D. Geana, and W. J. Lorenz, Electrochim. Acta 1975:273 (1975).
63. J. Bessone, L. Karakaya, P. Lobeer, and W. J. Lorenz, Electrochim. Acta 22:1155 (1977).
64. P. Lorbeer and W. J. Lorenz, Corros. Sci. 20:405 (1980).

65. K. J. Vetter and F. Gorn, Electrochim. Acta 18:321 (1973).
66. T. P. Hoar, Corros. Sci. 7:341 (1967).
67. H. H. Uhlig, Corros. Sci. 19:777 (1979).
68. J. D. Goodrich and N. Hackerman, J. Electrochem. Soc. 109:795 (1962).
69. D. Jones and N. Hackerman, Corros. Sci. 8:565 (1968).
70. H. H. Uhlig and G. Schick, J. Electrochem. Soc. 111:1211 (1964).
71. A. I. Tsinman, L. A. Danielyan, and V. S. Kuzub, Zaschita Metallov 9:156 (1973).
72. I. D. Meshcheryakova, T. P. Kashcheeva, and M. L. Rutkovskii, Zashchita Metallov 11:42 (1975).
73. K. Osseo-Asare, J. W. Lee, H. S. Kim, and H. W. Pickering, Metallurgical Transactions B 14:471 (1983).
74. H. S. Kim, Y. T. Kho, K. Osseo-Asare, and H. W. Pickering, Metallurgical Transactions B 22:323 (1991).
75. H. S. Kim, Y. T. Kho, H. W. Pickering, and K. Osseo-Asare, J. Electrochem. Soc. 138:1599 (1991).
76. Y. T. Kho, K. Osseo-Asare, and H. W. Pickering, J. Electrochem. Soc. 139:32 (1992).
77. G. Bech-Nielsen and J. C. Reeve, Proc. 6th Scand. Corros. Congr., Gothenburg, , 1971; p 8.
78. G. Bech-Nielsen, Electrochim. Acta 19:821 (1974).
79. Z. Szklarska-Smialowska, Corrosion Inhibition, Dallas, Texas, NACE, Houston, Texas, 1983; p 1.
80. N. Sato, Corros. Sci. 37:1947 (1995).
81. T. E. Pou, O. J. Murphy, V. Young, J. O. M. Bockris, and L. L. Tongson, J. Electrochem. Soc. 131:1243 (1984).
82. I. Epelboin, P. Morel, and H. Takenouti, J. Electrochem. Soc. 118:1282 (1971).
83. A. F. White, M. L. Peterson, and M. F. H. Jr, Geochimica et Cosmochimica Acta 58:1859 (1994).
84. D. S. Mancey, D. W. Shoesmith, J. Lipkowski, A. C. McBride, and J. Noel, J. Electrochem. Soc. 140:637 (1993).
85. Z. Y. Lu and D. M. Muir, J. App. Electrochem. 16:745 (1986).
86. P. H. Rieger, Electrochemistry, Prentice-Hall, Inc., New Jersey, 1987.

87. I. Epelboin, C. Gabrielli, M. Keddam, and H. Takenouti, in Electrochemical Corrosion Testing (U. Bertocci and F. Mansfeld, eds.), ASTM, Philidelphia, 1981, p. 150.
88. S. Barnartt, Corrosion 42:549 (1986).
89. M. Keddam, J.-F. Lizee, C. Pallotta, and H. Takenouti, J. Electrochem. Soc. 131:2016 (1984).
90. K. E. Heusler, B. Kusian, and D. McPhail, Ber. Bunsenges. Phys. Chem. 94:1443 (1990).
91. J. R. Park and D. D. Macdonald, Corrosion 45:563 (1989).
92. K. Kinoshita, Electrochemical Oxygen Technology, John Wiley & Sons, , 1992.
93. Y. V. Pleskov and V. Y. Filinovski, The Rotating Disk Electrode, Consultant Bureau, New York, 1976.
94. R. Babic and M. Metikos-Hukovic, J. App. Electrochem. 23:352 (1993).
95. S. Štrbac, N. A. Anastasijevic, and R. R. Adzic, Electrochim. Acta 37:983 (1994).
96. S. L. Gojkovic, S. K. Zecevic, and D. M. Drazic, Electrochim. Acta 39:975 (1994).
97. Z. A. Iofa and M. A. Makhuba, Zashch. Metal. 3:387 (1967).
98. A. Bonnel, F. Dabosi, C. Deslouis, M. Duprat, M. Keddam, and B. Tribollet, J. Electrochem. Soc. 130:753 (1983).
99. P. Delahay, J. Electrochem. Soc. 97:205 (1950).
100. V. Jovancicevic and J. O. M. Bockris, J. Electrochem. Soc. 133:1797 (1986).
101. S. Zecevic, D. M. Drazic, and S. Gojkovic, J. Electroanal. Chem. 265:179 (1989).
102. M. A. Genshaw, J. Electroanal. Chem. 15:173 (1967).
103. F. Crisafio, Honours Thesis, Curtin University of Technology, 1993.
104. P. G. T. Fogg and G. William, Solubility of Gases in Liquids: a Critical Evaluation of Gas/Liquid Systems in Theory and Practice, J. Wiley, Chichester, 1991.
105. H. A. Pray, C. E. Schweickert, and B. H. Minnich, Ind. Eng. Chem. 44:1146 (1952).
106. L. M. Zoss, S. N. Suciu, and W. L. Sibbitt, Trans. Am. Soc. Mech. Eng. 76:69 (1979).
107. S. D. Cramer, Ind. Eng. Chem. Process. Des. Dev. 19:300 (1980).
108. R. Battino, ed., Oxygen and Ozone, Solubility Data Series, Vol. 7, Oxford: Pergamon Press, New York, 1981.

109. A. Broden and R. Simonson, Swensk Papperstidning 87:541 (1978).
110. B. B. Benson, D. K. Jr., and M. A. Peterson, J. Solution Chem. 8:655 (1979).
111. E. L. Stephan, N. S. Hatfield, R. S. Peoples, and H. A. H. Pray, Report BMI-1067, Batelle Memorial Institute (1956).
112. E. Narita, F. Lawson, and K. N. Han, Hydrometallurgy 10:21 (1983).
113. A. J. Bard and L. R. Faulkner, Electrochemical Methods-Fundamentals and Applications, John Wiley and Sons, Brisbane, 1980.
114. D. S. Viswanath and G. Natarajan, Data Book on the Viscosity of Liquids, Hemisphere Publishing Corporation, New York, 1989.
115. R. H. Stokes and R. Mills, Viscosity of Electrolytes and Related Properties, Pergamon Press Ltd, London, 1965.
116. M. Stern and A. L. Geary, J. Electrochem. Soc. 104:56 (1957).
117. M. Stern, Corrosion 14:444 (1958).
118. R. Grauer, P. J. Moreland, and G. Pini, A literature review of polarisation resistance constant (B) values for the measurement of corrosion rate, NACE, Houston, Texas (1982).
119. J. C. Scully, The Fundamentals of Corrosion, 3rd Edition, Pergamon Press, Oxford, 1990.
120. C. Gabrielli and M. Keddam, Corrosion 48:794 (1992).
121. P. R. Roberge, E. Halliop, and V. S. Sastri, Corrosion 48:447 (1992).
122. W. J. Lorenz and F. Mansfeld, Corros. Sci. 21:647 (1981).
123. Z. Nagy, in Modern Aspects of Electrochemistry, Vol. 25 (J. O. M. Bockris, B. E. Conway, and R. E. White, eds.), Plenum Press, New York, 1993, p. 135.
124. I. Epelboin, M. Keddam, and H. Takenouti, J. App. Electrochem. 2:71 (1972).
125. D. D. Macdonald, in Techniques for the Characterization of Electrodes and Electrochemical Processes (R. Varma and J. R. Selman, eds.), John Wiley & Sons, Inc., New York, 1991, p. 515.
126. G. W. Walter, Corros. Sci. 17:983 (1977).
127. G. W. Walter, Corros. Sci. 29:1039 (1989).
128. F. Mansfeld and M. Kendig, Corrosion 37:545 (1981).
129. G. Rocchini, Corros. Sci. 36:1063 (1994).
130. D. D. Macdonald, J. Electrochem. Soc. 125:1443 (1978).
131. G. W. Walter, Corros. Sci. 18:927 (1978).

132. C. G. Arnold, in Corrosion and Corrosion Protection Handbook, Vol. 19 (P. A. Schweitzer, ed.), Marcel Dekker, Inc., New York, 1983, p. 469.
133. D. D. Macdonald and M. C. H. McKubre, in Modern Aspects of Electrochemistry, Vol. 14 (J. O. M. Bockris, B. E. Conway, and R. E. White, eds.), Plenum Press, New York, 1982, p. 61.
134. D. D. Macdonald, Electrochim. Acta 35:1509 (1990).
135. J. R. Macdonald, Electrochim. Acta 35:1483 (1990).
136. D. D. Macdonald, Corrosion 46:229 (1990).
137. F. Mansfeld, Electrochim. Acta 10:1533 (1990).
138. V. A. Safanov, Soviet Electrochemistry 29:139 (1991).
139. D. C. Silverman, Corrosion 49:824 (1989).
140. J. A. Beavers, N. G. Thompson, and D. C. Silverman, Corrosion 93, NACE, 1993; p 348/2.
141. P. R. Roberge, Corrosion 94, Houston, NACE, 1994; p 318/1.
142. P. R. Roberge and V. S. Sastri, Br. Corros. J. 29:38 (1994).
143. F. Mansfeld and W. J. Lorenz, in Techniques for the Characterization of Electrodes and Electrochemical Processes (R. Varma and J. R. Selman, eds.), John Wiley & Sons, Inc., New York, 1991, p. 581.
144. H. Schweickert, W. J. Lorenz, and H. Friedburg, J. Electrochem. Soc. 127:1693 (1980).
145. K. Hladky, L. M. Callow, and J. L. Dawson, Br. Corros. J. 15:20 (1980).
146. K. Juttner, Electrochim. Acta 35:1501 (1990).
147. K. Juttner, W. J. Lorenz, M. W. Kendig, and F. Mansfeld, J. Electrochem. Soc. 135:332 (1988).
148. D. You, N. Pebere, and F. Dobosi, Corros. Sci. 34:5 (1993).
149. V. Jovancicevic, J. Electrochem. Soc. 137:349 (1990).
150. A. Cox and S. B. Lyon, Corros. Sci. 36:1177 (1994).
151. D. C. Silverman and J. E. Carrico, Corrosion 44:280 (1988).
152. B. Yang, F. Lu, and K. Sotoudeh, Corrosion 93, NACE, 1993; p 357/2.
153. F. Mansfeld, M. W. Kendig, and W. J. Lorenz, J. Electrochem. Soc. 32:290 (1985).
154. F. L. Laque and H. R. Copson, The Corrosion Resistance of Metals and Alloys, Reinhold, New York, 1963.

155. EG&G, Model 398 Electrochemical Impedance Software, Ver. 1.00, EG&G Princeton Applied Research Corporation (1993).
156. A. Bewick, M. Kalaji, and G. Larramona, J. Electroanal. Chem. 318:207 (1991).
157. L. L. Shrier and G. T. Burnstein, eds., Corrosion, Vol. 1, Butterworth-Heinemann, Oxford, 1994.
158. B. A. Boukamp, Equivalent Circuit, Ver. 4.5, University of Twente (1993).
159. M. Keddam, O. R. Mattos, and H. Takenouti, J. Electrochem Soc. 128:257 (1981).
160. J. R. Park and D. D. Macdonald, Corros. Sci. 23:295 (1983).
161. U. Schwertmann and R. M. Cornell, Iron Oxides in the Laboratory, VCH, Weinheim, 1991.
162. E. Ahlberg and J. Asbjornsson, Hydrometallurgy 34:171 (1993).
163. Y. Marinovich, S. Bailey, J. Avraamides, and S. Jayasekera, The AusIMM Annual Conference, Perth, The Australian Institute of Mining and Metallurgy, 1996; p 237 .
164. D. G. Jones, Trans. Instn. Min. Metall. C 82:1 (1974).
165. M. F. Ashby and D. R. H. Jones, Engineering Materials 2, 1st Edition, Pergamon Press, Oxford, 1986.
166. J. Flis, Corros. Sci. 10:745 (1970).
167. I. E. Grey and A. F. Reid, Inst. Min. Met. Trans. 83C:39 (1974).
168. D. J. Shaw, Introduction to Colloid and Surface Chemistry, 4th Edition, Butterworth-Heinemann, Oxford, 1991.
169. L. Formaro, Corros. Sci. 19:631 (1979).
170. T. Ohtsuka, J.-C. Ju, S. Ito, and H. Einaga, Corros. Sci. 36:1257 (1994).
171. M. E. Rice, Z. Galus, and R. N. Adams, J. Electroanal. Chem. 143:89 (1983).
172. M. T. Mouhandess, F. Chassagneux, A. Accary, and R. M. Reeves, J. Electroanal. Chem. 181:93 (1984).
173. M. T. Mouhandess, F. Chassagneux, and O. Vittori, J. Electroanal. Chem. 131:367 (1982).
174. Z. Z. Sharara and O. Vittori, Electrochim. Acta 29:1689 (1984).
175. J. M. Lecuire and Y. Pillet, J. Electroanal. Chem. 91:99 (1978).
176. R. Freour, Electrochim. Acta 30:795 (1985).
177. M. Stratmann, K. Bohenkamp, and H. J. Engell, Corros. Sci. 23:969 (1983).
178. H. H. Le and E. Ghali, J Appl. Electrochem. 23:72 (1993).

179. R. S. S. Guzman, J. R. Vilche, and A. J. Arvia, Electrochim. Acta 24:395 (1979).

180. L. S. Rajeswari, P. N. M. Das, and A. D. Damodaran, Trans. Indian Inst. Met. 43:208 (1990).

181. Article in "Industry News" Vol. 10, Chemistry in Australia, 1994, p. 564.

182. V. E. Mironov, G. L. Pashkov, T. G. Padar, T. V. Stupko, and L. K. Novikov, Russian Journal of Chemistry 37:714 (1992).